Ministry of Science and Higher Education of the Russian Federation
ITMO University

ISSN 2220-8054

NANOSYSTEMS:

PHYSICS, CHEMISTRY, MATHEMATICS

2025, volume 16(5)

Наносистемы: физика, химия, математика

2025, том 16, № 5

N A N O
Ф &Х &М

NANOSYSTEMS:

PHYSICS, CHEMISTRY, MATHEMATICS

Address: ITMO University, Kronverkskiy pr., 49, St. Petersburg 197101, Russia.
Phone: +7(812)607-02-54, **Journal site:** http://nanojournal.ifmo.ru/,
E-mail: nanojournal@itmo.ru

AIM AND SCOPE

The scope of the journal includes all areas of nano-sciences. Papers devoted to basic problems of physics, chemistry, material science and mathematics inspired by nanosystems investigations are welcomed. Both theoretical and experimental works concerning the properties and behavior of nanosystems, problems of its creation and application, mathematical methods of nanosystem studies are considered.
The journal publishes scientific reviews (up to 30 journal pages), research papers (up to 15 pages) and letters (up to 5 pages). All manuscripts are peer-reviewed. Authors are informed about the referee opinion and the Editorial decision.

CONTENT

NANOSYSTEMS:
PHYSICS, CHEMISTRY, MATHEMATICS

Yuldashev T.K., et al. *Nanosystems: Phys. Chem. Math.*, 2025, **16** (5), 563–576.
http://nanojournal.ifmo.ru

Original article

DOI 10.17586/2220-8054-2025-16-5-563-576

Nonlinear optimal control problem in a two-point boundary regime for a pseudoparabolic equation with Samarskii–Ionkin type conditions

Tursun K. Yuldashev[1,2,a], Bakhtiyar J. Kadirkulov[3,b], Aysel T. Ramazanova[4,c], Zholdoshbek Zh. Shermamatov[2,d]

[1]Tashkent State Transport University, Temiryolchilar 1, Tashkent, 100174, Uzbekistan

[2]Osh State University, Lenin Avenue, 331, Osh 723500, Kyrgyzstan

[3]Alfraganus University, Tashkent, Uzbekistan

[4]Universitat Duisburg-Essen, Essen, Germany

[a]tursun.k.yuldashev@gmail.com, [b]b.kadirkulov@afu.uz, [c]ramazanovaaysel897@gmail.com, [d]jshermamatov@oshsu.kg

Corresponding author: T. K. Yuldashev, tursun.k.yuldashev@gmail.com

ABSTRACT This paper is devoted to study a optimal movable point control problem for a pseudoparabolic equation with nonlinear control function in a two-point nonlinear boundary condition. The equation is studied with Samarskii–Ionkin type boundary conditions on spatial variable x. Spectral problem is studied and eigenvalues, eigenfunctions and optimality conditions are found. Loaded nonlinear functional equations are obtained with respect to control function. We prove the existence and uniqueness of the control function by the method of compressing mapping. The state function is determined. Convergence of the Fourier series for the state function is proved.

KEYWORDS Nonlinear loaded functional equation, pseudoparabolic equation, two-point boundary condition, Samarskii-Ionkin type conditions, eigenvalues, eigenfunctions, Fourier series, existence and uniqueness theorems

FOR CITATION Yuldashev T.K., Kadirkulov B.J., Ramazanova A.T., Shermamatov Zh.Zh. Nonlinear optimal control problem in a two-point boundary regime for a pseudoparabolic equation with Samarskii–Ionkin type conditions. *Nanosystems: Phys. Chem. Math.*, 2025, **16** (5), 563–576.

1. Formulation of the problem statement

Differential equations of mathematical physics have direct applications in the theory of nanosystems (see, for example [1–13] and [14]). Partial differential and integro-differential equations of parabolic and pseudoparabolic types with initial and boundary conditions were investigated widely by large number of scientists and have different applications in sciences and technology (see, for example [15–28]). The spectral problems for finding eigenvalues and eigenfunctions play an important role in solving mixed and boundary problems for differential equations of mathematical physics [29–37].

Optimal control theory is one of the most relevant branches of mathematical science. Many applied problems are reduced to finding the optimal control function and the corresponding state function. A large number of analytical and numerical methods for solving optimal control problems have been developed and are effectively used in solving various problems of optimization process in science and technology (see, for example, [38–50]). In the works [51–54], the time-optimal control problems for partial differential equations are studied.

It is well known that differential equations of parabolic type are associated with heat and diffusion processes. Neutron diffusion plays a significant role in the operation of nuclear reactors. The diffusion equation makes it possible to calculate the neutron density inside the core of a nuclear reactor, the neutron flux from the moderator surface, and the reflection and transmission of neutrons by biological protection structures. We note that the processes describing by parabolic equations can be studied more exactly by pseudoparabolic equations. Moreover, studying some problems for parabolic equations is more difficult than studying this problem for pseudoparabolic equations. When investigating the parabolic equation $u_t - u_{xx} = f(t,x)$ on $[0,T] \times [0,l]$ with final time condition $u(T,x) = \varphi(x)$ and the Dirichlet boundary conditions $u(t,0) = u(t,l) = 0$, we obtain the function $\exp\{\lambda_n T\}$, which goes to infinity as $\lambda_n \to \infty$, where $\lambda_n > 0$ is eigenvalues of the spectral problem $\vartheta''(x) + \lambda\,\vartheta(x) = 0, \;\; \vartheta(0) = \vartheta(l) = 0$. Consequently, the present paper is devoted to study an optimal control problem for a pseudoparabolic equation with nonlinear control function in a two-point boundary condition. Control of the function in two-point boundary condition is important in metallurgy, partially, in aluminum production. The equation is studied with Samarskii–Ionkin type boundary value conditions on spatial variable x. Samarskii–Ionkin type boundary value conditions are nonlocal. It is used in the study of processes related to the gas lift oil production.

The eigenvalues and eigenfunctions problem is studied. So, in the domain $\Omega \equiv (0,T) \times (0,1)$, we consider the equation

$$\left(\frac{\partial}{\partial t} + \frac{\partial^5}{\partial t\, \partial x^4} + \frac{\partial^4}{\partial x^4}\right) U(t,x) = f(t,x) \tag{1}$$

with boundary value conditions

$$\alpha(t)U(0,x) + \omega\beta(t)U(T,x) = \delta\big(x - \eta(t)\big)\, \varphi(t,x,p(t)), \tag{2}$$

$$U(t,1) = 0, \quad U_{xx}(t,0) = 0, \tag{3}$$

$$U_x(t,0) = U_x(t,1), \quad U_{xxx}(t,0) = U_{xxx}(t,1), \quad 0 \le t \le T, \tag{4}$$

where $\varphi(t,x,p(t))$ is nonlinear function depending from the control function $p(t)$, $f(t,x)$ is given function, $\alpha(t) \neq 0$, $\beta(t) \neq 0$ are given real functions, ω is real nonzero parameter.

The function $\eta(t) \in C[0,T]$ describes the change in the position of a moving point source in the range from zero to 1. It is defined as the solution to the following Cauchy problem

$$\eta'(t) = \omega(t,\eta(t)), \;\; \eta(0) = \eta_0 = \text{const},$$

where $\omega(t,\eta) \in C^{0,1}(\Omega)$.

We consider the control function $p(t) \in \big\{p : |\, p(t)\,| \le M^*,\ t \in [0,T],\ 0 < M^* = \text{const}\big\}$ and the following functional of quality

$$J[p] = \int\limits_0^1 \left[U(T,y) - \xi(y)\right]^2 dy + \gamma_1 \int\limits_0^T p^2(t)dt + \gamma_2 \int\limits_0^T \eta^2(t)dt, \tag{5}$$

where $0 < \gamma_\kappa = \text{const}$, $\kappa = 1,2$ and $\xi(x)$ is a given continuous function.

Problem. We find a pair of functions $\big\{U(t,x);\, p(t) \in \big\{p : |\, p(t)\,| \le M^*\big\}\big\}$, first of which satisfies the differential equation (1), the two-point boundary condition (2), the Samarskii-Ionkin type boundary conditions (3), (4), belongs to the class of functions

$$U \in C^{1,3}_{t,x}(\overline{\Omega}), \quad U_{txxx} \in C(\Omega), \quad U_{xxxx} \in C(\Omega), \tag{6}$$

and the second of which deliver a minimum to the functional (5).

2. Some auxiliary materials about Riesz bases

Let $\big\{\vartheta_n(x)\big\}$ and $\big\{\sigma_n(x)\big\}$ be two complete systems of functions from $L_2(a,b)$. Let us denote by $\big(\vartheta,\sigma\big)_0$ the scalar product of functions $\vartheta(x)$ and $\sigma(x)$ in $L_2(a,b)$:

$$\big(\vartheta,\sigma\big)_0 = \big(\vartheta,\sigma\big)_{L_2(a,b)} = \int\limits_a^b \vartheta(x)\sigma(x)dx.$$

We use some known facts from the book [55].

1. Let the systems $\big\{\vartheta_n(x)\big\}$ and $\big\{\sigma_n(x)\big\}$ form a biorthonormal system in some interval $[a,b]$:

$$\big(\vartheta_n,\sigma_k\big)_0 = \int\limits_a^b \vartheta_n\sigma_k dx = \delta_{nk} = \begin{cases} 0, & n \neq k, \\ 1, & n = k. \end{cases}$$

Then the system $\big\{\sigma_n(x)\big\}$ is called biorthogonally adjoint to the system $\big\{\vartheta_n(x)\big\}$ in the interval $[a,b]$.

2. Let no element of the system $\big\{\vartheta_n(x)\big\}$ belongs to the closure of the linear span of the other elements of this system. Then the system $\big\{\vartheta_n(x)\big\}$ is called minimal in $L_2(a,b)$.

The minimality of the system ensures the existence of a biorthogonally conjugate system.

3. The biorthogonal expansion of a function $f \in L_2(a,b)$ in a system $\big\{\vartheta_n(x)\big\}$ is a series

$$f(x) \sim \sum_{n=1}^{\infty} c_n\vartheta_n(x),$$

where $c_n = (f,\sigma_n)_0$.

4. Let for any function $f \in L_2(a,b)$ there hold

$$\sum_{n=1}^{\infty} \big|\, \big(f,\sigma_n\big)_0\,\big|^2 < \infty,$$

where $\big\{\sigma_n\big\}$ is biorthogonally conjugate system to $\big\{\vartheta_n(x)\big\}$. Then a complete and minimal system of functions $\big\{\vartheta_n(x)\big\}$ is called Besselian.

5. A complete and minimal system of functions $\big\{\vartheta_n(x)\big\}$ is called a Hilbert system, if for any sequence $\big\{c_n\big\}$ with

$\sum_{k=1}^{\infty} c_n^2 < \infty$ there is one and only one function $f \in L_2(a,b)$, for which $\{c_n\} = (f, \sigma_n)_0$ are coefficients of its biorthogonal expansion in $\{\vartheta_n(x)\}$.

6. A complete and minimal system is called a Riesz basis, if it is both Bessel and Hilbert basis.

Theorem 1 ([56]). The following statements are equivalent:

1). The sequence of functions $\{\sigma_j(x)\}_1^{\infty}$ forms a basis, equivalent to the orthonormal one, in the space R;

2). The sequence of functions $\{\sigma_j(x)\}_1^{\infty}$ will be an orthonormal basis of the space R with the appropriate replacement of the scalar product (f,g) by some new one $(f,g)_1$, topologically equivalent to the original one;

3). The sequence of functions $\{\sigma_j(x)\}_1^{\infty}$ is complete in R and there exist positive constants $a_1,\ a_2$, such that for any natural n and any complex numbers $\gamma_1, \gamma_2, ..., \gamma_n$ there holds

$$a_2 \sum_{j=1}^{n} |\gamma_j|^2 \le \sum_{j=1}^{n} |\gamma_j \sigma_j|^2 \le a_1 \sum_{j=1}^{n} |\gamma_j|^2;$$

4). The sequence of functions $\{\sigma_j(x)\}_1^{\infty}$ is complete in R and its Gram matrix $(\sigma_j(x), \sigma_k(x))_1^{\infty}$ generates a bounded invertible operator in space ℓ_2;

5). The sequence of functions $\{\sigma_j(x)\}_1^{\infty}$ is complete in R, corresponds to complete biorthogonal sequence of functions $\{\chi_j(x)\}_1^{\infty}$ and for any $f(x) \in R$ it is true that

$$\sum_{j=1}^{n} \left|(f, \sigma_j)\right|^2 < \infty, \quad \sum_{j=1}^{n} \left|(f, \chi_j)\right|^2 < \infty.$$

Lemma 1([57]). Let be $f(x) \in L_2(0,1)$ and $a_k = \int_0^1 f(x) e^{-\lambda k x} dx,\ b_k = \int_0^1 f(x) e^{\lambda k (x-1)} dx$, where λ is an arbitrary complex number $\lambda = \alpha + i\beta$ with a positive real part $\alpha > 0$. Then the series $\sum_{k=1}^{\infty} |\, a_k \,|^2,\ \sum_{k=1}^{\infty} |\, b_k \,|^2$ converges.

3. Eigenvalues and eigenfunctions

First, we consider the following homogeneous differential equation

$$\frac{\partial U(t,x)}{\partial t} + \frac{\partial^5 U(t,x)}{\partial t\, \partial x^4} + \frac{\partial^4 U(t,x)}{\partial x^4} = 0. \tag{7}$$

We will look for a non-trivial particular solution of the equation in the form $U(t,x) = u(t) \cdot \vartheta(x)$. Substituting this product of functions, depending on different variables, into equation (7), we obtain

$$-\frac{u'(t)}{u'(t) + u(t)} = \frac{\vartheta^{(IV)}(x)}{\vartheta(x)}.$$

Hence, equating second fraction into λ, we obtain

$$\vartheta^{(IV)}(x) - \lambda \vartheta(x) = 0, \quad \lambda \ge 0. \tag{8}$$

Using conditions (3) and (4), from the product of two functions, we obtain conditions for the eigenvalues λ and eigenfunctions $\vartheta(x)$:

$$\vartheta(1) = 0, \quad \vartheta''(0) = 0, \quad \vartheta'(0) = \vartheta'(1), \quad \vartheta'''(0) = \vartheta'''(1). \tag{9}$$

Solving the spectral problem (8), (9), we derive the eigenvalues

$$\lambda_n = (2\pi n)^4, \quad n = 0, 1, 2, \ ... \tag{10}$$

Eigenfunctions, corresponding to the eigenvalues (10), have the forms

$$\vartheta_0(x) = 2(1-x), \quad \vartheta_{1n}(x) = -2\sin 2\pi n x, \quad \vartheta_{2n}(x) = \frac{e^{2\pi n x} - e^{2\pi n (1-x)}}{e^{2\pi n} - 1} - \cos 2\pi n x. \tag{11}$$

The spectral problem (8), (9) is not self-adjoint and it is easy to see that the following problem is adjoint to it

$$\sigma^{(IV)}(x) - \lambda \sigma(x) = 0, \quad 0 < x < 1, \tag{12}$$

$$\sigma(0) = \sigma(1), \quad \sigma'(1) = 0, \quad \sigma''(0) = \sigma''(1), \quad \sigma'''(0) = 0. \tag{13}$$

We also consider adjoint to it problem (12), (13). Solving this problem, it is not difficult to see that the eigenfunctions, corresponding to eigenvalues (10), have the form

$$\sigma_0(x) = 1, \quad \sigma_{1n}(x) = \frac{e^{2\pi n x} + e^{2\pi n (1-x)}}{e^{2\pi n} - 1} - \sin 2\pi n x, \quad \sigma_{2n}(x) = -2\cos 2\pi n x. \tag{14}$$

It should be noted that (11) and (14) are non-orthogonal system of functions. For example, for system (11), we have

$$\left(\vartheta_0(x),\, \vartheta_{1,n}(x)\right)_0 = -4\int\limits_0^1 (1-x)\sin 2\pi nx dx = -\frac{2}{\pi n} \neq 0.$$

Let us study the issues of the basis of systems (11) and (14) in $L_2(0,1)$.

Lemma 2. Systems of functions (11) and (14) are biorthogonal systems in $L_2(0,1)$:

$$\left(\vartheta_0, \sigma_0\right)_0 = 1,\ \left(\vartheta_{ik}, \sigma_{jn}\right)_0 = \begin{cases} 1, & k=n,\ i=j \\ 0, & k\neq n,\ i\neq j \end{cases}, \quad i,j=1,2, \quad n,k=1,2,\ ...$$

Proof. We present the proof of Lemma 2 for the functions $\vartheta_{1n}(x)$ and $\sigma_{1n}(x)$. We calculate the integral

$$\left(\vartheta_{1k}, \sigma_{1n}\right)_0 = -\frac{2}{e^{2\pi n}-1}\int\limits_0^1 (e^{2\pi nx} + e^{2\pi n(1-x)})\sin 2\pi kx dx + 2\int\limits_0^1 \sin 2\pi nx \sin 2\pi kx dx = I_{kn} + J_{kn},$$

where

$$I_{kn} = -\frac{2}{e^{2\pi n}-1}\int\limits_0^1 \left(e^{2\pi nx} + e^{2\pi n(1-x)}\right)\sin 2\pi kx dx = 0, \quad k,n \in N,$$

$$J_{kn} = 2\int\limits_0^1 \sin 2\pi kx \cdot \sin 2\pi nx dx = \begin{cases} 1, & k=n \\ 0, & k\neq n \end{cases}, \quad k,n \in N.$$

Consequently, $(\vartheta_{1n}, \sigma_{1n})_0 = 1$ for $k=n$ and $(\vartheta_{1n}, \sigma_{1n})_0 = 0$ for $k\neq n$. The Lemma 2 is proved. □

Lemma 3. The systems of functions (11) and (14) are minimal in $L_2(0,1)$.

The *proof* of Lemma 3 follows from the existence of a biorthonormal system which was established in Lemma 2.

Theorem 2. The system of functions (11) and (14) is complete in the space $L_2(0,1)$.

Proof. First, we prove the completeness of (11). Assume the opposite, let the system of functions (11) be incomplete in $L_2(0,1)$. Then there exists a function $\psi(x)$ from $L_2(0,1)$, that is orthogonal to all functions of system (11). We will expand the function $\psi(x)$ into the Fourier series

$$\psi(x) = a_0 + \sum_{n=1}^{\infty}(a_n \cos 2\pi nx + b_n \sin 2\pi nx),$$

which converges in $L_2(0,1)$. Since $\psi(x)$ is orthogonal to the system $\left\{-2\sin 2\pi nx\right\}_{n=1}^{\infty}$, the last expansion will take the form

$$\psi(x) = a_0 + \sum_{n=1}^{\infty} a_n \cos 2\pi nx. \tag{15}$$

By assumption, $\psi(x)$ is orthogonal to all functions of the form $\vartheta_0(x)$, $\vartheta_{2k}(x)$. Next, multiplying the series (15) successively by these functions and integrating over the interval $[0,1]$, we have

$$0 = 2\int\limits_0^1 \psi(x)(1-x)dx = 2a_0\int\limits_0^1 (1-x)dx + 2\sum_{n=1}^{\infty} a_n \int\limits_0^1 (1-x)\cos 2\pi nx dx = a_0,$$

$$0 = \sum_{n=1}^{\infty} a_n \int\limits_0^1 \left(\frac{e^{2\pi kx} - e^{2\pi k(1-x)}}{e^{2\pi k}-1} - \cos 2\pi kx\right)\cos 2\pi nx dx = -\frac{1}{2}a_k, \quad k=1,2,3,\ ...$$

Hence, it follows that $a_k = 0,\ \ k = 0,1,2,\ ...$ Therefore, from (15), we obtain that $\psi(x) = 0$ on $[0,1]$ which contradicts the condition $\psi(x) \neq 0$. Thus, system (11) is complete in the space $L_2(0,1)$.

Now, we will prove the completeness of system (14). Let there $\psi(x)$ be a function from $L_2(0,1)$, different from zero, orthogonal to all functions of system (14). Since the function $\psi(x)$ is orthogonal to system $\{-2\cos 2\pi nx\}_{n=0}^{\infty}$, it can be represented in $L_2(0,1)$ as a sine series

$$\psi(x) = \sum_{n=1}^{\infty} b_n \sin 2\pi nx. \tag{16}$$

Next, multiplying the last series by $\sigma_{1k}(x)$ and integrating over the interval $[0,1]$, taking into account the orthogonality of the functions $\psi(x)$ and $\sigma_{1k}(x)$, we obtain

$$0=\sum_{n=0}^{\infty}b_n\int\limits_0^1\left(\frac{e^{2\pi kx}+e^{2\pi k(1-x)}}{e^{2\pi k}-1}-\sin 2\pi kx\right)\sin 2\pi nxdx=-\frac{1}{2}b_k,\quad k=1,2,\ \dots,$$

i.,e. $b_k=0,\ n=1,2,\dots$ Then from (16), it follows that $\psi(x)=0$ on $[0,1]$. Consequently, the system (14) is complete in $L_2(0,1)$. Theorem 2 is proved. □

Theorem 3. The system of functions (13) and (14) forms the Riesz basis in $L_2(0,1)$.

Proof. To prove the Riesz basis property of systems (11) and (14), according to Theorem 1, it is sufficient to establish the completeness of these systems and the convergence for any $\psi(x)\in L_2(0,1)$ of the following series:

$$(\psi(x),2(1-x))_0^2+\sum_{n=1}^{\infty}(\psi(x),-2\sin 2\pi nx)_0^2+$$

$$+\sum_{n=1}^{\infty}\left(\psi(x),\frac{1}{e^{2\pi n}-1}\left(e^{2\pi nx}-e^{2\pi n(1-x)}\right)-\cos 2\pi nx\right)_0^2,\tag{17}$$

$$(\psi(x),1)_0^2+\sum_{n=1}^{\infty}(\psi(x),-2\cos 2\pi nx)_0^2+$$

$$+\sum_{n=1}^{\infty}\left(\frac{1}{e^{2\pi n}-1}(e^{2\pi nx}+e^{2\pi n(1-x)})-\sin 2\pi nx,\psi(x)\right)_0^2.\tag{18}$$

The completeness of systems (11) and (14) follows from Lemma 2 and therefore we show the convergence of series (17) and (18). Let us consider the series (11) and use the notation

$$I_1=4\big(\psi(x),\,(1-x)\big)_0^2,\quad I_2=4\sum_{n=1}^{\infty}\big(\psi(x),\,\sin 2\pi nx\big)_0^2,$$

$$I_3=\sum_{n=1}^{\infty}\left(\psi(x),\frac{e^{2\pi nx}-e^{2\pi n(1-x)}}{e^{2\pi n}-1}-\cos 2\pi nx\right)_0^2.$$

Applying the Cauchy-Shwartz inequality, for I_1 we obtain

$$I_1=4\left(\int\limits_0^1(1-x)\psi(x)dx\right)^2\le 4\int\limits_0^1(1-x)^2dx\int\limits_0^1\psi^2(x)dx=\frac{4}{3}\parallel\psi(x)\parallel_{L_2(0,1)}^2<\infty.$$

Further, we have

$$I_2=4\sum_{n=1}^{\infty}\big(\psi(x),\sin 2\pi nx\big)_0^2=2\sum_{n=1}^{\infty}\big(\psi(x),\sqrt{2}\sin 2\pi nx\big)^2=2\sum_{n=1}^{\infty}c_n^2,$$

where $c_n=\big(\psi(x),\sqrt{2}\sin 2\pi nx\big)$ are the Fourier coefficients of a function $\psi(x)$ in an orthonormal system $\big\{\sqrt{2}\sin 2\pi nx\big\}$. Hence, applying Bessel's inequality, we obtain that

$$I_2=2\sum_{n=1}^{\infty}c_n^2\le 2\parallel\psi(x)\parallel_{L_2(0,1)}^2<\infty.$$

Next, we consider I_3. Since

$$A=\left(\left(\psi(x),\frac{e^{2\pi nx}-e^{2\pi n(1-x)}}{e^{2\pi n}-1}\right)-\big(\psi(x),\cos 2\pi nx\big)\right)_0^2,$$

applying the inequality $(a+b)^2\le 2\big(a^2+b^2\big)$, we obtain

$$A\le 2\left(\left(\psi(x),\frac{e^{2\pi nx}}{e^{2\pi n}-1}\right)-\left(\psi(x),\frac{e^{2\pi n(1-x)}}{e^{2\pi n}-1}\right)\right)_0^2+2\big(\psi(x),\cos 2\pi nx\big)_0^2.$$

Applying the previous inequality again, we get that

$$A\le 4\left(\psi(x),\frac{e^{2\pi nx}}{e^{2\pi n}-1}\right)_0^2+4\left(\psi(x),\frac{e^{2\pi n(1-x)}}{e^{2\pi n}-1}\right)_0^2+2\left(\psi(x),\cos 2\pi nx\right)_0^2.$$

Hence, we obtain

$$I_3 \le 4\sum_{n=1}^{\infty}\left(\psi(x), \frac{e^{2\pi nx}}{e^{2\pi n}-1}\right)_0^2 + 4\sum_{n=1}^{\infty}\left(\psi(x), \frac{e^{2\pi n(1-x)}}{e^{2\pi n}-1}\right)_0^2 + 2\sum_{n=1}^{\infty}\left(\psi(x), \cos 2\pi nx\right)_0^2 = J_1 + J_2 + J_3.$$

For J_3, we have

$$J_3 = 2\sum_{n=1}^{\infty}\left(\psi(x), \cos 2\pi nx\right)^2 = \sum_{n=1}^{\infty} a_n^2,$$

where $a_n = \left(\psi(x), \sqrt{2}\cos 2\pi nx\right)$ are the Fourier coefficients for function $\psi(x)$ in orthonormal system $\left\{\sqrt{2}\cos 2\pi nx\right\}$. Then, applying Bessel's inequality, we obtain that

$$J_3 = \sum_{n=1}^{\infty} a_n^2 \le \| \psi(x) \|_{L_2(0,1)}^2 < \infty.$$

Since

$$\left(\psi(x), \frac{e^{2\pi nx}}{e^{2\pi n}-1}\right)_0^2 \le 4\left(\int_0^1 \psi(x) e^{2\pi n(x-1)} dx\right)^2,$$

for J_1, we derive

$$J_1 \le 16\sum_{n=1}^{\infty}\left(\int_0^1 \psi(x) e^{2\pi n(x-1)} dx\right)^2 = 16\sum_{n=1}^{\infty} b_n^2, \quad b_n = \int_0^1 \psi(x) e^{2\pi n(1-x)} dx.$$

Hence, taking into account Lemma 1, we obtain that J_1 is finite. Similarly, we obtain that J_2 is also finite. Thus, the series I_1 and I_2 converge. Therefore, the series (17) also converges. The convergence of the series (18) is proved by similar way. Theorem 3 is proved. □

4. Construction of solution of the boundary value problem

Taking into account the formulas (11) and (14) we look for a solution to the problem (1)-(4) in the form of the following Fourier series:

$$U(t,x) = u_0(t)\,\vartheta_0(x) + \sum_{n=1}^{\infty}\left(u_{1,n}(t)\,\vartheta_{1,n}(x) + u_{2,n}(t)\,\vartheta_{2,n}(x)\right), \tag{19}$$

where

$$u_0(t) = \int_0^1 U(t,y)\sigma_0(y)dy, \quad u_{1,n}(t) = \int_0^1 U(t,y)\sigma_{1,n}(y)dy, \tag{20}$$

$$u_{2,n}(t) = \int_0^1 U(t,y)\sigma_{2,n}(y)dy. \tag{21}$$

Let the function $U(t,x)$ be a solution to the mixed problem (1)-(4). Then, substituting representation (19) into equation (1) and taking (11) and (14) into account, we obtain

$$u_0'(t)\vartheta_0(x) + \sum_{n=1}^{\infty}\left(u_{1,n}'(t)\,\vartheta_{1,n}(x) + u_{2,n}'(t)\,\vartheta_{2,n}(x)\right) +$$

$$+\sum_{n=1}^{\infty}\lambda_n\left[u_{1,n}'(t)\,\vartheta_{1,n}(x) + u_{2,n}'(t)\vartheta_{2,n}(x)\right] + \sum_{n=1}^{\infty}\lambda_n\left[u_{1,n}(t)\,\vartheta_{1,n}(x) + u_{2,n}(t)\vartheta_{2,n}(x)\right] +$$

$$= f_0(t)\vartheta_0(x) + \sum_{n=1}^{\infty}\Big(f_{1,n}(t)\,\vartheta_{2,n}(x) + f_{2,n}(t)\,\vartheta_{2,n}(x)\Big),$$

where

$$f_0(t) = \int_0^1 f(t,y)\sigma_0(y)dy, \tag{22}$$

$$f_{\kappa,n}(t) = \int_0^1 f(t,y)\sigma_{\kappa,n}(y)dy. \tag{23}$$

Hence, by virtue of (20)-(23), we obtain

$$u_0'(t) = f_0(t), \tag{24}$$

$$u'_{\kappa,n}(t) + \mu_n u_{\kappa,n}(t) = \frac{f_{\kappa,n}(t)}{1+\lambda_n}, \quad \kappa = 1,2, \tag{25}$$

where $\mu_n = \dfrac{\lambda_n}{1+\lambda_n}$, $\quad \lambda_n = (2n\pi)^4$. Taking into account the formulas (11) and (14), we consider the function $\varphi(x)$ as in the case of (19):

$$\varphi(t,x,p) = \varphi_0(t,p)\,\vartheta_0(x) + \sum_{n=1}^{\infty}\Big(\varphi_{1,n}(t,p)\,\vartheta_{1,n}(x) + \varphi_{2,n}(t,p)\,\vartheta_{2,n}(x)\Big). \tag{26}$$

The differential equation (24) is simple. The differential equation (25) is the countable system of differential equations. Taking (26) into account, from the two-point condition (2), we obtain

$$\alpha(t)u_0(0) + \omega\beta(t)u_0(T) = \int_0^1 \big[\alpha(t)U_0(0,y) + \omega\beta(t)U_0(T,y)\big]\sigma_0(y)dy =$$

$$= \int_0^1 \varphi_0(t,y,p(t))\sigma_0(y)dy = \varphi_0(t,p(t)), \tag{27}$$

$$\alpha(t)u_{\kappa,n}(0) + \omega\beta(t)u_{\kappa,n}(T) = \int_0^1 \Big[\alpha(t)U_\kappa(0,y) + \omega\beta(t)U_\kappa(T,y)\Big]\sigma_{\kappa,n}(y)dy =$$

$$= \int_0^1 \varphi_\kappa(t,y,p(t))\sigma_{\kappa,n}(y)dy = \varphi_{\kappa,n}(t,p(t)), \quad \kappa = 1,2. \tag{28}$$

First, we solve equation (24):

$$u_0(t) = u_0(0) + \int_0^t f_0(s)ds. \tag{29}$$

Substituting the presentation (29) into two-point boundary condition (27), we obtain

$$u_0(0) = \frac{\varphi_0(t,p(t))}{\alpha(t)+\omega\beta(t)} - \omega\,\frac{\beta(t)}{\alpha(t)+\omega\beta(t)}\int_0^T f_0(s)ds. \tag{30}$$

Substituting the presentation (30) into (29), we have

$$u_0(t) = a_0(t)\varphi_0(t,p(t)) + \int_0^T K_0(t,s)f_0(s)ds, \tag{31}$$

where $a_0(t) = (\alpha(t)+\omega\beta(t))^{-1}$, $K_0(t,s) = \begin{cases} 1-\omega\,a_0(t)\beta(t), & 0 \le s \le t, \\ -\omega\,a_0(t)\beta(t), & s \le t \le T. \end{cases}$

We consider such values of the parameter ω, for which $\alpha(t)+\omega\beta(t) \neq 0$. These values of the parameter ω are called the first regular values of the parameter ω. For the first regular values of the parameter ω, the presentation (31) is the solution of the problem (24), (27).

Now we solve the countable system (25) of ordinary differential equations with two-point boundary value condition (28). In this purpose, we rewrite the equation (20) as

$$u'_{\kappa,n}(t) = -\mu_n u_{\kappa,n}(t) + \frac{f_{\kappa,n}(t)}{1+\lambda_n}, \quad \kappa = 1,2. \tag{32}$$

Solving equation (32), we obtain

$$u_{\kappa,n}(t) = u_{\kappa,n}(0)\exp\big\{-\mu_n t\big\} + \frac{1}{1+\lambda_n}\int_0^t \exp\big\{-\mu_n(t-s)\big\}f_{\kappa,n}(s)ds, \quad \kappa = 1,2. \tag{33}$$

Substituting the presentation (33) into two-point boundary condition (30), we get

$$u_{\kappa,n}(0) = \frac{\varphi_{\kappa,n}(t,p(t))}{\alpha(t)+\omega\beta(t)\exp\big\{-\mu_n T\big\}} -$$

$$-\frac{\omega}{1+\lambda_n}\,\frac{\beta(t)}{\alpha(t)+\omega\beta(t)\exp\big\{-\mu_n T\big\}}\int_0^T \exp\big\{-\mu_n(T-s)\big\}f_{\kappa,n}(s)ds, \quad \kappa = 1,2.$$

Hence, taking into account (33), we derive that

$$u_{\kappa,n}(t)=\varphi_{\kappa,n}(t,p(t))\frac{\exp\{\mu_n(T-t\}}{a_{2,n}(t)}+\frac{1}{1+\lambda_n}\int\limits_0^T K_n(t,s)f_{\kappa,n}(s)ds,\ \ \kappa=1,2, \tag{34}$$

where $K_n(t,s)=\begin{cases}\exp\big\{-\mu_n(t-s)\big\}-\dfrac{\omega\beta(t)}{a_{2,n}(t)}\exp\big\{-\mu_n(t-s)\big\}, & 0\le s\le t,\\ -\dfrac{\omega\beta(t)}{a_{2,n}(t)}\exp\big\{-\mu_n(t-s)\big\}, & t\le s\le T,\end{cases}$

$a_{2,n}(t)=\omega\beta(t)+\alpha(t)\exp\{\mu_nT\}$, $\mu_n=\dfrac{\lambda_n}{1+\lambda_n}$, $\lambda_n=\big(2n\pi\big)^4$, $n=1,\,2,\,...$

We consider such values of the parameter ω, for which $a_{2,n}(t)=\omega\beta(t)+\alpha(t)\exp\{\mu_nT\}\neq 0$. These values of the parameter ω are called the second regular values of the parameter ω. For the second regular values of the parameter ω, presentation (34) is the representation of solution of the problem (32), (30).

The sets of the first and the second regular values of the parameter ω is denoted by Λ_1 and Λ_2, respectively. We consider the intersection $\Lambda_1\cap\Lambda_2$ of these values of the parameter ω. So, for regular values of the parameter ω from this intersection $\Lambda_1\cap\Lambda_2$, we have to consider the Fourier series

$$U(t,x)=\vartheta_0(\eta(t))\,a_0(t)\varphi_0(t,p(t))+\vartheta_0(x)\int\limits_0^T K_0(t,s)\,f_0(s)ds+$$

$$+\sum_{n=1}^{\infty}\sum_{\kappa=1}^{2}\left[\vartheta_{\kappa,n}(\eta(t))\,\varphi_{\kappa,n}(t,p(t))a_{1,n}(t)+\vartheta_{\kappa,n}(x)\frac{1}{1+\lambda_n}\int\limits_0^T K_n(t,s)\,f_{\kappa,n}(s)ds\right]. \tag{35}$$

Smoothness condition S**.** Let the functions $\varphi(t,x,p(t))$ and $f(t,x)$ be satisfying the conditions

$$\varphi_\kappa(t,x,p)\in C^{0,5}_{t,x}(\bar\Omega),\quad \varphi_\kappa(t,1,p)=\frac{\partial^2}{\partial x^2}\varphi_\kappa(t,0,p)=\frac{\partial^4}{\partial x^4}\varphi_\kappa(t,1,p)=0,$$

$$\frac{\partial}{\partial x}\varphi_\kappa(t,0,p)=\frac{\partial}{\partial x}\varphi_\kappa(t,1,p),\quad \frac{\partial^3}{\partial x^3}\varphi_\kappa(t,0,p)=\frac{\partial^3}{\partial x^3}\varphi_\kappa(t,1,p),$$

$$f(t,x)\in C^{0,1}_{t,x}(\bar\Omega\times R),\quad f(t,0)=0.$$

Then, we integrate by parts (27), (28) five times and (22), (23) one time with respect to variable x, respectively, and obtain

$$\varphi_{1,n}(t,p)=-\left(\frac{1}{2\pi}\right)^5\frac{\varphi^{(V)}_{1,n}(t,p)}{n^5},$$

$$\varphi^{(V)}_{1,n}(t,p)=\int\limits_0^1\frac{\partial^5\varphi(t,z,p)}{\partial(z)^5}\left(\frac{e^{2\pi nz}-e^{2\pi n(1-z)}}{e^{2\pi n}-1}+\cos 2\pi nz\right)dz,\ \ z=\eta(t),$$

$$\varphi_{2,n}(t,p)=\left(\frac{1}{2\pi}\right)^5\frac{\varphi^{(V)}_{2,n}(t,p)}{n^5},\quad \varphi^{(V)}_{2,n}(t,p)=2\int\limits_0^1\frac{\partial^5\,\varphi(t,z,p)}{\partial(z)^5}\sin 2\pi nz\,dz,\ \ z=\eta(t),$$

$$f_{1,n}(t)=-\frac{1}{2\pi}\frac{f^{(I)}_{1,n}(t)}{n},\quad f^{(I)}_{1,n}(t)=\int\limits_0^1\frac{\partial f(t,y)}{\partial y}\left(\frac{e^{2\pi ny}-e^{2\pi n(1-y)}}{e^{2\pi n}-1}+\cos 2\pi ny\right)dy,$$

$$f_{2,n}(t)=\frac{1}{2\pi}\frac{f^{(I)}_{2,n}(t)}{n},\quad f^{(I)}_{2,n}(t)=2\int\limits_0^1\frac{\partial f(t,y)}{\partial y}\sin 2\pi ny\,dy.$$

In addition, we have

$$\Big\|\,\vec\varphi^{(V)}_\kappa(t,p)\,\Big\|_{\ell_2}\le C_1\left\|\,\frac{\partial^5\varphi_k(t,z,p)}{\partial\,z^5}\,\right\|_{L_2[0,1]},\quad \Big\|\,\vec f^{(I)}_\kappa(t)\,\Big\|_{\ell_2}\le C_2\left\|\,\frac{\partial f_\kappa(t,x)}{\partial\,x}\,\right\|_{L_2(0,1)}.$$

5. Unique solvability of the problem (1)–(4)

Theorem 4. If there exists a solution of Problem (1)-(4), then it is unique for regular values of the parameter ω from the intersection $\Lambda_1 \cap \Lambda_2$.

Proof. We consider the regular values of the parameter ω from the intersection $\Lambda_1 \cap \Lambda_2$. Suppose that there exist two different solutions $\overline{U}_1(t,x)$ and $\overline{U}_2(t,x)$ to the problem (1)-(4). Then the difference $U(t,x) = \overline{U}_1(t,x) - \overline{U}_2(t,x)$ is a solution of equation (1), satisfying the conditions (2)-(4) with functions $\varphi(t,x,p) \equiv 0,\ \ f(t,x) \equiv 0$. Then, it follows from formulas (20)-(23) and (35) that $u_{\kappa,n}(t) = \int\limits_0^1 U(t,y)\sigma_{\kappa,n}(y)dy \equiv 0,\ \ \kappa = 1,2$. From this, due to the completeness of system (14) in the space $L_2(0,1)$, it follows that $U(t,x) = 0$ is valid almost everywhere on $[0,1]$ for any $t \in [0,T]$. Since $U \in C(\bar{\Omega})$, it follows that $U(x,t) \equiv 0$ in $\bar{\Omega}$. Theorem 4 is proved. □

Theorem 5. Let the smoothness conditions S be satisfied. Then, for the regular values of the parameter ω from the intersection $\Lambda_1 \cap \Lambda_2$ and fixed values of control function $p(t)$, the function (35) belongs to the class of functions (6).

Proof. We consider the series (35) and

$$\frac{\partial^4}{\partial t \partial x^3} U_\kappa(t,x) = \sum_{n=1}^{\infty} \left[\vartheta'''_{\kappa,n}(z) \left(a_{1,n}(t)\right)' \varphi_{\kappa,n}(t,p(t)) + \vartheta'''_{\kappa,n}(z)\, a_{1,n}(t)\, \frac{d}{dt}\varphi_{\kappa,n}(t,p(t)) + \right.$$

$$\left. + \frac{\vartheta'''_{\kappa,n}(x)}{1+\lambda_n} \int\limits_0^T K'_n(t,s) f_{\kappa,n}(s) ds \right], \tag{36}$$

$$\frac{\partial^5}{\partial t \partial x^4} U_\kappa(t,x) = \sum_{n=1}^{\infty} \lambda_n \left[\vartheta_{\kappa,n}(z) \left(a_{1,n}(t)\right)' \varphi_{\kappa,n}(t,p(t)) + \vartheta_{\kappa,n}(z)\, a_{1,n}(t)\, \frac{d}{dt}\varphi_{\kappa,n}(t,p(t)) + \right.$$

$$\left. + \frac{\vartheta_{\kappa,n}(x)}{1+\lambda_n} \int\limits_0^T K'_n(t,s) f_{\kappa,n}(s) ds \right], \tag{37}$$

$$\frac{\partial^4}{\partial x^4} U_\kappa(t,x) = \sum_{n=1}^{\infty} \lambda_n \left[\vartheta_{\kappa,n}(z)\, a_{1,n}(t)\, \varphi_{\kappa,n}(t,p(t)) + \frac{\vartheta_{\kappa,n}(x)}{1+\lambda_n} \int\limits_0^T K'_n(t,s) f_{\kappa,n}(s) ds \right], \tag{38}$$

where $\kappa = 1,2,\ z = \eta(t)$.

The proofs of convergence of the series (36)-(38) are similar. So, we will prove of convergence for the series (37). Applying the smoothness conditions to (37), we have:

$$\left| \frac{\partial^5 U_\kappa(t,x)}{\partial t \partial x^4} \right| \le \chi_0 \max_{0 \le t \le T} \left[\chi_1 \frac{1}{(2\pi)^5} \left(\left\| \frac{\partial^5 \varphi(t,x,p(t))}{\partial\, x^5} \right\|_{L_2(0,1)} + \left\| \frac{d}{dt} \frac{\partial^5 \varphi(t,x,p(t))}{\partial\, x^5} \right\|_{L_2(0,1)} \right) + \right.$$

$$\left. + \frac{1}{2\pi} \left\| \frac{\partial f(t,x)}{\partial x} \right\|_{L_2(0,1)} \right] < \infty, \tag{39}$$

where $\chi_0 = \max \left\{ \| a_{1,n}(t) \|;\ \| \left(a_{1,n}(t)\right)' \|;\ \max\limits_{t \in [0,T]} \int\limits_0^T | K'_n(t,s) |\, ds \right\}$, $\chi_1 = \sqrt{\sum\limits_{n=1}^{\infty} \frac{1}{n^{10}}}$,

$\chi_2 = \sqrt{\sum\limits_{n=1}^{\infty} \frac{1}{n^2}} = \sqrt{\frac{\pi^2}{6}}$.

From estimate (39), it implies the convergence of the series (37). The convergence of the remaining series is proved similarly. Theorem 5 is proved. □

6. Optimal control function

Let $p^*(t)$ is optimal control function: $\Delta J\left[p^*(t)\right] = J\left[p^*(t) + \Delta p^*(t)\right] - J\left[p^*(t)\right] \ge 0$, where $p^*(t) + \Delta p^*(t) \in C[0,T]$. We consider the following function

$$Q_0(t,\eta(t))\vartheta_0(\eta(t))\left[a_0(t)\varphi_0\left(t,p_0^*(t)\right) + b_0(t)\right] = \gamma_1 \left[p_0^*(t)\right]^2 + \gamma_2 \left[\eta(t)\right]^2, \tag{40}$$

$$Q_\kappa(t,\eta(t)) \left[\sum_{n=1}^{\infty} a_{1,n}(t)\vartheta_{\kappa,n}(\eta(t))\varphi_{\kappa,n}(t,p_\kappa^*(t)) + \sum_{n=1}^{\infty} \frac{b_{\kappa,n}(t)}{1+\lambda_n}\vartheta_{\kappa,n}(\eta(t)) \right] =$$

$$= \gamma_1 \left[p_\kappa^*(t)\right]^2 + \gamma_2 \left[\eta(t)\right]^2, \tag{41}$$

where

$$a_0(t)=\frac{1}{\alpha(t)+\omega\beta(t)},\quad a_{1,n}(t)=\frac{\exp\left\{\mu_n(T-t\right\}}{a_{2,n}(t)},$$

$$b_0(t)=\int\limits_0^T K_0(t,s)\,f_0(s)ds,\quad b_{\kappa,n}(t)=\int\limits_0^T K_n(t,s)f_{\kappa,n}(s)ds,\quad \kappa=1,2.$$

The functions $Q_j(t,x)$ are defined by solving the following mixed problem

$$Q_{jt}(t,x)+Q_{jtxxxx}(t,x)-Q_{jxxxx}(t,x)=0,\quad j=0,1,2,\quad (t,x)\in\Omega, \tag{42}$$

$$Q_j(T,x)=-2\left[U_j(T,x)-\xi_j(x)\right],\quad Q_j(t,1)=0,\quad Q_{jxx}(t,0)=0, \tag{43}$$

$$Q_{jx}(t,0)=Q_{jx}(t,1),\quad Q_{jxxx}(t,0)=Q_{jxxx}(t,1),\quad 0\le t\le T, \tag{44}$$

which is conjugated to problem (1)-(4). We note that

$$\xi(x)=\xi_0\vartheta_0(x)+\sum_{n=1}^{\infty}\left[\xi_{1,n}\vartheta_{1,n}(x)+\xi_{2,n}\vartheta_{2,n}(x)\right],\ \ \xi_0=\int\limits_0^1\xi_0(y)\sigma_0(y)dy,$$

$$\xi_{\kappa,n}=\int\limits_0^1\xi_\kappa(y)\sigma_{\kappa,n}(y)dy,\quad |\,\xi_0\,|+\sum_{n=1}^{\infty}|\,\xi_{1,n}\,|+\sum_{n=1}^{\infty}|\,\xi_{2,n}\,|<\infty.$$

We will find the partial derivatives with respect to the control function in (40) and (41) and come to the following necessary conditions for optimality

$$Q_0(t,\eta(t))\vartheta_0(\eta(t))a_0(t)\frac{\partial}{\partial p_0^*(t)}\varphi_0\left(t,p_0^*(t)\right)=2\gamma_1 p_0^*(t), \tag{45}$$

$$Q_\kappa(t,\eta(t))\sum_{n=1}^{\infty}a_{1,n}(t)\vartheta_{\kappa,n}(\eta(t))\frac{\partial}{\partial p_\kappa^*(t)}\varphi_{\kappa,n}(t,p_\kappa^*(t))=2\gamma_1 p_\kappa^*(t), \tag{46}$$

where $\dfrac{\partial}{\partial p(t)}\varphi_0\left(t,p(t)\right)$ means that $\dfrac{\partial}{\partial\xi}\varphi_0(t,\xi)\Big|_{\xi=p(t)}$.

Calculating partial derivatives in (45) and (46) again with respect to control function, we obtain another necessary conditions for optimality

$$Q_0(t,\eta(t))\vartheta_0(\eta(t))a_0(t)\frac{\partial^2}{\partial\left[p_0^*(t)\right]^2}\varphi_0\left(t,p_0^*(t)\right)<2\gamma_1, \tag{47}$$

$$Q_\kappa(t,\eta(t))\sum_{n=1}^{\infty}a_{1,n}(t)\vartheta_{\kappa,n}(\eta(t))\frac{\partial^2}{\partial\left[p_\kappa^*(t)\right]^2}\varphi_{\kappa,n}\left(t,p_\kappa^*(t)\right)<2\gamma_1. \tag{48}$$

We solve the adjoint problem (42)-(44) by the same way as we used for solving the problem (1)-(4). According to the second condition of (43), the nonzero solution of the equation (42) are found from the system of differential equations

$$q_0'(t)=0, \tag{49}$$

$$q_{\kappa,n}'(t)=\mu_n q_{\kappa,n}(t), \tag{50}$$

where $q_{k,n}(t)=\int\limits_0^1 Q_k(t,y)\sigma_{k,n}(y)dy$.

The solution of equation (49) is the arbitrary constant

$$q_0(t)=C_0,\quad C_0=\text{const}. \tag{51}$$

The solution of equation (50) is

$$q_{\kappa,n}(t)=C_\kappa\exp\left\{\mu_n t\right\},\quad C_\kappa=\text{const},\quad \kappa=1,2. \tag{52}$$

To find C_0 and C_κ in (49) and (50), we rewrite (43) in the following form

$$q_{j,n}(T)=-2\int\limits_0^1\left[U_j(T,y)-\xi_j(y)\right]\sigma_{j,n}(y)dy,\quad j=0,1,2. \tag{53}$$

Taking (31), (34), from condition (53), we obtain

$$C_0=-2\int\limits_0^1\frac{\varphi_0(T,z,p_0(T))}{a_0(T)}\sigma_0(z)dz-2\int\limits_0^1\left[b_0(T,y)-\xi_0(y)\right]\sigma_0(y)dy,\ \ z=\eta(t), \tag{54}$$

$$C_\kappa = -2\exp\{-\mu_n T\}\int\limits_0^1 \frac{\varphi_\kappa(T,z,p_\kappa(T))}{a_{2,n}(T)}\sigma_{\kappa,n}(z)dz+$$

$$+2\exp\{-\mu_n T\}\int\limits_0^1 [\xi_\kappa(y)+b_\kappa(T,y)]\,\sigma_{\kappa,n}(y)dy, \quad \kappa=1,2, \quad z=\eta(t), \tag{55}$$

where $a_{2,n}(t)=\omega\beta(t)+\alpha(t)\exp\{\mu_n T\}$.

Substituting (54) and (55) into (51) and (52), we, respectively, obtain

$$q_0(t) = -2\int\limits_0^1 \left[\frac{\varphi_0(T,y,p_0(T))}{a_0(T)} + b_0(T,y) - \xi_0(y)\right]\sigma_0(y)dy, \tag{56}$$

$$q_{\kappa,n}(t) = -2\exp\{-\mu_n(T-t)\}\int\limits_0^1 \left[\frac{\varphi_\kappa(T,y,p_\kappa(T))}{a_{2,n}(T)} + b_\kappa(T,y) - \xi_\kappa(y)\right]\sigma_{\kappa,n}(y)dy. \tag{57}$$

From (56) and (57), we obtain the series

$$Q_0(t,y) = -2\vartheta_0(y)\int\limits_0^1 \left[\frac{\varphi_0(T,y,p_0(T))}{a_0(T)} + b_0(T,y) - \xi_0(y)\right]\sigma_0(y)dy, \tag{58}$$

$$Q_\kappa(t,y) = -2\sum_{n=1}^{\infty}\vartheta_{\kappa,n}(y)\exp\{-\mu_n(T-t)\}\times$$

$$\times\int\limits_0^1 \left[\frac{\varphi_\kappa(T,y,p_\kappa(T))}{a_{2,n}(T)} + b_\kappa(T,y) - \xi_\kappa(y)\right]\sigma_{\kappa,n}(y)dy. \tag{59}$$

Substituting presentations (58) and (59) into (45) and (46), respectively, we have

$$p_0(t) = J_0(t;p_0(t)) \equiv -\frac{\vartheta_0^2(\eta(t))}{\gamma_1}\left[\frac{\varphi_0(T,p_0(T))}{a_0(T)} + b_0(T) - \xi_0\right]a_0(t)\frac{\partial}{\partial p_0}\varphi_0\big(t,p_0(t)\big), \tag{60}$$

$$p_\kappa(t) = J_\kappa(t;p_\kappa(t)) \equiv -\frac{1}{\gamma_1}\sum_{n=1}^{\infty}\vartheta_{\kappa,n}(\eta(t))\exp\{-\mu_n(T-t)\}\times$$

$$\times\left[\frac{\varphi_{\kappa,n}(T,p_\kappa(T))}{a_{2,n}(T)} + b_{\kappa,n}(T) - \xi_{\kappa,n}\right]\sum_{n=1}^{\infty}a_{1,n}(t)\vartheta_{\kappa,n}(\eta(t))\frac{\partial}{\partial p_\kappa}\varphi_{\kappa,n}\big(t,p_\kappa(t)\big). \tag{61}$$

For determination of control functions $p_0(t)$ and $p_\kappa(t)$ ($\kappa=1,2$), we have two functional equations (60) and (61).

Theorem 6. Let the following conditions be fulfilled:

1). $\|\,\varphi_0\,(t,p_0(t))\,\|_{C[0,T]} \le M_{01}, \quad 0<M_{01}=\text{const}$;

2). $\left\|\,\frac{\partial\varphi_0\,(t,p_0(t))}{\partial p_0(t)}\,\right\|_{C[0,T]} \le M_{02}, \quad 0<M_{02}=\text{const}$;

3). $|\,\varphi_0\,(t,p_0(t)) - \varphi_0\,(t,\bar p_0(t))\,| \le L_{01}\,|\,p_0(t)-\bar p_0(t)\,|\,, \quad 0<L_{01}=\text{const}$;

4). $\left|\,\frac{\partial}{\partial p_0(t)}\varphi_0\,(t,p_0(t)) - \frac{\partial}{\partial \bar p_0(t)}\varphi_0\,(t,\bar p_0(t))\,\right| \le L_{02}\,|\,p_0(t)-\bar p_0(t)\,|\,, \quad 0<L_{02}=\text{const}$;

5). $\rho_0 = \max\left\{\frac{L_{02}}{\gamma_1 a_0}M_{01};\ \rho_{01}\frac{L_{01}}{\gamma_1 a_0}M_{02}\right\} < 1$, where $\rho_{01} = \frac{1}{\gamma_1 a_0}(L_{01}M_{02}+L_{02}M_{01})$.

Then, for the first regular values of the parameter ω, from the set Λ_1, the functional equation (60) has a unique control function $p_0(t)$ (solution) on the segment $[0,T]$. This solution can be found by the iteration process:

$$\begin{aligned} p_0^0(t) &= -\frac{\vartheta_0^2(\eta(t))}{\gamma_1}a_0(t)(b_0(T)-\xi_0), \\ p_0^{m+1}(t) &= J_0\big(t;p_0^m(t)\big). \end{aligned} \tag{62}$$

Proof. By virtue of conditions of the theorem 6, from (62), we have

$$\left\|\,p_0^0(t)\,\right\|_{C[0,T]} \le \frac{4(1-\eta(t))^2}{\gamma_1}a_0\,(b_0(T)+|\,\xi_0\,|) \le \frac{4}{\gamma_1}a_0\,(b_0(T)+|\,\xi_0\,|) < \infty, \tag{63}$$

where $a_0 = \max\limits_{0\le t\le T}|\,a_0(t)\,|$;

$$\left\|\,p_0^{m+1}(t)-p_0^m(t)\,\right\| \le \frac{L_{01}}{\gamma_1 a_0}M_{02}\left\|\,p_0^m(T)-p_0^{m-1}(T)\,\right\| + \frac{L_{02}}{\gamma_1 a_0}M_{01}\left\|\,p_0^m(t)-p_0^{m-1}(t)\,\right\|. \tag{64}$$

For $t = T$ from (64), we have

$$\| p_0^{m+1}(T) - p_0^m(T) \|_{C[0,T]} \le \frac{L_{01}}{\gamma_1 a_0} M_{02} \| p_0^m(T) - p_0^{m-1}(T) \|_{C[0,T]} +$$

$$+ \frac{L_{02}}{\gamma_1 a_0} M_{01} \| p_0^m(T) - p_0^{m-1}(T) \|_{C[0,T]} \le \rho_{01} \| p_0^m(T) - p_0^{m-1}(T) \|_{C[0,T]}, \tag{65}$$

where $\rho_{01} = \dfrac{1}{\gamma_1 a_0}\big(L_{01}M_{02} + L_{02}M_{01}\big)$.

From the estimates (64) and (65), we obtain that there holds the estimate

$$\| p_0^{m+1}(t) - p_0^m(t) \|_{C[0,T]} + \| p_0^{m+1}(T) - p_0^m(T) \|_{C[0,T]} \le$$

$$\le \rho_0 \left[\| p_0^{m+1}(t) - p_0^m(t) \|_{C[0,T]} + \| p_0^{m+1}(T) - p_0^m(T) \|_{C[0,T]} \right], \tag{66}$$

where $\rho_0 = \max\left\{ \dfrac{L_{02}}{\gamma_1 a_0} M_{01};\ \rho_{01} \dfrac{L_{01}}{\gamma_1 a_0} M_{02} \right\}$. From the estimates (63) and (66), it implies that the operator on the right-hand side of equation (60) is compressing mapping and the functional equation has unique solution on the interval $[0, T]$. □

Theorem 7. Let the smoothness conditions S and the following conditions be fulfilled:

1). $\| \vec{\varphi}_\kappa\big(t, p_\kappa(t)\big) \|_{\ell_2} \le M_{\kappa 1}$, $0 < M_{\kappa 1} = \text{const}$, $\kappa = 1, 2$;

2). $\left\| \dfrac{\partial}{\partial p_\kappa} \vec{\varphi}_\kappa\big(t, p_\kappa(t)\big) \right\|_{\ell_2} \le M_{\kappa 2}$, $0 < M_{\kappa 2} = \text{const}$;

3). $\big| \varphi_\kappa\big(t, p_\kappa(t)\big) - \varphi_\kappa\big(t, \bar{p}_\kappa(t)\big) \big| \le L_{\kappa 1} \, | p_\kappa(t) - \bar{p}_\kappa(t) \, |$, $0 < L_{\kappa 1} = \text{const}$;

4). $\left| \dfrac{\partial}{\partial p_\kappa(t)} \varphi_\kappa\big(t, p_\kappa(t)\big) - \dfrac{\partial}{\partial \bar{p}_\kappa(t)} \varphi_\kappa\big(t, \bar{p}_\kappa(t)\big) \right| \le L_{\kappa 2} \, | p_\kappa(t) - \bar{p}_\kappa(t) \, |$, $0 < L_{\kappa 2} = \text{const}$;

5). $\rho_\kappa = \max\left\{ \dfrac{L_{\kappa 2}}{\gamma_1 a_\kappa} M_{\kappa 1};\ \rho_{\kappa 1} \dfrac{L_{\kappa 1}}{\gamma_1 a_\kappa} M_{\kappa 2} \right\} < 1$, where $\rho_{\kappa 1} = \dfrac{1}{\gamma_1 a_\kappa}\big(L_{\kappa 1}M_{\kappa 2} + L_{\kappa 2}M_{\kappa 1}\big)$.

Then, for the second regular values of the parameter ω from the set Λ_2, functional equation (61) has a unique solution on the segment $[0, T]$. This solution can be found by the iteration process:

$$p_\kappa^0(t) = -\frac{1}{\gamma_1} \sum_{n=1}^{\infty} \vartheta_{\kappa,n}(\eta(t)) \exp\big\{ -\mu_n(T - t) \big\} \big(b_{\kappa,n}(T) - \xi_{\kappa,n} \big),$$

$$p_k^{m+1}(t) = J_\kappa\big(t; p_\kappa^m(t)\big).$$

Proof of the theorem 7 is similar to the proof of the Theorem 6.

We substitute the found values of the control functions $p_j(t)$, $j = 0, 1, 2$ into the functions (35). Then we uniquely determine the state function $U(t, x)$. The proof of this statement is similar to the proofs of the Theorems 4 and 5.

7. Conclusion

In the domain $\Omega = \big\{ t \in (0, T),\ x \in (0, 1) \big\}$, we consider a pseudoparabolic type differential equation with nonlinear boundary conditions in regard to time variable. Samarskii–Ionkin type boundary value conditions in regard to spatial variable x are used in solving the nonlocal optimal movable point control problem.

The scalar and countable system of nonlinear functional integral equations are obtained. The properties of eigenfunctions and unique solvability of scalar and countable system of nonlinear functional integral equations with respect to state function is proved for fixed values of the control function. The optimality conditions are found. The equations with product of nonlinear functions are obtained for control function. The Picar iteration process is built. The uniform convergence of the Fourier series is proved. The results of this work make it possible to determine the solutions of huge set of problems.

Moreover, the results obtained in this work will allow us in the future to investigate direct and inverse optimal control problems for other kind of partial differential equations of mathematical physics with different quality functionals. Parabolic type differential equations, such as the heat equations or the diffusion equations, have different applications. In [14], the problem of fast forward evolution of the processes described in terms of the heat equation is considered. The matter is considered on an adiabatically expanding time-dependent box. Attention is paid to acceleration of heat transfer processes. As the physical realization, the heat transport in harmonic crystals is considered. In [11], Sibatov R. T., Svetukhin V. V. are studied the subdiffusion kinetics of nanoprecipitate growth and destruction in solid solutions. The authors of the work [58] are proposed a numerical method for estimating the effective thermal conductivity coefficient of hydrate-bearing rock samples using synchrotron-based microtomography data. In the work [59], is studied the development of magnetorotation instability in the accreting envelope of a protostar in the non-isothermal case. The paper [60] is devoted to the development of a multiscale approach to calculating gas flows near solid surfaces taking into account microscopic effects. The work [61] discusses approaches to conducting comprehensive optimization of devices that protect against

ultrawideband interference, known as modal filters. These devices can take the form of strip N-conductor structures with a various number of conducting layers, as well as cables. Optimization is one of the important stages of their design.

References

[1] Blinova I.,V., Grishanov E.N., Popov A.I., Popov I.Y., Smolkina M.O. On spin flip for electron scattering by several delta-potentials for 1D Hamiltonian with spin-orbit interaction. *Nanosystems: Phys. Chem. Math.*, 2023, **14**(4), P. 413–417.

[2] Deka H., Sarma J. A numerical investigation of modified Burgers' equation in dusty plasmas with non-thermal ions and trapped electrons. *Nanosystems: Phys. Chem. Math.*, 2023, **14**(1), P. 5–12.

[3] Dweik J., Farhat H., Younis J. The Space Charge Model. A new analytical approximation solution of Poisson-Boltzmann equation: the extended homogeneous approximation. *Nanosystems: Phys. Chem. Math.*, 2023, **14**(4), P. 428–437.

[4] Fedorov E.G., Popov I.Yu. Analysis of the limiting behavior of a biological neurons system with delay. *J. Phys.: Conf. Ser.*, 2021, **2086**(012109).

[5] Fedorov E.G., Popov I.Yu. Hopf bifurcations in a network of Fitzhigh-Nagumo biological neurons. *International Journ. Nonlinear Sciences and Numerical Simulation*, 2021.

[6] Fedorov E.G. Properties of an oriented ring of neurons with the FitzHugh-Nagumo model. *Nanosystems: Phys. Chem. Math.*, 2021, **12**(5), P. 553–562.

[7] Irgashev B.Yu. Boundary value problem for a degenerate equation with a Riemann-Liouville operator. *Nanosystems: Phys. Chem. Math.*, 2023, **14**(5), P. 511–517.

[8] Kuljanov U.N. On the spectrum of the two-particle Schrodinger operator with point potential: one dimensional case. *Nanosystems: Phys. Chem. Math.*, 2023, **14**(5), P. 505–510.

[9] Parkash C., Parke W.C., Singh P. Exact irregular solutions to radial Schrodinger equation for the case of hydrogen-like atoms. *Nanosystems: Phys. Chem. Math.*, 2023, **14**(1), P. 28–43.

[10] Popov I.Y. A model of charged particle on the flat Mobius strip in a magnetic field. *Nanosystems: Phys. Chem. Math.*, 2023, **14**(4), P. 418–420.

[11] Sibatov R.T., Svetukhin V.V. Subdiffusion kinetics of nanoprecipitate growth and destruction in solid solutions. *Theor. Math. Phys.*, 2015, **183**, P. 846–859.

[12] Vatutin A.D., Miroshnichenko G.P., Trifanov A.I. Master equation for correlators of normalordered field mode operators. *Nanosystems: Phys. Chem. Math.*, 2022, **13**(6), P. 628–631.

[13] Uchaikin V.V., Sibatov R.T. Fractional kinetics in solids: Anomalous charge transport in semiconductors, dielectrics and nanosystems. CRC Press, Boca Raton, FL, 2013.

[14] Matrasulov J., Yusupov J.R., Saidov A.A. Fast forward evolution in heat equation: Tunable heat transport in adiabatic regime. *Nanosystems: Phys. Chem. Math.*, 2023, **14**(4), P. 421–427.

[15] Galaktionov V.A., Mitidieri E., Pohozaev S. Global sign-changing solutions of a higher order semilinear heat equation in the subcritical Fujita range. *Advanced Nonlinear Studies*, 2012, **12**(3), P. 569–596.

[16] Galaktionov V.A., Mitidieri E., Pohozaev S.I. Classification of global and blow-up sign-changing solutions of a semilinear heat equation in the subcritical Fujita range: second-order diffusion. *Advanced Nonlinear Studies*, 2014, **14**(1), P. 1–29.

[17] Denk R., Kaip M. Application to parabolic differential equations. In: General Parabolic Mixed Order Systems in L_p and Applications. Operator Theory: Advances and Applications, **239**. Birkhäuser, Cham., 2013.

[18] Van Dorsselaer H., Lubich C. Inertial manifolds of parabolic differential equations under high-order discretizations. *Journ. of Numer. Analysis*, 1099, **19**(3), P. 455–471.

[19] Ivanchov N.I. Boundary value problems for a parabolic equation with integral conditions. *Differen. Equat.*, 2004, **40**(4), P. 591–609.

[20] Mulla M., Gaweash A., Bakur H. Numerical solution of parabolic in partial differential equations (PDEs) in one and two space variable. *Journ. Applied Math. and Phys.*, 2022, **10**(2), P. 311–321.

[21] Nguyen H., Reynen J. A space-time least-square finite element scheme for advection-diffusion equations. *Computer Methods in Applied Mech. and Engin.*, 1984, **42**(3), P. 331–342.

[22] Pinkas G. Reasoning, nonmonotonicity and learning in connectionist networks that capture propositional knowledge. *Artificial Intelligence*, 1995, **77**(2), P. 203–247.

[23] Pohozaev S.I. On the dependence of the critical exponent of the nonlinear heat equation on the initial function. *Differ. Equat.*, 2011, **47**(7), P. 955–962.

[24] Pokhozhaev S.I. Critical nonlinearities in partial differential equations. *Russ. J. Math. Phys.*, 2013, **20**(4), P. 476–491.

[25] Yuldashev T.K. Mixed value problem for a nonlinear differential equation of fourth order with small parameter on the parabolic operator. *Comput. Math. Math. Phys.*, 2011, **51**(9), P. 1596–1604.

[26] Yuldashev T.K. Mixed value problem for nonlinear integro-differential equation with parabolic operator of higher power. *Comput. Math. Math. Phys.*, 2012, **52**(1), P. 105–116.

[27] Yuldashev T.K. Nonlinear optimal control of thermal processes in a nonlinear Inverse problem. *Lobachevskii Journ. Math.*, 2020, **41**(1), P. 124–136.

[28] Zonga Y., Heb Q., Tartakovsky A.M. Physics-informed neural network method for parabolic differential equations with sharply perturbed initial conditions. *arXiv:2208.08635[math.NA]*, 2022, P. 1–50.

[29] Ashurov R., Kadirkulov B., Jalilov M. On an inverse problem of the Bitsadze-Samarskii type for a parabolic equation of fractional order. *Boletin de la Sociedad Matematica Mexicana*, 2023, **29**(3). P. 1–21.

[30] Berdyshev A.S., Kadirkulov B.J. A Samarskii-Ionkin problem for two-dimensional parabolic equation with the Caputo fractional differential operator. *Intern. J. Pure and Appl. Math.*, 2017, **113**(4), P. 53–64.

[31] Berdyshev A.S., Cabada A., Kadirkulov B.J. The Samarskii-Ionkin type problem for the fourth order parabolic equation with fractional differential operator. *Inter. J. Computers and Math. with Appl.*, 2011, **62**(10), P. 3884–3893.

[32] Bilalov B.T., Sezer Y., Ildiz U., Hagverdi T. On the basicity of one trigonometric system in Orlicz spaces. *Trans. Issue Math., Azerb. Nat. Academy of Sci.*, 2024, **44**(1). P. 31–45.

[33] Hadiyeva S.S. Basis property of the system of eigenfunctions corresponding to a problem with a spectral parameter in the boundary condition. *J. Contemp. Appl. Math.*, 2024, **14**(2), P. 8–11.

[34] Il'in V.A. On the solvability of mixed problems for hyperbolic and parabolic equations. *Russian Math. Surveys*, 1960, **15**(2), P. 85–142.

[35] Ionkin N.I., Moiseev E.I. A problem for heat transfer equation with two-point boundary conditions. *Differentsial'nye Uravneniya*, 1979, **15**(7), P. 1284–1295. (in Russian)

[36] Karahan D., Mamedov Kh.R., Yuldashev T.K. On a q-Dirichlet-Neumann problem with discontinuity conditions. *Lobachevskii J. Math.*, 2022, **43**(11), P. 3192–3197.

[37] Nasibova N.P. Basicity of a perturbed system of exponents in Lebesgue spaces with a variable summability exponent. *Baku Math. J.*, 2022, **1**(1), P. 96–105.
[38] Abdullayev V.M. Numerical solution to optimal control problems with multipoint and integral conditions. *Proc. of the Inst. of Math. and Mech.*, 2018, **44**(2), P. 171–186.
[39] Ashirbaev B.Y., Yuldashev T.K. Derivation of a controllability criteria for a linear singularly perturbed discrete system with small step. *Lobachevskii J. Math.*, 2024, **45**(3), P. 938–948.
[40] Butkovsky A.G., Pustylnikov L.M. *Theory of mobile control of systems with distributed parameters*. Moscow, Nauka, 1980. 384 p. (in Russian)
[41] Deineka V.S. Optimal control of the dynamic state of a thin compound plate. *Cybernetics and Systems Analysis*, 2006, **42**(4), P. 151–157.
[42] Deumlich R., Elster K.H. Duality theorems and optimality, conditions for nonconvex optimization problems. *Math. Operations Forsch. Statist. Ser. Optimiz.*, 1980, **11**(2), P. 181–219.
[43] Kerimbekov A.K., Nametkulova R.J., Kadirimbetova A.K. Optimality conditions in the problem of thermal control with integral-differential equation. *Vestnik Irkutsk Gos. Univers., Matematika*, 2016, **15** P. 50–61. (in Russian)
[44] Kerimbekov A.K., Abdyldaeva E.F. On the solvability of the tracking problem in nonlinear vector optimization of oscillatory processes. *Trudy IMM UrO RAN*, 2024, **30**(2), P. 103–115.
[45] Mahmudov E.N. Infimal convolution and duality in convex optimal control problems with second order evolution differential inclusions. *Evol. Equ. Contr. Theory*, 2021, **10**(1), P. 37–59.
[46] Mahmudov E.N., Mardanov M.J. Optimization of the Nicoletti boundary value problem for second order differential inclusions. *Proc. of the Inst. of Math. and Mech.*, 2023, **49**(1), P. 3–15.
[47] Mardanov M.J., Melikov T.K. A method for studying the optimality of controls in discrete systems. *Proc. Inst. Math. Mech.*, 2014, **40**(2), P. 5–13.
[48] Ramazanova A. Necessary conditions for the existence of a saddle point in one optimal control problem for systems of hyperbolic equations. *European J. Pure and Appl. Math.* 2021, **14**(4), P. 1402–1414.
[49] Ramazanova A.T., Abdullozhonova A.N., Yuldashev T.K. Optimal mobile control in inverse problem for Barenblatt–Zheltov–Kochina type fractional order equation. *Lobachevskii J. Math.*, 2025, **46**(1), P. 488–501.
[50] Yuldashev T.K., Ashirbaev B.Y. Optimal feedback control problem for a singularly perturbed discrete system. *Lobachevskii J. Math.*, 2023, **44**(2), P. 661–668.
[51] Albeverio S., Alimov Sh.A. On a time-optimal control problem associated with the heat exchange process. *Applied Math. and Optimiz.*, 2008, **57**(1), P. 58–68.
[52] Azamov A.A., Ibragimov G.I., Mamayusupov K., Ruzibaev M.B. On the stability and null controllability of an infinite system of linear differential equations. *J. Dynam. and Contr. Syst.*, 2021.
[53] Azamov A.A., Ruziboev M.B. The time-optimal problem for evolutionary partial differential equations. *J. Appl. Math. and Mech.*, 2013. **77**(2), P. 220–224.
[54] Yuldashev T.K., Ramazanova A.T., Shermamatov Zh.Zh. Optimal control problem for a linear pseudoparabolic equation with final condition, degeneration and Gerasimov-Caputo operator. *Azerbaijan Journal of Mathematics*, 2025, **15**(1), P. 257–283.
[55] Bari N.K. Biorthogonal systems and bases in Hilbert space. *Uch. Zap. MGU*, 1951, **148**(4), P. 69–107. (in Russian)
[56] Gokhberg I.S., Krein M.G. Introduction to the theory of linear non-selfadjoint operators. Moscow, Nauka, 1965. (in Russian)
[57] Keselman G.M. On non-conditional convergence of expansions by eigenfunctions of some differential operators. *Izv. vuzov. Matem.*, 1969, **2**, P. 82–93. (in Russian)
[58] Fokin M.I., Markov S.I., Shtanko E.I. A Numerical method for estimating the effective thermal conductivity coefficient of Hydrate-Bearing Rock Samples using synchrotron microtomography data. *Math. Models Comput. Simul.*, 2024, **16**, P. 896–905.
[59] Lugovsky A.Y., Lukin V.V. About the influence of accounting for the energy equation on the formation model of a large-scale vortical flow in the accreting envelope of a protostar. *Math. Models Comput. Simul.*, 2024, **16**, P. 676–686.
[60] Polyakov S.V., Podryga V.O. On a boundary model in problems of the gas flow around solids. *Math. Models Comput. Simul.*, 2024, **16**, P. 752–761.
[61] Belousov A.O., Gordeyeva V.O. Optimization of protective devices with modal phenomena using global optimization algorithms. *Math. Models Comput. Simul.*, 2024, **16** (Suppl. 1), P. S12–S35.

Submitted 11 June 2025; revised 28 July 2025; accepted 20 August 2025

Information about the authors:

Tursun K. Yuldashev – Tashkent State Transport University, Temiryolchilar 1, Tashkent, 100174, Uzbekistan; Osh State University, Lenin Avenue, 331, Osh 723500, Kyrgyzstan; ORCID 0000-0002-9346-5362; tursun.k.yuldashev@gmail.com

Bakhtiyar J. Kadirkulov – Alfraganus University, Tashkent, Uzbekistan; ORCID 0000-0001-8937-0523; b.kadirkulov@afu.uz

Aysel T. Ramazanova – Universitat Duisburg-Essen, Essen, Germany; ORCID 0000-0003-0166-6018; ramazanovaaysel897@gmail.com

Zholdoshbek Zh. Shermamatov – Osh State University, Lenin Avenue, 331, Osh 723500, Kyrgyzstan; ORCID 0009-0002-1325-0044; jshermamatov@oshsu.kg

Conflict of interest: the authors declare no conflict of interest.

NANOSYSTEMS:
PHYSICS, CHEMISTRY, MATHEMATICS

Original article

Akhmadova M.O., et al. *Nanosystems: Phys. Chem. Math.*, 2025, **16** (5), 577–585.
http://nanojournal.ifmo.ru
DOI 10.17586/2220-8054-2025-16-5-577-585

Spectral analysis of two-particle Hamiltonians with short-range interactions

Mukhayyo O. Akhmadova[1,a], Mukammal A. Azizova[1,b]

[1]Samarkand State University, 140104, Samarkand, Uzbekistan

[a]mukhayyo.akhmadova@mail.ru, [b]mukammal.azizova@gmail.com

Corresponding author: M. O. Akhmadova, mukhayyo.akhmadova@mail.ru

ABSTRACT We analyze the spectral characteristics of lattice Schrödinger operators, denoted as $H_{\gamma\lambda\mu}(K)$, $K \in (-\pi, \pi]^3$, which represent a system of two identical bosons existing on $\mathbb{Z}^3$ lattice. The model includes on-site and nearest-neighbor interactions, parameterized by $\gamma, \lambda, \mu \in \mathbb{R}$. Our study of $H_{\gamma\lambda\mu}(0)$ reveals an invariant subspace on which its restricted form, $H^{\rm ea}_{\lambda\mu}(0)$, is solely dependent on λ and μ. To elucidate the mechanisms of eigenvalue birth and annihilation for $H^{\rm ea}_{\lambda\mu}(0)$, we define a critical operator. A detailed criterion is subsequently developed within the plane spanned by λ and μ. This involves: (i) the derivation of smooth critical curves that mark the onset of criticality for the operator, and (ii) the proof of exact conditions for the existence of precisely α eigenvalues below and β eigenvalues above the essential spectrum, where $\alpha, \beta \in \{0, 1, 2\}$ and $\alpha + \beta \leq 2$.

KEYWORDS Two-particle system, lattice Schrödinger operator, essential spectrum, bound states, Fredholm determinant.

ACKNOWLEDGEMENTS The authors are grateful to the referee for valuable insights. Support for this work was provided by the Fundamental Science Foundation of Uzbekistan, Grant No. FL-9524115052.

FOR CITATION Akhmadova M.O., Azizova M.A. Spectral analysis of two-particle Hamiltonians with short-range interactions. *Nanosystems: Phys. Chem. Math.*, 2025, **16** (5), 577–585.

1. Introduction

Lattice models are fundamental to mathematical physics, particularly few-body Hamiltonians [1], which simplify Bose-Hubbard models to finite particle interactions. Decades of research underscore their importance [2–16].

These discrete Hamiltonians also provide effective approximations for their continuous counterparts [17]. A prime illustration is the Efimov effect [18], rigorously proven for continuous three-particle systems [19–22], and demonstrably presented in lattice three-particle systems as well [2, 4, 9, 23]. The bound state energies of one- and two-particle systems, situated in two adjacent 3D layers linked by a window, were numerically reported in [24].

Beyond theoretical significance, discrete Schrödinger operators model few-particle systems in periodic structures, exemplified by ultracold atoms in optical crystals [25, 26]. Recent years have seen a surge in studying ultracold few-atom systems in optical lattices, driven by precise control over parameters like temperature and interaction potentials [25, 27–29]. This control facilitates experimental observation of phenomena like stable repulsively bound pairs [26, 30], which challenges the typical formation of stable objects through attractive forces.

Lattice Hamiltonians also find application in fusion physics. For example, [14] showed that a one-particle one-dimensional lattice Hamiltonian could enhance nuclear fusion probability in specific lattice structures.

A key challenge in lattice few-particle problems, unlike their continuous analogues, is the general inability to separate center-of-mass motion. However, for a lattice Hamiltonian H on $\mathbb{T}^{n\cdot d}$, the von Neumann direct integral decomposition provides a solution:

$$\mathrm{H} \simeq \int\limits_{K\in\mathbb{T}^d}^{\oplus} H(K)\, dK,$$

where $\mathbb{T}^d$ is the d-dimensional torus. This decomposition effectively transforms the problem into analyzing the fiber Hamiltonians $H(K)$, which act on $\mathbb{T}^{(n-1)d}$ and critically depend on the quasi-momentum $K \in \mathbb{T}^d$ [2, 3, 31].

In the present work, we focus on the spectral properties of $H_{\gamma\lambda\mu}(K)$ for $K \in \mathbb{T}^3$, acting on $L^{2,e}(\mathbb{T}^3)$ as

$$H_{\gamma\lambda\mu}(K) := H_0(K) + V_{\gamma\lambda\mu}.$$

The unperturbed operator $H_0(K)$ defined by multiplication with the dispersion function $\mathcal{E}_K$ defined in (3). The interaction potential $V_{\gamma\lambda\mu}$ is independent of the quasi-momentum $K \in \mathbb{T}^3$. Notably, the coupling constants γ, λ, and μ denote the on-site, first-neighbor, and second-nearest-neighbor interactions within the lattice system, respectively.

The operators $H_0(K)$ and $V_{\gamma\lambda\mu}$ (with $\gamma, \lambda, \mu \in \mathbb{R}$) are both bounded and self-adjoint. Because $V_{\gamma\lambda\mu}$ has finite rank, Weyl's theorem establishes that $\sigma_{ess}(H_{\gamma\lambda\mu}(K))$ coincides with $\sigma(H_0(K))$. This spectrum spans the interval $[\mathcal{E}_{\min}(K), \mathcal{E}_{\max}(K)]$, defined by (5).

The Hilbert space $L^{2,\mathrm{e}}(\mathbb{T}^3)$ is decomposed into the direct sum of invariant subspaces for the operator $H_{\gamma\lambda\mu}(0)$:

$$L^{2,\mathrm{e}}(\mathbb{T}^3) = L^{2,\mathrm{e},\mathrm{a}_{12}}(\mathbb{T}^3) \oplus \left[L^{2,\mathrm{e},\mathrm{a}_{12}}(\mathbb{T}^3)\right]^{\perp}. \tag{1}$$

Here, $L^{2,\mathrm{e},\mathrm{a}_{12}}(\mathbb{T}^3)$ comprises functions in $L^{2,\mathrm{e}}(\mathbb{T}^3)$ that are antisymmetric in their first two variables, and $\left[L^{2,\mathrm{e},\mathrm{a}_{12}}(\mathbb{T}^3)\right]^{\perp}$ is its orthogonal complement.

The decomposition (1) leads to the following spectral representation for $H_{\gamma\lambda\mu}(0)$:

$$\sigma(H_{\gamma\lambda\mu}(0)) = \sigma(H_{\gamma\lambda\mu}(0)|_{L^{2,\mathrm{e},\mathrm{a}_{12}}(\mathbb{T}^3)}) \cup \sigma(H_{\gamma\lambda\mu}(0)|_{[L^{2,\mathrm{e},\mathrm{a}_{12}}(\mathbb{T}^3)]^{\perp}}), \tag{2}$$

where $A\,\big|_{\mathcal{K}}$ denotes the restriction of A onto its reducing subspace $\mathcal{K}$. Consequently, the spectrum of the Hamiltonian $H_{\gamma\lambda\mu}(0)$ can be studied separately for its restrictions to $L^{2,\mathrm{e},\mathrm{a}_{12}}(\mathbb{T}^3)$, and $\left[L^{2,\mathrm{e},\mathrm{a}_{12}}(\mathbb{T}^3)\right]^{\perp}$.

Importantly, the restriction $V^{\mathrm{ea}}_{\lambda\mu}$ of $V_{\gamma\lambda\mu}$ to $L^{2,\mathrm{e},\mathrm{a}_{12}}(\mathbb{T}^3)$ is independent of γ and has a rank of at most two. Consequently, the restriction $H^{\mathrm{ea}}_{\lambda\mu}(0)$ of $H_{\gamma\lambda\mu}(0)$ to $L^{2,\mathrm{e},\mathrm{a}_{12}}(\mathbb{T}^3)$ is also independent of γ, and it possesses no more than two isolated eigenvalues.

To investigate the exact number of discrete eigenvalues of $H^{\mathrm{ea}}_{\lambda\mu}(0)$, we reduce the task of identifying these eigenvalues to determining the zeros of its Fredholm determinant $\Delta_{\lambda\mu}(z)$ by constructing a rank-two Lippmann-Schwinger operator $B^{\mathrm{ea}}_{\lambda\mu}(0)$.

Near the upper and lower threshold of $\sigma_{ess}(H_{\gamma\lambda\mu}(0))$, we have found the asymptotic expansions of $\Delta_{\lambda\mu}(z)$. The leading terms in these expansions are defined as the algebraic forms $P^{+}(\lambda,\mu)$ and $P^{-}(\lambda,\mu)$, respectively. As demonstrated by Lemma 5, the polynomial $P^{\pm}(\lambda,\mu)$ has a null set consisting of two separated smooth unbounded connected curves $\tau_0^{\pm}, \tau_1^{\pm}$. As a result, the (λ,μ)-plane is split by these curves into three connected regions, denoted $\mathcal{C}_0^{\pm}$, $\mathcal{C}_1^{\pm}$, and $\mathcal{C}_2^{\pm}$.

Our first main result, Theorem 2 shows that the number of eigenvalues of $H^{\mathrm{ea}}_{\lambda\mu}(0)$ lying in $(24,+\infty)$ (resp. $(-\infty,0)$) remains constant within each connected component $\mathcal{C}_\alpha^{+}$ (resp. $\mathcal{C}_\alpha^{-}$), $\alpha = 0,1,2$. Theorem 3 subsequently provides the exact value of this constant. Moreover, Corollary 1 provides a criterion, expressed in terms of the perturbation parameters $\lambda,\mu \in \mathbb{R}$, for the operator $H^{\mathrm{ea}}_{\lambda\mu}(0)$ to possess exactly α eigenvalues below or above $[0,24]$, where $\alpha \in \{0,1,2\}$. Notably, we have also derived a an imprecise lower boundary for the eigenvalue count of $H_{\gamma\lambda\mu}(K)$, $K \in \mathbb{T}^3$ (detailed in Theorem 5), depending only on λ and μ.

In order to better explain the necessary and sufficient conditions on parameters λ and μ for eigenvalue birth and annihilation, near the upper and lower thresholds of $\sigma_{ess}(H_{\gamma\lambda\mu}(0))$, we introduce the concept of a *critical operator* (for more details see Definition 1). To conclude, we provide a clear characterization of this criticality in terms of interaction parameters (Theorem 1).

First, in [32], the authors studied discrete Schrödinger operators involving a particle under the influence of an external field on a three-dimensional lattice. The interaction energies of the system were non-negative and denoted by γ,λ, and the eigenvalue characteristics, including their count and whereabouts were determined as functions of these parameters.

Subsequent works [11,12,33] extended these results to two-boson systems with on-site and nearest-neighbor interactions for $d = 1,2$, where the interactions are described by real parameters γ and λ.

For a system of two identical bosons on a d-dimensional lattice $\mathbb{Z}^d$ $(d = 1,2)$ with on-site (γ), nearest-neighbor (λ), and next-nearest-neighbor (μ) interactions, the discrete spectrum of the associated two-particle Schrödinger operator $H_{\gamma\lambda\mu}(k)$, $k \in \mathbb{T}^d$ has been studied and determined the number and position of isolated eigenvalues for all values of the interaction parameters in [34–36].

Here's how this paper is structured. Section 2 introduces the fiber Schrödinger operators for particle pairs at a fixed quasi-momentum. Section 3 outlines the auxiliary information crucial for stating our primary findings. Our main results, along with the definition of critical operators, are presented in Section 4. Finally, Section 5 contains the proofs.

2. Two-boson system Hamiltonian on the $\mathbb{Z}^3$ lattice

2.1. Quasimomentum-fixed Schrödinger operator for particle pairs

For $\gamma,\lambda,\mu \in \mathbb{R}$ and $K \in \mathbb{T}^3$, the Schrödinger operator $H_{\gamma\lambda\mu}(K)$ describes interacting particle pairs. This operator is bounded and self-adjoint in $L^{2,e}(\mathbb{T}^3)$ ([3], [11], [35]), defined as:

$$H_{\gamma\lambda\mu}(K) := H_0(K) + V_{\gamma\lambda\mu}.$$

The unperturbed operator, $H_0(K)$, acts as a multiplication operator, defined by the quasi-momentum-dependent pair dispersion relation:

$$(H_0(K)f)(p) = \mathcal{E}_K(p)f(p),$$

where the dispersion function $\mathcal{E}_K(\cdot)$ is given by:

$$\mathcal{E}_K(p) = 4\sum_{i=1}^{3}\left(1 - \cos\tfrac{K_i}{2}\,\cos p_i\right), \quad p = (p_1,p_2,p_3) \in \mathbb{T}^3. \tag{3}$$

The perturbation operator $V_{\gamma\lambda\mu}$ is given by:

$$\begin{aligned}(V_{\gamma\lambda\mu}f)(p) =& \frac{\gamma}{8\pi^3}\int\limits_{\mathbb{T}^3} f(q)\mathrm{d}q + \frac{\lambda}{4\pi^3}\sum_{i=1}^{3}\cos p_i \int\limits_{\mathbb{T}^3}\cos q_i f(q)\mathrm{d}q \\ &+ \frac{\mu}{4\pi^3}\sum_{i=1}^{3}\cos 2p_i \int\limits_{\mathbb{T}^3}\cos 2q_i f(q)\mathrm{d}q.\end{aligned} \tag{4}$$

The rank of $V_{\gamma\lambda\mu}$ varies with $\gamma, \lambda, \mu \in \mathbb{R}$ but is always at most seven. By Weyl's theorem [37], $\sigma_{\mathrm{ess}}(H_{\gamma\lambda\mu}(K))$ is unaffected by these parameters. It coincides with $\sigma(H_0(K))$, $K \in \mathbb{T}^3$, forming the closed interval $[\mathcal{E}_{\min}(K), \mathcal{E}_{\max}(K)]$, where:

$$\begin{aligned}\mathcal{E}_{\min}(K) &:= \min_{p\in\mathbb{T}^3}\mathcal{E}_K(p) = 4\sum_{i=1}^{3}\left(1-\cos\tfrac{K_i}{2}\right) \geq \mathcal{E}_{\min}(0) = 0,\\ \mathcal{E}_{\max}(K) &:= \max_{p\in\mathbb{T}^3}\mathcal{E}_K(p) = 4\sum_{i=1}^{3}\left(1+\cos\tfrac{K_i}{2}\right) \leq \mathcal{E}_{\max}(0) = 24.\end{aligned} \tag{5}$$

3. Auxiliary statements

3.1. Invariant subspaces of the fiber Schrödinger operators $H_{\gamma\lambda\mu}(0)$

We define $L^{2,\mathrm{e},a_{12}}(\mathbb{T}^3)$ as the set of functions within $L^{2,e}(\mathbb{T}^3)$ that are antisymmetric with respect to their first two coordinates, specifically,

$$L^{2,\mathrm{e},\mathrm{a}_{12}}(\mathbb{T}^3) = \{f \in L^{2,\mathrm{e}}(\mathbb{T}^3) :\ f(p_1,p_2,p_3) = -f(p_2,p_1,p_3)\}.$$

Let $\left(L^{2,\mathrm{e},\mathrm{a}_{12}}(\mathbb{T}^3)\right)^{\perp}$ be its orthogonal complement within $L^{2,e}(\mathbb{T}^3)$. Notably, $L^{2,\mathrm{e},\mathrm{a}_{12}}(\mathbb{T}^3)$ and its orthogonal complement $\left(L^{2,\mathrm{e},\mathrm{a}_{12}}(\mathbb{T}^3)\right)^{\perp}$ are both closed subspaces of $L^{2,e}(\mathbb{T}^3)$. Then the Direct Sum Theorem yields the decomposition (1).

Since $\mathcal{E}_0(p) = 2\epsilon(p)$ exhibits symmetry in its first two coordinates, and $H_0(0)$ corresponds to multiplication by $\mathcal{E}_0(p)$, the subspace $L^{2,\mathrm{e},\mathrm{a}_{12}}(\mathbb{T}^3)$, as well as $\left(L^{2,\mathrm{e},\mathrm{a}_{12}}(\mathbb{T}^3)\right)^{\perp}$ is invariant for self-adjoint operator $H_0(0)$. Taking into account the identity

$$\begin{aligned}2\cos A\cos B + 2\cos C\cos D =& (\cos A+\cos C)(\cos B+\cos D)\\ &+ (\cos A-\cos C)(\cos B-\cos D),\ \text{for any } A,B,C,D\in\mathbb{R},\end{aligned}$$

from (4) one derives that

$$\begin{aligned}(V_{\gamma\lambda\mu}f)(p) =& \frac{\gamma}{8\pi^3}\int_{\mathbb{T}^3} f(q)\,\mathrm{d}q + \frac{\lambda}{8\pi^3}(\cos p_1+\cos p_2)\int_{\mathbb{T}^3}(\cos q_1+\cos q_2)f(q)\,\mathrm{d}q\\ &+ \frac{\lambda}{8\pi^3}(\cos p_1-\cos p_2)\int_{\mathbb{T}^3}(\cos q_1-\cos q_2)f(q)\,\mathrm{d}q\\ &+ \frac{\mu}{8\pi^3}(\cos 2p_1+\cos 2p_2)\int_{\mathbb{T}^3}(\cos 2q_1+\cos 2q_2)f(q)\,\mathrm{d}q\\ &+ \frac{\mu}{8\pi^3}(\cos 2p_1-\cos 2p_2)\int_{\mathbb{T}^3}(\cos 2q_1-\cos 2q_2)f(q)\,\mathrm{d}q\\ &+ \frac{\lambda}{4\pi^3}\cos p_3\int_{\mathbb{T}^3}\cos q_3 f(q)\,\mathrm{d}q + \frac{\mu}{4\pi^3}\cos 2p_3\int_{\mathbb{T}^3}\cos 2q_3 f(q)\,\mathrm{d}q,\end{aligned} \tag{6}$$

which implies that $L^{2,\mathrm{e},\mathrm{a}_{12}}(\mathbb{T}^3)$, and $\left(L^{2,\mathrm{e},\mathrm{a}_{12}}(\mathbb{T}^3)\right)^{\perp}$ are invariant for $V_{\gamma\lambda\mu}$ and, hence, for $H_{\gamma\lambda\mu}(0)$. Thus, (1) implies the spectral decomposition (2).

Let us denote by $V^{\mathrm{ea}}_{\lambda\mu}$ and $H^{\mathrm{ea}}_{\lambda\mu}(0)$ the corresponding restrictions of the operators $V_{\gamma\lambda\mu}$ and $H_{\gamma\lambda\mu}(0)$ onto the subspace $L^{2,\mathrm{e},\mathrm{a}_{12}}(\mathbb{T}^3)$. Then (6) implies that

$$\begin{aligned}\left(V^{\mathrm{ea}}_{\lambda\mu}f\right)(p) =& \frac{\lambda}{8\pi^3}(\cos p_1-\cos p_2)\int_{\mathbb{T}^3}(\cos q_1-\cos q_2)f(q)\,\mathrm{d}q\\ &+ \frac{\mu}{8\pi^3}(\cos 2p_1-\cos 2p_2)\int_{\mathbb{T}^3}(\cos 2q_1-\cos 2q_2)f(q)\,\mathrm{d}q\end{aligned}$$

and

$$H^{\mathrm{ea}}_{\lambda\mu}(0) = H_0(0) + V^{\mathrm{ea}}_{\lambda\mu}.$$

3.2. The Lippmann–Schwinger operator

Let $\{\alpha_1, \alpha_2\}$ be a system of orthonormal vectors in $L^{2,\mathrm{e},\mathrm{a}_{12}}(\mathbb{T}^3)$, with

$$\alpha_1(p) = \frac{\cos p_1 - \cos p_2}{\sqrt{8\pi^3}}, \quad \alpha_2(p) = \frac{\cos 2p_1 - \cos 2p_2}{\sqrt{8\pi^3}}, \tag{7}$$

By using the orthonormal system (7) one obtains

$$V^{\mathrm{ea}}_{\lambda\mu} f = \lambda(f, \alpha_1)\alpha_1 + \mu(f, \alpha_2)\alpha_2, \tag{8}$$

where $(\cdot, \cdot)$ denotes the inner product in $L^{2,\mathrm{e},\mathrm{a}_{12}}(\mathbb{T}^3)$. For any $z \in \mathbb{C}\setminus[0,\ 24]$, we define the Lippmann-Schwinger operator (or its transpose, see, e.g., [38]) as:

$$B^{\mathrm{ea}}_{\lambda\mu}(0, z) = -V^{\mathrm{ea}}_{\lambda\mu} R_0(0, z),$$

where $R_0(0, z) := [H_0(0) - zI]^{-1}$ is the resolvent of the operator $H_0(0)$.

Lemma 1. *Given $\lambda, \mu \in \mathbb{R}$, $z \in \mathbb{C} \setminus [0, 24]$ is an eigenvalue of $H^{\mathrm{ea}}_{\lambda\mu}(0)$ with multiplicity m if and only if $B^{\mathrm{ea}}_{\lambda\mu}(0, z)$ has an eigenvalue of 1 with multiplicity m.*

Proof. Let $\lambda, \mu \in \mathbb{R}$. For $z \in \mathbb{R} \setminus [0, 24]$, the operator $R_0(0, z) = [H_0(0) - zI]^{-1}$ is well-defined within the space $L^{2,\mathrm{e},\mathrm{a}_{12}}(\mathbb{T}^3)$. Therefore, the equation

$$H^{\mathrm{ea}}_{\lambda\mu}(0)\varphi = z\varphi,\ \varphi \in L^{2,\mathrm{e},\mathrm{a}_{12}}(\mathbb{T}^3)$$

is equivalent to $(H_0(0) - zI)\varphi = -V^{\mathrm{ea}}_{\lambda\mu}\varphi$, and further to

$$\varphi = -V^{\mathrm{ea}}_{\lambda\mu} R_0(0, z)\varphi,\ \varphi \in L^{2,\mathrm{e},\mathrm{a}_{12}}(\mathbb{T}^3).$$

This equivalence proves the above relationship between the eigenvalues. □

Remark 1. *Lemma 1 reduces the spectral analysis of the non-compact operator $H^{\mathrm{ea}}_{\lambda\mu}(0)$ to that of the compact operator $B^{\mathrm{ea}}_{\lambda\mu}(0, z)$. Since $V^{\mathrm{ea}}_{\lambda\mu}$ has a rank of at most two, $B^{\mathrm{ea}}_{\lambda\mu}(0, z)$ also has a rank of at most two. Consequently, the self-adjoint operator $H^{\mathrm{ea}}_{\lambda\mu}(0)$ possesses at most two (real) eigenvalues in $\mathbb{R} \setminus [0, 24]$.*

Equation (8) establishes the equivalence between the Lippmann-Schwinger equation,

$$B^{\mathrm{ea}}_{\lambda\mu}(0, z)\varphi = \varphi,\ \varphi \in L^{2,\mathrm{e},\mathrm{a}_{12}}(\mathbb{T}^3), \tag{9}$$

and the following algebraic linear system:

$$\begin{cases} [1 + \lambda a_{11}(z)]x_1 + \mu a_{12}(z)x_2 = 0, \\ \lambda a_{21}(z)x_1 + [1 + \mu a_{22}(z)]x_2 = 0, \end{cases}$$

where

$$a_{ij}(z) := (\alpha_i, R_0(0, z)\alpha_j) = \int\limits_{\mathbb{T}^3} \frac{\alpha_i(p)\alpha_j(p)}{\mathcal{E}_0(p) - z}\mathrm{d}p,\ i, j \in \{1, 2\}.$$

Let $z \in \mathbb{R} \setminus [0,\ 24]$ and

$$\Delta_{\lambda\mu}(z) := \det[I - B^{\mathrm{ea}}_{\lambda\mu}(0, z)] = \begin{vmatrix} 1 + \lambda a_{11}(z) & \mu a_{12}(z) \\ \lambda a_{12}(z) & 1 + \mu a_{22}(z) \end{vmatrix}.$$

The following lemma outlines the established relation between the operator $H^{\mathrm{ea}}_{\lambda\mu}(0)$ and the function $\Delta_{\lambda\mu}(\cdot)$.

Lemma 2. *Given $\lambda, \mu \in \mathbb{R}$, a real number $z \in \mathbb{R} \setminus [0, 24]$ is an eigenvalue of $H^{\mathrm{ea}}_{\lambda\mu}(0)$ with the multiplicity m precisely when it is a zero of $\Delta_{\lambda\mu}(\cdot)$ of the multiplicity m. Additionally, $\Delta_{\lambda\mu}(\cdot)$ has at most two zeros within the interval $\mathbb{R} \setminus [0, 24]$.*

Proof. Assume that $z \in \mathbb{R} \setminus [0, 24]$ is an eigenvalue of $H^{\mathrm{ea}}_{\lambda\mu}(0)$ with multiplicity $m \geq 1$, i.e. 1 is an eigenvalue of compact operator $B^{\mathrm{ea}}_{\lambda\mu}(0, z)$ with the same multiplicity.

First, an eigenvalue $z \in \mathbb{R}\setminus[0,\ 24]$ of $H^{\mathrm{ea}}_{\lambda\mu}(0)$ corresponds to 1 being an eigenvalue of the Birman-Schwinger operator $B^{\mathrm{ea}}_{\lambda\mu}(0, z)$, which implies $\Delta_{\lambda\mu}(z) = 0$ (see [37, Chapter XIII.14]).

Since $B^{\mathrm{ea}}_{\lambda\mu}(0, z)$ is compact operator of rank at most two, for any its isolated eigenvalue, its algebraic multiplicity equals its geometric multiplicity (see [39, Chapter IV, Sections 3.1-3.5]). Furthermore, the multiplicity of a zero z of the Fredholm determinant $\det(I - B^{\mathrm{ea}}_{\lambda\mu}(0, z))$ corresponds precisely to the algebraic multiplicity of the number 1 as an eigenvalue of the compact operator $B^{\mathrm{ea}}_{\lambda\mu}(0, z)$, provided $B^{\mathrm{ea}}_{\lambda\mu}(0, z)$ depends analytically on z (for more details, see [39, Chapter IV, Section 5.3]). Combining these results, one directly establishes that the multiplicity of z as an eigenvalue of $H^{\mathrm{ea}}_{\lambda\mu}(0)$ is identical to its multiplicity as a zero of $\Delta_{\lambda\mu}(z)$.

Finally, the fact that $\Delta_{\lambda\mu}(\cdot)$ has at most two zeros in $\mathbb{R} \setminus [0,\ 24]$ follows directly from $B^{\mathrm{ea}}_{\lambda\mu}(0, z)$ being of rank at most two. □

The forthcoming lemma details the global properties and asymptotic expansions of $a_{ij}(z)$.

Lemma 3. *The functions $a_{ij}(z)$, $i,j\in\{1,2\}$ are real-valued and exhibit the following behavior:*

(i) *The functions $a_{ii}(z)$, $i=1,2$ are strictly increasing and positive on $(-\infty,0]$, and strictly increasing and negative on $[24,+\infty)$.*

(ii) *The equality*

$$\lim_{z\to\pm\infty} a_{ij}(z)=0$$

holds for all $i,j=1,2$.

(iii) *The limits $a_{ij}(0)=\lim\limits_{z\nearrow 0} a_{ij}(z)$ and $a_{ij}(24)=\lim\limits_{z\searrow 24} a_{ij}(z)$ both exist and satisfy the relations*

$$\begin{aligned}&a_{ij}(24)=(-1)^{i+j+1}a_{ij}(0),\\ &a_{11}(0)>0,\quad a_{22}(0)>0,\ a_{11}(0)a_{22}(0)>a_{12}^2(0).\end{aligned}$$

(iii) *The functions $a_{ij}(z)$ admit the following asymptotics:*

$$\begin{aligned}a_{ij}(z)=&a_{ij}(0)+O(-z),\quad z\nearrow 0,\\ a_{ij}(z)=&(-1)^{i+j+1}\left[a_{ij}(0)+O(z-24)\right],\quad z\searrow 24.\end{aligned}$$

Proof. The equality

$$a_{11}(0)a_{22}(0)-a_{12}^2(0)=\frac{1}{2}\int\limits_{\mathbb{T}^3\times\mathbb{T}^3}\frac{[\alpha_1(p)\alpha_2(q)-\alpha_1(q)\alpha_2(p)]^2}{\mathcal{E}_0(p)\mathcal{E}_0(q)}\mathrm{d}p\mathrm{d}q$$

(where α_1,α_2 are as in (7)), along with the monotonicity of the Lebesgue integral, directly implies $a_{11}(0)a_{22}(0)-a_{12}^2(0)>0$. For the remaining statements of this lemma, a demonstration similar to Proposition 1 in [35] can be employed. □

Lemma 4. *For any $\lambda,\mu\in\mathbb{R}$ the function $\Delta_{\lambda\mu}(z)$ is holomorphic in $z\in\mathbb{R}\setminus[0,24]$. Furthermore, this function is real analytic for $z\in\mathbb{R}\setminus[0,24]$ and possesses the following asymptotics:*

(i) $\lim\limits_{z\to\pm\infty}\Delta_{\lambda\mu}(z)=1$,

(ii) $\lim\limits_{z\nearrow 0}\Delta_{\lambda\mu}(z)=P^-(\lambda,\mu)$,

(iii) $\lim\limits_{z\searrow 24}\Delta_{\lambda\mu}(z)=P^+(\lambda,\mu)$,

where

$$P^{\pm}(\lambda,\mu)=a\left[(\lambda\mp\lambda_0)(\mu\mp\mu_0)-b\right],\tag{10}$$

and

$$\begin{aligned}a=a_{11}(0)a_{22}(0)-a_{12}^2(0),\quad b=\left[\frac{a_{12}(0)}{a_{11}(0)a_{22}(0)-a_{12}^2(0)}\right]^2,\\ \lambda_0=\frac{a_{22}(0)}{a_{11}(0)a_{22}(0)-a_{12}^2(0)},\qquad \mu_0=\frac{a_{11}(0)}{a_{11}(0)a_{22}(0)-a_{12}^2(0)}\end{aligned}$$

are positive real numbers.

Proof. In view of Lemma 3, the proof is obtained by a simple inspection. □

Lemma 5. *In $\mathbb{R}^2$, the set of points satisfying $P^{\pm}(\lambda,\mu)=0$ precisely forms the graph of the function*

$$\mu^{\pm}(\lambda)=\frac{b}{\lambda\mp\lambda_0}\pm\mu_0.$$

This graph consists of two isolated smooth unbounded simple connected curves:

$$\begin{aligned}\tau_0^{\pm}=\{(\lambda,\mu)\in\mathbb{R}^2:\mu=\frac{b}{\lambda\mp\lambda_0}\pm\mu_0,\ \pm\lambda<\lambda_0\},\\ \tau_1^{\pm}=\{(\lambda,\mu)\in\mathbb{R}^2:\mu=\frac{b}{\lambda\mp\lambda_0}\pm\mu_0,\ \pm\lambda<\lambda_0\}.\end{aligned}$$

and separates the (λ,μ)-parameter plane into three unbounded, contiguous, and connected components:

$$\begin{aligned}
\mathcal{C}_0^{\pm} =&\{(\lambda,\mu)\in\mathbb{R}^2 : \pm\mu < \frac{b}{\pm\lambda-\lambda_0}+\mu_0,\ \pm\lambda<\lambda_0\},\\
\mathcal{C}_1^{\pm} =&\{(\lambda,\mu)\in\mathbb{R}^2 : \pm\mu > \frac{b}{\pm\lambda-\lambda_0}+\mu_0,\ \pm\lambda<\lambda_0\}\cup\{(\pm\lambda_0,\mu)\in\mathbb{R}^2\},\\
&\{(\lambda,\mu)\in\mathbb{R}^2 : \pm\mu < \frac{b}{\pm\lambda-\lambda_0}+\mu_0,\ \pm\lambda>\lambda_0\},\\
\mathcal{C}_2^{\pm} =&\{(\lambda,\mu)\in\mathbb{R}^2 : \pm\mu > \frac{b}{\pm\lambda-\lambda_0}+\mu_0,\ \pm\lambda>\lambda_0\}
\end{aligned} \tag{11}$$

The proof of Lemma 5 resembles that of Lemma 1 in [40].

4. Main results

4.1. Critical operators

To elucidate the mechanisms of eigenvalue birth and annihilation, we introduce the concept of a *critical operator*.

Definition 1. *A parameter point (λ_0,μ_0) is lower-critical for $H^{\mathrm{ea}}_{\lambda\mu}(0)$ if the number of discrete eigenvalues below the essential spectrum is non-constant in every neighborhood of (λ_0,μ_0). Upper-critical points are defined analogously for eigenvalues above the essential spectrum.*

The following theorem characterizes criticality of the operator $H^{\mathrm{ea}}_{\lambda\mu}(0)$ through its interaction parameters.

Theorem 1. *A parameter point $(\lambda_0,\mu_0)\in\mathbb{R}^2$ is:*

(i) *Lower-critical for $H^{\mathrm{ea}}_{\lambda\mu}(0)$ iff $P^-(\lambda_0,\mu_0)=0$*
(ii) *Upper-critical for $H^{\mathrm{ea}}_{\lambda\mu}(0)$ iff $P^+(\lambda_0,\mu_0)=0$*

The following theorem, establishes that the number of isolated eigenvalues of the operator $H^{\mathrm{ea}}_{\lambda\mu}(0)$ lying above (resp. below) its essential spectrum is constant within each connected component $\mathcal{C}_\alpha^-$ (resp. $\mathcal{C}_\alpha^+$), $\alpha=0,1,2$.

Theorem 2. *Let $\mathcal{C}^-$ resp. $\mathcal{C}^+$ be one of the open connected components $\mathcal{C}_\alpha^-$ resp. $\mathcal{C}_\alpha^+$,$\alpha=0,1,2$, of the (λ,μ)-plane defined in* (11)*. Then for any $(\lambda,\mu)\in\mathcal{C}^-$ resp. $(\lambda,\mu)\in\mathcal{C}^+$ the number of eigenvalues of $H^{\mathrm{ea}}_{\lambda\mu}(0)$, lying below resp. above the essential spectrum remains constant (counting multiplicities).*

Proof. Theorem 2 can be proved analogously to [36, Theorem 3.2]. □

We will now determine the exact number of eigenvalues of the operator $H^{\mathrm{ea}}_{\lambda\mu}(0)$ lying below and above the essential spectrum within the connected components $\mathcal{C}_\zeta^-$ and $\mathcal{C}_\zeta^+$, $\zeta=0,1,2$.

Theorem 3. *Let $\lambda,\mu\in\mathbb{R}$ and $\zeta=0,1,2$. If $(\lambda,\mu)\in\mathcal{C}_\zeta^-$ (resp. $(\lambda,\mu)\in\mathcal{C}_\zeta^+$) then the operator $H^{\mathrm{ea}}_{\lambda\mu}(0)$ has exactly ζ eigenvalues lying below (resp. above) its essential spectrum.*

The next theorem demonstrates the exact number of eigenvalues of the operator $H^{\mathrm{ea}}_{\lambda\mu}(0)$ that lie below and above the essential spectrum within different unbounded smooth curves τ_ζ^- and τ_ζ^+, $\zeta=0,1$, respectively.

Theorem 4. *Let $\lambda,\mu\in\mathbb{R}$ and $\zeta=0,1$. If $(\lambda,\mu)\in\tau_\zeta^-$ (resp. $(\lambda,\mu)\in\tau_\zeta^+$) then the operator $H^{\mathrm{ea}}_{\lambda\mu}(0)$ has ζ eigenvalues, which lie below (resp. above) the essential spectrum.*

Let us define the partitions $\{\mathcal{P}_\zeta^-\}_{\zeta=0}^2$ and $\{\mathcal{P}_\zeta^+\}_{\zeta=0}^2$ of the plane $\mathbb{R}^2$:

$$\mathcal{P}_\zeta^{\pm} := \mathcal{C}_\zeta^{\pm}\cup\tau_\zeta^{\pm},\ \zeta=0,1 \quad\text{and}\quad \mathcal{P}_2^{\pm}:=\mathcal{C}_2^{\pm}.$$

Now, we present a criterion, based on the perturbation parameters $\lambda,\mu\in\mathbb{R}$, detailing when the operator $H^{\mathrm{ea}}_{\lambda\mu}(0)$ has exactly α eigenvalues in $(-\infty,0)$ or $(24,+\infty)$, $\alpha\in\{0,1,2\}$.

Corollary 1. *Let $\lambda,\mu\in\mathbb{R}$ and $\zeta\in\{0,1,2\}$. The operator $H^{\mathrm{ea}}_{\lambda\mu}(0)$ has exactly ζ eigenvalues in $(-\infty,0)$ if and only if $(\lambda,\mu)\in\mathcal{P}_\zeta^-$. Similarly, it has exactly ζ eigenvalues in $(24,+\infty)$ if and only if $(\lambda,\mu)\in\mathcal{P}_\zeta^+$.*

Let us define

$$\mathcal{G}_{\alpha\beta}=\mathcal{P}_\alpha^-\cap\mathcal{P}_\beta^+,\quad \alpha,\beta=0,1,2. \tag{12}$$

Corollary 2. *Let $\lambda,\mu\in\mathbb{R}$ and the number $\alpha,\beta=0,1,2$ satisfies $\alpha+\beta\le 2$. Then, $H^{\mathrm{ea}}_{\lambda\mu}(0)$ has α eigenvalues below and β eigenvalues above its essential spectrum if and only if $(\lambda,\mu)\in\mathcal{G}_{\alpha\beta}$.*

Proof. Corollary 2 can be proved by combining Corollary 1 and (12). □

The following theorem offers a lower estimate for the number of eigenvalues of the operator $H_{\gamma\lambda\mu}(K), K \in \mathbb{T}^3$, dependent only on λ, μ.

Theorem 5. *Let $\gamma, \lambda, \mu \in \mathbb{R}$ and $\alpha, \beta \in \{0,1,2\}$. If $(\lambda,\mu) \in \mathcal{G}_{\alpha\beta}$, then for each $K \in \mathbb{T}^3$, the operator $H_{\gamma\lambda\mu}(K)$ has at least α eigenvalues below and at least β eigenvalues above its essential spectrum.*

Proof of Theorem 5. Theorem 5 can be proved as Theorem 3 in [40]. □

5. Proof of the main results

Proof of Theorem 1. Due to symmetry, we only prove the statement for the upper threshold.

Assume that $P^+(\lambda,\mu) = 0$. Then Lemma 5 shows that $(\lambda,\mu) \in \tau_\alpha^+$ for some $\alpha \in \{0,1\}$, and any neighborhood of a point $(\lambda,\mu) \in \tau_\alpha^+$ contains points from both $\mathcal{C}_\alpha^+$ and $\mathcal{C}_{\alpha+1}^+$. Moreover, Lemma 4 states that:

$$\lim_{z\to+\infty} \Delta_{\lambda\mu}(z) = 1 \quad \text{and} \quad \lim_{z\searrow 24} \Delta_{\lambda\mu}(z) = P^+(\lambda,\mu).$$

Since $P^+(\lambda,\mu)$ exhibits different signs within $\mathcal{C}_\alpha^+$ and $\mathcal{C}_{\alpha+1}^+$ for each $\alpha = 0,1$, this implies that $\Delta_{\lambda\mu}(\cdot)$ has a different number of zeros on $(24,+\infty)$ in these regions. Consequently, by Lemma 2, the number of eigenvalues of $H_{\lambda\mu}^{\mathrm{ea}}(0)$ lying in $(24,+\infty)$ is not constant in any neighborhood of (λ,μ). This indicates that $H_{\lambda\mu}^{\mathrm{ea}}(0)$ is *critical* at the upper threshold.

We now assume that $H_{\lambda\mu}^{\mathrm{ea}}(0)$ is critical at the upper threshold for some $(\lambda,\mu) \in \mathbb{R}^2$, and proceed to prove that $P^+(\lambda,\mu) = 0$. Assume for contradiction, that $P^+(\lambda,\mu) \neq 0$. Then, Lemma 5 implies $(\lambda,\mu) \in \mathcal{C}_\alpha^+$ for some $\alpha \in \{0,1,2\}$. Since $\mathcal{C}_\alpha^+$ is an open set, there exists a neighborhood $U_\delta(\lambda,\mu) \subseteq \mathcal{C}_\alpha^+$. Within this neighborhood $U_\delta(\lambda,\mu)$, Theorem 2 ensures a constant number of eigenvalues of $H_{\lambda\mu}^{\mathrm{ea}}(0)$ lying above the essential spectrum and therefore $H_{\lambda\mu}^{\mathrm{ea}}(0)$ is not critical at its upper threshold, leading to a contradiction.

□

Note that $H_{\lambda\mu}^{\mathrm{ea}}(0)$ has at most two discrete eigenvalues. Let us denote these eigenvalues, arranged in increasing order, by $z_1(H_{\lambda\mu}^{\mathrm{ea}}(0))$ and $z_2(H_{\lambda\mu}^{\mathrm{ea}}(0))$.

Lemma 6. (i) *For each fixed $\mu \in \mathbb{R}$, the maps*

$$\lambda \mapsto z_1(H_{\lambda\mu}^{\mathrm{ea}}(0)) \quad \textit{and} \quad \lambda \mapsto z_2(H_{\lambda\mu}^{\mathrm{ea}}(0))$$

are non-decreasing on $\mathbb{R}$.

(ii) *Analogously, for each fixed $\lambda \in \mathbb{R}$, the maps*

$$\mu \mapsto z_1(H_{\lambda\mu}^{\mathrm{ea}}(0)) \quad \textit{and} \quad \mu \mapsto z_2(H_{\lambda\mu}^{\mathrm{ea}}(0))$$

are non-decreasing on $\mathbb{R}$.

Proof. (i) Let $\mu \in \mathbb{R}$ be fixed and $\lambda_1 < \lambda_2$ be an arbitrary real numbers. Then, the representation (8) and the inequality $\lambda_1 < \lambda_2$ imply that

$$(H_{\lambda_1\mu}^{\mathrm{ea}}(0)\psi,\psi) - (H_{\lambda_2\mu}^{\mathrm{ea}}(0)\psi,\psi) = (\lambda_1-\lambda_2)(\psi,\alpha_1)^2 \le 0, \text{ i.e.}$$
$$(H_{\lambda_1\mu}^{\mathrm{ea}}(0)\psi,\psi) \le (H_{\lambda_2\mu}^{\mathrm{ea}}(0)\psi,\psi), \ \forall \psi \in L^{2,\mathrm{e},\mathrm{a}_{12}}(\mathbb{T}^2).$$

For each $n = 1,2$, the last inequality leads that

$$\begin{aligned} z_n(H_{\lambda_1\mu}^{\mathrm{ea}}(0)) &:= \sup_{\phi_1,\dots,\phi_{n-1}\in L^{2,\mathrm{e},\mathrm{a}_{12}}(\mathbb{T}^2)} \ \inf_{\psi\in[\phi_1,\dots,\phi_{n-1}]^\perp,\,\|\psi\|=1} (H_{\lambda_1\mu}^{\mathrm{ea}}(0)\psi,\psi) \\ &\le \sup_{\phi_1,\dots,\phi_{n-1}\in L^{2,\mathrm{e},\mathrm{a}_{12}}(\mathbb{T}^2)} \ \inf_{\psi\in[\phi_1,\dots,\phi_{n-1}]^\perp,\,\|\psi\|=1} (H_{\lambda_2\mu}^{\mathrm{ea}}(0)\psi,\psi) = z_n(H_{\lambda_2\mu}^{\mathrm{ea}}(0)). \end{aligned}$$

(ii) For every fixed $\lambda \in \mathbb{R}$, the case of $\mu \in \mathbb{R} \mapsto z_n(H_{\lambda\mu}^{\mathrm{ea}}(0))$, $n = 1,2$ can be proved similarly. □

Proof of Theorem 3. We'll prove the "plus" case, as the "minus" case follows a similar logic and its proof is omitted for brevity.

Let us start the proof with the case $\alpha = 1$ and assume that $(\lambda,\mu) \in \mathcal{C}_1^+$. From (10) and (11), we deduce that

$$P^+(\lambda,\mu) = a\,[(\lambda-\lambda_0)(\mu-\mu_0) - k] < 0.$$

Then, Lemma 4 demonstrates that

$$\lim_{z\to+\infty} \Delta_{\lambda\mu}(z) = 1 \text{ and } \lim_{z\searrow 24} \Delta_{\lambda\mu}(z) = P^+(\lambda,\mu) < 0.$$

Since $\Delta_{\lambda\mu}(\cdot)$ changes sign on $(24,+\infty)$, it has at least one there. If there were more zeros, the endpoint sign changes would require at least three, contradicting Lemma 2. Thus, $\Delta_{\lambda\mu}(\cdot)$ has exactly one zero in $(24,+\infty)$, which Lemma 2 then implies to a unique eigenvalue of $H_{\lambda\mu}^{\mathrm{ea}}(0)$ in the same interval.

Case $\alpha = 0$. Assuming $(\lambda,\mu) \in \mathcal{C}_0^+$, we have from (11) that

$$\mu < \frac{k}{\lambda-\lambda_0} - \mu_0 \quad \text{and} \quad \lambda < \lambda_0, \tag{13}$$

which implies $P^+(\lambda,\mu)>0$. Lemma 4 then allows us to obtain

$$\lim_{z\to+\infty}\Delta_{\lambda\mu}(z)=1 \text{ and } \lim_{z\searrow 24}\Delta_{\lambda\mu}(z)=P^+(\lambda,\mu)>0. \tag{14}$$

Relation (14) and Lemma 2 imply that $\Delta_{\lambda\mu}(z)$ possesses either zero or two zeros above the essential spectrum. Assume, for contradiction, that there are two such zeros, $z_1(H^{\rm ea}_{\lambda\mu}(0))$ and $z_2(H^{\rm ea}_{\lambda\mu}(0))$, satisfying

$$24<z_1(H^{\rm ea}_{\lambda\mu}(0))\le z_2(H^{\rm ea}_{\lambda\mu}(0)). \tag{15}$$

In other hand, (11) states that

$$(\lambda_0,\mu)\in\mathcal{C}_1^+\ \forall\mu\in\mathbb{R}.$$

Further, the inequality $\lambda<\lambda_0$ in (13), the relation (15), and Lemma 6 yield

$$z_2(H^{\rm ea}_{\lambda_0\mu}(0))\ge z_2(H^{\rm ea}_{\lambda\mu}(0))>24,$$

indicating that $H^{\rm ea}_{\lambda_0\mu}(0)$ has at least two eigenvalues located in $(24,+\infty)$, contradicting the previous result. Thus, for all $(\lambda,\mu)\in\mathcal{C}_0^+$, $H^{\rm ea}_{\lambda\mu}(0)$ lacks eigenvalues in $(24,+\infty)$.

Take any $(\lambda,\mu)\in\mathcal{C}_2^+$. Then, (10) and (11) provide the inequalities

$$\begin{aligned}&P(\lambda,\mu)=a\left[(\lambda-\lambda_0)(\mu-\mu_0)-k\right]>0,\\ &\mu>\mu_0,\quad \lambda>\lambda_0.\end{aligned} \tag{16}$$

Using Lemma 4 and (16), we find that

$$\lim_{z\to+\infty}\Delta_{\lambda\mu}(z)=1\quad\text{and}\quad\lim_{z\searrow 24}\Delta_{\lambda\mu}(z)=P^+(\lambda,\mu)>0. \tag{17}$$

Note that $(\lambda_0,\mu)\in\mathcal{C}_1^+$ and so $H^{\rm ea}_{\lambda_0\mu}(0)$ has exactly one eigenvalue $z_1(H^{\rm ea}_{\lambda_0\mu}(0))>24$. Then the relation $\lambda>\lambda_0$ in (16) and Lemma 6 give that

$$z_1(H^{\rm ea}_{\lambda\mu}(0))\ge z_1(H^{\rm ea}_{\lambda_0\mu}(0))>24,$$

which yields that $H^{\rm ea}_{\lambda\mu}(0)$ has at least one eigenvalue in $(24,+\infty)$. Then, Lemma 2 implies that $\Delta_{\lambda\mu}(\cdot)$ has at least one zero in $(24,+\infty)$. On the other hand, (17) indicates that $\Delta_{\lambda\mu}$ has the same sign at the endpoints of $(24,+\infty)$; therefore, it must possess an even number of zeros (counting multiplicities). Thus, $H^{\rm ea}_{\lambda\mu}(0)$ has exactly two (simple) eigenvalues located in $(24,+\infty)$. □

Proof of Theorem 4. The function $(\lambda,\mu)\to n_+(H^{\rm ea}_{\lambda\mu}(0))$ (resp. $(\lambda,\mu)\to n_-(H^{\rm ea}_{\lambda\mu}(0))$) is continuous on each $\mathcal{P}^+_\zeta$ (respectively, on each $\mathcal{P}^-_\zeta$), for $\zeta=0,1,2$, where, $n_+(H^{\rm ea}_{\lambda\mu}(0))$ (respectively, $n_-(H^{\rm ea}_{\lambda\mu}(0))$) denotes the number of isolated eigenvalues of $H^{\rm ea}_{\lambda\mu}(0)$ located in $(24,+\infty)$ (resp. $(-\infty,0)$). This proves the assertion. □

Proof of Corollary 1. Let $(\lambda,\mu)\in\mathcal{P}^+_\alpha$. Then Theorem 3 implies that $H^{\rm ea}_{\lambda\mu}(0)$ has exactly α eigenvalues in $(24,+\infty)$.

For the converse, assume $H^{\rm ea}_{\lambda\mu}(0)$ has precisely α eigenvalues in $(24,+\infty)$. We proceed by contradiction to establish that $(\lambda,\mu)\in\mathcal{P}^+_\alpha$. Suppose $(\lambda,\mu)\notin\mathcal{P}^+_\alpha$. Since $\{\mathcal{P}^+_0,\mathcal{P}^+_1,\mathcal{P}^+_2\}$ forms a partition of $\mathbb{R}^2$, there exists $\beta\neq\alpha$ such that $(\lambda,\mu)\in\mathcal{P}^+_\beta$. Theorem 3 then implies that $H^{\rm ea}_{\lambda\mu}(0)$ has exactly $\beta\neq\alpha$ eigenvalues above its essential spectrum, directly contradicting our initial assumption. □

6. Conclusion

This paper meticulously analyzed the spectral characteristics of the lattice Schrödinger operators, $H_{\gamma\lambda\mu}(K)$, which model two identical bosons on $\mathbb{Z}^3$ with on-site and nearest-neighbor interactions. Our study of $H_{\gamma\lambda\mu}(0)$ revealed an invariant subspace where its restricted form, $H^{\rm ea}_{\lambda\mu}(0)$, depends only on λ and μ. To elucidate eigenvalue birth and annihilation for $H^{\rm ea}_{\lambda\mu}(0)$, we defined a critical operator and developed a detailed criterion in the $\lambda-\mu$ plane. This involved: (i) deriving smooth critical curves that delineate the onset of criticality; and (ii) proving exact conditions for the existence of precisely α eigenvalues below and β eigenvalues above the essential spectrum, with $\alpha,\beta\in\{0,1,2\}$ and $\alpha+\beta\le 2$.

References

[1] Mattis D. The few-body problem on a lattice. *Rev. Mod. Phys.*, **58**, P. 361–379, 1986.

[2] Albeverio S., Lakaev S.N., Muminov Z.I. Schrödinger operators on lattices. The Efimov effect and discrete spectrum asymptotics. *Ann. Henri Poincaré*, 2004, **5**, P. 743–772.

[3] Albeverio S., Lakaev S.N., Makarov K.A., Muminov Z.I. The Threshold Effects for the Two-particle Hamiltonians on Lattices. *Comm. Math. Phys.*, 2006, **262**, P. 91–115.

[4] Albeverio S., Lakaev S.N., Khalkhujaev A.M. Number of Eigenvalues of the Three-Particle Schrödinger Operators on Lattices. *Markov Process. Relat. Fields*, 2012, **18**, P. 387–420.

[5] Bach V., W. de Siqueira Pedra, Lakaev S.N. Bounds on the discrete spectrum of lattice Schrödinger operators. *J. Math. Phys.*, 2017, **59**(2), P. 022109.

[6] P.A. Faria Da Veiga, Ioriatti L., O'Carroll M. Energy-momentum spectrum of some two-particle lattice Schrödinger Hamiltonians. *Phys. Rev. E*, 2002, **66**, P. 016130.

[7] Hiroshima F., Muminov Z., Kuljanov U. Threshold of discrete Schrödinger operators with delta-potentials on N-dimensional lattice. *Linear and Multilinear Algebra*, 2020, **68**(11), P. 2267–2279.

[8] Kholmatov Sh.Yu., Lakaev S.N., Almuratov F.M. On the spectrum of Schrödinger-type operators on two dimensional lattices. *J. Math. Anal. Appl.*, 2022, **504**(2), P. 126363.
[9] Lakaev S.N. The Efimov's effect of the three identical quantum particle on a lattice. *Funct. Anal. Appl.*, 1993, **27**, P. 15–28.
[10] Lakaev S.N., Abdukhakimov S.Kh. Threshold effects in a two-fermion system on an optical lattice. *Theoret. and Math. Phys.*, 2020, **203**(2), P. 251–268.
[11] Lakaev S.N., Kholmatov Sh.Yu., Khamidov Sh.I. Bose-Hubbard model with on-site and nearest-neighbor interactions; exactly solvable case. *J. Phys. A: Math. Theor.*, 2021, **54**, P. 245201.
[12] Lakaev S.N., Özdemir E. The existence and location of eigenvalues of the one particle Hamiltonians on lattices. *Hacettepe J. Math. Stat.*, 2016, **45**, P. 1693–1703.
[13] Lakaev S.N., Khalkhuzhaev A.M., Lakaev Sh.S. Asymptotic behavior of an eigenvalue of the two-particle discrete Schrödinger operator. *Theoret. and Math. Phys.*, 2012, **171**(3), P. 438–451.
[14] Motovilov A.K., Sandhas W., Belyaev V.B. Perturbation of a lattice spectral band by a nearby resonance. *J. Math. Phys.*, 2001, **42**, P. 2490–2506.
[15] Muminov M.I., Khurramov A.M., Bozorov I.N. On eigenvalues and virtual levels of a two-particle Hamiltonian on a d-dimensional lattice. *Nanosystems: Phys. Chem. Math.*, 2023, **14**(3), P. 295–303.
[16] Lakaev S.N., Kurbanov Sh.Kh., Alladustov Sh.U. Convergent Expansions of Eigenvalues of the Generalized Friedrichs Model with a Rank-One Perturbation. *Complex Analysis and Operator Theory*, 2021, **15**, P. 121.
[17] Faddeev L.D., Merkuriev S.P. *Quantum Scattering Theory for Several Particle Systems*. Kluwer Academic Publishers, Doderecht, 1993.
[18] Efimov V.N. Weakly Bound States of Three Resonantly Interacting Particles. *Yad. Fiz.*, 1970, **12**, P. 1080. [*Sov. J. Nucl. Phys.*, 1970, **12**, P. 589].
[19] Ovchinnikov Y.N., Sigal I.N. Number of bound states of three-body systems and Efimov's effect. *Ann. Phys.*, 1979, **123**(2), P. 274–295.
[20] Sobolev A.V. The Efimov effect. Discrete spectrum asymptotics. *Commun. Math. Phys.*, 1993, **156**(1), P. 101–126.
[21] Tamura H. The Efimov effect of three-body Schrödinger operators. *J. Funct. Anal.*, 1991, **95**(2), P. 433–459.
[22] Yafaev D.R. On the theory of the discrete spectrum of the three-particle Schrödinger operator. *Mat. Sb.*, 1974, **94**(136), P. 567–593.
[23] Dell'Antonio G., Muminov Z.I., Shermatova V.M. On the number of eigenvalues of a model operator related to a system of three particles on lattices. *Journal of Physics A: Mathematical and Theoretical*, 2011, **44**, P. 315302.
[24] Bagmutov A.S., Popov I.Y. (2020). Window-coupled nanolayers: window shape influence on one-particle and two-particle eigenstates. *Nanosystems: Physics, Chemistry, Mathematics*, **11**(6), P. 636–641.
[25] Bloch I. Ultracold quantum gases in optical lattices. *Nat. Phys.*, 2005, **1**, P. 23–30.
[26] Winkler K., Thalhammer G., Lang F., Grimm R., J. Hecker Denschlag, Daley A.J., Kantia A.n, Büchler H.P., Zoller P. Repulsively bound atom pairs in an optical lattice. *Nature*, 2006, **441**, P. 853–856.
[27] Jaksch D., Bruder C., Cirac J., Gardiner C.W., Zoller P. Cold bosonic atoms in optical lattices. *Phys. Rev. Lett.*, 1998, **81**, P. 3108–3111.
[28] Jaksch D., Zoller P. The cold atom Hubbard toolbox. *Ann. Phys.*, 2005, **315**, P. 52–79.
[29] Lewenstein M., Sanpera A., Ahufinger V. *Ultracold Atoms in Optical Lattices: Simulating Quantum Many-body Systems*. Oxford University Press, Oxford, 2012.
[30] Ospelkaus C., Ospelkaus S., Humbert L., Ernst P., Sengstock K., Bongs K. Ultracold heteronuclear molecules in a 3d optical lattice. *Phys. Rev. Lett.*, 2006, **97**, P. 120402.
[31] Reed M., Simon B. *Methods of Modern Mathematical Physics. III: Scattering Theory*. Academic Press, N.Y., 1978.
[32] Lakaev S.N., Bozorov I.N. The number of bound states of a one-particle Hamiltonian on a three-dimensional lattice. *Theoret. and Math. Phys.*, 2009, **158**, P. 360–376.
[33] Lakaev S.N., Alladustova I.U. The exact number of eigenvalues of the discrete Schrödinger operators in one-dimensional case. *Lobachevskii J. Math.*, 2021, **42**, P. 1294–1303.
[34] Akhmadova M.O., Alladustova I.U., Lakaev S.N. On the Number and Locations of Eigenvalues of the Discrete Schrödinger Operator on a Lattice. *Lobachevskii Journal of Mathematics*, 2023, **44**, P. 1091–1099.
[35] Lakaev S.N., Akhmadova M.O. The number and location of eigenvalues for the two-particle Schrödinger operators on lattices. *Complex Analysis and Operator Theory*, 2023, **17**, P. 104.
[36] Lakaev S.N., Motovilov A.K., Abdukhakimov S.Kh. Two-fermion lattice Hamiltonian with first and second nearest-neighboring-site interactions. *J. Phys. A: Math. Theor.*, 2023, **56**, P. 315202.
[37] Reed M., Simon B. *Methods of Modern Mathematical Physics. IV: Analyses of Operators*. Academic Press, N.Y., 1978.
[38] Lippmann B.A., Schwinger J. Variational principles for scattering processes. I. *Phys. Rev.*, 1950, **79**, P. 469.
[39] Kato T. *Perturbation Theory for Linear Operators* (2nd ed.). Springer-Verlag, 1995.
[40] Lakaev S.N., Khamidov Sh.I., Akhmadova M.O. Number of bound states of the Hamiltonian of a lattice two-boson system with interactions up to the next neighbouring sites. *Lobachevskii Journal of Mathematics*, 2024, **45**(12), P. 6409–6420.

Submitted 1 July 2025; revised 21 August 2025; accepted 22 August 2025

Information about the authors:

Mukhayyo O. Akhmadova – Samarkand State University, 140104, Samarkand, Uzbekistan; ORCID 0009-0000-9082-5986; mukhayyo.akhmadova@mail.ru

Mukammal A. Azizova – Samarkand State University, 140104, Samarkand, Uzbekistan; ORCID 0009-0001-5068-3204; mukammal.azizova@gmail.com

Conflict of interest: the authors declare no conflict of interest.

NANOSYSTEMS:
PHYSICS, CHEMISTRY, MATHEMATICS

Rasulov T., et al. *Nanosystems: Phys. Chem. Math.*, 2025, **16** (5), 586–592.
http://nanojournal.ifmo.ru
DOI 10.17586/2220-8054-2025-16-5-586-592

Original article

Asymptotic expansion of Fredholm determinant associated to a family of Friedrichs models arising in quantum mechanics

Tulkin Rasulov[1,a,b], Gulhayo Umirkulova[1,c]

[1]Faculty of Physics, Mathematics and Information Technologies Bukhara State University, Bukhara, Uzbekistan

[a]rth@mail.ru, [b]t.h.rasulov@buxdu.uz, [c]g.h.umirqulova@buxdu.uz

Corresponding author: T. Rasulov, rth@mail.ru, t.h.rasulov@buxdu.uz

ABSTRACT In this paper, we consider a family of Friedrichs models that arise in quantum mechanics and corresponding to the Hamiltonian of a two-particle system on a one-dimensional lattice. The number, location, and existence conditions of eigenvalues of this family were analyzed. An asymptotic expansion for the associated Fredholm determinant in a neighborhood of the origin has been derived.

KEYWORDS Friedrichs model, quantum mechanics, lattice, two-particle system, Fredholm determinant, eigenvalue, expansion.

ACKNOWLEDGEMENTS The authors express their sincere gratitude for the support received from the Foundation for Basic Research of the Republic of Uzbekistan (Grant No. FL-9524115052). We are greatly indebted to the anonymous referees for a number of constructive and useful comments.

FOR CITATION Rasulov T., Umirkulova G. Asymptotic expansion of Fredholm determinant associated to a family of Friedrichs models arising in quantum mechanics. *Nanosystems: Phys. Chem. Math.*, 2025, **16** (5), 586–592.

1. Introduction

The Friedrichs model is among the most fundamental and classical frameworks in spectral theory and quantum mechanics [1–3]. It was introduced by Kurt Friedrichs as a simplified model to investigate how discrete spectra may become embedded in, or interact with, the continuous spectrum under perturbations. The Friedrichs model, also referred to as the Friedrichs-Lee model, is a quantum mechanical framework describing the interaction between a discrete energy level and a continuous spectrum. It is worth noting that the properties of the Friedrichs model find applications in various fields, including the quantum field theory of unstable particles, non-relativistic quantum electrodynamics, and quantum optics.

It should be noted that the Friedrichs model is among the most widely used and powerful theoretical tools for the mathematical analysis of quantum decay, resonances, and energy leakage into the continuum in nanosystems [4]. This model enables both analytical and numerical investigations of the stability of quantum dots, the lifetimes of resonance states, energy exchange processes, and decoherence phenomena.

In [5], a family of Friedrichs models $h_\mu(p)$, with $\mu > 0$ and $p \in (-\pi;\pi]^3$ of the generalized Friedrichs model featuring a rank-one perturbation, associated with a two-particle system moving on a one-dimensional lattice, is studied. The existence of a unique eigenvalue below the bottom of the essential spectrum of $h_\mu(p)$ for all non-trivial values of p is established under the assumption that $h_\mu(0)$ possesses either a threshold energy resonance (virtual level) or a threshold eigenvalue. The threshold energy expansion of the Fredholm determinant associated with a family of the Friedrichs models has also been derived.

In [6], a family $H_\mu(p)$, $\mu > 0$, $p \in (-\pi;\pi]$ of the generalized Friedrichs model with perturbation of rank one, associated with a system of two particles, moving on the one-dimensional lattice is considered. The existence of a unique eigenvalue $E(\mu,p)$, of the operator $H_\mu(p)$ lying below the essential spectrum, is established. Moreover, for all p in a neighborhood of the origin, the Puiseux series expansion of the eigenvalue $E(\mu,p)$ at the point $\mu = \mu(p) \to 0$ is derived. Furthermore, the asymptotic behavior of $E(\mu,p)$ as $\mu \to +\infty$ is established.

In [7], a family of the generalized Friedrichs models $H_\mu(p)$, $\mu > 0$, $p \in (-\pi;\pi]^3$ with the perturbation of rank one is investigated. An absolutely convergent expansion for the eigenvalue at the coupling constant threshold is obtained. It is shown that the form of this expansion crucially depends on whether the lower edge of the essential spectrum corresponds to a threshold resonance or a threshold eigenvalue.

In the present paper, we consider a family of Friedrichs models $h_\mu^{(\gamma)}(k)$, depending on the parameters $\mu, \gamma > 0$ and $k \in (-\pi;\pi]$ with the rank-one perturbation associated to a system of two arbitrary or identical quantum mechanical particles moving on the one-dimensional lattice. Here we note that the kinetic part of $h_\mu^{(\gamma)}(k)$ contains a parameter $\gamma > 0$ and differs from the above-mentioned works in this respect. One of the important aspect of studying such type Friedrichs models is that they describe the Hamiltonian for systems of both bosons and fermions (see, for example, [8–11]). It is

important that when considering three particle model Hamiltonian on a lattice, the role of two-particle discrete Schrödinger operators is played by a family of Friedrich's models [12–14]. For each fixed number $\gamma > 0$, it is proved that there exists a critical point μ_γ^0 such that for any $\mu \in (0; \mu_\gamma^0]$ the Friedrichs model $h_\mu^{(\gamma)}(0)$ has no negative eigenvalues, and for any $\mu \in (\mu_\gamma^0; +\infty)$ the Friedrichs model $h_\mu^{(\gamma)}(0)$ has a unique simple negative eigenvalue. For any fixed $\mu > 0$ and $\gamma > 0$ we study the expansion for the Fredholm determinant $\Delta_\mu^{(\gamma)}(k\,; z)$ associated to $h_\mu^{(\gamma)}(k)$ with respect to the spectral parameters k and z.

2. Statement of the problem

Let $\mathbb{T}$ be the one-dimensional torus and $L_2(\mathbb{T})$ be the Hilbert space of square integrable (complex) functions defined on $\mathbb{T}$.

For any fixed $\mu > 0$ and $\gamma > 0$, we consider a family of Friedrichs models $h_\mu^{(\gamma)}(k)$, $k \in \mathbb{T}$, acting in the Hilbert space $L_2(\mathbb{T})$, given by

$$h_\mu^{(\gamma)}(k) := h_0^{(\gamma)}(k) - \mu v,$$

where $h_0^{(\gamma)}(k)$ is the multiplication operator by the function $E_\gamma(k; \cdot)$:

$$(h_0^{(\gamma)}(k)f)(x) = E_\gamma(k, x)f(x), \quad f \in L_2(\mathbb{T}),$$
$$E_\gamma(k, x) := \varepsilon(k) + \varepsilon(x) + \gamma\varepsilon(k + x), \quad \varepsilon(x) := 1 - \cos x,$$

and v is a non-local interaction operator:

$$(vf)(x) = \sin(x) \int_{\mathbb{T}} \sin(t) f(t) dt.$$

It is clear that the family of Friedrichs models $h_\mu^{(\gamma)}(k)$, $k \in \mathbb{T}$ is a linear, bounded and self-adjoint operator in $L_2(\mathbb{T})$.

We note that in [15, 16], by analyzing the spectra of two Friedrichs models with rank-two perturbations, the existence of eigenvalues located inside the spectrum, within the spectral gap, and below the bottom of the essential spectrum of the tensor sum of these Friedrichs models has been established.

Throughout the paper, the notations $\sigma(\cdot)$, $\sigma_{\rm ess}(\cdot)$, $\sigma_{\rm p}(\cdot)$ and $\sigma_{\rm disc}(\cdot)$ are employed to represent the spectrum, the essential spectrum, the point spectrum, and the discrete spectrum, respectively, of a bounded self-adjoint operator. For the reader's convenience, we provide the definitions of the essential and discrete spectra for a linear, bounded, and self-adjoint operator $\mathcal{A}$ in a Hilbert space $\mathcal{H}$. The set of all isolated eigenvalues of finite multiplicity of the operator $\mathcal{A}$ is called the discrete spectrum of the operator $\mathcal{A}$. The complement set $\sigma(\mathcal{A}) \setminus \sigma_{\rm disc}(\mathcal{A})$ is called the essential spectrum of the operator $\mathcal{A}$.

The perturbation operator v corresponding to the unperturbed operator $h_0^{(\gamma)}(k)$ is a self-adjoint operator of rank one. Hence, according to the Weyl theorem regarding the invariance of the essential spectrum under finite-rank perturbations, the essential spectra of the operators $h_\mu^{(\gamma)}(k)$ and $h_0^{(\gamma)}(k)$ coincide. It is evident that the unperturbed operator $h_0^{(\gamma)}(k)$ has a purely essential spectrum and the essential spectrum $\sigma_{\rm ess}(h_0^{(\gamma)}(k))$ equals $[m_\gamma(k); M_\gamma(k)]$, where the numbers $m_\gamma(k)$ and $M_\gamma(k)$ are defined by

$$m_\gamma(k) := \min_{x \in \mathbb{T}} E_\gamma(k, x), \quad M_\gamma(k) := \max_{x \in \mathbb{T}} E_\gamma(k, x).$$

Consequently, the essential spectrum $\sigma_{\rm ess}(h_\mu^{(\gamma)}(k))$ equals $[m_\gamma(k); M_\gamma(k)]$, and does not depend on the parameter $\mu > 0$. Notably, when $k = 0$ the following equality

$$\sigma_{\rm ess}(h_\mu^{(\gamma)}(0)) = [0; 2(1 + \gamma)]$$

holds.

For any $\mu, \gamma > 0$ and $k \in \mathbb{T}$ we define an analytic function $\Delta_\mu^{(\gamma)}(k\,; \cdot)$ (the Fredholm determinant corresponding to the Friedrichs model $h_\mu^{(\gamma)}(k)$) in $\mathbb{C} \setminus [m_\gamma(k); M_\gamma(k)]$ by

$$\Delta_\mu^{(\gamma)}(k\,; z) := 1 - \mu \int_{\mathbb{T}} \frac{\sin^2(t)\, dt}{E_\gamma(k, t) - z}.$$

The following lemma is a straightforward consequence of the Birman-Schwinger principle and the Fredholm theorem.

Lemma 2.1. *Let $\mu, \gamma > 0$ and $k \in \mathbb{T}$ be fixed. The Friedrichs model $h_\mu^{(\gamma)}(k)$ has an eigenvalue $z_{\mu,\gamma}(k) \in \mathbb{C} \setminus [m_\gamma(k); M_\gamma(k)]$ if and only if $\Delta_\mu^{(\gamma)}(k\,; z_{\mu,\gamma}(k)) = 0$.*

Lemma 2.1 thus yields the following equality

$$\sigma_{\rm disc}(h_\mu^{(\gamma)}(k)) = \{z \in \mathbb{C} \setminus [m_\gamma(k); M_\gamma(k)] : \Delta_\mu^{(\gamma)}(k\,; z) = 0\}$$

for the discrete spectrum of $h_\mu^{(\gamma)}(k)$.

At this point, we specify the number and location of the eigenvalues of the Friedrichs model $h_\mu^{(\gamma)}(k)$.

Lemma 2.2. *For any fixed $\mu,\gamma>0$ and $k\in\mathbb{T}$, the Friedrichs model $h_\mu^{(\gamma)}(k)$ has at most one simple eigenvalue to the left of $m_\gamma(k)$ and no eigenvalues to the right of $M_\gamma(k)$.*

The proof of Lemma 2.2 relies on the monotonicity of the function $\Delta_\mu^{(\gamma)}(k\,;\cdot)$ over $(-\infty;m_\gamma(k))$, the inequality $\Delta_\mu^{(\gamma)}(k\,;z)>1$ for all $z>M_\gamma(k)$, and Lemma 2.1.

Since for any $\gamma>0$ the function $E_\gamma(\cdot,\cdot)$ has non-degenerate global minimum equal to zero at the point $(0,0)\in\mathbb{T}^2$, the following expansion

$$E_\gamma(x,y)=\frac{1}{2}\left(\frac{\partial^2E_\gamma(0,0)}{\partial x^2}x^2+2\frac{\partial^2E_\gamma(0,0)}{\partial x\partial y}xy+\frac{\partial^2E_\gamma(0,0)}{\partial y^2}y^2\right)+o(x^2)+o(y^2)$$

holds as $x,y\to0$. Hence, one can find positive constants $C_1(\gamma),C_2(\gamma)>0$ and $\delta>0$ for which the following estimates

$$C_1(\gamma)(x^2+y^2)\le E_\gamma(x,y)\le C_2(\gamma)(x^2+y^2),\quad (x,y)\in(-\delta;\delta)\times(-\delta;\delta),\tag{2.1}$$

$$E_\gamma(x,y)\ge C_1(\gamma),\quad (x,y)\notin(-\delta;\delta)\times(-\delta;\delta)\tag{2.2}$$

are valid. Using inequalities (2.1), (2.2), together with the asymptotic relation $\sin x\sim x$ as $x\to0$ one can easily see that the following integral

$$\int_{\mathbb{T}}\frac{\sin^2(t)dt}{E_\gamma(k,t)}$$

is positive and finite for any $\gamma>0$ and $k\in\mathbb{T}$. Thus, the Lebesgue dominated convergence theorem implies that $\Delta_\mu^{(\gamma)}(0\,;0)=\lim\limits_{k\to0}\Delta_\mu^{(\gamma)}(k\,;0)$, and, consequently, the function $\Delta_\mu^{(\gamma)}(\cdot\,;0)$ is continuous on $\mathbb{T}$.

Set

$$\mu_\gamma^0:=(1+\gamma)\left(\int_{\mathbb{T}}\frac{\sin^2(t)\,dt}{\varepsilon(t)}\right)^{-1}.$$

This implies that $\Delta_\mu^{(\gamma)}(0\,;0)=0$ if and only if $\mu=\mu_\gamma^0$.

We now examine the eigenvalues of the Friedrichs model $h_\mu^{(\gamma)}(k)$ when $k=0$.

Theorem 2.3. *Suppose $\gamma>0$ is fixed. When $\mu\in(0;\mu_\gamma^0]$, the Friedrichs model $h_\mu^{(\gamma)}(0)$ does not have any eigenvalues. Whenever $\mu>\mu_\gamma^0$, the Friedrichs model $h_\mu^{(\gamma)}(0)$ admits single negative eigenvalue.*

Proof. Assume $\mu\in(0;\mu_\gamma^0]$. To start, let us prove the following inequality

$$\Delta_\mu^{(\gamma)}(0\,;z)>\Delta_\mu^{(\gamma)}(0\,;0)\ge\Delta_{\mu_\gamma^0}^{(\gamma)}(0\,;0)$$

for all $z<0$.

Since the function $\Delta_\mu^{(\gamma)}(0\,;\cdot)$ is monotonically decreasing on the interval $(-\infty;0)$, it follows that

$$\Delta_\mu^{(\gamma)}(0\,;z)>\Delta_\mu^{(\gamma)}(0\,;0)$$

for every $z<0$.

Now, we turn to the proof of the inequality

$$\Delta_\mu^{(\gamma)}(0\,;0)\ge\Delta_{\mu_\gamma^0}^{(\gamma)}(0\,;0)$$

for any $\mu\in(0;\mu_\gamma^0]$. As a matter of fact, we have

$$\Delta_\mu^{(\gamma)}(0\,;0)=1-\mu\int_{\mathbb{T}}\frac{\sin^2(t)\,dt}{(1+\gamma)\varepsilon(t)}\ge1-\mu_\gamma^0\int_{\mathbb{T}}\frac{\sin^2(t)\,dt}{(1+\gamma)\varepsilon(t)}=\Delta_{\mu_\gamma^0}^{(\gamma)}(\,0;0).$$

Alternatively, using the definition of μ_γ^0, we find

$$\Delta_{\mu_\gamma^0}^{(\gamma)}(0;0)=1-(1+\gamma)\left(\int_{\mathbb{T}}\frac{\sin^2(t)\,dt}{\varepsilon(t)}\right)^{-1}\int_{\mathbb{T}}\frac{\sin^2(t)\,dt}{(1+\gamma)\varepsilon(t)}=0.$$

Employing the definition of $\Delta_\mu^{(\gamma)}(0;\cdot)$, we deduce that

$$\lim_{z\to-\infty}\Delta_\mu^{(\gamma)}(0;z)=1\tag{2.3}$$

and

$$\lim_{z\to0^-}\Delta_\mu^{(\gamma)}(0;z)=\Delta_\mu^{(\gamma)}(0;0).$$

Since $\Delta_\mu^{(\gamma)}(0;z)>0$ for all $z<0$, it follows from Lemma 2.1 that the Friedrichs model $h_\mu^{(\gamma)}(0)$ has no eigenvalues in $(-\infty;0)$ (see Figure 1).

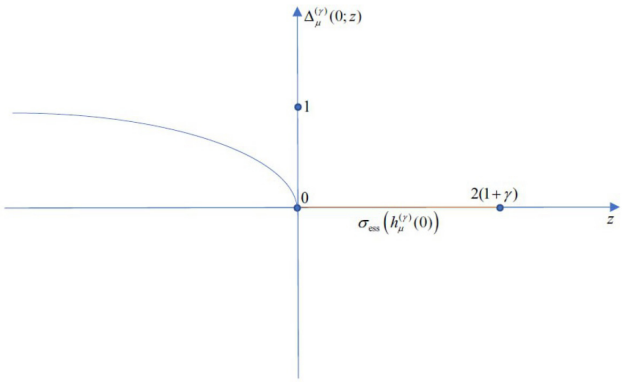

FIG. 1. An absence of the eigenvalue of $h_\mu^{(\gamma)}(0)$ for $0 < \mu \leq \mu_\gamma^0$.

Let us now assume that $\mu > \mu_\gamma^0$. It can be easily seen from simple calculations that

$$\mu > \mu_\gamma^0 \Longrightarrow \mu(\mu_\gamma^0)^{-1} > 1 \Longrightarrow 1 - \mu(\mu_\gamma^0)^{-1} < 0.$$

The last inequality is expressed equivalently by the following relation

$$\Delta_\mu^{(\gamma)}(0\,;0) = 1 - \mu \int_{\mathbb{T}} \frac{\sin^2(t)\,dt}{(1+\gamma)\varepsilon(t)} < 0.$$

Since the function $\Delta_\mu^{(\gamma)}(0\,;\cdot)$ is monotone decreasing on the interval $(-\infty;0)$ and $\Delta_\mu^{(\gamma)}(0\,;z) < 0$, it follows from equality (2.3) that $\Delta_\mu^{(\gamma)}(0\,;\cdot)$ has unique negative zero $z_{\mu,\gamma}$ (see Figure 2).

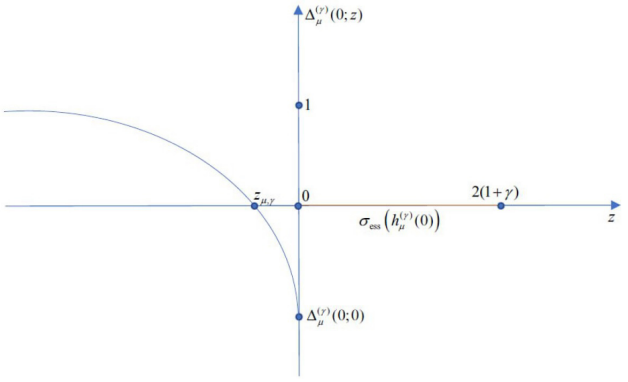

FIG. 2. An existence of the eigenvalue of $h_\mu^{(\gamma)}(0)$ for $\mu > \mu_\gamma^0$.

According to 2.1 the number $z_{\mu,\gamma}$ is an eigenvalue of the Friedrichs model $h_\mu^{(\gamma)}(0)$. □

3. Expansion for the Fredholm determinant

In this section, we obtain an asymptotic expansion for the Fredholm determinant, which is important in analyzing the number of eigenvalues of the model operator corresponding to the energy operator of a system of three particles on a lattice.

Now we formulate the main result of the present paper.

Theorem 3.1. *Let $\mu, \gamma > 0$ be a fixed. The following expansion*

$$\Delta_\mu^{(\gamma)}(k\,;z) = \Delta_\mu^{(\gamma)}(0\,;0) + \frac{2\mu\pi(1+2\gamma-\gamma^2)}{(1+\gamma)^2\sqrt{1+2\gamma}}\sqrt{k^2 - \frac{2(1+\gamma)}{1+2\gamma}z} + O(k^2) + O(\sqrt{|z|})$$

holds as $k \to 0$ and $z \to -0$.

Proof. Let $\delta > 0$ be sufficiently small and $\mathbb{T}_\delta := \mathbb{T} \setminus (-\delta; \delta)$. We rewrite the function $\Delta_\mu^{(\gamma)}(\cdot\,;\cdot)$ in the from $\Delta_\mu^{(\gamma)}(k\,;z) = \Delta_\mu^{(\gamma,1)}(k\,;z) + \Delta_\mu^{(\gamma,2)}(k\,;z)$, where

$$\Delta_\mu^{(\gamma,1)}(k\,;z) := 1 - \mu \int_{\mathbb{T}_\delta} \frac{\sin^2(t)\,dt}{E_\gamma(k,t) - z},$$

$$\Delta_\mu^{(\gamma,2)}(k\,;z) := -\mu \int_{-\delta}^{\delta} \frac{\sin^2(t)\,dt}{E_\gamma(k,t) - z}.$$

Since $\Delta_\mu^{(\gamma,1)}(\cdot\,;z)$ is an even analytic function on $\mathbb{T}$ for any $z \le 0$, we have

$$\Delta_\mu^{(\gamma,1)}(k\,;z) = \Delta_\mu^{(\gamma,1)}(0\,;0) + O(k^2) + O(|z|) \tag{3.1}$$

as $k \to 0$ and $z \to -0$. Using the relations

$$\sin k = k + O(k^3), \quad 1 - \cos k = \frac{1}{2}k^2 + O(k^4)$$

as $k \to 0$, we obtain

$$\Delta_\mu^{(\gamma,2)}(k\,;z) := -2\mu \int_{-\delta}^{\delta} \frac{t^2 dt}{(1+\gamma)k^2 + 2\gamma kt + (1+\gamma)t^2 - 2z} + O(k^2) + O(|z|)$$

as $k \to 0$ and $z \to -0$. For the convenience, we rewrite the latter integral as

$$\int_{-\delta}^{\delta} \frac{t^2 dt}{(1+\gamma)k^2 + 2\gamma kt + (1+\gamma)t^2 - 2z} =$$

$$= \frac{2\delta}{1+\gamma} - \frac{\gamma k}{1+\gamma} \int_{-\delta}^{\delta} \frac{2t dt}{(1+\gamma)k^2 + 2\gamma kt + (1+\gamma)t^2 - 2z} -$$

$$- \frac{(1+\gamma)k^2 - 2z}{1+\gamma} \int_{-\delta}^{\delta} \frac{dt}{(1+\gamma)k^2 + 2\gamma kt + (1+\gamma)t^2 - 2z}.$$

Now, we will analyze each integral in the previous equality. Evaluating the integral in the second summand, we obtain

$$\int_{-\delta}^{\delta} \frac{2t dt}{(1+\gamma)k^2 + 2\gamma kt + (1+\gamma)t^2 - 2z} = \frac{1}{1+\gamma} \log \left| 1 + \frac{4\gamma\delta k}{(1+\gamma)k^2 - 2\gamma\delta k + (1+\gamma)\delta^2 - 2z} \right|$$

$$- \frac{2\gamma k}{1+\gamma} \int_{-\delta}^{\delta} \frac{dt}{(1+\gamma)k^2 + 2\gamma kt + (1+\gamma)t^2 - 2z}.$$

Since

$$\log \left| 1 + \frac{4\gamma\delta k}{(1+\gamma)k^2 - 2\gamma\delta k + (1+\gamma)\delta^2 - 2z} \right| = O(k)$$

as $k \to 0$, from the comparison of the last expressions, we derive

$$\int_{-\delta}^{\delta} \frac{t^2 dt}{(1+\gamma)k^2 + 2\gamma kt + (1+\gamma)t^2 - 2z} = \frac{2\delta}{1+\gamma} -$$

$$- \left(\frac{1 + 2\gamma - \gamma^2}{(1+\gamma)^2} k^2 - \frac{2}{1+\gamma} z \right) \int_{-\delta}^{\delta} \frac{dt}{(1+\gamma)k^2 + 2\gamma kt + (1+\gamma)t^2 - 2z} + O(k^2) + O(|z|)$$

as $k \to 0$ and $z \to -0$. Applying the identity

$$\int_a^b \frac{dt}{k^2 + t^2} = \frac{1}{|k|} \left(\arctan \frac{b}{|k|} - \arctan \frac{a}{|k|} \right),$$

we obtain

$$\int\limits_{-\delta}^{\delta}\frac{dt}{(1+\gamma)k^2+2\gamma kt+(1+\gamma)t^2-2z}=\frac{1}{1+\gamma}\int\limits_{-\delta}^{\delta}\frac{dt}{\left(t+\frac{\gamma}{1+\gamma}k\right)^2+\frac{1+2\gamma}{(1+\gamma)^2}k^2-\frac{2}{1+\gamma}z}=$$

$$\frac{1}{(1+\gamma)\sqrt{\frac{1+2\gamma}{(1+\gamma)^2}k^2-\frac{2}{1+\gamma}z}}\left(\arctan\frac{\delta+\frac{\gamma}{1+\gamma}k}{\sqrt{\frac{1+2\gamma}{(1+\gamma)^2}k^2-\frac{2}{1+\gamma}z}}+\arctan\frac{\delta-\frac{\gamma}{1+\gamma}k}{\sqrt{\frac{1+2\gamma}{(1+\gamma)^2}k^2-\frac{2}{1+\gamma}z}}\right).$$

From the properties of the arctan function listed below

$$\arctan y+\arctan\frac{1}{y}=\frac{\pi}{2},\quad y\geq 0$$

and $\arctan y=O(y)$, $y\to 0$, we conclude that

$$\int\limits_{-\delta}^{\delta}\frac{dt}{(1+\gamma)k^2+2\gamma kt+(1+\gamma)t^2-2z}=$$

$$\left(\frac{1+2\gamma-\gamma^2}{(1+\gamma)^2}k^2-\frac{2}{1+\gamma}z\right)\frac{\pi}{(1+\gamma)\sqrt{\frac{1+2\gamma}{(1+\gamma)^2}k^2-\frac{2}{1+\gamma}z}}+O\left(\sqrt{\frac{1+2\gamma}{(1+\gamma)^2}k^2-\frac{2}{1+\gamma}z}\right)$$

as $k\to 0$ and $z\to -0$. In view of the fact that

$$\left(\frac{1+2\gamma-\gamma^2}{(1+\gamma)^2}k^2-\frac{2}{1+\gamma}z\right)\frac{\pi}{(1+\gamma)\sqrt{\frac{1+2\gamma}{(1+\gamma)^2}k^2-\frac{2}{1+\gamma}z}}=$$

$$\pi\frac{1+2\gamma-\gamma^2}{(1+\gamma)^2\sqrt{1+2\gamma}}\sqrt{k^2-\frac{2(1+\gamma)}{2\gamma+1}z}+O(\sqrt{-z}),$$

we obtain

$$\Delta_{\mu}^{(\gamma,2)}(k\,;z):=\Delta_{\mu}^{(\gamma,2)}(0\,;0)+\frac{2\mu\pi(1+2\gamma-\gamma^2)}{(1+\gamma)^2\sqrt{1+2\gamma}}\sqrt{k^2-\frac{2(1+\gamma)}{2\gamma+1}z}+O(k^2)+O(\sqrt{-z})\tag{3.2}$$

as $k\to 0$ and $z\to -0$. The equalities (3.1) and (3.2) finalize the proof of the theorem. □

Since $\Delta_{\mu}^{(\gamma)}(0\,;0)=0$ if and only if $\mu=\mu_{\gamma}^0$, it follows from Theorem 3.1 that the following assertion holds.

Corollary 3.2. *Assume that $\gamma>0$ is fixed. If $\mu=\mu_{\gamma}^0$, then the following expansion*

$$\Delta_{\mu_{\gamma}^0}^{(\gamma)}(k\,;z)=\frac{2\pi\mu_{\gamma}^0(1+2\gamma-\gamma^2)}{(1+\gamma)^2\sqrt{1+2\gamma}}\sqrt{k^2-\frac{2(1+\gamma)}{1+2\gamma}z}+O(k^2)+O(\sqrt{|z|})$$

holds as $k\to 0$ and $z\to -0$.

As a consequence of Corollary 3.2, the following estimates for $\Delta_{\mu_{\gamma}^0}^{(\gamma)}(k\,;0)$ are obtained.

Corollary 3.3. *Let $\gamma>0$ be a fixed parameter. If $\mu=\mu_{\gamma}^0$, then there exist the numbers $C_1(\gamma),C_2(\gamma)>0$ and $\delta>0$ such that the inequalities*
(i) $C_1(\gamma)|k|\leq\Delta_{\mu_{\gamma}^0}^{(\gamma)}(k\,;0)\leq C_2(\gamma)|k|$ *for any* $k\in(-\delta;\delta)$;
(ii) $\Delta_{\mu_{\gamma}^0}^{(\gamma)}(k\,;0)\geq C_1(\gamma)$ *for any* $k\in\mathbb{T}\setminus(-\delta;\delta)$
are satisfied.

Conclusion. In the present paper, we investigate a class (family) of Friedrichs models that arise in quantum mechanical problem. It represents the energy operator (Hamiltonian) for a two-particle system defined on a one-dimensional lattice. We analyze the number, distribution, and existence criteria for the eigenvalues associated with this family. As the main result, we derive an asymptotic expansion of the associated Fredholm determinant in a neighborhood of the origin. This asymptotic expansion, along with Corollaries 3.2 and 3.3, plays a crucial role in proving the infiniteness (respectively, finiteness) of the number of eigenvalues lying below the essential spectrum of the corresponding three-particle lattice model Hamiltonian. It should be noted that the results on the infinite number of eigenvalues of the three-particle discrete Schrödinger operators and the corresponding model Hamiltonians are very important in quantum mechanics, modern mathematical physics, and the spectral theory of operators. The eigenvalues correspond to bound states in the quantum system. If the number of eigenvalues is infinite, then this means that there are infinitely many energy levels in the system. In [17] it was shown that the number of eigenvalues of the three-particle discrete Schrödinger operator is infinite in the case where the masses of two particles in a three-particle system are infinite.

References

[1] Friedrichs K.O. On the perturbation of continuous spectra. *Communications on Pure and Applied Mathematics*, 1948, **1**(4), P. 361–406.

[2] Friedrichs K.O. Perturbation of spectra in Hilbert space. *Amer. Math. Soc. Providence*, Rhole Island, 1965.

[3] Reed M., Simon B. *Methods of modern mathematical physics. IV: Analysis of Operators*. Academic Press, New York, 1979.

[4] Vakhrushev A.V. *Computational multiscale modeling of multiphase nanosystems: theory and applications*. Apple Academic Press, New York, 2017.

[5] Albeverio S., Lakaev S.N., Muminov Z.I. The threshold effects for a family of Friedrichs models under rank one perturbations. *Journal of Mathematical Analysis and Applications*, 2007, **330**(2), P. 1152–1168.

[6] Lakaev S., Darus M., Kurbanov Sh. Puiseux series expansion for an eigenvalue of the generalized Friedrichs model with perturbation of rank 1. *Journal of Physics A Mathematical General*, 2013, **46**(20), P. 205304.

[7] Kurbanov Sh.K., Dustov S.T. Puiseux series expansion for eigenvalue of the generalized Friedrichs model with the perturbation of rank one. *Lobachevskii J. Math.*, 2023, **44**, P. 1365–1372.

[8] Muminov M.I., Hurramov A.M., Bozorov I.N. On eigenvalues and virtual levels of a two-particle Hamiltonian on a d-dimensional lattice. *Nanosystems: Physics, Chemistry, Mathematics*, 2023, **14**(3), P. 295–303.

[9] Muminov M.I., Lokman C. Finiteness of discrete spectrum of the two-particle Schrödinger operator on diamond lattices. *Nanosystems: Physics, Chemistry, Mathematics*, 2017, **8**(3), P. 310–316.

[10] Muminov M.I., Khurramov A.M. Spectral properties of a two-particle hamiltonian on a d-dimensional lattice. *Nanosystems: Physics, Chemistry, Mathematics*, 2016, **7**(5), P. 880–887.

[11] Muminov M.I., Rasulov T.H. Universality of the discrete spectrum asymptotics of the three-particle Schrödinger operator on a lattice. *Nanosystems: Physics, Chemistry, Mathematics*, 2015, **6**(2), P. 280–293.

[12] Albeverio S., Lakaev S.N., Muminov Z.I. On the number of eigenvalues of a model operator associated to a system of three-particles on lattices. *Russ. J. Math. Phys.*, 2007, **14**(4), P. 377–387.

[13] Rasulov T.Kh., Rasulova Z.D. On the spectrum of a three-particle model operator on a lattice with non-local potentials. *Siberian Electronic Mathematical Reports*, 2015, **12**, P. 168–184.

[14] Rasulov T.Kh. Essential spectrum of a model operator associated with a three particle system on a lattice. *Theoretical and Mathematical Physics*, 2011, **166**(1), P. 81–93.

[15] Rasulov T.H., Bahronov B.I. Existence of the eigenvalues of a tensor sum of the Friedrichs models with rank 2 perturbation. *Nanosystems: Physics, Chemistry, Mathematics*, 2023, **14**(2), P. 151–157.

[16] Bahronov B.I., Rasulov T.H., Rehman M. Conditions for the existence of eigenvalues of a three-particle lattice model Hamiltonian. *Russian Mathematics*, 2023, **67**(7), P. 1–8.

[17] Muminov M.E.,Aliev N.M. Spectrum of the three-particle Schrödinger operator on a one-dimensional lattice. *Theoret. and Math. Phys.*, 2012, **171**(3), P. 754–768.

Submitted 27 July 2025; revised 16 August 2025; accepted 18 August 2025

Information about the authors:

Tulkin Rasulov – Faculty of Physics, Mathematics and Information Technologies Bukhara State University M. Ikbol str. 11, 200100 Bukhara, Uzbekistan; ORCID 0000-0002-2868-4390; rth@mail.ru, t.h.rasulov@buxdu.uz

Gulhayo Umirkulova – Faculty of Physics, Mathematics and Information Technologies Bukhara State University M. Ikbol str. 11, 200100 Bukhara, Uzbekistan; ORCID 0000-0002-6254-413X; g.h.umirqulova@buxdu.uz

Conflict of interest: the authors declare no conflict of interest.

NANOSYSTEMS:
PHYSICS, CHEMISTRY, MATHEMATICS

Shitov A.E., et al. *Nanosystems: Phys. Chem. Math.*, 2025, **16** (5), 593–596.
http://nanojournal.ifmo.ru
DOI 10.17586/2220-8054-2025-16-5-593-596

Original article

Inclusions of metastable superconducting phase of gallium in $SmGa_2$

Alexander E. Shitov[1,a], Mikhail P. Volkov[1,b]

[1]Ioffe Institute, 26 Politekhnicheskaya st., Saint Petersburg, 194021, Russia

[a]a.shitov@mail.ioffe.ru, [b]m.volkov@mail.ioffe.ru

Corresponding author: A. E. Shitov, a.shitov@mail.ioffe.ru

PACS 74.25.Dw

ABSTRACT The magnetization M of the $SmGa_2$ compound has a paramagnetic character in a wide temperature range, and when the temperature decreases below 30 K, a significant increase in magnetization is observed, which indicates the formation of a magnetically ordered state. At temperatures below 5 K, a sharp feature is observed on the M(H) dependences, which is the contribution from the magnetization of superconducting submicron gallium inclusions. Analysis of the M(H) dependences measured at different temperatures below 5 K allowed us to assume the presence of two superconducting gallium phases. The critical temperature T_C = 5.9 K and the critical field H_C (0) = 560 Oe correspond to the formation of a metastable β-phase of gallium, and the critical temperature T_C = 8.4 K and the critical field H_C (0) = 1100 Oe can be associated with the formation of a thin layer of amorphous gallium on the surface of the β-phase inclusions.

KEYWORDS magnetization, superconductivity, microparticles, metastable phase, gallium.

FOR CITATION Shitov A.E., Volkov M.P. Inclusions of metastable superconducting phase of gallium in $SmGa_2$. *Nanosystems: Phys. Chem. Math.*, 2025, **16** (5), 593–596.

1. Introduction

Gallium is a component of many binary and multicomponent compounds, in particular such technically important compounds as the semiconductor GaAs and rare earth compounds with strong magnetic properties. In the study of gallium-containing compounds, it was discovered that in a number of cases, small particles of pure gallium precipitate, usually with a metastable β-Ga structure, having a critical superconductivity temperature T_C from 5.9 K to 6.2 K. In our work, we investigated the magnetic properties of the binary compound $SmGa_2$ and observed low-temperature features of magnetization associated with the presence of superconducting gallium inclusions in the compound.

2. Method

The $SmGa_2$ compound was obtained by the solution-melt method [1]. The sample was a intergrowth of small single crystals with dimensions of $3\times2\times0.5$ mm^3 and a mass of 20 mg. X-ray structural analysis confirmed the formation of the AlB_2 crystallographic structure and the absence of other phases ($<$2% by volume). The dependences of the magnetization M on the magnetic field H and temperature T were obtained using a vibration magnetometer of the PPMS setup (Physical Property Measurement System, Quantum Design), which is a system for measuring the physical properties of materials at low temperatures and in strong magnetic fields.

3. Results and discussion

The dependence of the magnetic moment M on the temperature T, shown in Fig. 1a, was obtained in the cooling mode in a magnetic field H = 300 Oe. The magnetization of $SmGa_2$ smoothly increases with decreasing temperature to T$\approx$30 K, but the Curie-Weiss law is not satisfied. When the temperature T decreases below $\sim$30 K, a significant increase in magnetization is observed, which indicates the formation of a magnetically ordered state. A flattening of the dependence of the susceptibility on temperature below 5 K was observed, which corresponds to ferromagnetic ordering. The non-fulfillment of the Curie-Weiss law in the high-temperature (paramagnetic) region was observed in ref. [2] for $SmGa_2$ and is characteristic of samarium-containing compounds [3]. The increase in magnetization in the low-temperature region, associated with the formation of a magnetically ordered state, were also observed in [2].

Figure 1b shows the magnetic field dependences of the magnetic moment of $SmGa_2$ at temperatures T = 2–12 K. The dependence M(H) at T = 12 K is practically linear at H $>$5 kOe, and nonlinearity in low magnetic fields reflects the onset of ferromagnetic ordering. At lower temperatures, the nonlinear region expands up to maximal magnetic field. The magnetization values increased with decreasing temperature and only at the lowest temperature (T = 2 K) a slight decrease in M(H) was observed in high field, as in [2]. In general, the features of the temperature and field dependences of the magnetic moment are in good agreement with the results of ref. [2] at T $>$ 5 K.

At T $\leq$ 5 K, an unusual feature is observed in the dependence M(H) in the region of low fields. This feature is shown on an enlarged scale for T = 5 K on Fig. 1b (upper inset). The lower inset shows that at a higher temperature T = 6 K this feature is not observed, and the dependence M(H) demonstrates a small ferromagnetic loop.

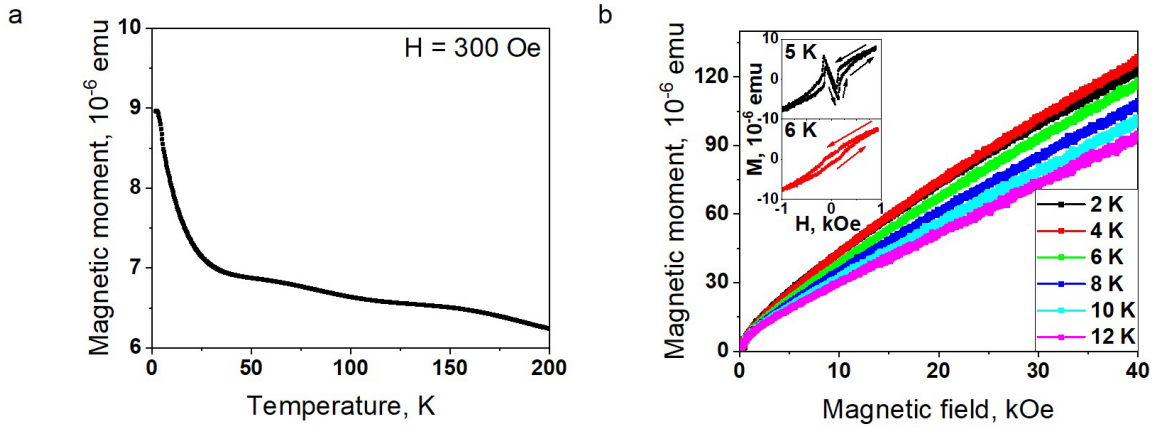

FIG. 1. Dependences of the magnetic moment M on (a) temperature T in magnetic field H = 300 Oe and (b) on the magnetic field at temperatures T = 2–12 K in the $SmGa_2$ compound. The insets to Fig. 1b show the region up to H $\approx$ 1 kOe at T = 5 and 6 K, the arrows indicate the direction of the magnetic field changes

Figure 2a shows the ΔM(H) dependences at temperatures T $<$ 6 K up to the region of magnetic fields H $\approx$ 1 kOe, where the ΔM(H) values were obtained by subtracting a small ferromagnetic hysteresis loop M(H,6K) from the measured M(H,T) dependences at these temperatures. The obtained dependences of the magnetic moment ΔM(H) are weakly hysteresis loops typical for type I superconductor and connected with submicron inclusions of pure gallium in the $SmGa_2$ compound, and the critical parameters of the superconducting phase of gallium can be determined.

Gallium exhibits a high degree of polymorphism with one stable orthorhombic phase (α-Ga) [4, 5] and several metastable phases (β, γ, δ, ε) [6, 7] at atmospheric pressure and additional phases (Ga-II, Ga-III and Ga-V) under pressure [8, 9]. Many of these phases are superconducting (α, β, γ, δ, ε and Ga-II). The metastable β-Ga phase has a monoclinic structure, and shows transition to the superconducting state at temperatures ranging from 5.9 K to 6.2 K [10–12].

An analysis of the ΔM(H) dependences (Fig. 2b) allows us to determine the phase of the superconducting gallium inclusions in the $SmGa_2$ sample. In general, the ΔM(H) dependence is similar to the weakly hysteretic dependence of the magnetization of a type I superconductor (which should be expected for submicron gallium inclusions), but the sharp break in the descending branch of the dependence allows us to assume that there is a superposition of individual dependences from two superconducting phases of gallium.

In the ΔM(H) dependences, one can distinguish two characteristic magnetic fields H_{C1} and H_{C2} (indicated by arrows in the inset to Fig. 2a). The field H_{C1} was determined by extrapolation of linear decreasing path of M(H) dependence, the field H_{C2} was determined as the field of the beginning of magnetic hysteresis. The values of these fields can by determined with the accuracy $\pm$ 5 Oe. Taking into account that the dependence of the critical magnetic field of the superconductor H_C can be represented as $H_C(T) = H_C(0)\left(1 - \left(\frac{T}{T_C}\right)^2\right)$, Fig. 2b shows the dependences of the critical magnetic fields H_{C^1} and H_{C^2} on the square of the temperature $H_C(T^2)$. Extrapolation of these dependences to H = 0 leads to two critical temperatures T_{C^1} = 5.9 $\pm$ 0.1 K and T_{C^2} = 8.4 $\pm$ 0.1 K.

The first critical temperature T_{C^1} = 5.9 K can naturally be associated with the formation of the metastable phase β-Ga, in which gallium microinclusions in gallium-containing compounds usually crystallize and which has a T_C in the range from 5.9 K to 6.2 K [9–11]. Additional evidence in favor of the formation of this phase is the coincidence of the measured dependence $H_{C^1}(T^2)$ (black dots and dotted line in Fig. 2b) with the dependence $H_{C^1}(T^2)$ obtained in [11] for β-Ga (blue solid line in Fig. 2b).

The second critical temperature T_{C^2} = 8.4 K can be associated with the formation of the amorphous phase of gallium, which, according to [13], has T_C = 8.5 K. This amorphous phase of gallium can be formed as a thin layer on the surface of β-Ga inclusions, the formation of individual inclusions of the amorphous phase is unlike, since, as shown in [13], the amorphous phase formed during irradiation of thin gallium films at T = 4 K crystallizes into the β-phase already upon heating to 16 K. Another possibility is the additional formation of gallium particles in the metastable γ phase, which, as shown in [10], has a critical temperature of T_C = 7.6 K and a critical field of H_C(6.3K) = 600 Oe , which is close to the extrapolated values of H_{C^2} at this temperature.

The formation of small superconducting inclusions of gallium (in most cases, the metastable β-Ga phase [6, 7, 10–12, 14]) was observed for a number of gallium-containing compounds obtained by different methods:

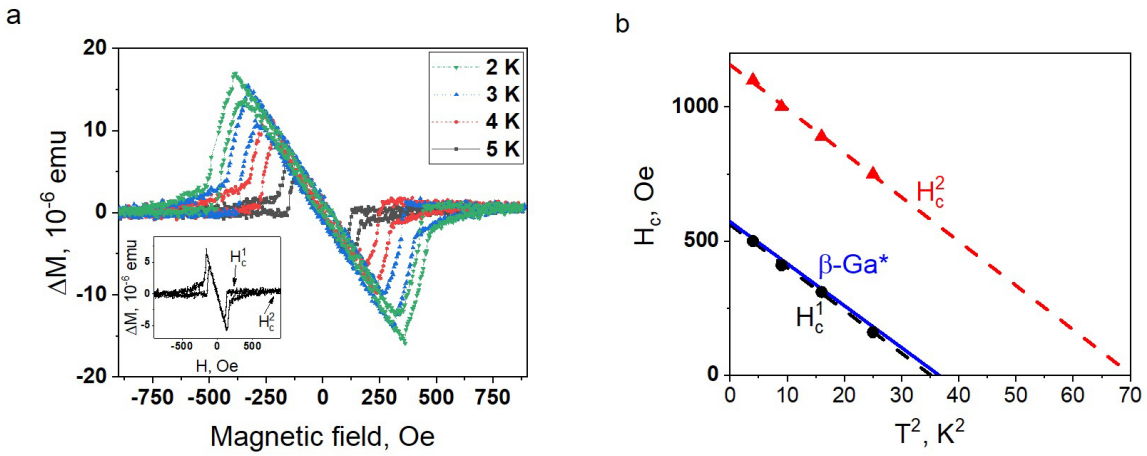

FIG. 2. (a) Dependence ΔM(H) = M(H,T) – M(H,6K) at H$\leq$1 kOe and temperatures T = 2–5 K. The inset shows the dependence ΔM(H) at T = 5 K, the arrows indicate the critical magnetic fields H_{C^1} and H_{C^2}. (b) Dependences $H_{C^1}(T^2)$ and $H_{C^2}(T^2)$ – dots – experiment, dotted line – extrapolation, and blue solid line – literature data for β-Ga* [12]

- In rare earth compounds with gallium, for example, in $YbGa_5$, superconducting properties below T_C $\approx$2 K were observed during magnetic measurements, associated, as the authors believe, with Ga filaments formed at grain boundaries [15].
- In GaN compounds doped with transition metals (Fe, Cr, Mn), superconducting properties with T_C $\approx$6 K and H_C $\approx$600 Oe were observed, associated with gallium clusters [16].
- In gallium oxide Ga_2O_3 films with a large oxygen deficiency, Ga clusters are formed with a superconducting transition temperature depending on the size of the Ga inclusions [17, 18].
- In gallium-doped Si films, gallium nanoinclusions exhibited superconducting properties at temperatures T$\leq$7 K [19].

In some cases, the observation of superconductivity in gallium-containing compounds may also be associated with the formation of inclusions of superconducting phases of pure gallium, since the critical parameters of these compounds (T_C and H_C) are close to the values characteristics of gallium phases. Thus, one can note reports on the superconductivity of the GeGa compound with T_C $\leq$6 K and $H_C(0)$ $\approx$7 kOe [20], the AGa_xSi_{2-x} (A = Sr, Ba, Ca) compound with T_C = 4.4–5.2 K [21], and the semiconductor compounds GaSb and GaAs with T_C $\approx$10 K [22]. Earlier, there were cases when superconductivity was reported in compounds, which, as further analysis showed, was associated with metal microinclusions, for example, in InN compounds with inclusions of superconducting indium [23].

4. Conclusion

Thus, the measurement of the magnetization of the $SmGa_2$ compound showed that in a wide temperature range the dependence M(T) has a paramagnetic character, not obeying the Curie-Weiss law. When the temperature decreases below 30 K, a significant increase in magnetization is observed, which indicates the formation of a magnetically ordered state. At T = 12 K, the dependence M(H) in magnetic fields H $\geq$ 10 kOe is almost linear. At lower temperatures, the dependence M(H) becomes increasingly nonlinear, and upon transition to the lowest temperature T = 2 K, a slight decrease in magnetization in high fields is observed.

At T $\leq$ 5 K, the M(H) dependence exhibits a feature in the low-field region, which is a contribution from the magnetization of superconducting submicron gallium inclusions. The critical temperature T_C = 5.9 K and the critical field $H_C(0)$ = 560 Oe correspond to the formation of a metastable β-phase of gallium. The second critical temperature T_C = 8.4 K and the critical field $H_C(0)$ = 1100 Oe can be associated with the formation of a thin layer of amorphous gallium on the surface of the β-phase inclusions or formation of the metastable γ-Ga particles. The formation of gallium inclusions in gallium-containing compounds is a frequently observed effect and can be detected in low-temperature magnetic measurements.

References

[1] Kanatzidis M.G., Pöttgen R., Jeitschko W. The metal flux: A preparative tool for the exploration of intermetallic compounds. *Angew. Chem. Int. Ed.*, 2005, **44**, P. 6996–7023.
[2] Blanco J.A., Gignoux D., J.C. Gomez Sal et al. Magnetic properties of $SmGa_2$. *Physica B: condensed matter*, 1991, **175**(4), P. 349–353.
[3] Ballou R., Barthem V.M.T.S. and Gignoux D. Crystal field effects in the hexagonal $SmNi_5$ compound. *Physica B*, 1988, **149**, P. 340.
[4] W.J. De Haas, Voogd J. On the superconductivity of the gallium. *Commun. Phys. Lab. Univ. Leiden*, 1929, **199d**, P. 733–734.
[5] Roberts B.W. Survey of superconductive materials and critical evaluation of selected properties. *J. Phys. Chem. Ref. Data*, 1976, **5**, P. 581–821.

[6] Sharma B.D. and Donohue J. A refinement of the crystal structure of gallium. *Zeitschrift für Kristallographie*, 1962, **117**, P. 293.
[7] Bosio L., Curien H., Dupont M. et al. Structure cristalline de Gaδ. *Acta Crystallographica Section B*, 1973, **29**, P. 367.
[8] Bosio L. Crystal structures of Ga(II) and Ga(III). *The Journal of Chemical Physics*, 1978, **68**, P. 1221.
[9] Degtyareva O., McMahon M.I., Allan D.R. et al. Structural Complexity in Gallium under High Pressure: Relation to Alkali Elements. *Phys. Rev. Lett.*, 2004, **93**, P. 205502.
[10] Feder J., Kiser S., Rothwarf F. et al. Hysteresis effects in three superconducting phases of gallium. *Solid State Comm.*, 1966, **4**, P. 611.
[11] Parr H. and Feder J. Superconductivity in β-Phase Gallium. *Phys. Rev. B*, 1973, **7**, P. 166.
[12] D. Campanini, Z. Diao, and A. Rydh. Raising the superconducting T_C of gallium: In situ characterization of the transformation of α-Ga into β-Ga. *Phys. Rev. B*, 2018, **97**, P. 184517.
[13] Frohlingsdorf J., Stritzker B. Amorphous gallium produced by pulsed excimer laser irradiation. In: Draper C.W., Mazzoldi P. (eds) Laser surface treatment of metals. NATO ASI series vol 115 Springer Dordrecht, 1986.
[14] Moura K.O., Pirota K.R., Béron F. et al. Superconducting Properties in Arrays of Nanostructured β-Gallium. *Scientific Reports*, 2017, **7**, P. 15306.
[15] Giedigkeit R., Niewa R., Schnelle W. et al. On the Binary Compound $YbGa_5$. *ZAAC*, 2002, **628**, P. 1692–1696.
[16] Gosk J.B., Boćkowski M., Tokarczyk M. et al. Superconductivity Study of GaN Highly Doped by Transition Metals. *Acta Physica Polonica A*, 2013, **124**(5), P. 877–880.
[17] Petitmangin A., Gallas B., Hebert C. et al. Characterization of oxygen deficient gallium oxide films grown by PLD. *Applied Surface Science*, 2013, **278**, P. 153–157.
[18] Petitmangin A., Hébert C., Perriére J. et al. Metallic clusters in nonstoichiometric gallium oxide films. *J. Appl. Phys.*, 2011, **109**, P. 013711.
[19] Heera V., Fiedler J., Hübner R. et al. Silicon films with gallium-rich nanoinclusions: from superconductor to insulator. *New J. Phys.*, 2013, **15**, P. 083022.
[20] Sun Y.B., Di Z.F., Hu T., et al. The Insulator to Superconductor Transition in Ga-Doped Semiconductor Ge Single Crystal Induced by the Annealing Temperature. *Adv. in Cond. Matt. Phys.*, 2015, **4**, P. 963768.
[21] Meng R.L., Lorenz B., Wang Y.S. et al. Study of binary and pseudo-binary intermetallic compounds with AlB_2 structure. *Physica C*, 2002, **382**, P. 113–116.
[22] Demishev S.V., Kosichkin Yu.V., Sluchanko N.E. et al. Crystallization of metastable phases and superconductivity in amorphous gallium antimonide. *JETP*, 1993, **77**(1), P. 68.
[23] Komissarova T.A., Parfeniev R.V., Ivanov S.V. Comment on "Superconductivity in heavily compensated Mg-doped InN" [*Appl. Phys. Lett.*, 2009, **94**, P. 142108]. *Appl. Phys. Lett.*, 2009, **95**, P. 086101.

Submitted 11 July 2025; revised 15 September 2025; accepted 21 September 2025

Information about the authors:

Alexander E. Shitov – Ioffe Institute, 26 Politekhnicheskaya st., Saint Petersburg, 194021, Russia; ORCID 0000-0002-2184-7054; a.shitov@mail.ioffe.ru

Mikhail P. Volkov – Ioffe Institute, 26 Politekhnicheskaya st., Saint Petersburg, 194021, Russia; ORCID 0000-0003-4007-5640; m.volkov@mail.ioffe.ru

Conflict of interest: the authors declare no conflict of interest.

NANOSYSTEMS:
PHYSICS, CHEMISTRY, MATHEMATICS

Deepika Aggarwal, et al. *Nanosystems: Phys. Chem. Math.*, 2025, **16** (5), 597–605.
http://nanojournal.ifmo.ru
DOI 10.17586/2220-8054-2025-16-5-597-605

Original article

Unpredictable and uniform random number generation based on time of arrival using InGaAs detectors

Deepika Aggarwal[1,a], Anindita Banerjee[1,b], Ankush Sharma[1,c], Ganesh Yadav[1,d]

[1]QuNu Labs Pvt. Ltd., M.G. Road, Bangalore, Karnataka, India

[a]deepika@qnulabs.com, [b]anindita@qnulabs.com, [c]ankush@qnulabs.com, [d]ganesh@qnulabs.com

Corresponding author: Deepika Aggarwal, deepika@qnulabs.com

ABSTRACT Quantum random number generators are becoming mandatory in a demanding technological world of high-performing learning algorithms and security guidelines. Our implementation, based on the principles of quantum mechanics, enables us to achieve the required randomness. We have generated high-quality quantum random numbers from a weak coherent source at the telecommunication wavelength. The entropy is based on the time of arrival of quantum states within a predefined time interval. The detection of photons by the InGaAs single-photon detectors and high-precision time measurement of 5 ps enables us to generate 16 random bits per arrival time, which is the highest reported to date. We have presented the theoretical analysis and experimental verification of the random number generation methodology. The method eliminates the requirement of any randomness extractor, thereby leveraging the principles of quantum physics to generate random numbers. The output data rate averages 2.4 Mbps. The generated raw quantum random numbers are compared with the NIST-prescribed Blum-Blum-Shub pseudo-random number generator and an in-house-built hardware random number generator from FPGA, on the ENT and NIST platform.

KEYWORDS random number generation, InGaAs detector.

FOR CITATION Deepika Aggarwal, Anindita Banerjee, Ankush Sharma, Ganesh Yadav Unpredictable and uniform random number generation based on time of arrival using InGaAs detectors. *Nanosystems: Phys. Chem. Math.*, 2025, **16** (5), 597–605.

1. Introduction

In the present era, random numbers play a significant role in statistical analysis, stochastic simulations, cyber security applications, gaming, cryptography and many others. Random numbers can be generated via two approaches: pseudo-random number generators (PRNGs) [1], which rely on deterministic algorithms, and true random number generators (TRNGs), which derive randomness from physical processes. While PRNGs risk predictability due to seed reuse or algorithmic backdoors, TRNGs leverage physical entropy sources. Quantum random number generators (QRNGs), a subset of TRNGs, exploit the inherent unpredictability of quantum mechanics to produce unbiased and irreproducible outputs.

A random bit sequence is characterized by two fundamental properties, i.e., uniformity and unpredictability, of which the latter is the most important. Uniformity is achievable by mathematical algorithms, however, for unpredictability, none other than the inherent randomness of quantum mechanics can be trusted. Quantum random numbers can be generated from several sources, for example, radioactive decay [2, 3], branching path [4], photon arrival times [5–9], quantum vacuum fluctuations [10–14], laser phase fluctuations [15, 16], optical parametric oscillators [17], amplified spontaneous emission [18] etc. Several optical QRNG schemes [19] have been proposed on the principle of time of arrival (ToA) of photon. The arrival time of photon is considered as a quantum random variable and it can generate n random bits, where, n depends on the precision of time measurement. Software [6, 7, 20] and hardware [21] approaches were investigated to eliminate the bias and improve the quality of throughput from the time of arrival entropy. The authors in [8] showed that when an external time reference is used, the raw random numbers are generated from the photon arrival in time bins within the external time reference and are uniformly distributed in time. Hence, we can consider this quantum entropy source to be one of the ideal candidates for TRNG.

In this paper, we have reported our work on QRNG based on ToA principle using an external time reference. We have implemented the scheme using InGaAs detectors. We have used a different method for generating random numbers and could extract 16 random bits per detection event. This is the highest reported entropy per detection event among time-of-arrival based QRNGs. In our work, we have adhered to the quantum noise random number generator architecture recommended by ITU-T X.1702 [22] and this is presented in Fig. 1. The raw data is extracted by performing a measurement on a quantum state and we are deriving the random numbers from the data acquisition process. Minimum entropy is accessed by estimating the implementation imperfections. The quantum state is prepared using an optical process and the quantum measurement is based on the Poisson nature of photon detection by single-photon detector (SPD). Raw data

is generated by digitizing the output from the SPD. Continuous monitoring of laser parameters, detector parameters and amplitude of the quantum signal at the detector enables assessment of entropy for evaluation of quantum randomness in the random number sequence. The implementation imperfections lead to an increase in the classical noise, therefore, these are identified, continuously monitored and eliminated.

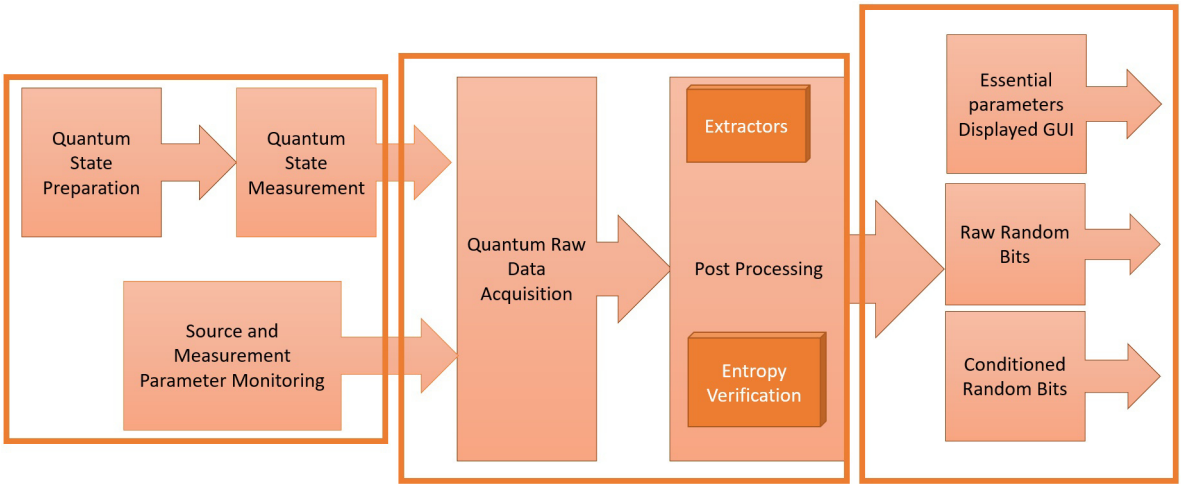

FIG. 1. Schematic of the quantum random number generator architecture. The process involves quantum state preparation using a coherent source, photon detection via InGaAs single-photon detectors, and continuous parameter monitoring to ensure entropy quality. Time-of-arrival measurements generate raw data, which undergoes direct processing and entropy verification to guarantee uniformity and unpredictability. Post-processed bitstreams and essential parameters are displayed through a graphical user interface (GUI) [22]

Section 2 of this paper explains the source of quantum randomness. In section 3, we have discussed the principle of time of arrival along with its theoretical analysis and sources of bias in the implementation. Section 4 presents the experimental setup and section 5 discusses the entropy estimation. Finally, we have concluded the work in section 6.

2. Source of randomness

The quantum randomness in the presented QRNG arises from the collapse of the coherent state during photon detection. Since our QRNG method is based on the ToA principle, it is important to briefly discuss the coherent state and present a mathematical description of the photon. The coherent state α is the quantum mechanical counterpart of monochromatic light. It can be represented by amplitude and phase, $\alpha = |\alpha| e^{i\theta}$, where the complex number specifies the amplitude in photon number units. The coherent state can be represented in Dirac notation as $|\alpha\rangle$. The wave function of a highly attenuated laser state (coherent state) can be represented as a product of all the coherent states within the coherence time,

$$|\phi\rangle = \bigotimes_{t=1}^{n_c} |\alpha_t\rangle \tag{1}$$

where, n_c is the number of time bins within the coherence time of the laser. The Fock-state representation of a coherent state distributed over n_c time bins can be written as

$$|\phi\rangle = \sum_{k=0}^{\infty} \sqrt{P_k} \left(\frac{1}{\sqrt{n_c}} \sum_{t=1}^{n_c} a_t^\dagger \right)^k |0\rangle, \tag{2}$$

where $P_k = e^{-n_c\mu}(n_c\mu)^k/k!$ is the Poisson probability of having k photons with mean photon number $n_c\mu$, and $a_t^\dagger$ is the photon creation operator in the t-th time bin. This equation shows that each photon is in a superposition of all time bins, and the collapse of the wavefunction upon detection gives rise to intrinsic quantum randomness.

2.1. Photon statistics within a time segment

It is known that the photon number distribution of perfectly coherent light within a fixed time segment follows a Poisson distribution [23]. Consider a beam segment corresponding to a predefined time segment with an average photon count represented by $\mu = \phi T$, where ϕ is the average optical flux. We divide the time segment into small time bins. It is then demonstrated that the probability of finding n photons within a time segment (T) containing N time bins follows a Poisson distribution. Let the probability of detecting n photons within the time segment T be represented by $P(n)$. Consider the probability of finding n time bins containing 1 photon and $N-n$ time bins containing no photons, which is denoted as p_1 and calculated as $p_1 = \mu/N$. This probability is given by a binomial distribution,

$$\begin{aligned} P(n) &= \frac{N!}{n!(N-n)!} p_1^n (1-p_1)^{N-n} \\ &= \frac{N!}{n!(N-n)!N^n} \mu^n \left(1-\frac{\mu}{N}\right)^{N-n}. \end{aligned} \tag{3}$$

In the limit $N \to \infty$, the probability is $\lim_{N\to\infty}[P(n)] = \frac{1}{n!}\mu^n e^{-\mu}$. Thus, the probability of finding n photons in the time segment T follows a Poisson distribution, denoted as $P(n)$. It is important to mention that we have considered ideal detectors with $100\,\%$ efficiency.

2.2. Quantum theory of photon detection

When conducting an experiment to leverage the Poisson nature of photon statistics of coherent light, we have to consider the optical losses and imperfections in the devices. These are inefficient optics, absorption and imperfect detectors. These lead to a random sampling of photons, which degrades the photon statistics. The quantum theory of photon detection [23] establishes a connection between the photon count statistics recorded by the detector within a time segment T and the photon statistics incident upon the detector. The variance in the photo count number is denoted by $(\triangle C)^2$ and the variance in the photon number is denoted by $(\triangle n)^2$. The relationship between these two parameters is established by

$$(\triangle C)^2 = \eta^2 (\triangle n)^2 + \eta(1-\eta)\mu. \tag{4}$$

If the detector was perfect (i.e. $\eta = 1$), then the photon count statistics would have been equal to the photon statistics. Consider a coherent source with $(\triangle n)^2 = \mu$ and an imperfect detector, such as a PMT or SPAD. In this case, equation 4 becomes $(\triangle C)^2 = \mu\eta = C$. Thus, the photo count statistics (C) and the photon statistics (μ) both follow the Poisson distribution for all values of detection efficiencies.

3. Time of arrival generators

ToA-based QRNG systems encode the arrival time of photons. During the short time periods, the arrival of a photon at the detector follows an exponentially distributed time, $\lambda e^{-\mu T}$. The time between the two arrivals is the difference between two exponential random variables, which is also exponential. The randomness in the exponential distribution can be converted to a uniform bit sequence using post-processing algorithms. Another approach to flatten the exponential distribution is by taking short time bins from an external reference and considering the time of arrivals within those bins. Nie *et al.* [8] have explained that when randomness is extracted from the arrival time, the generated random numbers are biased. They have proposed a new method to generate uniform random numbers from photon clicks within a fixed time duration $(t, t+T)$. The fixed time period is divided into small time bins with precision t_{min}. The time period is always less than the dead time of the detector, allowing single detection. This method offers advantages of low bias and high throughput compared to other methods of quantum random number generation.

3.1. Theoretical analysis

The photon flux, which is an average number of photons passing through a cross-section of a coherent beam, follows a Poisson process. Precisely, a coherent beam with well-defined average photon number will exhibit photon number fluctuation in a short time interval. This fluctuation occurs because we cannot predict the positions of these photons. Consider a 1550 nm laser emitting 0 dBm of power, this will have an average flux of 7.78×10^{15} photons s^{-1}. If we apply 60 dB attenuation to this, the average flux will then be 7.7×10^9 photons s^{-1}. We can interpret this as an average of 7.7 photons in the 1 ns time segment. Also, consider a time segment of 100 ps, corresponding to an average flux of 0.77. To summarize, if the coherent beam is attenuated to an extent that the beam segment contains few photons, say, on an average of 0.77 photons and we make measurements of some n samples, then, one can observe the random fluctuations in the photon number. This comes from the fact that the stimulated emission in the semiconductor laser is inherently random. Considering a time segment T, with mean photon number of μT, then the probability distribution of k photons arriving in time interval T is given by $P(k) = \frac{e^{-\lambda \mathrm{T}}(\mu T)^k}{k!}$. The photon number follows a Poisson distribution. Hence, the time interval between the arrival of consecutive photons also follows the Poisson process [6]. For $\lambda T = 0.1$, there is 90.5%

probability of detecting no photons, 9% of detecting single photons and finite probability of 0.5% of detecting multi-photons in time segment T. The time period is divided into N_b time bins and each time bin is $\tau_i = \left(\frac{i-1}{N_b}T, \frac{i}{N_b}T\right)$. In the case of an ideal detector ($\eta = 1$), there would have been multiple clicks in T, and the first detection would be the minimum value of the random variable representing photon arrival times. However, since the dead time of the detector is more than T, there is a single detection in T. For a detection event, the conditional probability of getting a detection at i^{th} position, given k photons appear in period T, is given by $P(i\,|k)$. It represents the probability of a detection occurring at τ_i when k photons are present in a period,

$$\begin{aligned} P(i \mid k) &= \frac{P(i,k)\cdot P(T-\tau_i, k=0)}{P(k)} \\ &= \frac{\frac{e^{-\lambda\tau_i}\left(\lambda\left(\frac{T-(i-1)T}{N_b}-\frac{T-iT}{N_b}\right)\right)^k}{k!}\cdot e^{-\lambda(T-\tau_i)}}{\frac{e^{-\lambda T}(\lambda T)^k}{k!}} \\ &= \left(\frac{1-(i-1)}{N_b}-\frac{1-i}{N_b}\right)^k \\ &= \left(\frac{1-(i-1)}{N_b}\right)^k - \left(\frac{1-i}{N_b}\right)^k. \end{aligned} \tag{5}$$

The probability distribution function of the arrival of a photon conditioned on the fact that only 1 photon is available in the time period T is (substituting k=1 in equation 5)

$$P(i|k=1) = \frac{1}{N_b} = \frac{1}{T/\tau} = \frac{\tau}{T}, \tag{6}$$

which clearly shows that the photon arrival time is uniformly distributed across all N_b bins of the interval T and the probability of a photon arriving at each time bin is $\frac{1}{N_b}$ [8, 9]. In this expression, τ is the independent variable of the probability distribution function. The probability density is given by $\frac{1}{T}$. Thus, the arrival time is uniformly distributed in $[0, T]$.

We have used binary code to encode the time bins. In Fig. 2, we have presented different methods for implementing time of arrival based QRNG. Wayne *et al.* [6] extracted random numbers by translating the time interval between detections into time bins. Nie *et al.* [8] generated raw quantum random numbers by considering time difference between the photon click and an external time reference. The distribution of time difference between the photon click and the external reference clock is approximately uniform. Yan *et al.* [9] have generated the highest-reported raw data bits of 128 Mbps by measuring the time of arrival from a common starting point. They have converted each arrival time into sum of fixed period and phase time. Thereafter, they have generated random numbers from the phase time. In this work, we address the arrival time of photon differently; we have considered an external time reference for the generation of raw bits. We have divided the external time reference T into N_T divisions. The arrival time is given by

$$A_n = \text{mod}[N_b, N_{T_i}], \tag{7}$$

where N_b is the total number of random digits that we want to generate. We do not restrict ourselves to modular arithmetic; rather, the purpose is to divide the time segment T into N_T fragments, with each fragment equal to the precision of the measurement device. These fragments are divided into N_b divisions to generate N_b random digits. The arrival of a photon will randomly fall within the range $1 \leq N_{T_i} \leq N_T$. Thus, applying equation 7, we can prove that N_{T_i} is uniformly distributed in $[0, T)$ [6, 8]. Table 1 compares the proposed work with existing works.

TABLE 1. Comparison of the proposed QRNG with existing works on the basis of the nature of source, detector, external reference clock, entropy per detection, precision of time measurement and throughput. CS stands for coherent source

Reference	Source	Detector	External reference clock	Entropy	Resolution	Rate (Mbps)
[6]	LED	SiAPD	—	5.5	5 ns	40
[8]	CS	SiAPD	40.96 ns	8	0.160 ns	109
[9]	CS	SiAPD	20 ns	8	20 ns	128
This work	CS	InGaAs	500 ns	16	0.005 ns	2.4

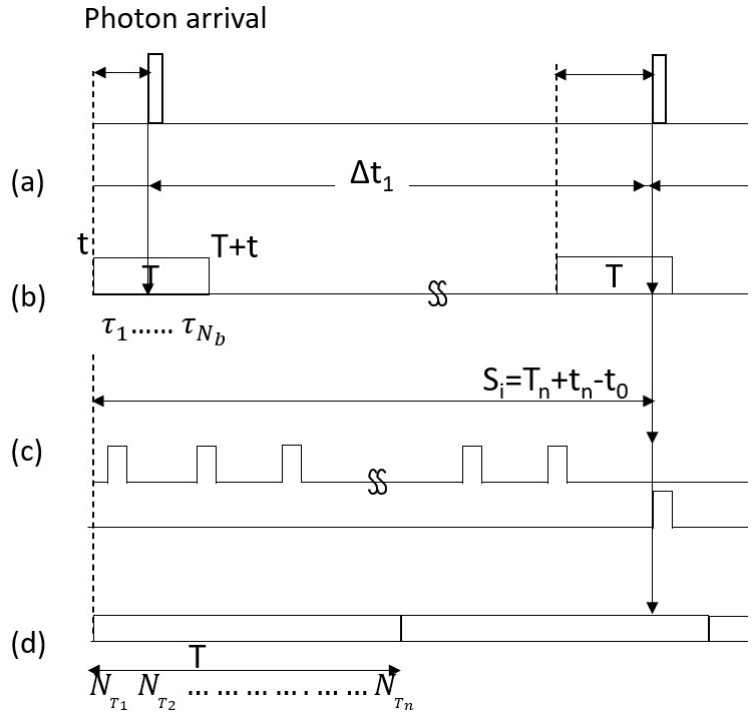

FIG. 2. Timing diagrams for photon arrival time methods: (a) Wayne *et al.* [6] uses intervals Δt_1 between detections; (b) Nie *et al.* [8] employs an external reference clock (SS: start signal); (c) Yan *et al.* [9] measures phase time relative to a fixed period; (d) Proposed method divides external reference T into N_T bins. Gray rectangles represent detection events, and dashed lines mark time bins

3.2. Source of bias

To quantitatively evaluate the randomness of the raw data, we need to model the system carefully and figure out the facts that would introduce bias. There are a few major device imperfections to be examined.

(1) The laser intensity must remain constant. We have analyzed the number of detections per $101\,\mu s$ to validate that the average photon count statistics is uniform. For an average photon number of 0.1 for 100 ns duration and a $10\,\mu s$ detector dead time, there should be one detection every 10100 ns or 10 detections every $101\,\mu s$. We take 100 samples of $1010\,\mu s$ interval to validate the mean photon number (this sample size is enough to ensure statistical confidence of photon statistics).

(2) Detector dark counts are random clicks in the absence of photons. Analyzing the effect of random noise from dark counts mixed with random numbers generated from photon arrival times would be insightful. The dark count rate (350–400 cps) is much less than the detection rate. Such negligible dark counts do not measurably affect uniformity or bias in raw data.

(3) In one of our implementations, we have considered a dead time of $5\,\mu s$, far greater than the duration of external reference, which is 100 ns. The dead time can be considered as a drift [8] and it does not affect the quality of random numbers.

(4) The probability for multi-photon emission from an attenuated continuous-wave (CW) laser is non-zero. If we use detectors capable of distinguishing between multi-photon and single-photon events, we can discard the multi-photon cases. This would reduce bias in the output. However, considering the mean photon number much less than 1 significantly reduces the chances of multi-photon events.

4. Experimental analysis

The experimental setup is presented in Fig. 3. It comprises a distributed feedback laser (DFB) operated in continuous mode with a wavelength of 1550 nm and an output power of 0.1 mW. We have two variable optical attenuators (VOAs) to adjust the amplitude of the weak coherent source to the desired value. One of them is kept fixed and the other is altered to achieve granularity. We have implemented SPD from CHAMPION Aurea in free-running mode. It has the flexibility of adjusting at variable efficiencies, for example, 10%, 20% and 30%. The dead time can be configured to achieve the required count rate for a specific efficiency. We have considered different values of N_b as 8, 100, 200, 256, 500 and 512 for an external clock of 100 ns. When we implemented the scheme with 500 ns clock reference, we have considered 65536 divisions and generated 16 bits per detection. This implies that each division is 7.6 ps. The jitter in the SPD is 180 ps, which ideally suggests that a division size greater than this period should be considered to mitigate timing uncertainty.

In our current experiments, we did not implement larger division sizes, but we fully recognize this approach's importance and will incorporate it into future experiments to improve randomness quality. At 10% efficiency and 10 μs dead time, the SPD recorded a dark count rate of 350-400 cps and a photon count rate of 90 Kcps, corresponding to a photon flux at the input of approximately 9×10^6 cps (equivalent to -89 dBm optical power) with a mean photon count of 0.09. In a separate experimental run with increased photon flux (achieved by adjusting the variable optical attenuator), the SPD count rate reached 96 Kcps, corresponding to 2.4×10^7 cps at the input and a mean photon count of 0.24 (-85 dBm). The adjustments in the optical attenuation settings between these runs were manual and static, not dynamically dependent on input optical power. In continuous operation, we have considered the SPD count rate as 9×10^4 cps. Fig. 4 presents the probability distribution of the generated random digits 1 to 256. We find that the throughput is almost uniform. We converted this data to binary and then tested it on the NIST and ENT test platforms [24, 25]. The dataset used for these tests comprised approximately 1 gigabit of raw quantum random data. At 5 μs dead time, we have considered a counting rate of 150 Kcps. A field-programmable gate array (FPGA) (Zynq UltraScale+ MPSoC) does the post-processing of the data. It also incorporates a time-to-digital converter (TDC) (TDC_AS6501), which can respond to an external clock reference from 2 MHz to 12.5 MHz. The TDC has an internal clock of 5 ps and can count till 500 ns. An external clock reference with frequency 10 MHz in one implementation and 2 MHz in other implementation, with a jitter of 3 ps is used as a reference clock and is edge synchronized with the TDC counter. The throughput at 150 Kcps count rate is 2.4 Mbps (raw QRNG data) with $5\mu s$ dead time.

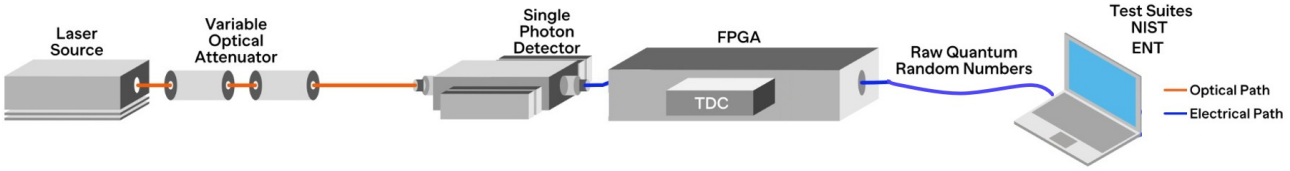

FIG. 3. Experimental setup

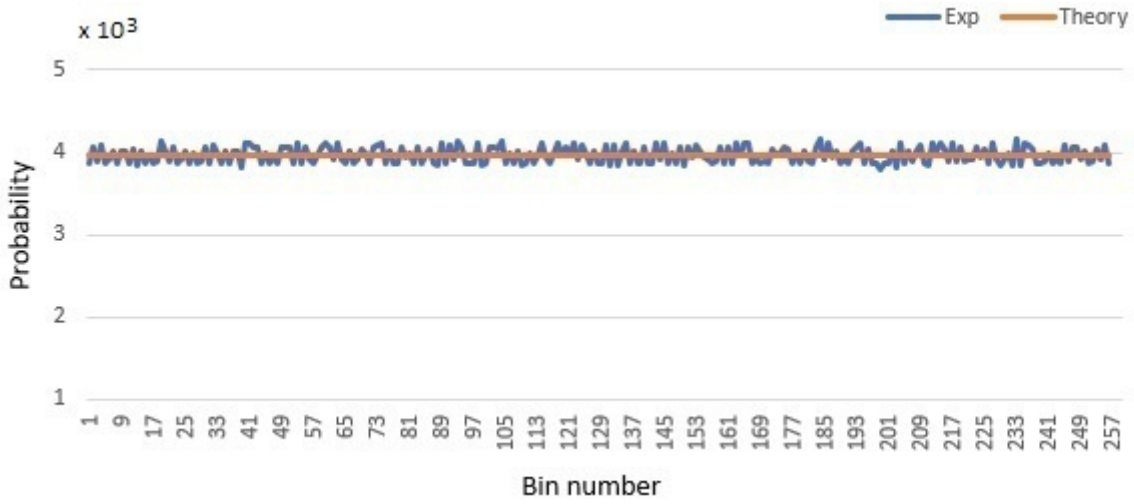

FIG. 4. Probability distribution for theoretical versus experimental values for 256 time bins with 90 Kb of raw data

5. Entropy estimation

Entropy in the information-theoretic sense is a measure of the randomness or unpredictability of the outputs of an entropy source. The larger the entropy, the greater the uncertainty in predicting the outcomes [26]. Estimating the amount of entropy available from a source is necessary to determine how many bits of randomness are available. If a discrete random variable X has n possible values, where the i^{th} outcome has probability p_i, then the Rényi entropy of order α is defined as [27]

TABLE 2. Results of ENT tests

ENT test item	QRNG	TRNG	Ideal value
Entropy (bits per bit)	1.000000	1.000000	1.000000
Chi-square distribution	45 %	15.11 %	10 % $\sim$ 90 %
Arithmetic mean value	0.4997	0.5001	0.5000
Monte Carlo value for Pi	3.1515369080	3.142180307	3.1415926536
Serial correlation coefficient	0.000590	0.000088	0.000000

TABLE 3. Results of NIST tests

NIST test item	BBS	QRNG	TRNG
	p-value	p-value	p-value
Frequency	0.816537	0.534146	0.213309
Block frequency	0.366918	0.122325	0.015598
Cumulative sums	0.955835	0.634146	0.851383
Runs	0.090936	0.739918	0.137282
Longest run	0.202268	0.534146	0.494392
Rank	0.202268	0.534146	0.383827
FFT	0.275709	0.350485	0.494392
Non overlapping template	0.764295	0.991468	0.883171
Overlapping template	0.455937	0.350485	0.779188
Universal	0.060806	0.213309	0.699313
Approximate entropy	0.971699	0.839918	0.739918
Random Excursions	0.534146	0.739918	0.186566
Random Excursions Variant	0.911413	0.457799	0.311542
Serial	0.739918	0.911413	0.779188
Linear complexity	0.145326	0.739918	0.289667

$$H_\alpha(X) = \frac{1}{1-\alpha}\log_2\left(\sum_{i=1}^{n} p_i^\alpha\right), \tag{8}$$

for $0 \leq \alpha \leq \infty$. As $\alpha \to \infty$, the Rényi entropy of X converges to the negative logarithm of the probability of the most likely outcome, called the min-entropy,

$$H_\infty(X) = \lim_{\alpha\to\infty} H_\alpha(X) = -\log_2 \max p_i. \tag{9}$$

The name min-entropy (H_∞) stems from the fact that it is the smallest in the family of Rényi entropies. In this sense, it is the most conservative approach to measuring the unpredictability of a set of outcomes or the randomness content of a distribution. The standard Shannon entropy, which measures the average unpredictability of the outcomes, offers only a rough estimation of randomness. On the other hand, H_∞ is used as a worst-case measure of the uncertainty associated with observations of X. It represents the best-case scenario for an adversary trying to guess an output from the noise source. For H_∞, p_i represents the detection probability at the i^{th} time bin and

$$H_\infty = -\frac{\log_2 P_{\max}}{\log_2 N_b} = 0.9971 \tag{10}$$

from the maximum frequency of 0.00397, which is higher than [8]. The maximum probability $P_{\max}$ was computed as the normalized frequency of the most populated time bin in the photon arrival histogram. As depicted by Fig. 4, the frequency distribution is almost uniform and the experimental values are close to the theoretical values.

We tested the QRNG output using ENT program and NIST test suite. ENT program computes some important statistical properties of the generated random bit-streams. It is a series of basic statistical tests that evaluate the random sequence by some elementary features such as the equal probabilities of ones and zeros, the serial correlation, etc. Testing results with ENT performed on a 1 GB dataset are presented in Table 2. The ENT test results indicate high-quality randomness, with only slight variations in arithmetic mean and serial correlation. These small deviations are attributed to residual classical noise sources. Each test in the NIST suite evaluates a p-value which should be larger than the significance level. The significance level in the tests is $\alpha = 0.01$. The test is considered successful if all the p-values satisfy $0.01 \leq$ p-value ≤ 0.99. In the tests producing multiple outcomes of p-values, the worst outcomes are selected. Testing results with NIST conducted on a 1 GB dataset are presented in Table 3. All the output p-values are larger than 0.01 and smaller than 0.99, which indicates that the generated random bits well pass the NIST tests. ENT and NIST were selected for initial validation due to their broad acceptance and comprehensive coverage of randomness properties. However, future work will expand the analysis to include other test suites as well to further ensure the robustness of the QRNG output. We have also compared raw quantum random numbers with the random numbers generated from NIST's Blum-Blum-Shub (BBS) algorithm and an in-house TRNG built from FPGA based on the asynchronous sampling of a ring oscillator.

6. Conclusion

We have designed and tested a practical high-speed QRNG based on the time-of-arrival quantum entropy from a CW laser at telecommunication wavelength. This study is the first to explore time-of-arrival QRNG using InGaAs detectors. These detectors have a greater dead time than silicon detectors, enabling us to increase the external reference time to 500 ns compared to previous values of 40.6 ns [8] and 20 ns [9]. We have implemented precision time measurement of 5 ps, which is reported here for the first time. Hence, we could extract 16 bits of entropy from one photon arrival time. The photon arrival time follows a Poisson distribution; an exponential waiting time introduces bias, which is overcome using an external reference clock. We successfully generated uniform random numbers with high entropy, particularly min-entropy always greater than 0.99 value. The method of time measurement of photons is simpler in implementation and higher in precision time measurement than earlier works [6,8,9]. We propose that implementing the time-of-arrival QRNG with InGaAs detectors and high precision time measurement will enable generating maximum entropy per detection event. The proposed work can be used to generate higher throughput by increasing the duration of the external reference clock; however, the increase in throughput will be linear. The proposed work also eliminates the need for any mathematical algorithm to generate uniform output; thus, the random numbers produced are derived from the quantum behavior of photons and are truly random.

References

[1] Knuth D.E. *Art of Computer Programming*, Volume 2: Seminumerical Algorithms, Addison-Wesley Professional (2014).

[2] chmidt H. Quantum-mechanical random-number generator, *J. Appl. Phys.*, 1970, **41**, P. 462–468.

[3] Aggarwal D., Ghatikar R., Chennuri S. and Banerjee A. Generation of 1 GB full entropy random numbers with the enhanced-NRBG method. *Physica Scripta*, 2023, **98**(12), P. 125112.

[4] Jennewein T., Achleitner U., Weihs G., Weinfurter H. and Zeilinger A. A fast and compact quantum random number generator. *Rev. Sci. Instruments*, 2000, **71**(4), P. 1675–1680.

[5] Stipcevic M. and Rogina B.M. Quantum random number generator based on photonic emission in semiconductors. *Rev. Sci. Instrum*, 2007, **78**, P. 045104.

[6] Wayne M.A., Jeffrey E.R., Akselrod G.M. and Kwiat P.G. Photon arrival time quantum random number generation. *J. Mod. Opt.*, 2009, **56**(4), P. 516–522.

[7] Wahl M., Leifgen M., Berlin M., Röhlicke T., Rahn H.-J. and Benson O. An ultrafast quantum random number generator with provably bounded output bias based on photon arrival time measurements. *Appl. Phys. Lett.*, 2011, **98**, P. 171105.

[8] Nie Y., Zhang H., Zhang Z., Wang J., Ma X., Zhang J. and Pan J. Practical and fast quantum random number generation based on photon arrival time relative to external reference. *Appl. Phys. Lett.*, 2014, **104**, P. 051110.

[9] Yan Q., Zhao B., Hua Z., Liao Q. and Yang H. High-speed quantum-random number generation by continuous measurement of arrival time of photons. *Rev. Sci. Instrum.*, 2015, **86**, P. 073113.

[10] Gabriel C., Wittmann C., Sych D., Dong R., Mauerer W., Andersen U.L., Marquardt C. and Leuchs G. A generator for unique quantum random numbers based on vacuum states. *Nat. Photonics*, 2010, **4**, P. 711–715.

[11] Shen Y., Tian L. and Zou H. Practical quantum random number generator based on measuring the shot noise of vacuum states. *Phys. Rev. A*, 2010, **81**, P. 063814.

[12] Symul T., Assad S.M. and Lam P.K. Real time demonstration of high bitrate quantum random number generation with coherent laser light. *Appl. Phys. Lett.*, 2011, **98**(23), P. 145.

[13] Bruynsteen C., Gehring T., Lupo C., Bauwelinck J. and Yin X. 100-Gbit/s integrated quantum random number generator based on vacuum fluctuations. *PRX Quantum*, 2023, **4**, P. 010330.

[14] Raffaelli F., Ferranti G., Mahler D.H., Sibson P., Kennard J.E., Santamato A., Sinclair G., Bonneau D., Thompson M.G. and Matthews J.C.F. A homodyne detector integrated onto a photonic chip for measuring quantum states and generating random numbers. *Quantum Sci. Technol.*, 2018, **3**, P. 025003.

[15] Guo H., Tang W., Liu Y. and Wei W. Truly random number generation based on measurement of phase noise of a laser. *Phys. Rev. E*, 2010, **81**, P. 051137.
[16] Qi B., Chi Y.-M., Lo H.-K. and Qian L. High-speed quantum random number generation by measuring phase noise of a single-mode laser. *Opt. letters*, 2010, **35**(3), P. 312–314.
[17] Marandi A., Leindecker N.C., Vodopyanov K.L. and Byer R.L. All-optical quantum random bit generation from intrinsically binary phase of parametric oscillators. *Opt. Express*, 2012, **20**, P. 19322–19330.
[18] Williams C.R.S., Salevan J.C., Li X., Roy R. and Murphy T.E. Fast physical random number generator using amplified spontaneous emission. *Opt. Express*, 2010, **18**, P. 23584–23597.
[19] Herrero-Collantes M. and Garcia-Escartin J.C. Quantum random number generators. *Rev. Mod. Phys.*, 2017, **89**, P. 015004.
[20] Li S., Wang L., Wu L.-An, Ma H.-Q. and Zhai G.-J.True random number generator based on discretized encoding of the time interval between photons. *J. Opt. Soc. Am. A*, 2013, **30**, P. 124.
[21] Wayne M.A. and Kwait P.G. Low-bias high-speed quantum random number generator via shaped optical pulses. *Opt. Express*, 2010, **18**, P. 9351.
[22] Series X: Data Networks Open System Communications and security, Quantum communication Quantum noise random number generator architecture, Recommendation X.1702 (11/19).
[23] Fox M. *Quantum optics: an introduction*. Oxford Univ. Press, Oxford, Oxford master series in atomic, optical, and laser physics, 2006.
[24] Bassham III L.E., et al. A statistical test suite for random and pseudorandom number generators for cryptographic applications. Nat. Inst. Standards Technol., Gaithersburg, MD, USA, Tech. Rep. SP 800-22 Rev. 1a, 2010.
[25] Walker J. ENT: A pseudo-random number sequence test program. http://www.fourmilab.ch/random/ (2008).
[26] Yuan X., Zhao Q., Girolami D. and Ma X. Quantum coherence and intrinsic randomness. *Advanced Quantum Technologies*, 2019, **2**(11), P. 1900053.
[27] A. Rényi. On Measures of Entropy and Information. Proceedings of the Fourth Berkeley Symposium on Mathematical Statistics and Probability, Volume 1: Contributions to the Theory of Statistics, P. 547–561, University of California Press, Berkeley, Calif., 1961.

Submitted 1 August 2025; revised 24 August 2025; accepted 25 August 2025

Information about the authors:

Deepika Aggarwal – QuNu Labs Pvt. Ltd., M.G. Road, Bangalore, Karnataka, India; ORCID 0000-0003-3238-382X; deepika@qnulabs.com

Anindita Banerjee – QuNu Labs Pvt. Ltd., M.G. Road, Bangalore, Karnataka, India; anindita@qnulabs.com

Ankush Sharma – QuNu Labs Pvt. Ltd., M.G. Road, Bangalore, Karnataka, India; ankush@qnulabs.com

Ganesh Yadav – QuNu Labs Pvt. Ltd., M.G. Road, Bangalore, Karnataka, India; ganesh@qnulabs.com

Conflict of interest: the authors declare no conflict of interest.

NANOSYSTEMS:
PHYSICS, CHEMISTRY, MATHEMATICS

Proskurnina E.V., et al. *Nanosystems: Phys. Chem. Math.*, 2025, **16** (5), 606–618.
http://nanojournal.ifmo.ru

Original article

DOI 10.17586/2220-8054-2025-16-5-606-618

Physicochemical aspects and cellular effects of nanoceria-human serum albumin conjugates

Elena V. Proskurnina[1,a], Svetlana V. Kostyuk[1,2,b], Madina M. Sozarukova[1,c], Elizaveta S. Ershova[1,2,d], Natalia N. Veiko[1,2,e], Matvei A. Popkov[1,f], Edmund V. Kostyuk[1,g], Andrey V. Martynov[1,h], Vladimir K. Ivanov[1,i]

[1]Kurnakov Institute of General and Inorganic Chemistry of the Russian Academy of Sciences, Moscow 119991, Russia

[2]Petrovsky Russian Scientific Center of Surgery, Institute of Longevity with a Clinic of Rehabilitation and Preventive Medicine, Moscow 119435, Russia

[a]proskurnina@gmail.com, [b]svet-vk@yandex.ru, [c]s_madinam@bk.ru, [d]es-ershova@rambler.ru, [e]satelit32006@yandex.ru, [f]ma_popkov@igic.ras.ru, [g]edmundvk@ya.ru, [h]avlamar@mail.ru, [i]van@igic.ras.ru

Corresponding author: E. V. Proskurnina, proskurnina@gmail.com

PACS 68.65.k, 81.20.n, 82.70.Dd, 87.68.+z

ABSTRACT Nanoceria exhibits unique catalytic properties towards reactive oxygen species (ROS), which act as mediators of key signaling pathways. Albumin is the most abundant blood protein, and its interaction with nanoceria modifies the properties of both nanoceria and albumin. Using an in vitro model of human embryonic lung fibroblasts, we investigated biochemical properties of nanoceria–albumin conjugates towards cell viability, intracellular reactive oxygen species, expression of NOX4, NRF2, and NF-κB, oxidative DNA damage/repair, apoptosis, cell proliferation, and autophagy. The results demonstrate that albumin binding alters the physicochemical properties of nanoceria, promoting efficient cellular uptake through modulation of surface interactions. This conjugation attenuates nanoceria's influence on intracellular reactive oxygen species equilibrium and mitochondrial membrane potential by modifying nanoparticle-protein interfacial dynamics. Notably, albumin-bound nanoceria induces a stronger activation of NOX4, resulting in increased genotoxic stress; however, the enhanced activation of DNA repair pathways mitigates this damage more efficiently than bare nanoceria. Furthermore, albumin-to-nanoceria conjugation modulates signaling pathways by enhancing suppression of the pro-inflammatory NF-κB cascade and stimulating autophagic processes. Overall, the physicochemical effects of nanoceria modification due to albumin conjugation reduce cytotoxicity of nanoceria while augmenting its anti-inflammatory and regenerative potential.

KEYWORDS nanoceria, human serum albumin, cytotoxicity, genotoxicity, oxidative metabolism genes, proliferation, autophagy, human lung embryonic fibroblasts.

ACKNOWLEDGEMENTS This study was supported by the Russian Science Foundation, project No. 24-13-00370.

FOR CITATION Proskurnina E.V., Kostyuk S.V., Sozarukova M.M., Ershova E.S., Veiko N.N., Popkov M.A., Kostyuk E.V., Martynov A.V., Ivanov V.K. Physicochemical aspects and cellular effects of nanoceria-human serum albumin conjugates. *Nanosystems: Phys. Chem. Math.*, 2025, **16** (5), 606–618.

1. Introduction

Nanoscale cerium dioxide (nanoceria) is a multifunctional catalyst for reactions involving reactive oxygen species (ROS). Acting as a nanozyme, nanoceria mimics the activities of enzymes such as superoxide dismutase (SOD) [1], peroxidase [2], catalase [3], oxidase [4,5], phosphatase [6], photolyase [7], phospholipase [8], and nuclease [9]. ROS play a central role in nearly all biological processes, positioning nanoceria as a key regulator of vital biochemical functions. Upon entry into biological fluids, nanoparticles interact primarily with proteins, altering the properties of both. Albumin, the predominant blood serum protein, exhibits high affinity for diverse compounds and contributes to redox balance via a single sulfhydryl group; its properties depend on its structural conformation [10]. Albumin functions as a transport protein and natural carrier within the organism, delivering drugs and metabolites [11], which ensures biocompatibility and strong binding characteristics when complexed with nanoparticles [12]. It is suitable as a drug delivery carrier due to its wide availability, low toxicity, biodegradability, non-immunogenicity, and preferential accumulation in tumors and inflamed tissues [13]. Conversely, when ceria nanoparticles enter the bloodstream, they bind to serum proteins,

including albumin [14]. Therefore, albumin is actively studied for nanoparticle binding to develop effective anticancer nanomedicines and to elucidate their cellular mechanisms of action [12, 15].

Inorganic nanoparticles intended for biomedical applications require surface modification due to their low hydrophilicity and colloidal stability in solutions. Conjugation of the nanoparticles with albumin, which has high hydrophilicity, numerous binding sites, and reductive activity, facilitates effective functionalization [16, 17]. Compared to human serum albumin (HSA), bovine serum albumin (BSA) is rich in functional groups such as carboxyl and amino groups and exhibits strong affinity for inorganic (e.g. metal oxide) nanoparticles; therefore, it is often used as a model for surface modification of the nanoparticles to improve their colloidal stability and biocompatibility while providing functionalization and low toxicity [18, 19]. Most studies on conjugation of the nanoparticles with albumin focus on silver, gold, copper, and iron oxide. In particular, it has been shown that albumin conjugation reduced the cytotoxicity of silver nanoparticles on mesenchymal stem cells while preserving bactericidal activity [20]. HSA-coated silver nanoparticles showed higher toxicity toward hepatocellular carcinoma cells [21]. Chen *et al.* developed gold nanoparticle-albumin complexes conjugated with cisplatin, which exhibited reduced side effects [22]. Studies also report on albumin conjugation with copper particles [23] and magnetic iron oxides [24]. Janani *et al.* analyzed the toxicity of ZnO nanoparticles with BSA and demonstrated that BSA coating reduces the toxic effect [25].

The potential for forming nanocomplexes of cerium dioxide with albumin is also being investigated. Bhushan *et al.* reported the synthesis of albumin nanoparticles encapsulated with nanoceria, which constitute a highly monodisperse and stable aqueous delivery system. They demonstrated that the superoxide dismutase activity of nanoceria remained unaffected, and the nanoparticles exhibited high biocompatibility and antioxidant potential towards human lung epithelial cells [26]. Yang *et al.* synthesized ceria-based nanostructures – including nanoclusters, nanoparticles, and nanochains – using bovine serum albumin. The resulting albumin-based ceria nanostructures preserved high SOD-like activity and good biocompatibility [27]. Yeni *et al.* evaluated quercetin-albumin-nanoceria particles for neurotoxicity using the MTT assay on primary neuronal cultures and reported significant protective effects against glutamate toxicity [28]. Roudbaneh *et al.* examined the interaction of nano-CeO_2 with human serum albumin (HSA), assessing antioxidant activity against peroxide-induced stress, bone marrow-derived mesenchymal stem cell viability, intracellular ROS, apoptosis, and antibacterial activity. Their findings indicated that hydrophilic interactions contribute to complex formation. No cytotoxicity was observed up to 50 mg/mL, and pre-treatment with this complex reduced cell death, ROS production, and apoptosis induced by peroxide stress. Cerium dioxide-albumin complex nanoparticles exerted significant antibacterial effects against all bacterial strains studied [29]. Although knowledge of the biological effects of the HSA-nanoceria complex remains limited and fragmented, it shows promising potential for biomedical applications. To date, no studies have addressed the effects of the HSA-nanoceria complex on human genes.

To summarize, complexation of nanoceria with human serum albumin (HSA) can be considered a promising approach for synthesizing new nanopharmacological agents. However, assessing the effects of surface modifiers on the efficacy and safety of cerium dioxide is essential to evaluate the benefits and risks in medical applications. Human embryonic lung fibroblasts serve as a widely used, reliable, and sensitive model for studying the effects of substances on gene expression. Here, we aimed to investigate the effects of the HSA-nanoceria conjugate on oxidative metabolism-related genes in human embryonic lung fibroblasts by examining: (1) cell viability and mitochondrial membrane potential, (2) intracellular reactive oxygen species (ROS), (3) expression levels of NOX4, NRF2, and NF-κB/STAT3, (4) oxidative DNA damage and repair, (5) cell proliferation, and autophagy.

2. Materials and methods

2.1. Synthesis and characterization of bare and HSA-nanoceria conjugate

The method for synthesizing an electrostatically stabilized CeO_2 sol involved the thermal hydrolysis of ammonium cerium(IV) nitrate (Sigma-Aldrich, #215473) [30]. Specifically, a 100 g/L aqueous solution of $(NH_4)_2Ce(NO_3)_6$ was incubated at 95°C for 24 hours. The product was centrifuged, washed three times with isopropanol, and then redispersed in deionized water. This suspension was boiled for 1 hour with stirring to remove residual isopropanol. In a separate preparation, albumin was dissolved in phosphate buffer. The HSA-CeO_2 conjugate was formed by the gradual, dropwise addition of the CeO_2 sol to the albumin solution at a 1:1 molar ratio under constant stirring. The mixture was stirred for another 30 minutes after addition to complete albumin adsorption onto the CeO_2 nanoparticles.

To determine the concentration of the stock CeO_2 sol, a gravimetric method was employed. Sample aliquots were placed in pre-dried crucibles until constant weight was achieved. These samples were then evaporated and subjected to high-temperature treatment in a muffle furnace, held at 900°C for 4 hours.

X-ray diffraction (XRD) characterization of the dried samples was performed using a Bruker D8 Advance instrument (Bruker, Billerica, MA, USA) with CuKα radiation. Data acquisition in θ–θ geometry covered a 2θ range from 3° to 120°, with a step size of 0.02° and an accumulation time of 0.3 seconds per point. Phase identification via diffraction peak analysis was referenced to the ICDD PDF-2 database. The Scherrer equation was applied to calculate the mean crystallite size.

The mean hydrodynamic diameter of the CeO_2 nanoparticles was measured by dynamic light scattering (DLS) using a Photocor Compact-Z analyzer (Photocor, Russia) with a 650 nm, 25 mW diode laser. Measurements were conducted at room temperature at a 90° scattering angle. Zeta potential was measured on a Malvern ZS Zetasizer (Malvern Panalytical, UK) according to the ISO/TR 19997:2018 standard. Both DLS and zeta potential analyses were carried out on aqueous nanoparticle dispersions at 1.5 mM concentration.

UV-Vis absorption spectra were recorded on a Cary 4000 spectrophotometer (Agilent Technologies, USA) using 1.0 cm path length quartz cuvettes at ambient temperature.

Binding affinity of ligand molecules to the cerium oxide nanoparticle surface was assessed by attenuated total reflectance-Fourier transform infrared spectroscopy (ATR-FTIR). Spectra were acquired using a Bruker VERTEX 70 spectrometer equipped with a PIKE Technologies GladiATR^{TM} diamond crystal attachment. Measurements covered the wavenumber range 4000 – 150 cm^{-1}, at 2 cm^{-1} resolution, averaging 64 scans for both sample and background. The ATR crystal was maintained at 50°C. For liquid samples, up to 5 μL were deposited onto the crystal and allowed to air-dry for 4 – 5 minutes before data acquisition.

2.2. Cell culture

Human embryonic lung fibroblasts (passage 4) were obtained from the Scientific Centre for Medical Genetics (Moscow, Russia). The cells were seeded at a concentration of 1.7×10^4 cells/mL in Dulbecco's Modified Eagle Medium (PanEco, Moscow, Russia) supplemented with 10% fetal calf serum (PAA, Vienna, Austria), 50 U/mL penicillin, 50 μg/mL streptomycin, and 10 μg/mL gentamicin. HELFs were cultured at 37°C for 24 hours, followed by exposure to either bare nanoceria or the HSA-nanoceria conjugates for 1, 3, 24, and 72 hours.

2.3. Cell viability and mitochondrial potential

The standardized 72-hour MTT assay (3-(4,5-dimethylthiazol-2-yl)-2,5-diphenyltetrazolium bromide) was employed to assess cell viability. Absorbance at 550 nm was measured using an EnSpire Plate Reader (EnSpire Equipment, Turku, Finland). Cells incubated without nanoparticles served as the negative control. Mitochondrial membrane potential was evaluated using the membrane-potential-sensitive dye tetramethylrhodamine methyl ester (TMRM) (Thermo Fisher, Waltham, MA, USA), following previously established protocols [31].

2.4. Visualization

An AxioImagerA2 microscope (Carl Zeiss, Oberkochen, Germany) was used for fluorescence imaging. Cells were cultured in slide flasks and exposed to either bare or HSA-bound nanoceria. Each slide-bottom flask was seeded with approximately 500,000 cells. Following medium removal, the cells were washed with phosphate buffered saline (PBS), and dichlorodihydrofluorescein diacetate (a 2 mg/mL stock solution diluted 1:200 with PBS) was added. After a 15-minute incubation, the cells were washed once more with PBS and immediately imaged. At least 100 fields of view were analyzed. Fluorescence intensity per cell and total fluorescence were quantified using the microscope software (ZEN 3.10).

2.5. Flow cytometry analysis

Intracellular reactive oxygen species (ROS) and protein expression were quantified using flow cytometry. To measure ROS, samples were incubated with a 10 μM solution of 2',7'-dichlorodihydrofluorescein diacetate (H2DCFH-DA) in phosphate-buffered saline (PBS) (Molecular Probes/Invitrogen, Carlsbad, CA, USA) for 15 minutes in the dark. Following incubation, the cells were washed with PBS, resuspended in PBS, and analyzed by flow cytometry using the FITC channel (CytoFlex S, Beckman Coulter, Brea, CA, USA).

For protein quantification, cells were washed with Versene solution (Thermo Fisher Scientific, Waltham, MA, USA), treated with 0.25% trypsin (Paneco, Moscow, Russia), washed with culture medium, and then resuspended in PBS (pH 7.4) (Paneco, Moscow, Russia). The cells were fixed with paraformaldehyde (PFA, Sigma-Aldrich, Saint Louis, MO, USA) at 37°C for 10 minutes, washed three times with 0.5% bovine serum albumin (BSA) in PBS, and permeabilized with either 0.1% Triton X-100 in PBS for 15 minutes at 20°C or 90% methanol at 4°C. After three washes with 0.5% BSA-PBS, cells were stained with conjugated antibodies (1 μg/mL) for 2 hours at room temperature, washed with PBS, and analyzed by flow cytometry (CytoFlex S, Beckman Coulter, Brea, CA, USA).

Primary antibodies were as follows: DyLight488-γH2AX (pSer139) (nb100-78356G, NovusBio, Centennial, CO, USA), FITC-NRF2, (bs1074r-fitc, Bioss Antibodies Inc. Woburn, MA, USA), FITC-BRCA1 (Nb100-598F, NovusBio, Centennial, CO, USA), PE-8-oxo-dG (sc-393871 PE, Santa Cruz Biotechnology, Dallas, TX, USA), CY5.5-NOX4 (bs-1091r-cy5-5, Bioss Antibodies Inc. Woburn, MA, USA), A350-BCL2 (bs-15533r-a350, Bioss Antibodies Inc. Woburn, MA, USA), NFKB (bs-0465r-cy7, Bioss Antibodies Inc. Woburn, MA, USA), LC3 (NB100-2220 NovusBio, Centennial, CO, USA), and PCNA (ab2426, Abcam plc, Cambridge, UK). The secondary anti-rabbit IgG-FITC (sc-2359, Santa Cruz Biotechnology, Dallas, TX, USA), was used.

TABLE 1. Physicochemical characteristics of CeO_2 sols

Sample	Particle Size, nm (Powder X-Ray Diffraction)	Particle Size, nm (Dynamic Light Scattering)	ζ, mV (Electrophoretic Light Scattering)
Bare CeO_2	3.2 ± 0.3	20.7 ± 0.3	$+40.2 \pm 0.1$
HSA-nanoceria conjugate	3.9 ± 0.1	9.2 ± 0.1, 180 ± 11	$+9.8 \pm 1.2$

2.6. Statistics

All experiments were performed in triplicate. Data are presented as the mean $\pm$ standard deviation. Differences were considered statistically significant at $p < 0.01$ according to the non-parametric Mann–Whitney test. Statistical analyses were conducted using StatPlus2007 Pro v4.9.2 software (AnalystSoft Inc., Walnut, CA, USA).

3. Results

3.1. Synthesis and characterization of nanoparticles

An electrostatically stabilized cerium dioxide sol was synthesized from ammonium cerium(IV) nitrate via thermal hydrolysis at 95°C [30]. The concentration of the CeO_2 colloidal dispersion, determined by thermogravimetric analysis, was 0.125 ± 0.003 mol/L (21.5 g/L). Crystallite sizes and zeta potential values of bare CeO_2 nanoparticles and the HSA-nanoceria conjugate, measured by powder X-ray diffraction (XRD), dynamic light scattering (DLS), and electrophoretic light scattering (ELS), are summarized in Table 1.

The XRD patterns of the ceria sols, both dried at a low temperature (50°C), are shown in Fig. 1. According to experimental data, powder samples contain single-phase fluorite-type cerium dioxide (PDF2 34-0394) with crystallite sizes in the range of 3.2 – 3.9 nm (Table 1). The XRD pattern of the HSA-nanoceria conjugate is similar to that of bare CeO_2 NPs, indicating that the crystalline structure of nanoscale cerium dioxide is retained after interaction with albumin.

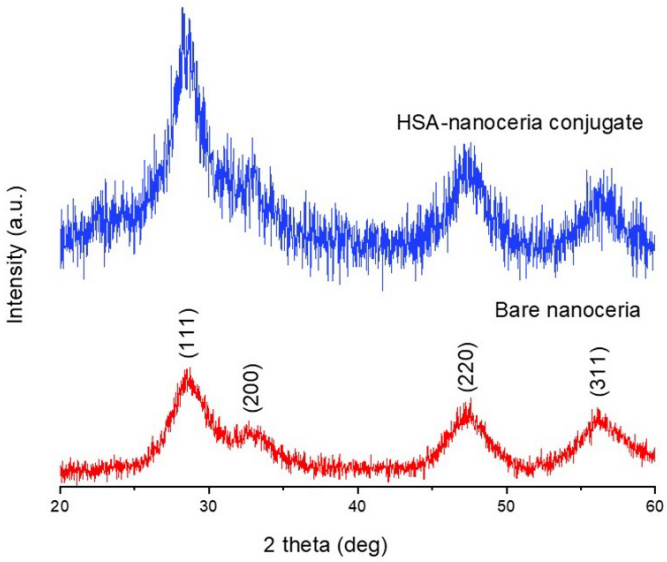

FIG. 1. XRD patterns of the dried sols of bare and HSA-coated CeO_2

Dynamic light scattering data on the particle size distribution of aggregates in CeO_2 sols are shown in Fig. 2. The non-stabilized CeO_2 sol (pH$\sim$3.0) exhibits a nearly monomodal size distribution of aggregates with an average hydrodynamic diameter of 20 nm (Table 1). The conjugation of albumin to CeO_2 nanoparticles (NPs) alters their degree of aggregation, resulting in larger aggregates with an average hydrodynamic diameter of 180 nm (Table 1). The small-size particles ($\sim$10 nm) that are present in the HSA-nanoceria conjugate dispersions are most probably the individual HSA moieties. The HSA characteristic size in different water solutions (5 – 30 nm) has been extensively studied earlier and corresponds well to the observed value [32–34]. These data indicate that not all the HSA was conjugated with ceria nanoparticles, however the relative amount of the free protein could be regarded as low.

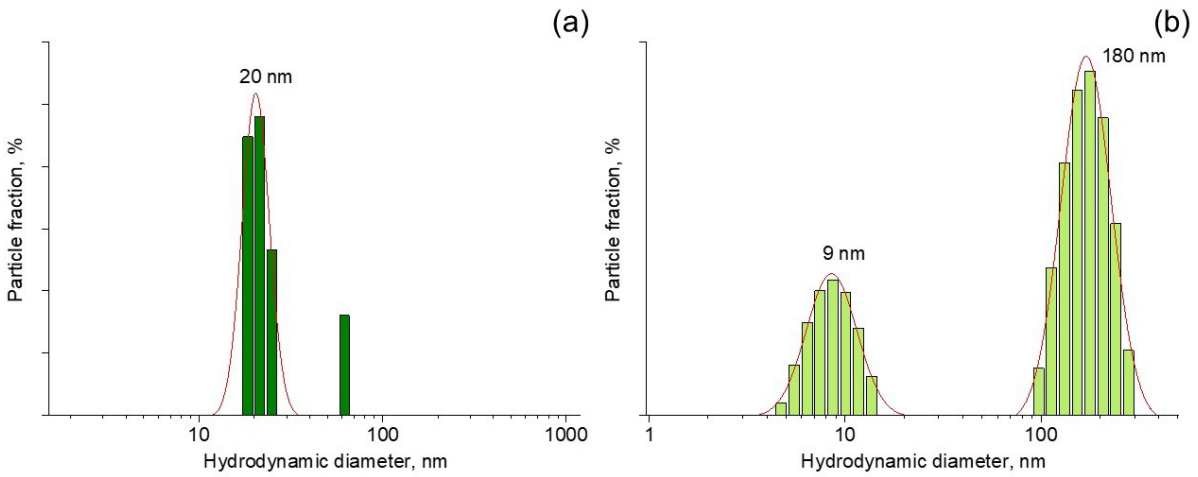

FIG. 2. Hydrodynamic diameters distributions for CeO_2 particles in aqueous sols (a) non-stabilized ceria sol and (b) HSA-nanoceria conjugate

According to the results of electrokinetic measurements (Table 1), the zeta potential of bare CeO_2 nanoparticles is $+40.2 \pm 0.1$ mV, indicating their high colloidal stability. As the non-stabilized CeO_2 sol has a pH of approximately 3.0, the positive surface charge is attributed to protonation of surface hydroxyl groups [35, 36]. Modification of the CeO_2 nanoparticles with albumin causes a sharp decrease in zeta potential to $+9.8 \pm 1.2$ mV. This decrease is consistent with protein adsorption onto the nanoparticle surface and the formation of a dense protein corona [37–39].

UV-vis absorption spectroscopy data (Fig. 3) show an absorption band in the 280 – 300 nm wavelength range. This band is characteristic of nanoscale cerium dioxide and corresponds to a band gap of $\sim$3.4 eV, which is consistent with values reported in the literature [40].

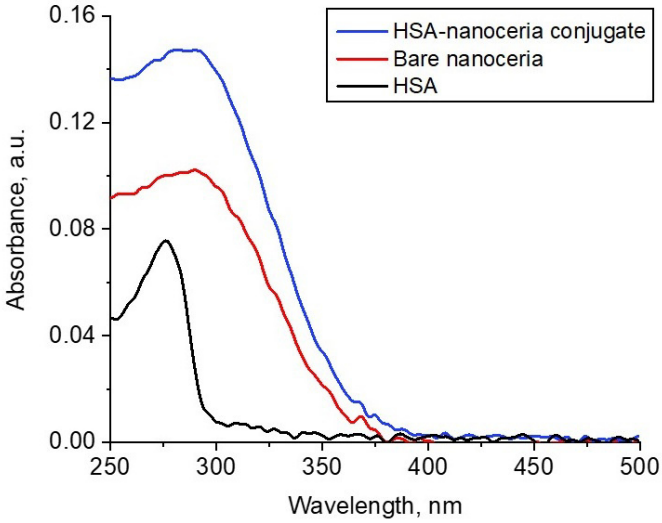

FIG. 3. UV-vis absorption spectra of ceria sols

The ceria sols were characterized using ATR-FTIR spectroscopy. The FTIR spectra of bare CeO_2 nanoparticles, human serum albumin, and the HSA-nanoceria conjugate are presented in Fig. 4.

The FTIR spectrum of the bare CeO_2 nanoparticles features characteristic absorption bands for Ce–O valence vibrations at 470 cm^{-1} and 285 cm^{-1}. Additional bands observed in the regions of 1600 – 1395 cm^{-1} and 3500 cm^{-1} are assigned to deformation and valence vibrations of water adsorbed on the ceria surface [41]. The absorption band at 1288 cm^{-1} corresponds to residual nitrate ions from the synthesis precursor, ammonium cerium(IV) nitrate ($(NH_4)_2Ce(NO_3)_6$) [42]. The absorption bands of the native HSA (Fig. 4) are consistent with those previously reported [43, 44]. The Amide I band, arising from C=O stretching vibrations, is located at 1655 cm^{-1}. The amide II band, which is attributed to C–N stretching coupled with N–H bending modes, appears at 1542 cm^{-1}. These bands are sensitive to changes in the secondary structure of the protein [43–45]. Presumably, the bands at 1085 cm^{-1} and 982 cm^{-1} are due to the phosphate buffer used to prepare the protein solution. The intense band at 530 cm^{-1} is due to the stretching vibrations of the S–S bonds of the

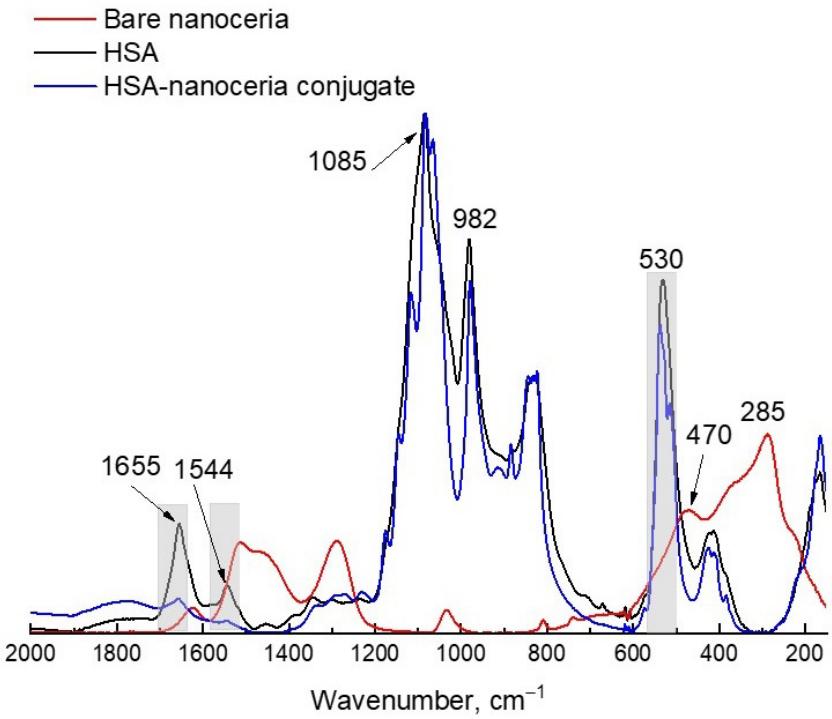

FIG. 4. Fourier-transform infrared spectra with attenuated total reflection for bare CeO_2, human serum albumin (HSA), and HSA-nanoceria conjugate

disulfide bridges present in human serum albumin [46]. The FTIR spectrum of the conjugate (Fig. 4) reveals a significant reduction in intensity and broadening of the amide I and II bands at $\sim$1655 cm^{-1} and at $\sim$1540 cm^{-1}, alongside a shift of the S–S band from 530 cm^{-1} to 540 cm^{-1}. All this indicates conformational changes in the protein structure as a result of interaction with CeO_2 nanoparticles. The shift in the disulfide bond vibration band may suggest that the nanoparticles interact with albumin domains containing cysteine residues [47]. These results confirm the successful formation of the conjugate and extend the previous findings on the interaction of nanoceria with proteins [37].

3.2. Cell viability and mitochondrial potential

Viability of cells exposed to bare nanoceria and HSA-nanoceria conjugate shows a similar pattern (Fig. 5a). There is a slight increase in toxicity around the concentration of 1 μmol/L, whereas nanoceria conjugated with albumin is also more toxic at higher concentrations (above 85 μmol/L). For gene and protein expression studies, a concentration of 1.5 μmol/L was selected, corresponding to the middle of the investigated range and providing satisfactory viability for both bare nanoceria and HSA-conjugated nanoceria.

Regarding mitochondrial membrane potential, the HSA-nanoceria conjugate exhibits a milder effect compared to bare nanoceria (Fig. 5b), although the maximum increase in membrane potential for both nanoparticles occurs after 3 hours of incubation. After 24 hours of incubation, the membrane potential returns to control levels.

3.3. Visualization and intracellular ROS

Nanoscale cerium dioxide yields fluorescence in the red region, enabling visualization of its accumulation within cells [48]. Images of cells exposed to nanoparticles (1.5 μmol/L) for 3 hours are presented in Fig. 6. The images indicate that during the first three hours, the HSA-nanoceria conjugate actively enters the cells.

Assessment of intracellular ROS levels using flow cytometry and H2DCFH-DA indicates that bare nanoceria exhibits an antioxidant effect during 1 and 3 hours of incubation, whereas albumin-bound nanoceria has little to no impact on intracellular ROS levels (Fig. 7).

3.4. Genotoxicity

Genotoxicity was evaluated using the oxidative damage marker 8-oxo-2'-deoxyguanosine (8-oxo-dG) (Fig. 8a) and the marker of double-strand breaks, phosphorylated histone γH2AX (Fig. 8b). Repair system activity was assessed by the key repair protein marker BRCA1 (Fig. 8c).

The genotoxicity dynamics differ slightly for bare nanoceria and HSA-nanoceria conjugate, with a peak at 3 hours of incubation. Bare nanoceria exhibits two phases of action, with peaks at 1 and 24 hours, while the peak effect for HSA-albumin conjugate is 3 hours. HSA-nanoceria conjugate is also characterized by higher levels of DNA damage and

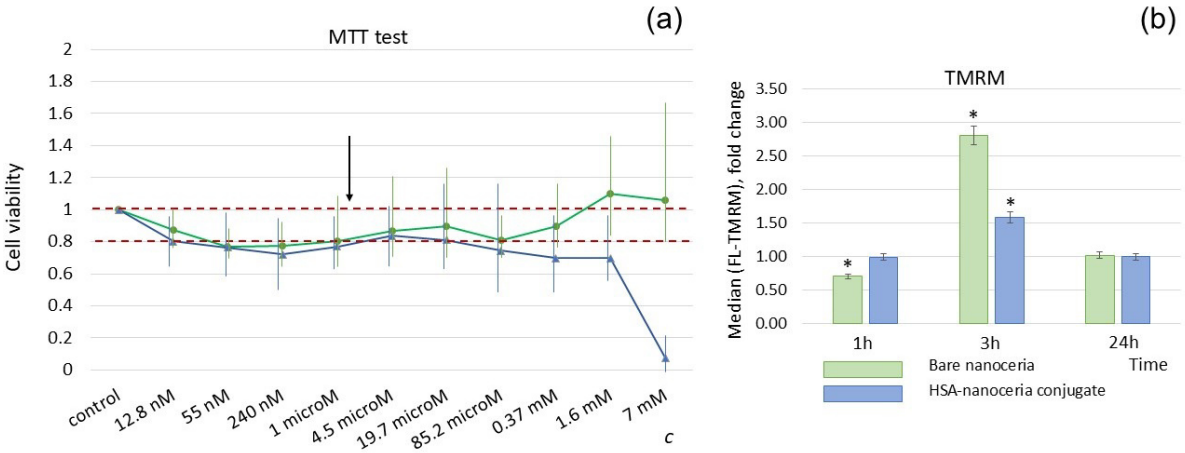

FIG. 5. (a) Cell viability in the presence of bare nanoceria (green line) and HSA-nanoceria conjugate (blue line), assessed by the MTT assay. The red dashed line indicates the acceptable viability range of 80 – 100 %. The arrow points to the concentration of 1.5 μmol/L selected for further studies; (b) Mitochondrial membrane potential relative to control, measured by the TMRM assay for cells exposed to bare and HSA-nanoceria conjugate; asterisks (*) indicate significant differences from the control according to the Mann–Whitney test ($p < 0.05$). The control consists of cells incubated without nanoparticles

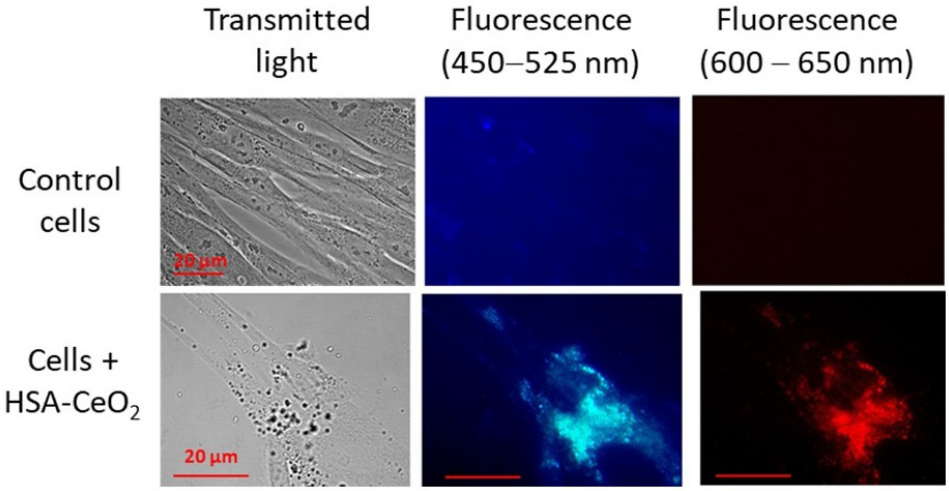

FIG. 6. Transmitted light and fluorescence images of HSA-nanoceria conjugate (1.5 μM) in human fetal lung fibroblasts; magnification, 100×

repair. After 72 hours of incubation, the level of DNA damage for both nanoparticles decreases significantly below the control level, with this effect being more pronounced for HSA-albumin conjugate.

3.5. Proteins of key ROS-dependent and inflammation signaling pathways

The primary prooxidant enzyme is the membrane-bound complex NOX4, whose expression is highest following 3 hours of incubation with the HSA-nanoceria conjugate (Fig. 9a). This correlates with the compensatory activation of the NRF2 anti-inflammatory pathway (Fig. 9b). The expression dynamics of NOX4 and NRF2 correspond to the patterns of oxidative DNA damage observed for both nanoparticles (compare Fig. 8a,b and Fig. 9a,b). The effects are more pronounced for the HSA-nanoceria conjugate than for bare nanoceria.

Regarding the pro-inflammatory NF-κB pathway, the HSA-nanoceria conjugate activated it only slightly after 24 hours of incubation, in contrast to the more pronounced effect of bare nanoceria (Fig. 9c). For the STAT3 pathway, the activating effect of both nanoparticles peaked after 3 hours of incubation and was virtually identical (Fig. 9d).

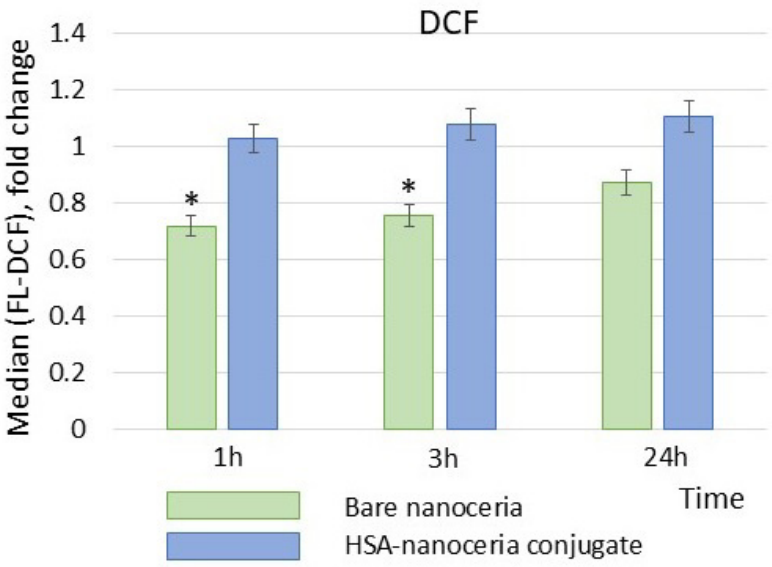

FIG. 7. Levels of intracellular reactive oxygen species (ROS), assessed by oxidation of the fluorescent probe H2DCFH-DA using flow cytometry. Incubation times with nanoparticles (1.5 μmol/L) are indicated in the figure. Results are shown relative to control cells incubated without nanoparticles; asterisks (*) denote significant differences according to the Mann–Whitney test ($p < 0.05$)

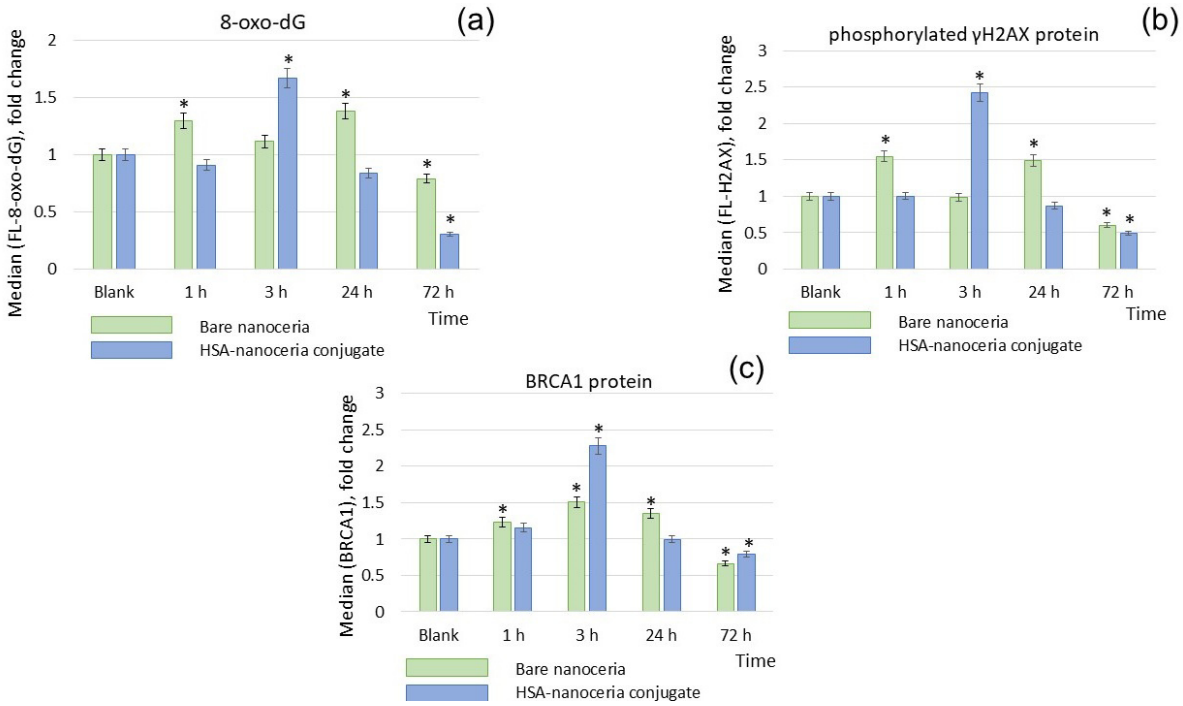

FIG. 8. (a) Levels of the DNA oxidative damage marker 8-oxo-2'-deoxyguanosine (8-oxo-dG), (b) levels of the DNA double-strand break marker phosphorylated histone γH2AX, and (c) expression levels of the DNA repair marker protein BRCA1; cells were incubated with bare and HSA-nanoceria conjugate (1.5 μmol/L) for 1 – 72 hours. Results are presented relative to control cells incubated without nanoparticles; asterisks (*) indicate significant differences according to the Mann–Whitney test ($p < 0.05$)

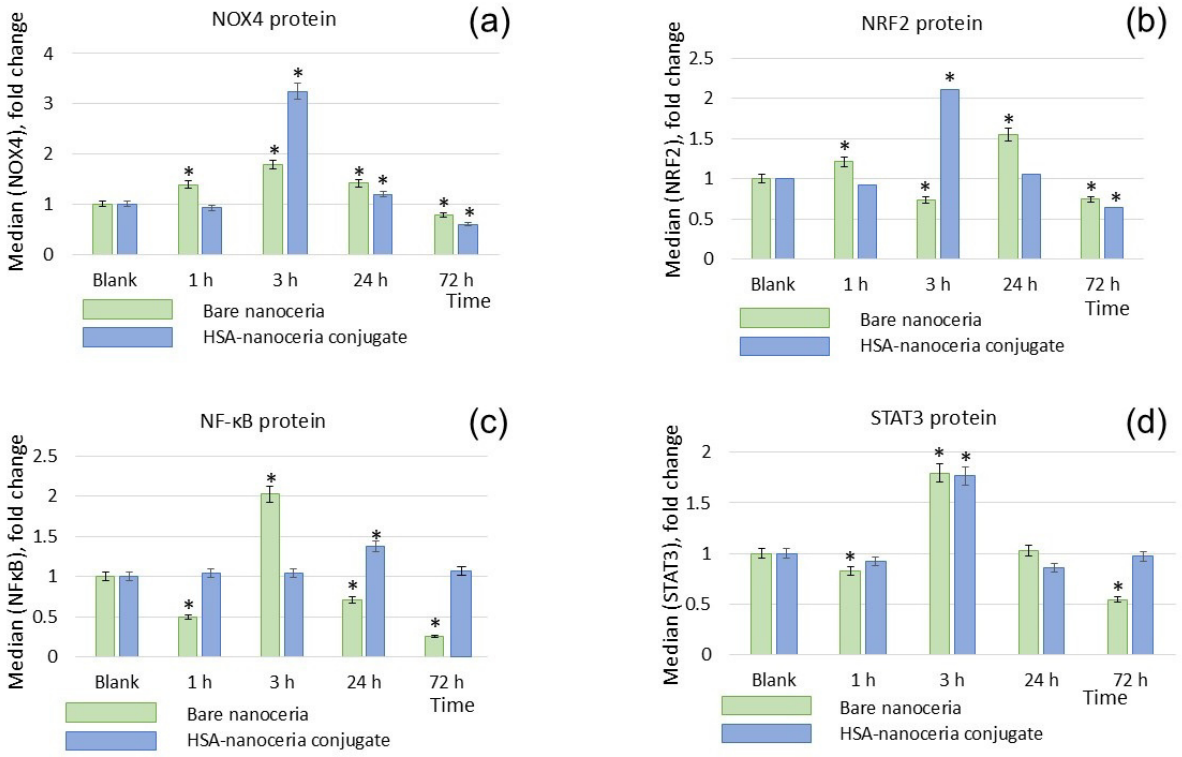

FIG. 9. Protein expression levels of (a) NOX4, (b) NRF2, (c) NF-κB, and (d) STAT3 in cells; data are presented relative to control cells incubated without nanoparticles. Asterisks (*) indicate significant differences according to the Mann–Whitney test ($p < 0.05$)

3.6. Proteins of proliferation and autophagy

Regarding the pro-inflammatory NF-κB pathway, the HSA-nanoceria conjugate activates it to a lesser extent after 24 hours of incubation, unlike the more pronounced effect of bare nanoceria (Fig. 10). For the STAT3 pathway, the activating effect of both nanoparticles is maximal at 3 hours of incubation and is practically the same.

4. Discussion

Nanoceria can be considered a promising nanopharmacological agent due to its regenerative and proliferative effects on normal cells and its cytotoxicity toward cancer cells. Therefore, the development of new pharmacological formulations, particularly those involving surface-modifying agents, is of great importance. The roles of surface modifiers vary depending on their chemical properties. The objectives of modification include stabilizing the colloidal system, facilitating nanoparticle cellular uptake, reducing toxicity, and enhancing the targeted therapeutic efficacy of nanoparticles. Multifunctional nanoparticle synthesis strategies enable the creation of novel therapeutic platforms for targeted cell therapy. In this study, we investigated albumin as a modifier of nanoceria properties and compared the resulting data with those of bare nanoceria.

The main findings for the HSA-nanoceria conjugate in this study are as follows: (1) HSA-nanoceria conjugate, like bare nanoceria, actively penetrates cells during the first three hours, indicating that albumin binding ensures effective cellular internalization within this timeframe; (2) unlike bare nanoceria, HSA-nanoceria conjugate does not alter intracellular ROS balance and has a less pronounced effect on mitochondrial membrane potential; (3) compared to bare nanoceria, HSA-nanoceria conjugate induces a more pronounced activation of NOX4 within 3 hours, resulting in greater genotoxicity (oxidative DNA damage and double-strand breaks); however, it also triggers stronger activation of DNA repair systems, leading to more effective neutralization of NOX4 activity and its effects after 72 hours; (4) no differences were observed between HSA-nanoceria conjugate and bare nanoceria in terms of proliferative properties and activation of the STAT3 cytokine pathway; (5) the HSA-nanoceria conjugate exhibits a pronounced suppressive effect on the proinflammatory NF-κB pathway after 72 hours; (6) the conjugate increases the level of the autophagy marker LC3.

Interestingly, HSA-nanoceria conjugate does not alter intracellular ROS levels, unlike bare nanoceria, which exhibits valuable redox activity properties. However, the HSA-nanoceria conjugate activates NOX4 approximately twice as strongly, leading to enhanced activation of NRF2, increased oxidative DNA damage, and stimulation of repair mechanisms. Albumin conjugation does not affect nanoceria's influence on the STAT3 cytokine pathway or cell proliferation. Regarding the NF-κB pathway, both bare and albumin-bound nanoceria initially activate and subsequently significantly

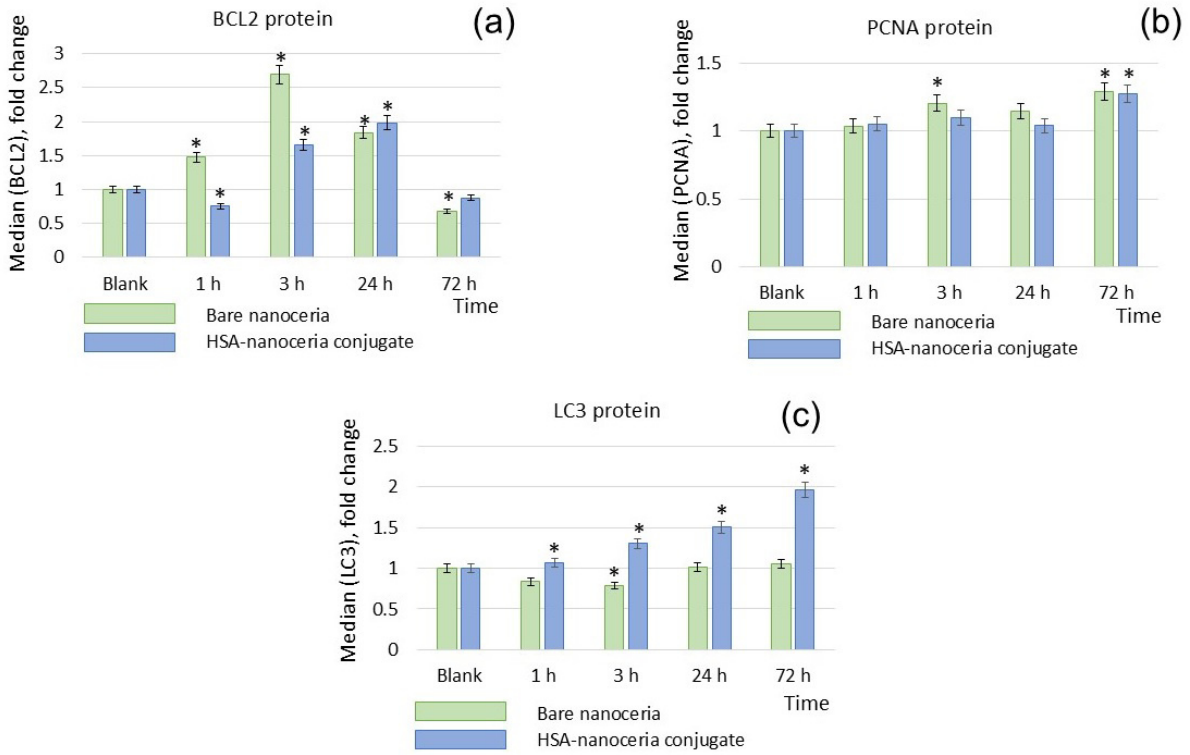

FIG. 10. Expression levels of proliferation proteins (a) PCNA, (b) BCL2, and (c) the autophagy protein LC3; data are presented relative to control cells incubated without nanoparticles; asterisks (*) indicate significant differences according to the Mann–Whitney test ($p < 0.05$)

suppress it. For bare nanoceria, NF-κB activation peaks at 3 hours, whereas for HSA-nanoceria conjugate, the peak occurs at 24 hours. Ultimately, after 72 hours, NF-κB activity decreases threefold with bare nanoceria and nearly to zero with HSA-nanoceria conjugate. Thus, HSA-nanoceria conjugate demonstrates a pronounced anti-inflammatory effect after prolonged incubation.

Studies on the interaction between bovine serum albumin and nanoceria confirm the formation of a BSA-nanoceria complex mediated by electrostatic interactions and accompanied by conformational changes in the protein [45, 49]. Liu *et al.* demonstrated that, for nanoparticles interacting with proteins of comparable size, a heteroaggregate model is more appropriate than the conventional protein corona concept. They showed that in heteroaggregates of nanoceria with BSA, the surface properties of the nanoparticles remain unchanged, while the protein structure undergoes alteration [50]. The unique spatial and redox characteristics of bovine serum albumin have been exploited for the targeted synthesis of cerium dioxide nanoparticles exhibiting effective nanozyme properties [27], highlighting the strong mutual influence between the protein and cerium dioxide nanoparticles. Albumin nanoparticles encapsulating cerium dioxide have been proposed as stable aqueous systems with potent nanozyme activities, and their biocompatibility has been demonstrated in vitro using human lung epithelial cell cultures [26].

Similar findings have been reported for human serum albumin. Butterfield *et al.* conducted proteomic analyses to identify plasma and serum proteins adsorbed onto nanoceria. They concluded that the protein corona can either enhance or inhibit cellular uptake of nanoceria and modulate subsequent biological effects. Moreover, interactions with nanoceria can induce structural and functional changes in proteins, including pro- and anti-inflammatory effects. The authors emphasize the need for a deeper understanding of nanoparticle-protein interactions prior to the therapeutic application of nanoceria [14]. Simon-Vazquez *et al.* demonstrated that HSA interaction with nanoceria leads to conformational changes predominantly involving the conversion of alpha-helices into beta-sheet structures, with these effects being pH-dependent [50]. We have previously confirmed the formation of HSA-nanoceria conjugates, noting that the transport function of HSA remains unaffected [37].

Although the molecular mechanisms of interaction between nanoceria and albumin have been well studied [29,45,49–51], few studies have addressed the biological activity of the albumin-nanoceria complex. Yang *et al.* demonstrated that nanoceria retains superoxide dismutase (SOD)-like properties [27]. Of particular interest is the study by Yeni *et al.*, who investigated the effects of quercetin-albumin-nanoceria triple nanoparticles on glutamate-induced neurotoxicity in an in vitro model [28]. Cytotoxicity was assessed using the MTT assay, along with oxidative stress parameters including lactate dehydrogenase, total oxidative status, total antioxidant capacity, and reduced glutathione. Treatment of glutamate-injured cells with these nanoparticles significantly enhanced cell survival and improved oxidative stress markers.

On the other hand, binding to nanoparticles can alter the properties of albumin [14] since the properties of albumin depend on its structure [10], and binding induces conformational changes. As nanoceria and albumin are antioxidants with different mechanisms of action – nanoceria exhibits nanozyme activity against reactive oxygen species, while albumin is a thiol-based antioxidant – it is important to study their mutual influence on each other's oxidative properties. Previously, we investigated the antioxidant activity of cerium dioxide nanoparticle conjugates [52] and showed that the interaction of CeO_2 nanoparticles with purified human serum albumin results in an approximately 1.5-fold decrease in both the antioxidant and prooxidant potential of albumin. This is presumably caused by the interaction of nanoscale CeO_2 with the sulfhydryl groups of the protein. We also studied the transport function of albumin upon interaction with nanoceria and confirmed the formation of HSA-CeO_2 nanoparticle conjugates. Changes in protein conformation did not affect albumin's drug-binding sites and, accordingly, did not impair HSA's transport function [37]. In the same study, we demonstrated that a 1:1 molar ratio of protein to nanoscale CeO_2 forms a conjugate, whereas at higher protein ratios, a protein corona forms around the nanoparticle.

5. Conclusions

Using an *in vitro* model of human embryonic lung fibroblasts, this study highlights the significant influence of albumin conjugation on the physicochemical behavior of nanoceria over prolonged incubation (72 hours). The albumin coating modulates the surface charge and colloidal stability of nanoceria, which in turn attenuates its impact on intracellular redox processes and mitochondrial membrane potential. The altered nanoparticle-protein interface facilitates enhanced control over reactive oxygen species dynamics, leading to more efficient suppression of pro-inflammatory signaling and oxidative DNA damage. Additionally, the conjugation promotes autophagic responses, reflecting a physicochemically driven modulation of cellular pathways. These findings underscore the importance of nanoparticle surface chemistry and protein interactions in tuning the bioactivity of cerium dioxide, supporting its potential as an anti-inflammatory and regenerative nanomaterial.

References

[1] Korsvik C., Patil S., Seal S. et al. Superoxide dismutase mimetic properties exhibited by vacancy engineered ceria nanoparticles. *Chem. Commun.*, 2007, **10**, P. 1056.

[2] Ivanov V.K., Usatenko A.V., Shcherbakov A.B. Antioxidant activity of nanocrystalline ceria to anthocyanins. *Russ. J. Inorg. Chem.*, 2009, **54**(10), P. 1522–1527.

[3] Pirmohamed T., Dowding J.M., Singh S. et al. Nanoceria exhibit redox state-dependent catalase mimetic activity. *Chem. Commun.*, 2010, **46**(16), P. 2736.

[4] Asati A., Santra S., Kaittanis C. et al. Oxidase-Like Activity of Polymer-Coated Cerium Oxide Nanoparticles. *Angew. Chemie Int. Ed.*, 2009, **48**(13), P. 2308–2312.

[5] Liu B., Huang Z., Liu J. Boosting the oxidase mimicking activity of nanoceria by fluoride capping: rivaling protein enzymes and ultrasensitive F^- detection. *Nanoscale*, 2016, **8**(28), P. 13562–13567.

[6] Yao T., Tian Z., Zhang Y. et al. Phosphatase-like Activity of Porous Nanorods of CeO_2 for the Highly Stabilized Dephosphorylation under Interferences. *ACS Appl. Mater. Interfaces*, 2019, **11**(1), P. 195–201.

[7] Tian Z., Yao T., Qu C. et al. Photolyase-Like Catalytic Behavior of CeO_2. *Nano Lett.*, 2019, **19**(11), P. 8270–8277.

[8] Khulbe K., Karmakar K., Ghosh S. et al. Nanoceria-Based Phospholipase-Mimetic Cell Membrane Disruptive Antibiofilm Agents. *ACS Appl. Bio Mater.*, 2020, **3**(7), P. 4316–4328.

[9] Xu F., Lu Q., Huang P.-J.J. et al. Nanoceria as a DNase I mimicking nanozyme. *Chem. Commun.*, 2019, **55**(88), P. 13215–13218.

[10] Wu N., Liu T., Tian M. et al. Albumin, an interesting and functionally diverse protein, varies from 'native' to 'effective' (Review). *Mol. Med. Rep.*, 2023, **29**(2), P. 24.

[11] Tao C., Chuah Y.J., Xu C. et al. Albumin conjugates and assemblies as versatile bio-functional additives and carriers for biomedical applications. *J. Mater. Chem. B*, 2019, **7**(3), P. 357–367.

[12] Qu N., Song K., Ji Y. et al. Albumin Nanoparticle-Based Drug Delivery Systems. *Int. J. Nanomedicine*, 2024, **19**, P. 6945–6980.

[13] Tincu C.-E., Andriţoiu C.V., Popa M. et al. Recent Advancements and Strategies for Overcoming the Blood–Brain Barrier Using Albumin-Based Drug Delivery Systems to Treat Brain Cancer, with a Focus on Glioblastoma. *Polymers* (Basel), 2023, **15**(19), P. 3969.

[14] Butterfield A.D., Wang B., Wu P. et al. Plasma and Serum Proteins Bound to Nanoceria: Insights into Pathways by which Nanoceria may Exert Its Beneficial and Deleterious Effects In Vivo. *J. Nanomed. Nanotechnol.*, 2020, **11**(4), P. 546.

[15] Fanciullino R., Ciccolini J., Milano G. Challenges, expectations and limits for nanoparticles-based therapeutics in cancer: A focus on nano-albumin-bound drugs. *Crit. Rev. Oncol. Hematol.*, 2013, **88**(3), P. 504–513.

[16] Zhu Y., Xue J., Chen W. et al. Albumin-biomineralized nanoparticles to synergize phototherapy and immunotherapy against melanoma. *J. Control. Release*, 2020, **322**, P. 300–311.

[17] Gou Y., Zhang Z., Qi J. et al. Folate-functionalized human serum albumin carrier for anticancer copper(II) complexes derived from natural plumbagin. *J. Inorg. Biochem.*, 2015, **153**, P. 13–22.

[18] Kim D., Amatya R., Hwang S. et al. BSA-Silver Nanoparticles: A Potential Multimodal Therapeutics for Conventional and Photothermal Treatment of Skin Cancer. *Pharmaceutics*, 2021, **13**(4), P. 575.

[19] Jaiswal V.D., Pangam D.S., Dongre P.M. Biophysical study of cisplatin loaded albumin-gold nanoparticle and its interaction with glycans of gp60 receptor. *Int. J. Biol. Macromol.*, 2023, **231**, P. 123368.

[20] Korolev D., Shumilo M., Shulmeyster G. et al. Hemolytic Activity, Cytotoxicity, and Antimicrobial Effects of Human Albumin- and Polysorbate-80-Coated Silver Nanoparticles. Nanomaterials, 2021, 11(6), P. 1484.

[21] Park H.-Y., Chung C., Eiken M.K. et al. Silver nanoparticle interactions with glycated and non-glycated human serum albumin mediate toxicity. *Front. Toxicol.*, 2023, **5**, P. 1081753.

[22] Chen J.L.-Y., Yang S.-J., Pan C.-K. et al. Cisplatin and Albumin-Based Gold–Cisplatin Nanoparticles Enhance Ablative Radiation Therapy–Induced Antitumor Immunity in Local and Distant Tumor Microenvironment. *Int. J. Radiat. Oncol.*, 2023, **116**(5), P. 1135–1149.
[23] Gou Y., Zhang Y., Qi J. et al. Enhancing the copper(II) complexes cytotoxicity to cancer cells through bound to human serum albumin. *J. Inorg. Biochem.*, 2015, **144**, P. 47–55.
[24] He C., Xie M., Hong F. et al. A Highly Sensitive Glucose Biosensor Based on Gold Nanoparticles/Bovine Serum Albumin/Fe_3O_4 Biocomposite Nanoparticles. *Electrochim. Acta*, 2016, **222**, P. 1709–1715.
[25] Janani B., Raju L.L., Thomas A.M. et al. Impact of bovine serum albumin – A protein corona on toxicity of ZnO NPs in environmental model systems of plant, bacteria, algae and crustaceans. *Chemosphere*, 2021, **270**, P. 128629.
[26] Bhushan B., Gopinath P. Antioxidant nanozyme: a facile synthesis and evaluation of the reactive oxygen species scavenging potential of nanoceria encapsulated albumin nanoparticles. *J. Mater. Chem. B*, 2015, **3**(24), P. 4843–4852.
[27] Yang Z., Luo S., Zeng Y. et al. Albumin-Mediated Biomineralization of Shape-Controllable and Biocompatible Ceria Nanomaterials. *ACS Appl. Mater. Interfaces*, 2017, **9**(8), P. 6839–6848.
[28] Yeni Y., Genc S., Nadaroglu H. et al. Effects of quercetin-immobilized albumin cerium oxide nanoparticles on glutamate toxicity: in vitro study. *Naunyn. Schmiedebergs. Arch. Pharmacol.*, 2025, **398**(5), P. 5147–5156.
[29] Khoshgozaran Roudbaneh S.Z., Kahbasi S., Sohrabi M.J. et al. Albumin binding, antioxidant and antibacterial effects of cerium oxide nanoparticles. *J. Mol. Liq.*, 2019, **296**, P. 111839.
[30] Shcherbakov A.B., Teplonogova M.A., Ivanova O.S. et al. Facile method for fabrication of surfactant-free concentrated CeO_2 sols. *Mater. Res. Express*, 2017, **4**(5), P. 055008.
[31] Creed S., McKenzie M. Measurement of Mitochondrial Membrane Potential with the Fluorescent Dye Tetramethylrhodamine Methyl Ester (TMRM). *Methods Mol. Biol.*, 2019, **1928**, P. 69–76.
[32] Luik A.I., Naboka Y.N., Mogilevich S.E. et al. Study of human serum albumin structure by dynamic light scattering: two types of reactions under different pH and interaction with physiologically active compounds. *Spectrochim. Acta Part A Mol. Biomol. Spectrosc.*, 1998, **54**(10), P. 1503–1507.
[33] Velichko E., Makarov S., Nepomnyashchaya E. et al. Molecular Aggregation in Immune System Activation Studied by Dynamic Light Scattering. *Biology* (Basel), 2020, **9**(6), P. 123.
[34] Bardik V., Gotsulskii V., Pavlov E. et al. Light scattering study of human serum albumin in pre-denaturation: Relation to dynamic transition in water at 42°C. *J. Mol. Liq.*, 2012, **176**, P. 60–64.
[35] Liu Y., Yang Z., Zhang X. et al. Shape/Crystal Facet of Ceria Induced Well-Dispersed and Stable Au Nanoparticles for the Selective Hydrogenation of Phenylacetylene. *Catal. Letters*, 2019, **149**(2), P. 361–372.
[36] Filippova A.D., Sozarukova M.M., Baranchikov A.E. et al. Peroxidase-like Activity of CeO_2 Nanozymes: Particle Size and Chemical Environment Matter. *Molecules*, 2023, **28**(9), P. 3811.
[37] Sozarukova M.M., Kochneva E.M., Proskurnina E.V. et al. Albumin Retains Its Transport Function after Interaction with Cerium Dioxide Nanoparticles. *ACS Biomater. Sci. Eng.*, 2023, **9**(12), P. 6759–6772.
[38] Pustulka S.M., Ling K., Pish S.L. et al. Protein Nanoparticle Charge and Hydrophobicity Govern Protein Corona and Macrophage Uptake. *ACS Appl. Mater. Interfaces*, 2020, **12**(43), P. 48284–48295.
[39] Lundqvist M., Stigler J., Elia G. et al. Nanoparticle size and surface properties determine the protein corona with possible implications for biological impacts. *Proc. Natl. Acad. Sci.*, 2008, **105**(38), P. 14265–14270.
[40] Chaudhary Y.S., Panigrahi S., Nayak S. et al. Facile synthesis of ultra-small monodisperse ceria nanocrystals at room temperature and their catalytic activity under visible light. *J. Mater. Chem.*, 2010, **20**(12), P. 2381.
[41] Barth A. The infrared absorption of amino acid side chains. *Prog. Biophys. Mol. Biol.*, 2000, **74**(3–5), P. 141–173.
[42] Diaconeasa Z., Barbu-Tudoran L., Coman C. et al. Cerium oxide nanoparticles and its cytotoxicity human lung cancer cells. *Rom. Biotechnol. Lett.*, 2015, **20**, P. 10679.
[43] Tang J., Luan F., Chen X. Binding analysis of glycyrrhetinic acid to human serum albumin: Fluorescence spectroscopy, FTIR, and molecular modeling. *Bioorg. Med. Chem.*, 2006, **14**(9), P. 3210–3217.
[44] Usoltsev D., Sitnikova V., Kajava A. et al. Systematic FTIR Spectroscopy Study of the Secondary Structure Changes in Human Serum Albumin under Various Denaturation Conditions. *Biomolecules*, 2019, **9**(8), P. 359.
[45] Umezawa M., Itano R., Sakaguchi N. et al. Infrared spectroscopy analysis determining secondary structure change in albumin by cerium oxide nanoparticles. *Front. Toxicol.*, 2023, **5**, P. 1237819.
[46] Kogelheide F., Kartaschew K., Strack M. et al. FTIR spectroscopy of cysteine as a ready-to-use method for the investigation of plasma-induced chemical modifications of macromolecules. *J. Phys. D. Appl. Phys.*, 2016, **49**(8), P. 084004.
[47] Patel V., Jose L., Philippot G. et al. Fluoride-assisted detection of glutathione by surface Ce^{3+}/Ce^{4+} engineered nanoceria. *J. Mater. Chem. B*, 2022, **10**(47), P. 9855–9868.
[48] Proskurnina E.V., Sozarukova M.M., Ershova E.S. et al. Lipid Coating Modulates Effects of Nanoceria on Oxidative Metabolism in Human Embryonic Lung Fibroblasts: A Case of Cardiolipin. *Biomolecules*, 2025, **15**(1), P. 53.
[49] Yuan D., Shen Z., Liu R. et al. Study on the binding of cerium to bovine serum albumin. *J. Biochem. Mol. Toxicol.*, 2011, **25**(4), P. 263–268.
[50] Simón-Vázquez R., Lozano-Fernández T., Peleteiro-Olmedo M. et al. Conformational changes in human plasma proteins induced by metal oxide nanoparticles. *Colloids Surfaces B Biointerfaces*, 2014, **113**, P. 198–206.
[51] Liu W., Rose J., Plantevin S. et al. Protein corona formation for nanomaterials and proteins of a similar size: hard or soft corona? *Nanoscale*, 2013, **5**(4), P. 1658.
[52] Sozarukova M.M., Proskurnina E.V., Baranchikov A.E. et al. Antioxidant Activity of Conjugates of Cerium Dioxide Nanoparticles with Human Serum Albumin Isolated from Biological Fluids. *Russ. J. Inorg. Chem.*, 2023, **68**(10), P. 1495–1502.

Submitted 8 October 2025; accepted 15 October 2025

Information about the authors:

Elena V. Proskurnina – Kurnakov Institute of General and Inorganic Chemistry of the Russian Academy of Sciences, Moscow 119991, Russia; ORCID 0000-0002-8243-6339; proskurnina@gmail.com

Svetlana V. Kostyuk – Kurnakov Institute of General and Inorganic Chemistry of the Russian Academy of Sciences, Moscow 119991, Russia; Petrovsky Russian Scientific Center of Surgery, Institute of Longevity with a Clinic of Rehabilitation and Preventive Medicine, Moscow 119435, Russia; ORCID 0000-0002-6336-9900; svet-vk@yandex.ru

Madina M. Sozarukova – Kurnakov Institute of General and Inorganic Chemistry of the Russian Academy of Sciences, Moscow 119991, Russia; ORCID 0000-0002-5868-4746; s_madinam@bk.ru

Elizaveta S. Ershova – Kurnakov Institute of General and Inorganic Chemistry of the Russian Academy of Sciences, Moscow 119991, Russia; Petrovsky Russian Scientific Center of Surgery, Institute of Longevity with a Clinic of Rehabilitation and Preventive Medicine, Moscow 119435, Russia; ORCID 0000-0003-1206-5832; es-ershova@rambler.ru

Natalia N. Veiko – Kurnakov Institute of General and Inorganic Chemistry of the Russian Academy of Sciences, Moscow 119991, Russia; Petrovsky Russian Scientific Center of Surgery, Institute of Longevity with a Clinic of Rehabilitation and Preventive Medicine, Moscow 119435, Russia; ORCID 0000-0003-1847-0548; satelit32006@yandex.ru

Matvei A. Popkov – Kurnakov Institute of General and Inorganic Chemistry of the Russian Academy of Sciences, Moscow 119991, Russia; ORCID 0000-0002-9811-6241; ma_popkov@igic.ras.ru

Edmund V. Kostyuk – Kurnakov Institute of General and Inorganic Chemistry of the Russian Academy of Sciences, Moscow 119991, Russia; ORCID 0000-0001-7033-6843; edmundvk@ya.ru

Andrey V. Martynov – Kurnakov Institute of General and Inorganic Chemistry of the Russian Academy of Sciences, Moscow 119991, Russia; ORCID 0000-0002-6697-8306; avlamar@mail.ru

Vladimir K. Ivanov – Kurnakov Institute of General and Inorganic Chemistry of the Russian Academy of Sciences, Moscow 119991, Russia; ORCID 0000-0003-2343-2140; van@igic.ras.ru

Conflict of interest: the authors declare no conflict of interest.

NANOSYSTEMS:
PHYSICS, CHEMISTRY, MATHEMATICS

Popov I.S., et al. *Nanosystems: Phys. Chem. Math.*, 2025, **16** (5), 619–627.
http://nanojournal.ifmo.ru
DOI 10.17586/2220-8054-2025-16-5-619-627

Original article

Bridging accuracy and efficiency: assessing universal ML potentials for niobium-oxygen clusters

Ilya S. Popov[1,a], Albina A. Valeeva[1,b], Andrey N. Enyashin[1,c]

[1]Institute of Solid State Chemistry, Ural Branch of Russian Academy of Sciences, Yekaterinburg, Russia

[a]popov@ihim.uran.ru, [b]anibla_v@mail.ru, [c]enyashin@ihim.uran.ru

Corresponding author: I. S. Popov, popov@ihim.uran.ru

ABSTRACT Machine Learning Interatomic Potentials (MLIPs) promise to combine the accuracy of DFT with the speed of classical force fields. However, their reliability for complex, multi-component systems requires rigorous validation. Here, we perform a targeted evaluation of three leading universal MLIPs using niobium oxide clusters (Nb_nO_m, $n \leq 6$, $m \leq 6$) as a challenging test case. The Nb–O system is very well suited for this task due to its complex electronic interactions, manifested in existence of the bulk phase with 25% vacancy-ordered lattice and, at nanoscale, by a diverse range of non-stoichiometric clusters. We employ a dataset of global minima structures identified via DFT-based evolutionary search as a strict reference. A comparative analysis is then performed by executing evolutionary searches with the MLIPs. By directly comparing predicted structures, energies, and relative stability, we provide a comprehensive assessment of the accuracy and limitations of current universal potentials for modeling complex nanoscale oxides.

KEYWORDS DFT, Machine learning potential, MLIP, Evolutionary algorithm, Niobium oxide, NbO, Nanoparticle, Cluster, USPEX.

ACKNOWLEDGEMENTS This work was supported by the Russian Science Foundation (project 19-73-20012-П, https://rscf.ru/en/project/19-73-20012/) and was performed at the Institute of Solid State Chemistry UB RAS.

FOR CITATION Popov I.S., Valeeva A.A., Enyashin A.N. Bridging accuracy and efficiency: assessing universal ML potentials for niobium-oxygen clusters. *Nanosystems: Phys. Chem. Math.*, 2025, **16** (5), 619–627.

1. Introduction

The rapid development of universal machine learning interatomic potentials (MLIPs) [1–3] has opened new avenues for high-throughput materials screening and the modeling of complex processes. Trained on extensive datasets [4–8] comprising millions of structures, these potentials claim to predict energies and forces for a wide range of chemical systems with accuracy close to that of the density functional theory (DFT) calculations, but at a fraction of the computational cost. Despite the emergence of general metrics and rankings (such as Matbench Discovery [9]), the reliability of these potentials for specific, particularly complex multi-component systems, remains questionable and requires rigorous validation against well-characterized reference data.

In this work, we perform a targeted evaluation of three top-ranked universal MLIPs according to the Matbench Discovery ranking (Summer 2025), using niobium oxide clusters (Nb_nO_m) as a reference test system. The choice of this system is motivated by a number of unique factors. Niobium monoxide (NbO) possesses a non-trivial crystal lattice (space group Pm-3m), which is derived from the B1 (NaCl) structure type with 25% ordered vacancies in both sublattices [10–13]. The stability of this vacancy-ordered crystal structure is due to complex electronic interactions involving the formation of Nb–Nb bonds via delocalized d-electrons [13, 14]. At nanoscale, the phase equilibria of the Nb–O system become even more complex: in processes such as magnetron sputtering, numerous clusters of diverse stoichiometric composition (NbO, NbO_2, Nb_2O_5, Nb_3O_7, and others) are observed [15–17], whose precise molecular structures have long remained an unresolved problem. Thus, the Nb–O system serves as an excellent testing ground for MLIPs, as it combines complex chemical bonding, a wide range of stoichiometries and sizes, as well as the presence of surfaces.

For this validation, we employ a previously curated reference dataset [18], generated via an exhaustive search for the global energy minima of Nb_nO_m clusters ($n \leq 6$, $m \leq 6$) using the USPEX evolutionary algorithm in combination with DFT calculations. The first part of the paper briefly summarizes the results of the creation and characterization of this reference dataset. In the second part, we conduct a large-scale comparative study by performing an evolutionary structural search for the same set of clusters using the three selected universal MLIPs. Through a direct comparison of the structures, energies, and predicted relative stability obtained by the DFT+USPEX and MLIPs+USPEX methods, we provide a comprehensive assessment of the accuracy, reliability, and limits of applicability of modern universal potentials for predicting the properties of complex nanoscale oxides.

2. Models and methods

The evolutionary search for the thermodynamically most stable Nb_nO_m clusters of a given composition was performed using the USPEX package [19, 20]. USPEX has been successfully applied previously to determine the structures of Si_n [21], Si_nO_m [20], $(TiO_n)_n$ [22], Ce_nO_m [23], Fe_nO_m [23], B_nP_n [24], Pd_nBi_m [25], Al_6CM_n (M = Li, Na, K; n = 2, 4, 6) [26], as well as Mg_n clusters using other evolutionary algorithms [27], among others. The criterion for "natural selection" in USPEX was the lowest value of the total energy of the crystal/molecular structure. Although evolutionary algorithms are effective in locating global and local minima on the potential energy surface, they require significant computational resources. The set of investigated clusters included Nb_nO_m compositions with $1 \leq n \leq 6$ and $0 \leq m \leq 6$. The population size per generation was 20 clusters (plus the most stable configurations from previous generations). The algorithm was terminated after 9 consecutive generations failed to yield a more stable structure. The initial population was generated by randomly selecting point groups and creating structures based on them. Subsequent generations were created based on the following ratio of variation operators: 50% heredity, 20% generation of random structures based on space groups, and 30% mutation. The contribution of variation operators was subsequently automatically adjusted by the program during the calculations to improve the performance of the evolutionary algorithm.

To create the reference set of structures, geometry optimization and total energy calculations for the Nb_nO_m clusters generated by USPEX were performed using the Density Functional Theory (DFT) method, as implemented in the VASP package [28]. Spin-polarized calculations for the clusters were conducted using the Gamma-point approximation, with a vacuum region of at least 12 Å separating the clusters. The exchange-correlation potential was described within the Generalized Gradient Approximation (GGA) using the Perdew-Burke-Ernzerhof (PBE) parameterization. The plane-wave basis set cutoff energy was set to 450 eV. The convergence criteria for the electronic self-consistent cycle and the ionic relaxation cycle were set to 10^{-5} eV and 10^{-4} eV, respectively.

An analogous procedure for searching for the most stable Nb_nO_m clusters was conducted using a combination of USPEX and MLIPs. The initial plan was to use three potentials leading the Matbench Discovery ranking as of summer 2025: eSEN-30M-OAM [29], ORB v3 [30], and SevenNet [31]. However, because the developers of the eSEN-30M-OAM potential denied access to this model, adhering to discriminatory restrictions against citizens of Russia, Belarus, and China, we used another potential from the same developers – UMA [32]. Two UMA potential variants uma-m-1.1 and uma-s-1.1 were used, differing in model size, performance, and forecast accuracy. From here on, the larger and smaller models will be referred to as UMA(m) and UMA(s), respectively. Both potentials were applied with the parameter task_name = "omat". In the case of the ORB v3 potential, the orb_v3_conservative_inf_omat model was used as the most accurate one within this family. For the SevenNet potential, the 7net-mf-ompa model was employed with the parameter modal = "omat24".

The Atomic Simulation Environment (ASE) library [33] was used as an interface for the selected MLIPs to perform geometry optimization of the Nb_nO_m clusters generated by the USPEX program. Since USPEX does not natively support the ASE library, two primary solutions were possible. The first involved writing a custom interface between USPEX and ASE. In this work, an alternative approach was implemented. Within the USPEX calculation parameters, the LAMMPS program [34] was specified for geometry optimization and energy evaluation. The command to launch LAMMPS was set to execute a custom Python script. This script performed the following steps: it converted the LAMMPS input files generated by USPEX into ASE-compatible formats, executed the ASE calculation, and subsequently converted the ASE output files back into the format of LAMMPS output files.

Atomic structure visualization of the clusters was performed using the OVITO program [35]. All graphs were generated using the matplotlib library [36].

3. Results and discussion

3.1. NbO nanoparticles generated by the USPEX and DFT

The search for stable Nb_nO_m clusters that could be based on coordination polyhedra different from those found in crystalline Nb_3O_3 and Nb_4O_4 polymorphs was conducted using the USPEX program. The evolutionary algorithm was run once for each chemical composition with given n and m indices, without repeated runs, due to the high computational costs and the long execution time of each calculation.

To illustrate the operation of the evolutionary algorithm, let us consider the study of Nb_6O_6 clusters as an example. Fig. 1 shows the total energies of all optimized Nb_6O_6 clusters generated by the USPEX algorithm, excluding clusters with very high total energy values. Horizontal lines separate configurations belonging to 13 sequentially generated populations, arranged from bottom to top. The configuration with the lowest total energy in a given generation is highlighted with a yellow circle. Configurations resulting from the action of heredity, random structure generation, and mutation variation operators, as well as the best configurations from previous generations, are denoted by red, green, blue, and gray dots, respectively. In the first generation, configuration number 13, characterized by an octahedral Nb atom framework, was the most stable. In the second and third generations, more stable configurations were identified, including Nb frameworks in the shape of a triangular prism or two tetrahedra sharing a common edge. Other even more stable clusters were not found in the fourth generation. The most stable configuration, number 93, was discovered in the fifth generation, after

which no new, more stable configurations were found. A total of 298 Nb_6O_6 configurations were investigated before the evolution stopping criteria were met. A configuration based on random generation proved to be the most stable only in the first generation, where other variation operators are not applied. Further reduction of the cluster's total energy was achieved by applying heredity and mutation operators to configurations obtained earlier. Nevertheless, random generation was continued to explore the configuration space and introduce greater diversity into the Nb_nO_m populations.

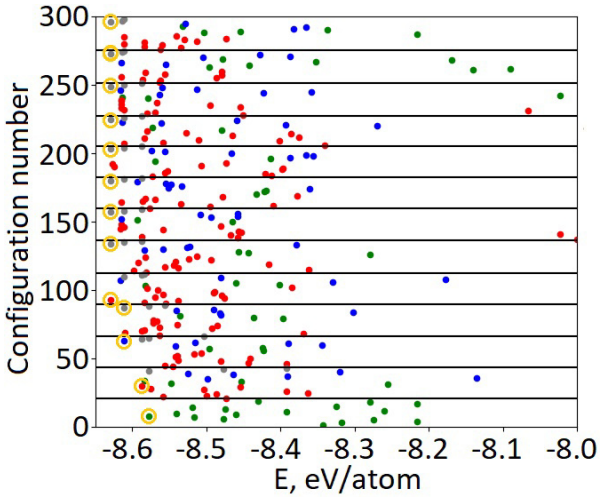

FIG. 1. Total energies of Nb_6O_6 clusters obtained during the USPEX evolutionary algorithm based on DFT calculations

The configurations of the most stable Nb_nO_m clusters for each of the investigated compositions are shown in Fig. 2. All clusters are characterized by dense atomic packing and minimal surface area. Clusters with an equal number of Nb atoms can be described by one or two types of Nb frameworks, to which O atoms are sequentially attached. For example, clusters with two Nb atoms form a dimer surrounded by oxygen atoms. Clusters with three Nb atoms tend to form a triangle of Nb atoms. Four Nb atoms in a cluster lead to the formation of a tetrahedral framework. For clusters with five Nb atoms, the frameworks were either a triangular bipyramid or a distorted square pyramid, depending on the number and position of the O atoms. Nb_6O_m clusters are characterized by an Nb atom framework forming either an octahedron or two tetrahedra sharing a common edge. The most favorable positions for O atoms in most clusters are located above the centers of Nb-Nb edges. A significant excess of oxygen leads to the formation of –O–O– bridges within the clusters, which possess a high excess energy. Nevertheless, such "peroxide-containing" clusters were still found to be more stable than the corresponding oxide clusters with the same number of atoms and individual O_2 molecules. In general, clusters in the studied size range tend to form symmetric or regular geometric configurations. It is likely that further growth in cluster size will lead to a reduction in cluster symmetry and the formation of more amorphous structures, as has been observed in other binary systems [22, 24].

A comparative study of the relative stability of clusters of different compositions was carried out using two descriptors [20]: the disproportionation energy (E_{disp}) of two identical clusters with the transfer of one Nb or O atom from one cluster to another, and the dissociation energy (E_{diss}) of a cluster into two fragments. Higher values of E_{disp} and E_{diss} indicate greater stability of the cluster and a lower tendency for decomposition or disproportionation. The results of the E_{disp} and E_{diss} calculations are shown in Fig. 3. Although the constructed E_{disp} and E_{diss} energy landscapes differ, the positions of the most of their main maxima coincide. According to our results, the most stable clusters have the compositions NbO, NbO_2, Nb_2O_5, Nb_2O_6, and Nb_4O_6. The existence of NbO, NbO_2, Nb_2O_5, and Nb_2O_6 clusters has been previously registered experimentally, along with heavier clusters such as Nb_3O_7, Nb_4O_9, and Nb_5O_{12} [15, 16], which are beyond the scope of our study.

$$E_{disp}(\mathrm{Nb}) = E(\mathrm{Nb}_{n+1}\mathrm{O}_m) + E(\mathrm{Nb}_{n-1}\mathrm{O}_m) - 2E(\mathrm{Nb}_n\mathrm{O}_m) \quad (1)$$

$$E_{disp}(\mathrm{O}) = E(\mathrm{Nb}_n\mathrm{O}_{m+1}) + E(\mathrm{Nb}_n\mathrm{O}_{m-1}) - 2E(\mathrm{Nb}_n\mathrm{O}_m) \quad (2)$$

$$E_{disp} = \min(E_{disp}(Nb),\ E_{disp}(\mathrm{O})) \quad (3)$$

$$E_{diss} = \min(E(\mathrm{Nb}_{n-x}\mathrm{O}_{m-y}) + E(\mathrm{Nb}_x\mathrm{O}_y) - E(\mathrm{Nb}_n\mathrm{O}_m)) \quad (4)$$

An estimate of the probability of detecting different configurations of particles of the same composition was made using the Boltzmann distribution as a thumb approximation. The corresponding distributions for the compositions Nb_2O_5, Nb_2O_6, and Nb_4O_6 are shown in Fig. 4. The graphs for Nb_2O_5 and Nb_2O_6 compositions at temperatures 1500–3000 K

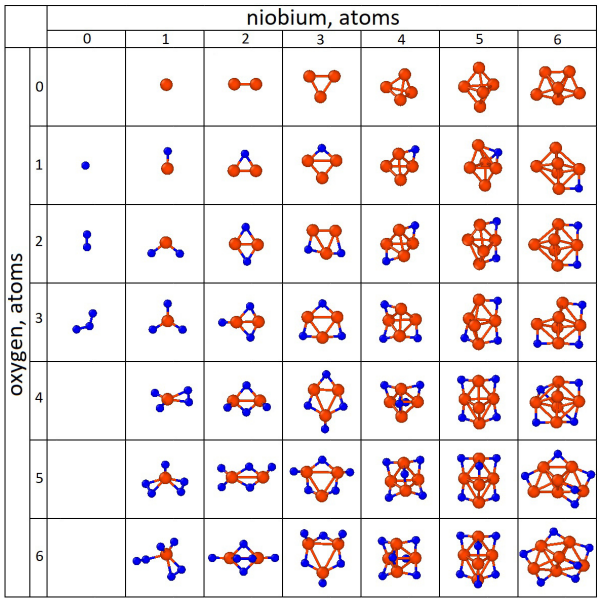

FIG. 2. Structure of the most stable Nb_nO_m clusters as a function of n and m indices, identified using the USPEX evolutionary algorithm coupled with DFT calculations. Nb and O atoms are represented by large orange and small blue spheres, respectively

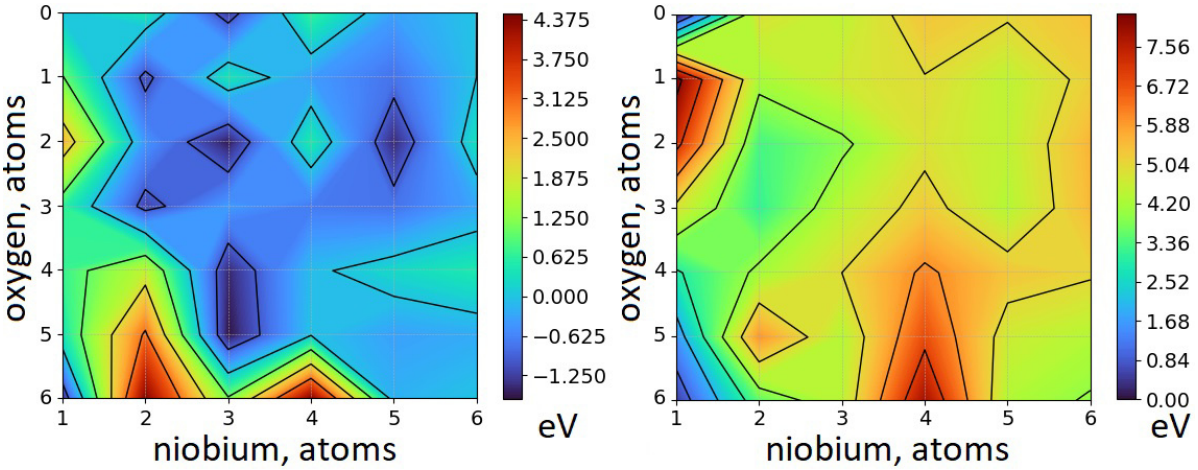

FIG. 3. Comparative analysis of the thermodynamic stability of Nb_nO_m clusters using the disproportionation energy, E_{disp} (left), and the dissociation energy, E_{diss} (right). Higher positive values indicate greater cluster stability. DFT calculations

demonstrate the coexistence of several cluster configurations, with the most stable configuration being predominant. It is quite probable that under the conditions of a high-temperature synthesis, several isomers of these clusters will coexist in the medium. The opposite picture is observed for the Nb_4O_6 composition. Due to the significant energy gap between the most stable cluster and the others, the most stable configuration, which possesses high symmetry, will dominate over the entire temperature range, while other isomers are expected only in trace amounts.

3.2. NbO nanoparticles generated by the USPEX and MLIPs

MLIPs were used in conjunction with evolutionary algorithms to search for the most stable structures of Nb_nO_m clusters, mirroring the approach previously taken with the DFT + evolutionary algorithms combination. The settings for the evolutionary algorithms remained unchanged. For the UMA(m) and SevenNet potentials, a single search without repeats was performed for each composition. For the UMA(s) and ORB potentials, the evolutionary algorithm was run three times to verify the reaching of the global minimum and to assess reproducibility. The structures of the clusters found during the global optimization process with ORB v3 and UMA(m) are shown in Figures S1–S2.

The results of comparing the most stable structures predicted by the MLIPs with those found by DFT are presented in Fig. 5. In the case of the UMA(m) potential, 25 out of 39 most stable Nb_nO_m structures with a total number of atoms between 3 and 12 match the DFT results. However, this potential is the most resource-consuming and computationally

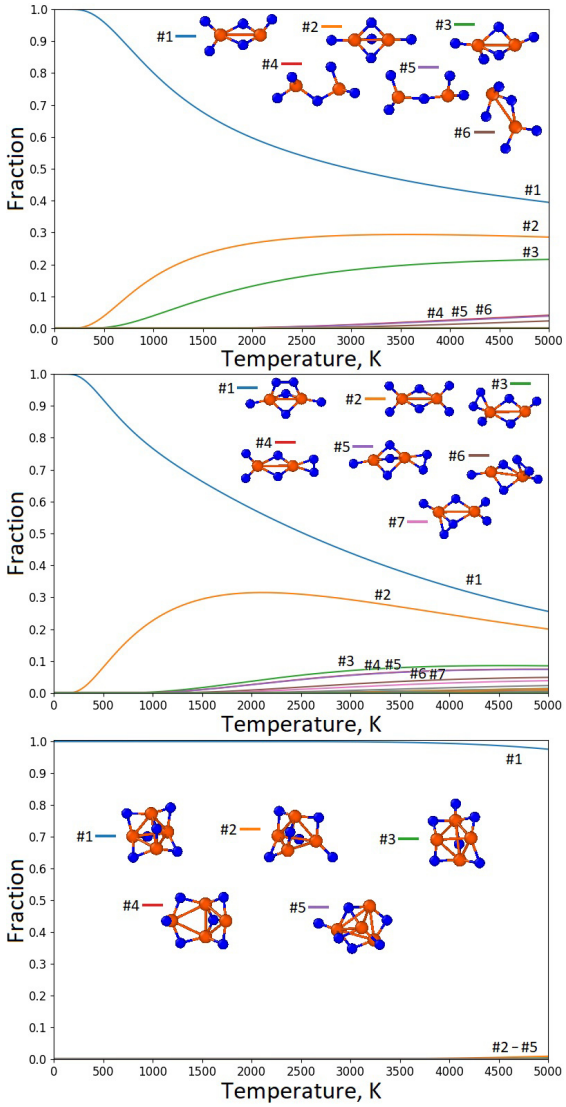

FIG. 4. Estimated probability of detecting different isomeric clusters using the Boltzmann distribution for: Nb_2O_5 (top), Nb_2O_6 (center), and Nb_4O_6 (bottom)

"heavy" compared to the others. The UMA(s) potential demonstrates the lower resource demands and the higher calculation speeds but shows a notable deterioration in results: 16, 14, and 14 out of 39 structures found in each independent run match the DFT results. When selecting the single most stable configuration from each set of three replicates, 14 out of 39 structures remain correctly identified. The structures correctly predicted by UMA(s) are, for the most part, also correctly predicted by UMA(m). The only exception is the Nb_5O_4 composition, where UMA(m) fails to find the most stable configuration according to DFT calculations.

The ORB potential correctly identifies the most stable configurations for 25, 22, and 19 structures in the first, second, and third independent runs, respectively. Combining the results from all independent runs and retaining only one most stable structure per composition yields 22 out of 39 correct structures. However, if the most stable clusters from all three replicates are considered together, they contain 28 out of 39 correctly identified configurations. The SevenNet potential correctly identifies the most stable configurations for 19 out of 39 Nb_nO_m compositions. This value is lower than that of the ORB potential, and almost all compositions correctly predicted by SevenNet are also correctly predicted by ORB.

Consequently, the best results can be achieved by using the UMA(m) and ORB potentials jointly. Their combined predictions allow for the correct identification of 29 out of 39 compositions. This value can be further increased by considering not only the most stable configurations but also several energy-rich configurations. Notably, incorporating the most stable configuration from three independent USPEX+ORB runs already elevates this count to 32 out of 39.

The most stable structures identified via DFT+USPEX were re-optimized using MLIPs. During structural relaxation with MLIP potentials, structural rearrangements were observed in the following cases: ORB v3 – the Nb_6 cluster adopts an octahedral shape; SevenNet – the same process occurs for Nb_6, along with structural changes in NbO_6; UMA(m) – modification of the NbO_6 cluster; UMA(s) – opening of the Nb_2O_2 cycle and deformation of the Nb_5 bipyramid into

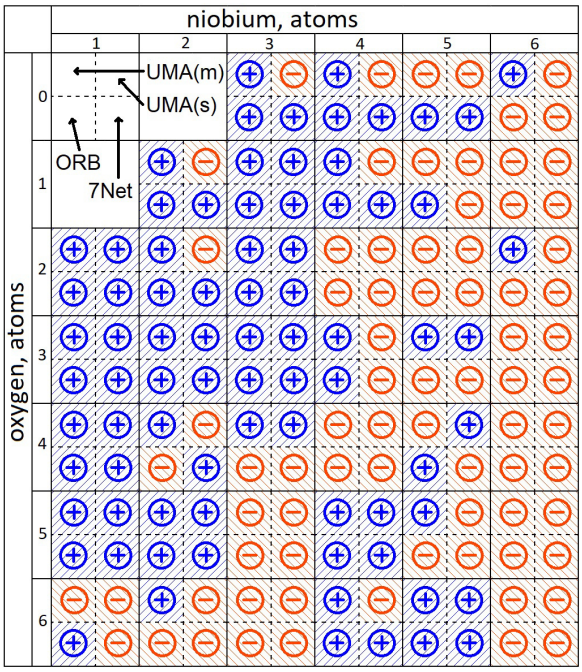

FIG. 5. Comparison of the most stable cluster configurations found using MLIPs and USPEX with the corresponding results from DFT and USPEX. A "+" sign indicates structural agreement, while a "-" sign indicates a discrepancy

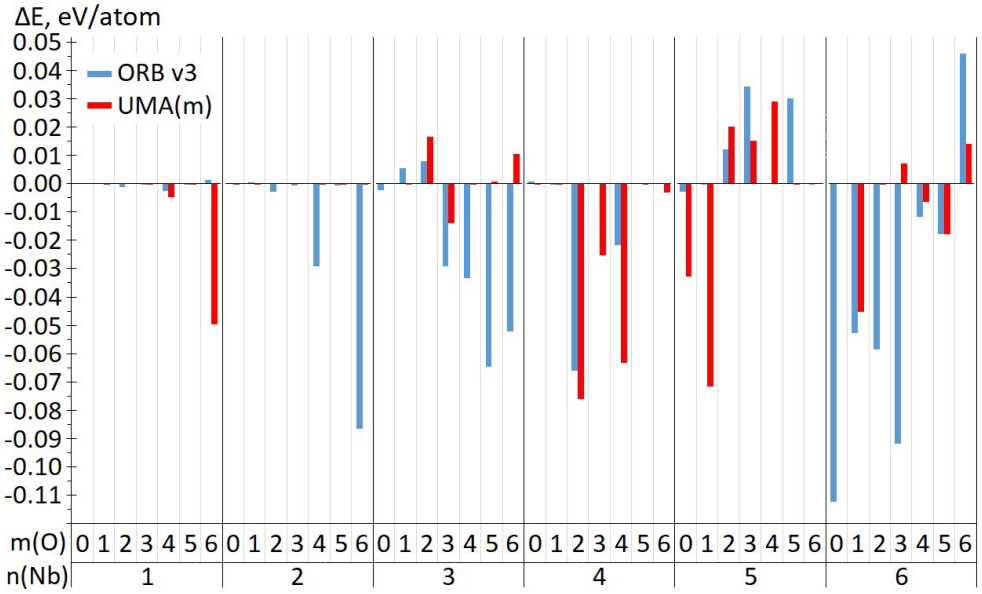

FIG. 6. Energy difference between the most stable clusters found by USPEX+MLIPs and USPEX+DFT. The global minimum structures found via the USPEX+DFT approach were re-optimized and their energies were recalculated using the MLIPs (ORB v3 and UMA(m) models)

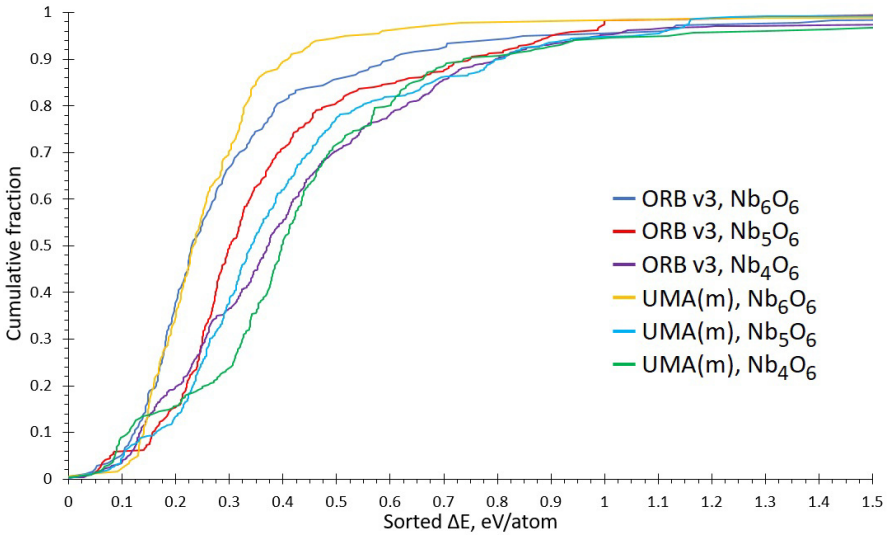

FIG. 7. Cumulative fraction of configurations in the evolutionary search that differ in total energy by no more than ΔE from the most stable configuration found

a planar configuration. In these cases, the total energy was taken from single-point calculations without relaxation. In all other instances, only minor changes in bond lengths and angles were observed. The re-optimization with MLIPs was performed to evaluate where the global minimum of the potential energy surface found via DFT is located on the MLIP potential energy surface and how significantly it differs from the MLIP global minima. The total energy differences are presented in Fig. 6 for ORB v3 and UMA(m), and in Figures S3–S4 for SevenNet and UMA(s). When the ΔE value in Fig. 6 is positive, a more stable structure is identified on the MLIP potential energy surface than that found in the USPEX+MLIP evolutionary search. A negative value indicates that such a configuration could have been discovered during the USPEX+MLIP evolutionary search. For ORB v3 and UMA(m) potentials, the vast majority of ΔE values do not exceed 0.1 eV/atom. In the case of SevenNet and UMA(s) potentials, the deviations can be more substantial, indicating their lower accuracy.

Subsequently, an approximate estimation was performed for the fraction of configurations that lag in total energy by a certain value ΔE from the most stable configuration. For this purpose, USPEX+ORB and USPEX+UMA(m) calculations for Nb_6O_6, Nb_5O_6, and Nb_4O_6 compositions were arbitrarily selected. During the analysis, the "keep best" configurations repeated every generation were removed from the sampling, but other possible duplicates were not eliminated. The results are presented in Fig. 7. The obtained data indicate that the number of configurations with ΔE less than 0.1 eV ranges between 5–10% of all configurations considered during the search. To accelerate the global minimum search for a given composition, one can perform such a search using USPEX+MLIPs, followed by DFT geometric re-relaxation for the top 5-10% most stable configurations. However, even within this computational scheme, a significant time saving would be achieved compared to pure DFT calculations for global minimum searches via evolutionary algorithms. Such a combined approach – rapid screening of a large number of configurations using MLIPs followed by the selection of a small number of the most stable candidates for re-evaluation with a more accurate DFT method – holds significant promise for discovering new material phases with desired properties by substantially reducing research time.

4. Conclusion

Using the USPEX evolutionary algorithm in combination with DFT calculations, we have identified the thermodynamically most stable structures of Nb_nO_m clusters ($1 \leq n \leq 6$, $0 \leq m \leq 6$). It was found that clusters with the same number of Nb atoms can be described by one or two types of Nb frameworks, to which O atoms are sequentially attached. The most stable compositions across the studied range were identified as NbO, NbO_2, Nb_2O_5, Nb_2O_6, and Nb_4O_6.

Furthermore, a comprehensive assessment of four universal machine learning interatomic potentials (MLIPs) – UMA(m), UMA(s), ORB and SevenNet – was performed. The results indicate varying levels of accuracy and computational cost. The UMA(m) potential demonstrated the highest accuracy, correctly predicting 25 out of 39 stable structures, albeit with the highest computational cost. The ORB potential showed strong performance and accuracy close to the UMA(m) potential. A synergistic approach, using the combined predictions of the UMA(m) and ORB potentials, allowed for the correct identification of 32 out of 39 compositions.

This study confirms that while even the best universal MLIPs may not yet be perfectly reliable for standalone global minimum search in complex systems like Nb–O clusters, they are highly valuable in a hybrid computational scheme. The most promising strategy involves the rapid preliminary screening of a vast configurational space using MLIPs, followed

by targeted re-evaluation of a limited number of low-energy candidates with high-precision DFT. This approach should significantly accelerate the discovery of new molecular species and crystal phases.

References

[1] Wan K., He J., Shi X. Construction of High Accuracy Machine Learning Interatomic Potential for Surface/Interface of Nanomaterials – A Review. *Adv. Mater.*, 2024, **36**(22), P. 2305758.

[2] Wang G., Wang C., Zhang X., Li Z., Zhou J., Sun Z. Machine learning interatomic potential: Bridge the gap between small-scale models and realistic device-scale simulations. *iScience*, 2024, **27**(5), P. 109673.

[3] Mortazavi B., Zhuang X., Rabczuk T., Shapeev A.V. Atomistic modeling of the mechanical properties: the rise of machine learning interatomic potentials. *Mater. Horiz.*, 2023, **10**, P. 1956–1968.

[4] Barroso-Luque L., Shuaibi M., Fu X., Wood B.M., Dzamba M., Gao M., Rizvi A., Zitnick C.L., Ulissi Z.W. Open Materials 2024 (OMat24) Inorganic Materials Dataset and Models. *arXiv*, 2024, **[cond-mat.mtrl-sci]**, arXiv:2410.12771.

[5] Ramlaoui A., Siron M., Djafar I., Musielewicz J., Rossello A., Schmidt V., Duval A. LeMat-Traj: A Scalable and Unified Dataset of Materials Trajectories for Atomistic Modeling. *arXiv*, 2025, **[cs.LG]**, arXiv:2508.20875.

[6] Jain A., Ong S.P., Hautier G., Chen W., Richards W.D., Dacek S., Cholia S., Gunter D., Skinner D., Ceder G., Persson K.A. Commentary: The Materials Project: A materials genome approach to accelerating materials innovation. *APL Materials*, 2013, **1**, P. 011002.

[7] Schmidt J., Cerqueira T.F.T., Romero A.H., Loew A., Jäger F., Wang H.-C., Botti S., Marques M.A.L. Improving machine-learning models in materials science through large datasets. *Materials Today Physics*, 2024, **48**, P. 101560.

[8] Saal J.E., Kirklin S., Aykol M., Meredig B., Wolverton C. Materials Design and Discovery with High-Throughput Density Functional Theory: The Open Quantum Materials Database (OQMD). *Jom.*, 2013, **65**(11), P. 1501–1509.

[9] Riebesell J., Goodall R.E.A., Benner P., Chiang Y., Deng B., Ceder G., Asta M., Lee A.A., Jain A., Persson K.A. A framework to evaluate machine learning crystal stability predictions. *Nat. Mach. Intell.*, 2025, **7**, P. 836–847.

[10] Okatz A.M., Keesom P.H. Specific heat and magnetization of the superconducting monoxides: NbO and TiO. *Phys. Rev. B*, 1975, **12**, P. 4917.

[11] Bowman A.L., Wallace T.C., Yarnell J.L., Wenzel R.G. The crystal structure of niobium monoxide. *Acta Crystallogr.*, 1966, **21**, P. 843.

[12] Kurmaev E.Z., Moewes A., Bureev O.G., Nekrasov I.A., Cherkashenko V.M., Korotin M.A., Ederer D.L. Electronic structure of niobium oxides. *J. Alloys Compd.*, 2002, **347**, P. 213–218.

[13] Hu Z., Qian G., Li S., Yang L., Chen X., Weng M., Tan W., Pan F. Discovery of space aromaticity in transition–metal monoxide crystal Nb_3O_3 enabled by octahedral Nb_6 structural units. *Sci. Bull.*, 2019, **65**, P. 367–372.

[14] Miura A., Takei T., Kumada N., Wada S., Magome E., Moriyoshi C., Kuroiwa Y. Bonding Preference of Carbon, Nitrogen, and Oxygen in Niobium-Based Rock-Salt Structures. *Inorg. Chem.*, 2013, **52**, P. 9699.

[15] Music D., Schmidt P., Mráz S. Adsorption of film-forming species on NbO and NbO_2 surfaces. *J. Vac. Sci. Technol. A.*, 2017, **35**, P. 061512.

[16] Fielicke A., Meijer G., Helden G. Infrared Spectroscopy of Niobium Oxide Cluster Cations in a Molecular Beam: Identifying the Cluster Structures. *J. Am. Chem. Soc.*, 2003, **125**, P. 3659–3667.

[17] Deng H.T., Kerns K.P., Castleman A.W. Formation, Structures, and Reactivities of Niobium Oxide Cluster Ions. *J. Phys. Chem.*, 1996, **100**, P. 13386–13392.

[18] Popov I.S., Valeeva A.A., Enyashin A.N. Identifying stable Nb–O clusters using evolutionary algorithm and DFT: A foundation for machine learning potentials. *Chem. Phys.*, 2025, **590**, P. 112533.

[19] Lyakhov A.O., Oganov A.R., Stokes H., Zhu Q. New developments in evolutionary structure prediction algorithm USPEX. *Comp. Phys. Comm.*, 2013, **184**, P. 1172–1182.

[20] Lepeshkin S.V., Baturin V.S., Uspenskii Y.A., Oganov A.R. Method for simultaneous prediction of atomic structure of nanoclusters in a wide area of compositions. *J. Phys. Chem. Lett.*, 2019, **10**, P. 102–106.

[21] Heydariyan S., Nouri M.R., Alaei M., Allahyari Z., Niehaus T.A. New candidates for the global minimum of medium-sized silicon clusters: A hybrid DFTB/DFT genetic algorithm applied to Si_n, n = 8–80. *J. Chem. Phys.*, 2018, **149**, P. 074313.

[22] Olvera-Neria O., García-Cruz R., Gonzalez-Torres J., García-Cruz L.M., Castillo-Sánchez J.L., Poulain E. Strongly Bound Frenkel Excitons on TiO_2 Nanoparticles: An Evolutionary and DFT Approach. *Int. J. Photoenergy*, 2024, **2024**, P. 4014216.

[23] Yu X., Oganov A.R., Zhu Q., Qi F., Qian G. The stability and unexpected chemistry of oxide clusters. *Phys. Chem. Chem. Phys.*, 2018, **20**, P. 30437.

[24] Mahdavifar Z. Prediction of unexpected B_nP_n structures: promising materials for non-linear optical devices and photocatalytic activities. *Nanoscale Adv.*, 2021, **3**, P. 2846.

[25] Sandu M.P., Kovtunov M.A., Baturin V.S., Oganov A.R., Kurzina I.A. Influence of the Pd:Bi ratio on Pd–Bi/Al_2O_3 catalysts: structure, surface and activity in glucose oxidation. *Phys. Chem. Chem. Phys.*, 2021, **23**, P. 14889.

[26] Zhou T., Ma L., Chen H. Electronic structure and stability of Al_6CM_n (M = Li, Na, K; n = 2, 4, 6) clusters. *Comput. Theor. Chem.*, 2020, **1178**, P. 112780.

[27] Steshin I.S., Panteleev S.V., Petukhov I.V., Ignatov S.K. Parametrization of Gaussian approximation potential for the global optimization of magnesium clusters Mg_N ($N \leq 100$). *Phys. Chem. Chem. Phys.*, 2025, **27**, P. 18960–18977.

[28] Kresse G., Furthmüller J. Efficient iterative schemes for ab initio total-energy calculations using a plane-wave basis set. *Phys. Rev. B*, 1996, **54**, P. 11169.

[29] Fu X., Wood B.M., Barroso-Luque L., Levine D.S., Gao M., Dzamba M., Zitnick C.L. Learning Smooth and Expressive Interatomic Potentials for Physical Property Prediction. *arXiv*, 2025, **[physics.comp-ph]**, arXiv:2502.12147.

[30] Rhodes B., Vandenhaute S., Šimkus V., Gin J., Godwin J., Duignan T., Neumann M. Orb-v3: atomistic simulation at scale. *arXiv*, 2025, **[cond-mat.mtrl-sci],** arXiv:2504.06231.

[31] Kim J., Kim J., Kim J., Lee J., Park Y., Kang Y., Han S. Data-efficient multi-fidelity training for high-fidelity machine learning interatomic potentials. *arXiv*, 2025, **[cond-mat.mtrl-sci]**, arXiv:2504.06231.

[32] Wood B.M., Dzamba M., Fu X., Gao M., Shuaibi M., Barroso-Luque L., Abdelmaqsoud K., Gharakhanyan V., Kitchin J.R., Levine D.S., Michel K., Sriram A., Cohen T., Das A., Rizvi A., Sahoo S.J., Ulissi Z.W., Zitnick C.L. UMA: A Family of Universal Models for Atoms. *arXiv*, 2025, **[cs.LG]**, arXiv:2506.23971.

[33] Larsen A.H., Mortensen J.J., Blomqvist J., Castelli I.E., Christensen R., Dułak M., Friis J., Groves M.N., Hammer B., Hargus C., Hermes E.D., Jennings P.C., Jensen P.B., Kermode J., Kitchin J.R., Kolsbjerg E.L., Kubal J., Kaasbjerg K., Lysgaard S., Maronsson J.B., Maxson T., Olsen T., Pastewka L., Peterson A., Rostgaard C., Schiøtz J., Schütt O., Strange M., Thygesen K.S., Vegge T., Vilhelmsen L., Walter M., Zeng Z., Jacobsen K.W. The atomic simulation environment – a Python library for working with atoms. *J. Phys.: Condens. Matter*, 2017, **29**, P. 273002.

[34] Thompson A.P., Aktulga H.M., Berger R., Bolintineanu D.S., Brown W.M., Crozier P.S., Veld P.J., Kohlmeyer A., Moore S.G., Nguyen T.D., Shan R., Stevens M.J., Tranchida J., Trott C., Plimpton S.J. LAMMPS – a flexible simulation tool for particle-based materials modeling at the atomic, meso, and continuum scales. *Comp. Phys. Comm.*, 2022, **271**, P. 10817.

[35] Stukowski A. Visualization and analysis of atomistic simulation data with OVITO – the Open Visualization Tool. *Modelling Simul. Mater. Sci. Eng.*, 2010, **18**, P. 015012.

[36] Hunter J.D. Matplotlib: A 2D Graphics Environment. *Computing in Science & Engineering*, 2007, **9**(3), P. 90–95.

Submitted 9 October 2025; accepted 15 October 2025

Information about the authors:

Ilya S. Popov – Institute of Solid State Chemistry, Ural Branch of Russian Academy of Sciences, Yekaterinburg, Russia; ORCID 0000-0001-8312-7071; popov@ihim.uran.ru

Albina A. Valeeva – Institute of Solid State Chemistry, Ural Branch of Russian Academy of Sciences, Yekaterinburg, Russia; ORCID 0000-0003-1656-732X; anibla_v@mail.ru

Andrey N. Enyashin – Institute of Solid State Chemistry, Ural Branch of Russian Academy of Sciences, Yekaterinburg, Russia; ORCID 0000-0001-6195-7971; enyashin@ihim.uran.ru

Conflict of interest: the authors declare no conflict of interest.

NANOSYSTEMS:
PHYSICS, CHEMISTRY, MATHEMATICS

Avdeeva Yu.A., et al. *Nanosystems: Phys. Chem. Math.*, 2025, **16** (5), 628–639.
http://nanojournal.ifmo.ru
DOI 10.17586/2220-8054-2025-16-5-628-639

Original article

Formation of highly dispersed V–C–O–Ni and V–N–O–Ni compositions under low-temperature nitrogen plasma conditions

Yuliya A. Avdeeva[1,a], Irina V. Luzhkova[1,b], Aidar M. Murzakaev[2,c], Alexey N. Ermakov[1,d]

[1]Institute of Solid State Chemistry of the Ural Branch of the Russian Academy of Sciences, Ekaterinburg, Russia

[2]Institute of Electrophysics of the Ural Branch of the Russian Academy of Sciences, Ekaterinburg, Russia

[a]y-avdeeva@list.ru, [b]key703@yandex.ru, [c]aidar@iep.uran.ru, [d]ermakovihim@yandex.ru

Corresponding author: Yu.A. Avdeeva, y-avdeeva@list.ru

PACS 61.46.+w, 61.46.-w, 61.66.Fn

ABSTRACT Under conditions of plasma-chemical synthesis in low-temperature (4000-6000 °C) nitrogen plasma, ultrafine and nanocrystalline powder compositions VC–Ni and VN–Ni were obtained from mechanical mixtures containing vanadium carbide or nitride with metallic nickel in the ratio 1:1. X-ray studies have shown that the obtained plasma-chemical particles contain vanadium oxycarbides and oxynitrides, metallic nickel, and are also characterized by the presence of oxide phases of the V–O system. Electron microscopic studies of nanocrystalline fractions of VC–Ni and VN–Ni powder compositions using high-resolution transmission electron microscopy visualized the structure of the obtained particles. Using the fast Fourier transform, it was shown that the refractory components and metallic nickel form individual nanometer-scale particles that do not come into contact with each other. A chemical mechanism of the organization of highly dispersed mechanical mixtures V–C–O–Ni and V–N–O–Ni under conditions of quenching processes in a turbulent flow of nitrogen gas proceeding at a speed of 10^5 °C/s has been formulated on the basis of the performed research.

KEYWORDS vanadium carbide, vanadium nitride, nickel, plasma-chemical synthesis, X-ray phase analysis, high-resolution transmission electron microscopy

ACKNOWLEDGEMENTS The work was carried out in accordance with the state assignment for the Institute of Solid State Chemistry of the Ural Branch of the Russian Academy of Sciences (Theme No. 124020600024-5).

FOR CITATION Avdeeva Yu.A., Luzhkova I.V., Murzakaev A.M., Ermakov A.N. Formation of highly dispersed V–C–O–Ni and V–N–O–Ni compositions under low-temperature nitrogen plasma conditions. *Nanosystems: Phys. Chem. Math.*, 2025, **16** (5), 628–639.

1. Introduction

The formation of highly dispersed powder compositions based on refractory compounds of elements of subgroups IV–VIA of the Periodic Table is of interest when they are used as wear-resistant coatings for various purposes [1], or as insoluble modifying additives [2] in foundry production, ensuring the improvement of physical and mechanical characteristics.

Under these conditions, refractory compositions based on titanium carbides, nitrides and carbonitrides, where Ni or Co are used as the metal component [3,4], are most common in terms of production and practical application. They can be present in the form of independent particles, including those in the nanometer range, which can be realized through the use of milling technologies [5], or have the ability to form highly dispersed core-shell structures [6]. The core will be made up of refractory compounds, and the metallic phases will form the shell. The synthesis of highly dispersed "core-shell" structures is carried out under conditions of extreme impact methods, one of which is plasma-chemical technology in a low-temperature gas plasma [2].

It is known from the literature [7, 8] that vanadium carbides and nitrides (VC_x, VN_y) are similar in properties to titanium carbide-nitride compounds. Their melting and evaporation temperatures differ significantly. This undoubtedly affects the structural and morphological characteristics of the final synthesis products. Considering that the crystallization temperatures of VC and VN [9] are comparable with the boiling point of metallic nickel [10], the formation of highly dispersed particles with a "core-shell" structure can be greatly hampered or practically impossible according to [6]. Another characteristic feature of VC and VN can be a high tendency to oxidation with TiC and TiN [11].

The aim of this work is to produce and certify highly dispersed powder compositions based on vanadium carbide and nitride with the participation of metallic Ni obtained under conditions of plasma-chemical synthesis in low-temperature nitrogen plasma.

2. Methods

Highly dispersed powder compositions VC–Ni and VN–Ni were obtained by plasma-chemical synthesis in a low-temperature (4000 – 6000 °C) nitrogen plasma (GNIIKhTEOS, Moscow) described in [12].

Mechanical mixtures consisting of microcrystalline powders of VC or VN and Ni were immersed in a piston-type dispenser and fed at a rate of 200 g/h into a plasma-chemical reactor with a capacity of 25 kW. The plasma flow velocity was 55 m/s. After evaporation, the steam-gas mixture entered the quenching chamber, where condensation of the vapors occurred in the turbulent flow of the cooling gas, followed by the formation of highly dispersed VC–Ni and VN–Ni particles. Subsequently, the particles were moved by pneumatic flow to classifier 1 – a vortex-type cyclone, where the ultra-dispersed fractions of the obtained powder compositions were separated, and the nanocrystalline fractions were moved by pneumatic transport to classifier 2 – a bag-type filter.

Technical nitrogen was used as a plasma-forming gas and a cooling gas. The total gas consumption was 25 – 30 m^3/h, namely: 6 m^3/h – for plasma formation, 19 – 24 m^3/h – for hardening, stabilization and transportation.

Deactivation of highly dispersed powder products was carried out by slowly flowing air into the separation units of the plasma-chemical installation after synthesis.

As a result of plasma-chemical synthesis, two fractions of powder products VC–Ni and VN–Ni were obtained (classifier 1 – cyclone, classifier 2 – filter), differing in the morphology and phase composition of powder compositions with a core-shell structure.

The resulting powder compositions were studied by the X-ray diffraction method (Shimadzu XRD 7000, Japan, STOE Stady-P, Germany, $2\Theta = 5 – 80^\circ$ with exposure of 1 – 20 s per point). The presence of free carbon was investigated by Raman spectroscopy (Renishaw inVia Reflex). The density of the formed highly dispersed mechanical mixtures was determined using an AccuPyc II 1340 V1.09 helium pycnometer. The specific surface area was determined in accordance with the BET method (Gemini VII 2390 V1.03 (V1.03 t) specific surface area analyzer).

Based on the density data and the BET method, in accordance with formula (1) [13], the calculated values of the average particle size of all fractions obtained were determined.

$$d = \frac{6}{S_{sp}\rho}, \tag{1}$$

where d is the average particle diameter, S_{sp} is the specific surface area, ρ is the density.

To confirm the highly dispersed state, the nanocrystalline components of the powder composites from the filter were studied using high-resolution transmission electron microscopy (HRTEM) (JEOL 2100, Japan).

3. Results and discussion

Experimental data from X-ray phase analysis, density measurements, specific surface area by the BET method and calculated values of the average particle size for highly dispersed VC–Ni and VN–Ni compositions are given in Table 1.

According to the X-ray phase analysis data, the highly dispersed composition extracted from the cyclone (Table 1, No. 1, Fig. 1), which was obtained from a mechanical mixture of vanadium carbide VC and metallic Ni in a ratio of 1:1, contains 37 wt.% of vanadium oxycarbide $VC_{0.78}O_{0.07}$ (sp. gr. Fm-3m) [14], 20 wt.% of metallic Ni (sp. gr. Fm-3m), tetrahedral (sp. gr. P42/mnm) and rhombohedral (sp. gr. R-3c) vanadium oxides VO_2 (9 wt.%) and V_2O_3 (12 wt.%), respectively. 6 wt.% of titanium-nickel nitride $TiN_{0.84}O_{0.11}$ (sp. gr. Fm-3m) [14], 1 wt.% of titanium-nickel nitride $Ti_{0.7}Ni_{0.3}N$ (sp. gr. P-6m2) [15] and carbon C of rhombohedral (sp. gr. R-3m, 9 wt.%) and hexagonal (sp. gr. P63/mmc, 6 wt.%) modifications were recorded as impurity phases.

The presence of oxygen-containing phases $VC_{0.78}O_{0.07}$, VO_2 and V_2O_3 in the overcondensed VC–Ni system is associated with the processes of deactivation of the final product. The presence of oxynitride $TiN_{0.84}O_{0.11}$ and titanium-nickel nitride $Ti_{0.7}Ni_{0.3}N$ is due to the fact that powdered titanium nickelide TiNi was used during the preliminary cleaning of the plasma-chemical installation, which, under the conditions of plasma-chemical synthesis in nitrogen plasma, forms highly dispersed powder compositions with a core-shell structure of the TiN–Ni composition [16]. Considering that complete titanium nitrides, in accordance with [10], are not wetted by metal melts, the recondensed highly dispersed particles contain refractory titanium nitride cores covered with a $Ti_{0.7}Ni_{0.3}N$ buffer layer and a Ni metal shell [17]. Condensation of free carbon occurs because the boiling and crystallization temperatures [18] significantly exceed those for VC, allowing the formation of a nucleus, on which vanadium carbide settles during condensation of the evaporated mechanical mixture of VC–Ni in the quenching chamber.

The recondensed fraction of the mechanical mixture VC–Ni from the bag-type filter (Table 1, No. 2, Fig. 1), according to X-ray diffraction data, contains 21 wt.% of $VC_{0.568}N_{0.398}$ (sp. gr. Fm-3m) [14], 26 wt.% of Ni (sp. gr. Fm-3m), 52 wt.% of V_2O_3 (sp. gr. R-3c) and 1 wt.% of $Ti_{0.7}Ni_{0.3}N$ (sp. gr. P-6m2). The formation of vanadium carbonitride $VC_{0.568}N_{0.398}$ is due to the fact that during the recondensation process, as shown on the example of work [19], at the crystallization stage two types of particles are formed in the quenching chamber of the plasma-chemical installation. Particles of the first type are formed from the evaporated initial components, where the refractory core is a “carbide – carbonitride” composition. Such particles subsequently settle in a vortex-type cyclone during separation. The second type of particles is formed on the basis of unevaporated residues of the initial refractory particles. In this case, the refractory

TABLE 1. Physico-chemical characteristics of highly dispersed powder compositions VC–Ni and VN–Ni obtained during plasma-chemical synthesis in a low-temperature nitrogen plasma of mechanical mixtures of vanadium carbide or nitride with nickel (1:1)

No.	Fraction	Phase composition, wt. %, a, b, c, nm	ρ, g/cm^3	S_{sp}, m^2/g	d, μm
1	VC–Ni (cyclone)	37 % $VC_{0.78}O_{0.07}$ (sp. gr. Fm-3m), $a = 0.415(2)$ 20 % Ni (sp. gr. Fm-3m), $a = 0.350(0)$ 9 % VO_2 (sp. gr. P42/mnm), $a = 0.455(0)$, $c = 0.286(3)$ 12 % V_2O_3 (sp. gr. R-3c), $a = 0.495(4)$, $c = 1.398(3)$ 6 % $TiN_{0.84}O_{0.11}$ (sp. gr. Fm-3m), $a = 0.424(2)$ 1 % $Ti_{0.7}Ni_{0.3}N$ (sp. gr. P-6m2), $a = 0.294(1)$, $c = 0.289(0)$ 9 % C (sp. gr. R-3m), $a = 0.249(6)$, $c = 1.013(0)$ 6 % C (sp. gr. P63/mmc), $a = 0.242(0)$, $c = 0.694(0)$	3.99	12.40	0.12
2	VC–Ni (filter)	21 % $VC_{0.568}N_{0.398}$ (sp. gr. Fm-3m), $a = 0.415(1)$ 26 % Ni (sp. gr. Fm-3m), $a = 0.350(8)$ 52 % V_2O_3 (sp. gr. R-3c), $a = 0.494(5)$, $c = 1.391(7)$ 1 % $Ti_{0.7}Ni_{0.3}N$ (sp. gr. P-6m2), $a = 0.294(4)$, $c = 0.290(9)$	3.22	59.10	0.03
3	VN–Ni (cyclone)	28 % VN (sp. gr. Fm-3m), $a = 0.413(8)$ 3 % VC (sp. gr. Fm-3m), $a = 0.416(6)$ 32 % Ni (sp. gr. Fm-3m), $a = 0.350(7)$ 12 % TiN (sp. gr. Fm-3m), $a = 0.424(3)$ 1 % $Ti_{0.7}Ni_{0.3}N$ (sp. gr. P-6m2), $a = 0.293(9)$, $c = 0.289(4)$ 16 % C (sp. gr. P63mc), $a = 0.245(9)$, $c = 1.340(5)$ 6 % Si (sp. gr. Fd-3m), $a = 0.542(6)$ 2 % Fe (sp. gr. Im-3m), $a = 0.286(5)$	5.14	9.80	0.12
4	VN–Ni (filter)	61 % $VN_{0.82}O_{0.14}$ (sp. gr. Fm-3m), $a = 0.414(0)$ 16 % V_2O_3 (sp. gr. R-3c), $a = 0.498(7)$, $c = 1.389(1)$ 23 % Ni (sp. gr. Fm-3m), $a = 0.351(7)$	4.20	59.60	0.02

cores will be a "carbonitride – nitride" composition, and the highly dispersed particles formed on their basis will settle on a bag-type filter. As in the previous case, the powder composition contains metallic Ni of cubic modification and hexagonal titanium-nickel nitride $Ti_{0.7}Ni_{0.3}N$. Its formation is due to the presence of nitride TiN, the determination of which by X-ray methods is difficult because of the isomorphism of refractory carbide-nitride compounds of titanium and vanadium and the nanocrystalline state of the sample (Table 1 No. 2, Fig. 1).

The next stage of the experimental work was the certification of highly dispersed compositions obtained from a mechanical mixture of powdered vanadium nitride VN with metallic Ni in a ratio of 1:1. It should be noted that the installation was not cleaned after recondensation of the mechanical mixture VC–Ni. In this regard, the phase composition of the recondensed powder composition VN–Ni from the cyclone can be described by the presence of compounds presented in Table 1 No. 3.

The formation of VN (28 wt.%, sp. gr. Fm-3m) and Ni (32 wt.%, sp. gr. Fm-3m) is regulated by the composition of the mechanical mixture. The presence of vanadium carbide VC (3 wt.%, sp. gr. Fm-3m), titanium nitride TiN (12 wt.%, sp. gr. Fm-3m), titanium-nickel nitride $Ti_{0.7}Ni_{0.3}N$ (1 wt.%, sp. gr. P-6m2) can be explained by the presence of impurities from previous experiments. The presence of 6 wt.% of Si (sp. gr. Fd-3m) is due to the fact that the main purpose of the plasma-chemical unit is to obtain powder silicon on a semi-industrial scale. The formation of free carbon C (sp. gr. P63mc), which in this case is an impurity element, is described above. The presence of iron Fe (2 wt.%, sp. gr. Im-3m) is a characteristic feature of the plasma-chemical synthesis technique since all units are made of steels of different grades.

The recondensed fraction of VN–Ni powder from the filter contains 61 wt.% of $VN_{0.82}O_{0.14}$ (sp. gr. Fm-3m), 16 wt.% of V_2O_3 (sp. gr. R-3c), 23 wt.% of Ni (sp. gr. Fm-3m). The presence of oxygen-containing compounds in this composition is explained above.

To clarify the phase composition of refractory cores, all powder compositions were subjected to chemical etching in a boiling solution of concentrated HCl. The etching time was 60 min.

The results of X-ray phase analysis of the etched compositions are given in Fig. 2(a,b) and in Table 2.

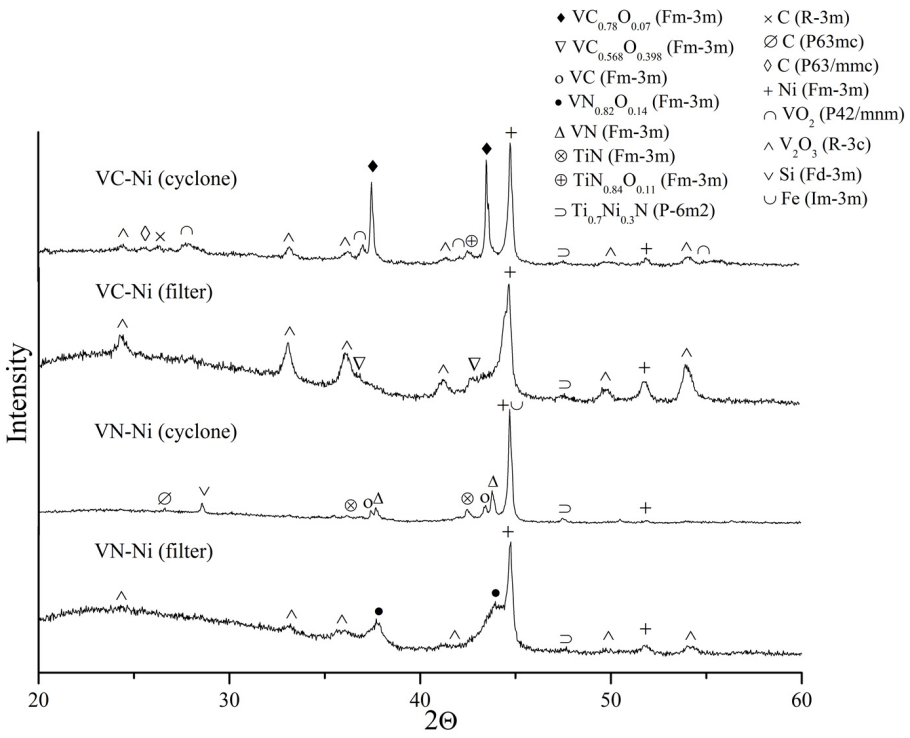

FIG. 1. X-ray diffraction patterns of highly dispersed VC–Ni and VN–Ni powder compositions obtained during plasma-chemical synthesis in low-temperature nitrogen plasma

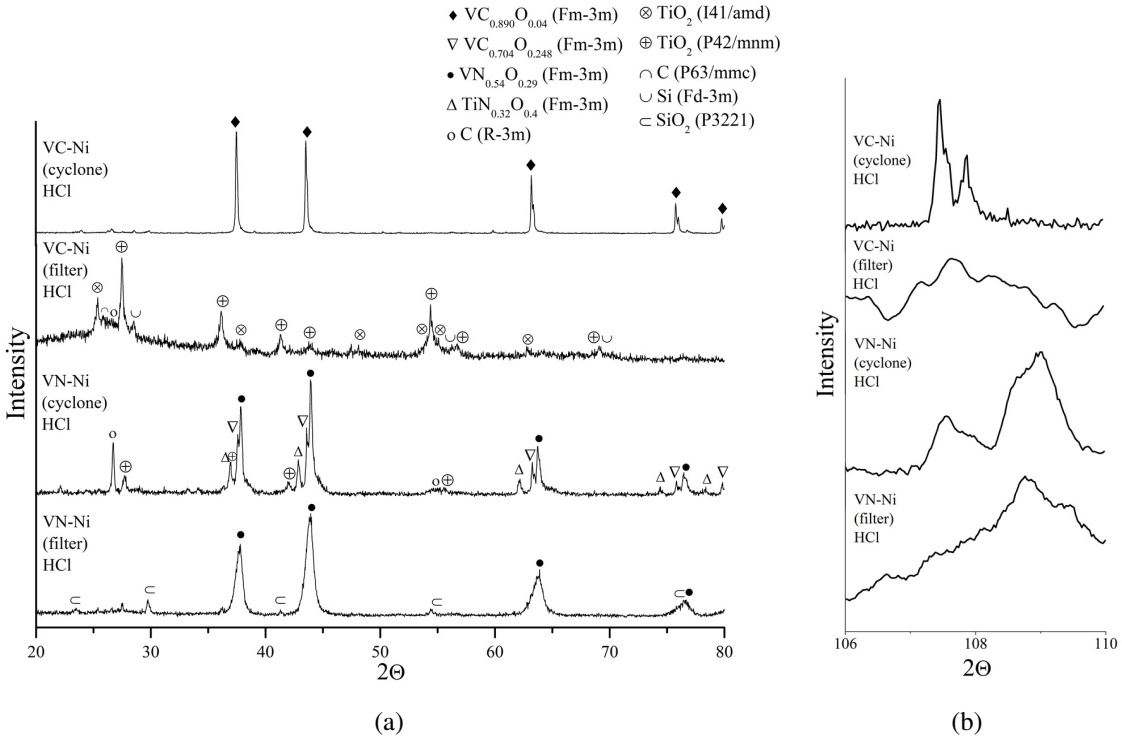

FIG. 2. Results of X-ray phase analysis of VC–Ni and VN–Ni powder compositions obtained during plasma-chemical synthesis after etching in HCl in the ranges of 2Θ = 20 – 80° (a) and 106 – 110° (331) (b)

TABLE 2. Physicochemical characteristics of highly dispersed powder compositions of VC–Ni and VN–Ni obtained during plasma-chemical synthesis after etching in HCl

No.	Fraction	Phase composition, wt.%, a, b, c, nm	Composition of the refractory phase [14] along line (331)
1	VC–Ni (cyclone) HCl	100 % $VC_{0.890}O_{0.040}$ (sp. gr. Fm-3m), $a = 0.417(3)$	$VC_{0.860}O_{0.060}$, $a = 0.416(3)$ nm $VC_{0.704}N_{0.248}$, $a = 0.415(4)$ nm
2	VC–Ni (filter) HCl	23 % C (sp. gr. R-3m), $a = 0.247(9)$, $c = 1.010(9)$ 16 % C (sp. gr. P63/mmc), $a = 0.242(0)$, $c = 0.689(9)$ 9 % Si (sp. gr. Fd-3m), $a = 0.542(7)$ 15 % TiO_2 (sp. gr. I41/amd), $a = 0.377(8)$, $c = 0.952(1)$ 37 % TiO_2 (sp. gr. P42/mnm), $a = 0.459(1)$, $c = 0.295(8)$	
3	VN–Ni (cyclone) HCl	11 % $VC_{0.704}O_{0.248}$ (sp. gr. Fm-3m), $a = 0.415(4)$ 47 % $VN_{0.540}O_{0.290}$ (sp. gr. Fm-3m), $a = 0.412(1)$ 10 % $TiN_{0.320}O_{0.400}$ (sp. gr. Fm-3m), $a = 0.422(0)$ 24 % C (sp. gr. R-3m), $a = 0.248(3)$, $c = 1.001(4)$ 8 % TiO_2 (sp. gr. P42/mnm), $a = 0.455(5)$, $c = 0.286(9)$	$VC_{0.82}O_{0.04}$, $a = 0.416(3)$ nm $VC_{0.704}N_{0.248}$, $a = 0.415(4)$ nm $VC_{0.57}O_{0.29}$, $a = 0.413(2)$ nm $VN_{0.56}O_{0.38}$, $a = 0.412(8)$ nm $VN_{0.56}O_{0.29}$, $a = 0.412(3)$ nm
4	VN–Ni (filter) HCl	85 % $VN_{0.540}O_{0.290}$ (sp. gr. Fm-3m), $a = 0.412(1)$ 15 % SiO_2 (sp. gr. P3221), $a = 0.435(2)$, $c = 0.497(0)$	$VN_{0.56}O_{0.38}$, $a = 0.412(8)$ nm

X-ray studies have shown that the etched recondensed composition based on vanadium carbide VC from the cyclone (Fig. 2(a), Table 2 No. 1) contains vanadium oxycarbide, which, in accordance with [14], is close to the composition $VC_{0.890}O_{0.040}$. Additionally, for a more thorough study of the composition, it is possible to present the results of X-ray phase analysis carried out based on the results of shooting of the etched sample at large angles (2Θ = 106 – 110°) (Fig. 2(b)). First of all, it should be noted that at first glance, the reflection (331) is decomposed into $K_{\alpha 1}$- and $K_{\alpha 2}$-components. However, according to the literature data [20–22], the processes of evaporation and condensation occurring under the conditions of plasma-chemical synthesis are non-equilibrium. This entails the absence of a homogeneous state of the obtained products. Under these conditions, a detailed study of the double reflections (311) showed that the etched refractory base is represented by two components, namely, oxycarbide $VC_{0.860}O_{0.060}$ and carbonitride $VC_{0.704}N_{0.248}$, which have similar unit cell parameters given in [14].

The X-ray diffraction pattern of the highly dispersed VC–Ni powder composition (filter fraction) after etching in HCl reveals the presence of oxide phase components in the form of two modifications of C, rutile and anatase forms of TiO_2 and cubic form of Si, shown in Fig. 2(a) and in Table 2 No. 2. The absence of refractory vanadium compounds can be explained by the fact that during the boiling process, all phase components containing vanadium and being in a nanocrystalline state, completely dissolved. Nanocrystalline particles containing vanadium carbide are significantly susceptible to oxidation during long-term storage. This subsequently suggests intensive decomposition in a boiling solution of concentrated HCl, as was shown in a number of studies [23]. The correctness of these judgments is confirmed by the presented image of the X-ray diffraction pattern in the angle interval 2Θ = 106 – 110 °, in which the (331) reflection is absent.

Etching of the VN–Ni fraction from the cyclone in a solution of boiling concentrated HCl showed that, according to the results of chemical reactions, based on X-ray data (Fig. 2(a), Table 2 No. 3), cubic $VC_{0.704}O_{0.248}$, $VN_{0.540}O_{0.290}$, $TiN_{0.320}O_{0.400}$ [14], rhombohedral C and TiO_2 in the form of rutile are present. Identification of the X-ray pattern taken in the angle interval 106 – 110° (Fig. 2b, Table 2 No. 3) shows that, as in the previous case with the etched recondensed mechanical mixture of VC and Ni (fraction from the cyclone) (Fig. 2a, b, Table No. 1), the reflections (331) for VC and VN are doubled. After determination of the unit cell parameters, it can be said that upon etching in boiling HCl, cubic oxycarbides $VC_{0.82}O_{0.04}$ ($a = 0.416(3)$ nm), $VC_{0.704}N_{0.248}$ ($a = 0.415(4)$ nm), $VC_{0.57}O_{0.29}$ ($a = 0.413(2)$ nm) and oxynitrides $VN_{0.56}O_{0.38}$ ($a = 0.412(8)$ nm), $VN_{0.56}O_{0.29}$ ($a = 0.412(3)$ nm) are present [14]. Cubic titanium oxynitride $TiN_{0.320}O_{0.400}$ acts as a refractory impurity phase, the (311) reflection of which overlaps with oxynitride phases. Carbon C (sp. gr. R-3m) and rutile TiO_2 are also included in the etched composition.

The recondensed fraction from the filter, etched for 1 hour in boiling concentrated HCl, obtained as a result of plasma-chemical synthesis of the mechanical mixture VN–Ni, according to the X-ray diffraction data in Fig. 2(a), Table 2 No. 4, contains cubic titanium oxynitride $VN_{0.540}O_{0.290}$ and hexagonal SiO_2 (sp. gr. P3221). A detailed study of the (311) reflection in the angle interval $2\Theta = 106 - 110^\circ$ (Fig. 2(b), Table 2 No. 4) shows that it corresponds to the composition of the oxynitride $VN_{0.56}O_{0.38}$ ($a = 0.412(8)$ nm).

To determine the presence and localization of phase components determined by X-ray diffraction, the nanocrystalline components of the powder fractions from the filter were studied using high-resolution transmission electron microscopy (Figs. 3–6).

First of all, it should be noted that the average particle size (Fig. 3(a-c)), according to the results of direct measurements, was 22.56 ± 0.15 nm for the fraction from the VC–Ni powder filter and 14.18 ± 0.19 nm for a similar fraction of VN–Ni powder.

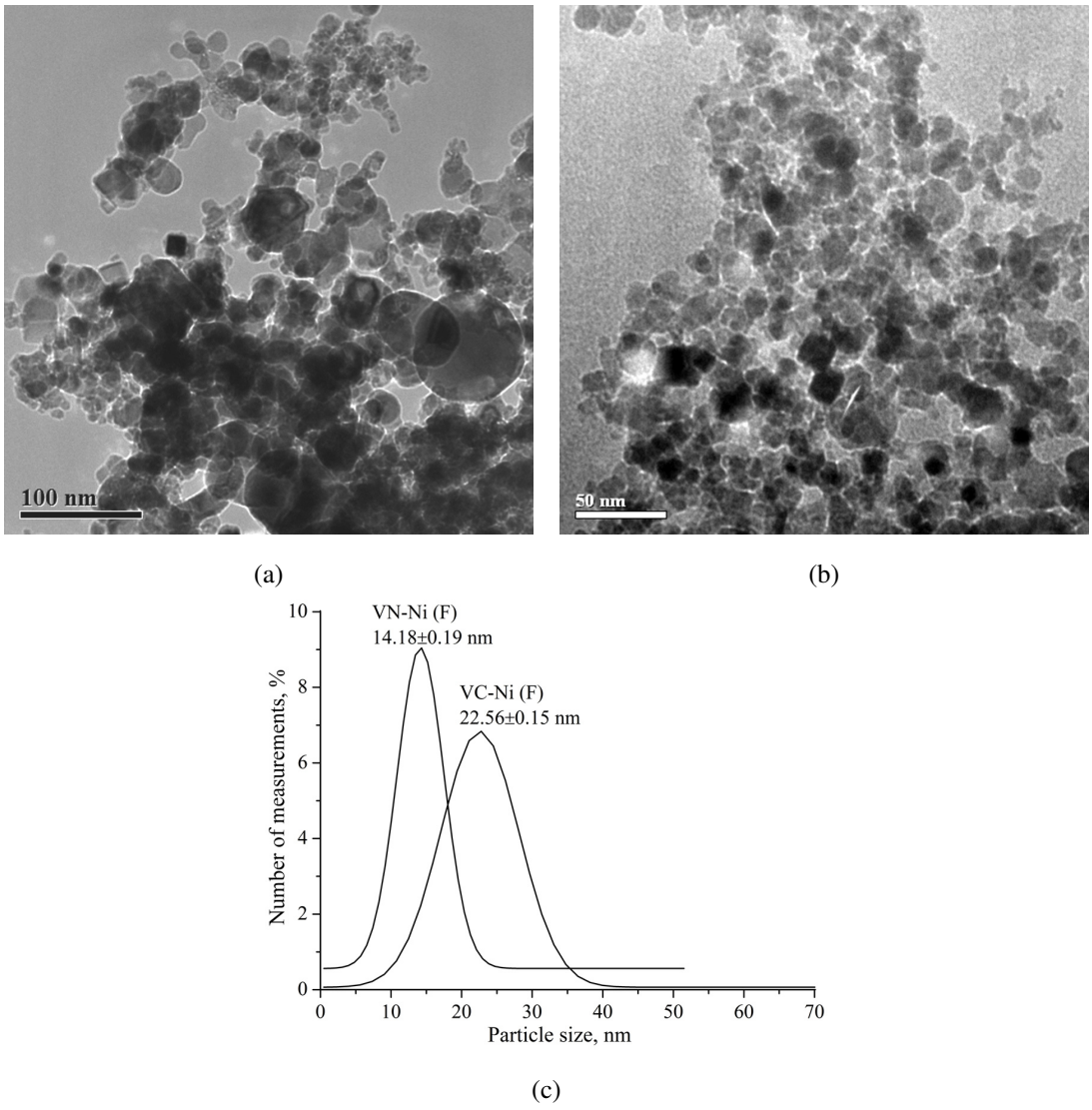

FIG. 3. Electron microscopic images of nanocrystalline components of plasma-chemical compositions VC–Ni (a), VN–Ni (b) and particle distribution histograms (c)

Figure 4(a) shows a nanocrystalline VC–Ni particle, on which vanadium oxide V_2O_3 of rhombohedral modification (sp. gr. R-3c) is present, interpreted based on the FFT results (Fig. 4(b)) of section 1 (Fig. 4(a)). In particular, $d_{(-1-13)} = 0.21$ nm; $d_{(113)} = 0.21$ nm; $d_{(110)} = 0.24$ nm; $d_{(116)} = 0.17$ nm; $d_{(006)} = 0.23$ nm are determined on the FFT. The correctness of the interpretation of the rhombohedral vanadium oxide V_2O_3 is confirmed by the similarity of the intersection angles of planes in the FFT picture (Fig. 4(b)) and the theoretical model of the V_2O_3 lattice shown in Fig. 4(c).

The presence of nanocrystalline Ni particles in the VC–Ni composition is shown in Fig. 5. Based on the results of microscopic studies taking into account FFT transformations and the results of profilometry in section 1 (Fig. 5(a,b)), the presence of moire contrast was determined when the (100) planes with $d_{(100)} = 0.21$ nm of two misoriented Ni crystallites of hexagonal structure (sp. gr. P63/mmc) are superimposed. The cubic structure of Ni (sp. gr. Fm-3m)

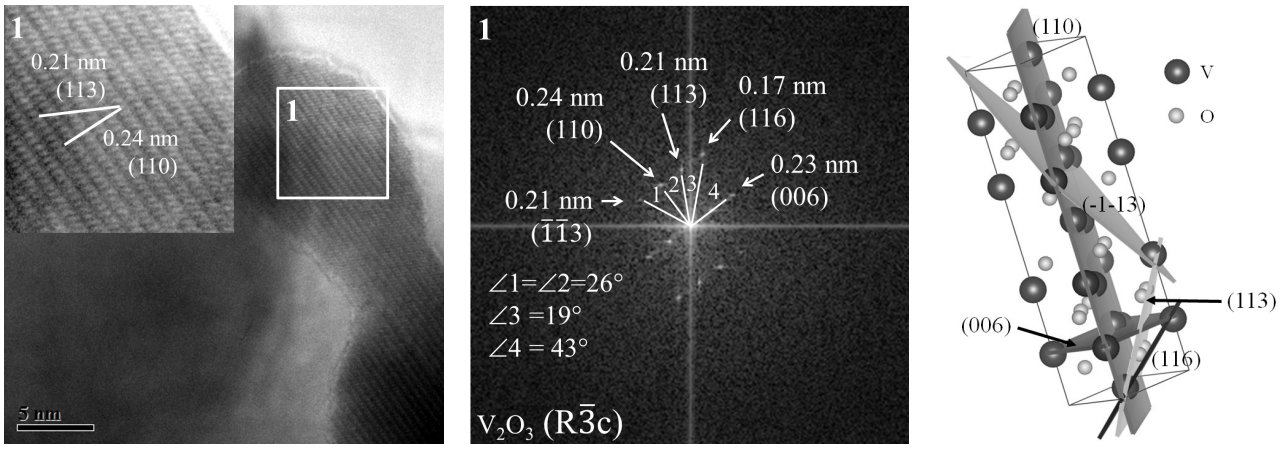

(a) (b) (c)

FIG. 4. TEM HR of the nanocrystalline component of the plasma-chemical composition obtained from the mechanical mixture VC–Ni: a – electron microscopic image with enlarged section 1; b – FFT transformation of section 1 and its interpretation; c – theoretical model of the V_2O_3 lattice (space group R-3c)

is illustrated in Fig. 5(a) (sections 2, 3), where, based on the results of FFT transformations (Fig. 5(c)), planes (111) and (200) with $d_{(111)} = 0.2$ nm and $d_{(200)} = 0.17$ nm intersecting at an angle of 57° are determined, which agrees well with the theoretical model of Ni crystal lattice shown in Fig. 5(d). In addition, it should be noted that cubic nickel covers the particle under study almost completely, as evidenced by the visualization of the family of (200) planes with $d_{(200)} = 0.17$ nm in Fig. 5(a) (section 3) and Fig. 5(d).

The electron microscopic studies of nanocrystalline particles VN–Ni showed (Fig. 6) that the refractory grain is represented by two cubic titanium oxynitrides $VN_{0.64}O_{0.08}$ (sp. gr. Fm-3m), $a = 0.4041$ nm and $VN_{0.19}O_{0.96}$ (sp. gr. Fm-3m), $a = 0.4106$ nm (Fig. 6(a,b)), see Table 1. According to the FFT data (Fig. 6(c)), $VN_{0.64}O_{0.08}$ is characterized by interplanar spacings $d_{(111)} = 0.238$ nm and $d_{(200)} = 0.207$ nm. The intersection angle of the presented planes, equal to 57°, is demonstrated in the enlarged image of the studied section of FFT transformation (Fig. 6(c)) and the theoretical model of cubic vanadium oxynitride $VN_{0.64}O_{0.08}$, which is crystallographically identical to the Ni model (Fig. 5(e)). The oxyntride $VN_{0.19}O_{0.96}$, in turn, is represented by the interplanar spacing $d_{(200)} = 2.099$ nm (Fig. 6(b)).

Based on the experimental results obtained in the work, it is possible to formulate the chemical mechanism of the organization of nanocrystalline particles VC–Ni and VN–Ni taking place in the quenching chamber of a plasma-chemical installation in a turbulent flow of nitrogen gas. This mechanism is based on the assumption that, in accordance with [24], the crystallization processes occurring in the quenching chamber of a plasma-chemical installation operating in a low-temperature plasma mode can be considered "quasi-equilibrium".

On this basis the quenching chamber, in which a turbulent flow of gaseous nitrogen is forcibly created, can be divided by temperature barriers. Table 3 shows the values of the boiling and melting temperatures of all phase components determined by X-ray diffraction [9, 10, 25, 26].

TABLE 3. Boiling and melting points of compounds included in the highly dispersed VC–Ni and VN–Ni compositions [9, 10, 25, 26]

Compound	T_{melt}, °C	T_{boil}, °C
$VC_{(cub.)}$	2800	3900
$VN_{(cub.)}$	2300	3100
Ni	1455	2900
C	3550	4827

The first temperature barrier, equal to 4000 °C, corresponds to the lower value of the temperature of existence of low-temperature plasma. Under these conditions, the evaporated carbon passes into a liquid state at 4827 °C and further crystallizes at 3550 °C, forming nuclei for subsequent crystallization of refractory vanadium compounds on them.

To verify the presence of free carbon, along with X-ray diffraction, the Raman scattering method was used to study the recondensed powders, Fig. 8. According to the results of the Raman studies, it can be said that carbon is present

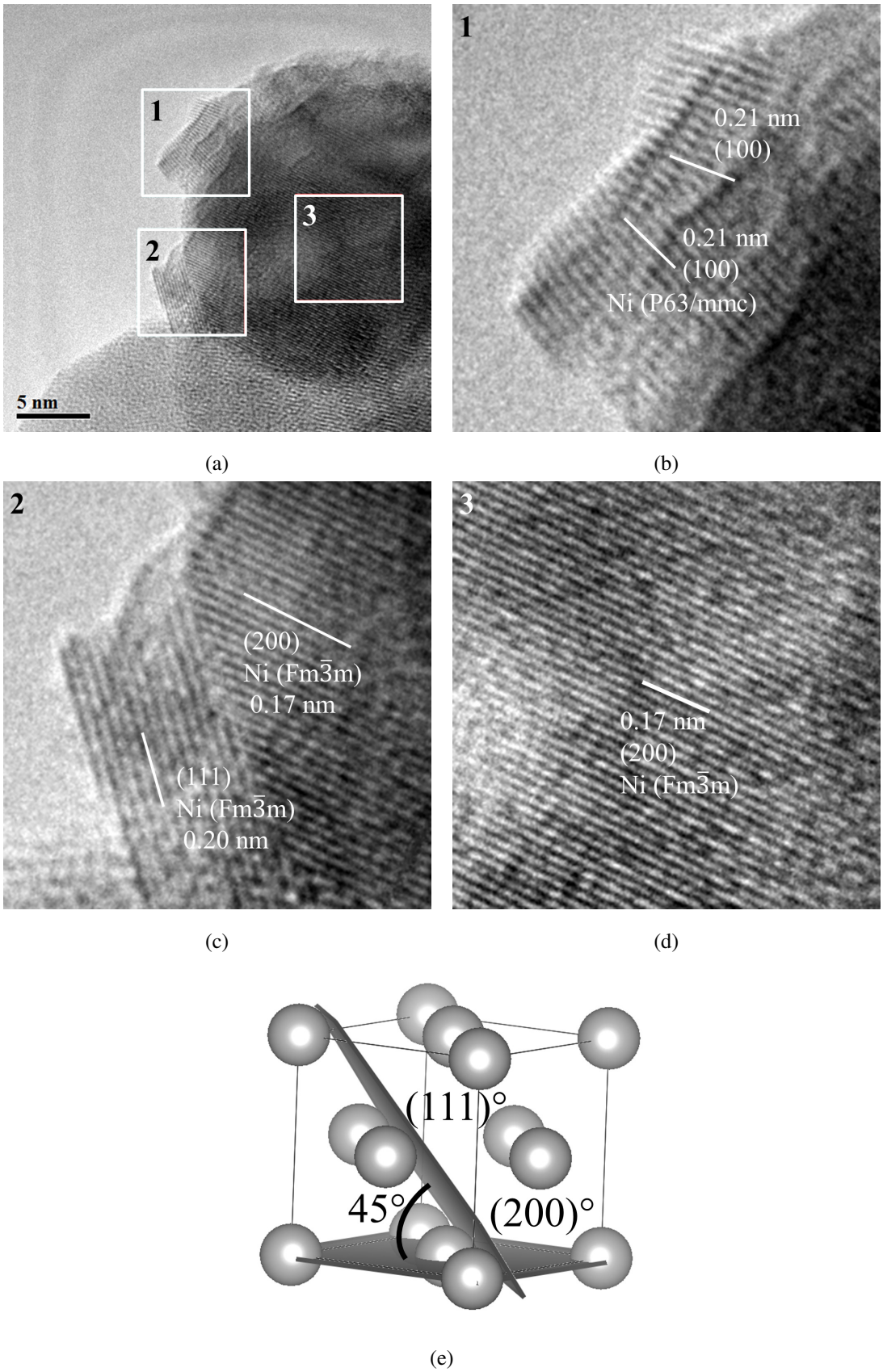

FIG. 5. HR TEM of surface layers of nickel in a nanocrystalline VC–Ni particle: a – electron microscopic image; b – enlarged image of section 1; c – enlarged image of section 2; d – enlarged image of section 3; e – theoretical model of Ni unit cell (sp. gr. Fm-3m) with planes (111) and (200)

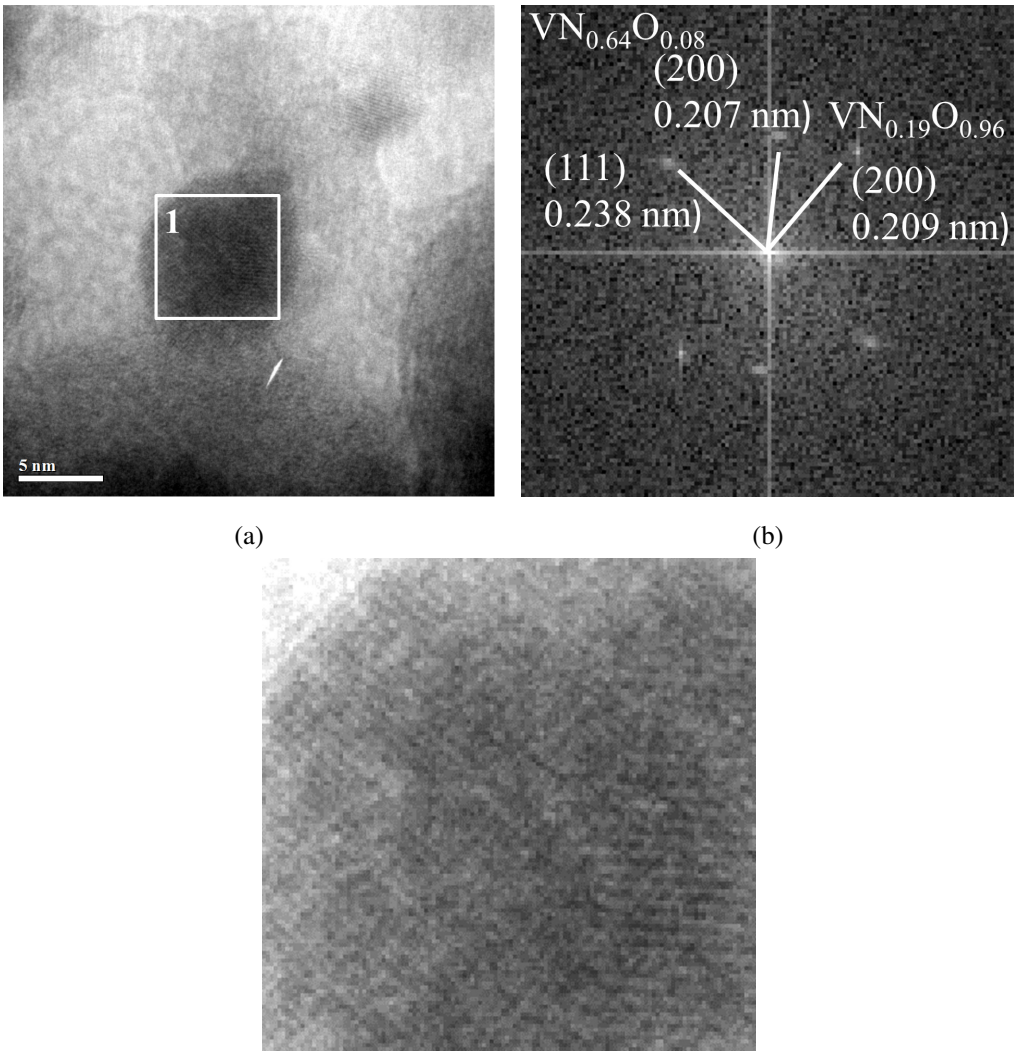

FIG. 6. HR TEM of a VN–Ni nanocrystalline particle with a core-shell structure: a – electron microscopic image with selected section 1; b – results of FFT transformation of section 1

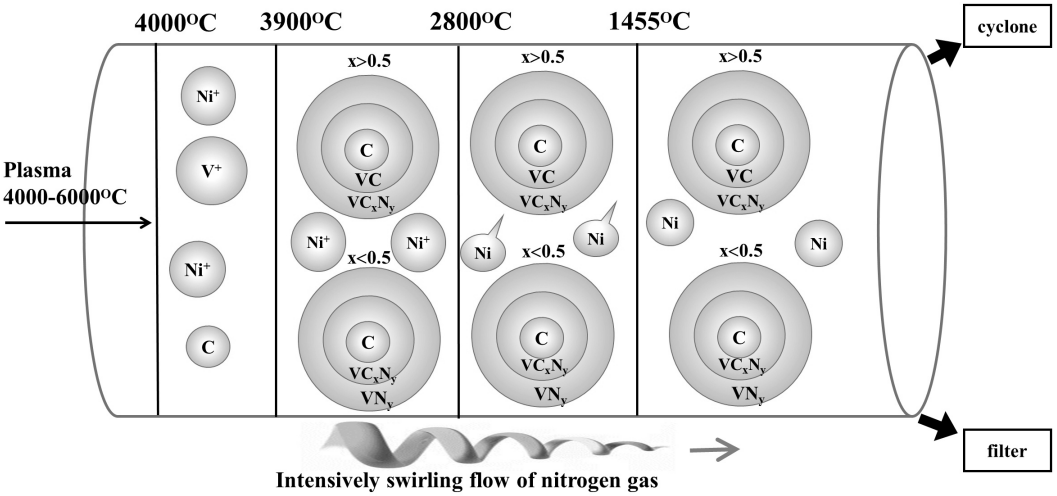

FIG. 7. Chemical mechanisms of organization of highly dispersed particles in the quenching chamber of a plasma-chemical installation, realized under conditions of low-temperature nitrogen plasma from mechanical mixtures of VC–Ni and VN–Ni

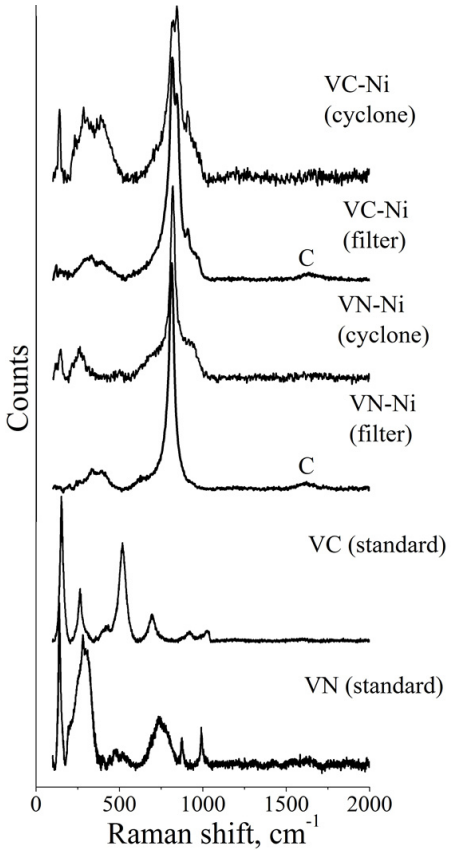

FIG. 8. Raman spectra of the obtained highly dispersed fractions of VC–Ni and VN–Ni

in nanocrystalline samples based on vanadium carbide (1634 cm^{-1}) and vanadium nitride from the filter (1619 cm^{-1}). Similar ultrafine fractions extracted from the cyclone do not exhibit any peaks of free carbon, which may indicate its presence in an amorphous state. The data of our studies of the chemical mechanisms in TiC–TiNi, TiC–Mo, TiC–Mo–Co can serve as an explanation for this effect [19, 26].

When passing the temperature barrier corresponding to the boiling point of vanadium carbide (3900 °C), the evaporated vanadium carbide VC condenses on the formed carbon nuclei. The resulting particles, due to the high crystallization temperature of VC (2800 °C), are formed in the form of refractory cores. The formation of oxycarbide and carbonitride phases is due to the presence of oxygen and nitrogen in the plasma-forming gas. The presence of oxygen in the system is due to the deactivation process.

The next stage of crystallization is the condensation of vanadium nitride VN, which boils at 3100 °C and crystallizes at 2300 °C. In this case, the formation of oxynitride phases occurs. The formation of vanadium oxides is due to the presence of oxygen in the system.

The final stage of crystallization is the condensation of metallic Ni, which boils at 2900 °C and crystallizes at 1455 °C. The formation of nickel particles occurs independently, which is confirmed by electron microscopic studies. The presence of vanadium in the nickel lattice was not detected.

Thus, the chemical mechanism of the organization of highly dispersed particles in the quenching chamber of a plasma-chemical installation, realized under conditions of low-temperature nitrogen plasma from mechanical mixtures of VC–Ni and VN–Ni, can be represented as follows (Fig. 9).

4. Conclusion

The work presents the results of studies of highly dispersed powder compositions based on vanadium carbide and vanadium nitride with metallic nickel, obtained under conditions of plasma-chemical synthesis in low-temperature nitrogen plasma.

X-ray studies have shown that the obtained plasma-chemical particles contain vanadium oxycarbides and oxynitrides, metallic nickel, and are also characterized by the presence of oxide phases of the V–O system. The presence of free carbon in the obtained compositions was confirmed by Raman spectroscopy.

Electron microscopic studies of nanocrystalline fractions of VC–Ni and VN–Ni powder compositions using high-resolution transmission electron microscopy visualized the structure of the obtained particles. Using the fast Fourier

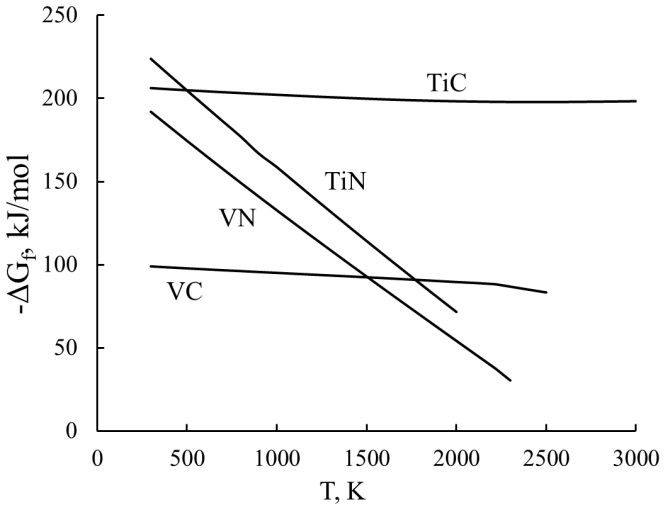

FIG. 9. Temperature dependences of $-\Delta G_f$ for VC, VN, TiC and TiN

transform, it was shown that the refractory components and metallic nickel form individual nanometer-scale particles that do not come into contact with each other.

A chemical mechanism of the organization of highly dispersed mechanical mixtures V–C–O–Ni and V–N–O–Ni under conditions of quenching processes in a turbulent flow of nitrogen gas proceeding at a speed of 10^5 °C/s has been formulated on the basis of the performed research.

References

[1] Ganji O., Sajjadi S.A., Yang Z.G., Mirjalili M., Najari M.R. On the formation and properties of chromium carbide and vanadium carbide coatings produced on W1 tool steel through thermal reactive diffusion (TRD). *Ceramics Int.*, 2020, **46** (16), P. 25320–25329.

[2] Zhukov M.F., Cherskiy I.N., Cherepanov A.N., Konovalov N.A., Saburov V.P., Pavlenko N.A., Galevskiy G.V., Andrianova O.A., Krushenko G.G. *Hardening of metallic polymeric and elastomer materials by ultrafine powders of plasma-chemical synthesis*. Novosibirsk: Nauka, 1999. 307 p.

[3] Carroll K. Core-shell nanoparticles: synthesis, design, and characterization. A dissertation submitted in partial fulfillment of the requirements for the degree of Doctor of Philosophy. Richmond, Virginia: Virginia Commonwealth University, 2010. 209 p.

[4] Pang W., Li Y., De Luca L.T., Liang D., Qin Z., Liu X., Xu H., Fan X. Effect of metal nanopowders on the performance of solid rocket propellants: a review. *Nanomaterials*, 2021, **11** (10), 2749.

[5] Zaki Z.I., El-Sadek M.H., Ali H.H., Ahmed H. Synthesis of vanadium carbide by mechanical activation assisted carbothermic reduction. *Materials*, 2020, **13** (19), 4408.

[6] Chalmers B. *Principles of solidification*. John Wiley and Sons, Springer: New York, Dordrecht, Heidelberg, London, 1964. 319 p.

[7] Samsonov G.V., Upadhaya G.Sh., Neshpor V.S. *Physical Materials Science of Carbides*. Kyiv: Naukova Dumka, 1974. 455 p. (In Russian)

[8] Samsonov G.V. *Nitrides*. Kyiv: Naukova Dumka, 1969. 380 p. (In Russian)

[9] Krzhizhanovsky R.E., Shtern Z.Yu. *Thermophysical properties of non-metallic materials (carbides)*. Handbook. Leningrad: Energy, 1976. 120 p. (In Russian)

[10] Kosolapova T.Ya. *Handbook of high temperature compounds: properties, production, applications*. New York, Washington, Philadelphia, London: CRC Press, 1990. 958 p.

[11] Voitovich R.F. *Oxidation of carbides and nitrides*. Kyiv: Naukova Dumka, 1981. 192 p. (In Russian)

[12] Storozhenko P.A., Guseinov Sh.L., Malashin S.I. Nanodispersed Powders: Synthesis Methods and Practical Applications. *Nanotechnologies in Russia*, 2009, **4**, P. 262–274.

[13] Sadovnikov S.I., Gusev A.I. Effect of particle size and specific surface area on the determination of the density of nanocrystalline silver sulfide Ag_2S powders. *Physics of the Solid State*, 2018, **60**, P. 877–881.

[14] Shveikin G.P., Alyamovsky S.I., Zainulin Yu.G., Gusev A.I., Gubanov V.A., Kurmaev E.Z. *Compounds of variable composition and their solid solutions*. UC USSR Academy of Sciences, Sverdlovsk, 1984, 292 p. (In Russian)

[15] Schönberg N. The tungsten carbide and nicel arsenide structures. *Acta Metallica*, 1954, **2**, P. 427–432.

[16] Ermakov A.N., Luzhkova I.V., Avdeeva Yu.A., Murzakaev A.M., Zainulin Yu.G., Dobrinsky E.K. Formation of complex titanium-nickel nitride $Ti_{0.7}Ni_{0.3}N$ in the "core-shell" structure of TiN – Ni. *Int. J. of Refractory Metals and Hard Materials*, 2019, **84**, 104996.

[17] Avdeeva Yu.A., Luzhkova I.V., Ermakov A.N. Mechanism of formation of nanocrystalline particles with core-shell structure based on titanium oxynitrides with nickel in the process of plasma-chemical synthesis of TiNi in a low-temperature nitrogen plasma. *Nanosystems: Physics, Chemistry, Mathematics*, 2022, **13** (2), P. 212–219.

[18] Carbon. Access URL: https://prosto-o-slognom.ru/chimia/506_uglerod_C.html

[19] Avdeeva Yu.A., Luzhkova I.V., Ermakov A.N. Plasmachemical synthesis of TiC–Mo–Co nanoparticles with a core–shell structure in a low-temperature nitrogen plasma. *Russian Metallurgy*, 2022, **9**, P. 1019–1026.

[20] Morokhov I.D., Trusov L.I., Chizhik S.P. *Ultradisperse metallic media*. Moscow: Atomizdat, 1977, 264 p. (In Russian)

[21] Andrievskiy R.A. The synthesis and properties of nanocrystalline refractory compounds. *Russian Chemical Reviews*, 1994, **63** (5), P. 411–427.

[22] Gusev A.I. *Nanocrystalline materials: methods of production and properties*. Ekaterinburg: Publishing house of NIS UB RAS, 1998, 199 p. (In Russian)

[23] Polovov I.B., Volkovich V.A., Shipulin S.A., Maslov S.V., Khokhryakov A.A., Vasin B.D., Griffiths T.R., Thied R.C. Chemistry of vanadium chlorides in molten salts: An electronic absorption spectroscopy study. *J. of Molecular Liquids*, 2003, **103–104**, P. 387–394.
[24] Polak L. Elementary chemical processes and kinetics in a non-equilibrium and quasi-equilibrium plasma. *Pure and Applied Chemistry*, 1974, **39** (3), P. 307–342.
[25] Knunyants I.L. *Chemical Encyclopedia: in 5 volumes*. Vol. 3. Moscow: Soviet Encyclopedia, 1992. 639 p. (In Russian)
[26] Avdeeva Yu.A., Luzhkova I.V., Murzakaev A.M., Ermakov A.N. Plasma-chemical synthesis of highly dispersed core-shell structures from a mechanical mixture of titanium carbide and titanium nickelide. *Powder Metallurgy and Functional Coatings*, 2024, **18** (3), P. 5–15.
[27] Gusev A.I. *Non-stoichiometry, disorder, short-range and long-range order in a solid*. M.: FIZMATLIT, 2007. 856 p. (In Russian)
[28] Samokhin A.V., Polyakov S., Astashov A.G., Tsvetkov Yu.V. Simulation of the process of synthesis of nanopowders in a plasma reactor jet type. I. Statement of the problem and model validation. *Fizika i khimiya obrabotki materialov*, 2013, **6**, P. 40–46. (In Russian)
[29] Samokhin A.V., Polyakov S., Astashov A.G., Tsvetkov Yu.V. Simulation of the process of nanopowder synthesis in a jet-type plasma reactor. II. Nanoparticles formation. *Inorganic Materials: Applied Research*, 2014, **5** (3), P. 224–229.
[30] Shiryaeva L.S., Gorbuzova A.K., Galevsky G.V. Production and application of titanium carbide (assessment, trends, forecasts). *Scientific and Technical J. of the St. Petersburg State Polytechnic University*, 2014, **2** (195), P. 100–107. (In Russian)

Submitted 14 June 2024; revised 5 December 2024; accepted 6 October 2025

Information about the authors:

Yuliya A. Avdeeva – Institute of Solid State Chemistry of the Ural Branch of the Russian Academy of Sciences Pervomaiskaya Street, 91, Ekaterinburg, 620990, Russia; ORCID 0000-0002-1470-0476; y-avdeeva@list.ru

Irina V. Luzhkova – Institute of Solid State Chemistry of the Ural Branch of the Russian Academy of Sciences Pervomaiskaya Street, 91, Ekaterinburg, 620990, Russia; ORCID 0000-0001-9123-5371; key703@yandex.ru

Aidar M. Murzakaev – Institute of Electrophysics of the Ural Branch of the Russian Academy of Sciences, Amundsen Street, 106, Ekaterinburg, 620216, Russia; ORCID 0000-0003-4440-427X; aidar@iep.uran.ru

Alexey N. Ermakov – Institute of Solid State Chemistry of the Ural Branch of the Russian Academy of Sciences Pervomaiskaya Street, 91, Ekaterinburg, 620990, Russia; ORCID 0000-0002-2746-5292; ermakovihim@yandex.ru

Conflict of interest: the authors declare no conflict of interest.

NANOSYSTEMS:
PHYSICS, CHEMISTRY, MATHEMATICS

Dabizha O.N. *Nanosystems:*
Phys. Chem. Math., 2025, **16** (5), 640–649.
http://nanojournal.ifmo.ru
DOI 10.17586/2220-8054-2025-16-5-640-649

Original article

Clinoptilolite zeolite mechanochemically modified with polyethylene glycol for the preparation of oil sorbents

Olga N. Dabizha[1,2]

[1]Transbaikal State University, Chita, Russia

[2]Branch of the Petersburg Nuclear Physics Institute named by B.P. Konstantinov of National Research Centre "Kurchatov Institute" – Institute of Silicate Chemistry, St. Petersburg, Russia

dabiga75@mail.ru

PACS 61.43.Gt, 61.46.-w, 82.33.Pt, 82.35.-x, 82.70.Dd

ABSTRACT The effect of 'soft' mechanochemical activation in an air atmosphere of a mixture of clinoptilolite zeolite rocks with 10 and 20 wt % polyethylene glycol PEG-4000 on structure, physical properties, and oil adsorption properties was investigated. The doses of the applied mechanical energy were 2.16 and 5.04 kJ·g^{-1}. It is shown that clinoptilolite rock modified by 10 wt % polyethylene glycol with a mechanical energy dose of 5.04 kJ·g^{-1} and clinoptilolite rock modified by 20 wt % of this polymer with an energy dose of 2.16 kJ·g^{-1} have an oil capacity on the solid surface of 1.4 g·g^{-1}. We compared our results with similar data for polymer modifiers such as polyvinyl alcohol and polyacrylamide. We identified regular changes in the structure that can be used as a predictive assessment for the expected increase in the oil capacity of organomineral sorbents. It was found that in the IR spectra of these samples the ratio of intensities of absorption bands due to valence vibrations of siloxane and hydroxyl groups is not less than 3.2, and the porosity is not less than 72 %. The correlation between oil capacity and polymer content, porosity, and structural changes was revealed.

KEYWORDS clinoptilolite zeolite, mechanochemical activation, polymer, polyethylene glycol, oil capacity

ACKNOWLEDGEMENTS The work on obtaining clinoptilolite rocks modified with polyethylene glycol was carried out within the state assignment of the Ministry of Science and Higher Education of the Russian Federation (theme No. 123102000012-2, agreement No. 075-03-2023-028/1 of 05.10.2023). The comparative analysis on the characteristics of clinoptilolite rocks modified with polyvinyl alcohol and polyacrylamide was carried out with topic GZ 1023033000122-7-1.4.3 at the branch of the National Research Center "Kurchatov Institute" – Petersburg Institute of Nuclear Physics–Institute of Silicate Chemistry.

FOR CITATION Dabizha O.N. Clinoptilolite zeolite mechanochemically modified with polyethylene glycol for the preparation of oil sorbents. *Nanosystems: Phys. Chem. Math.*, 2025, **16** (5), 640–649.

1. Introduction

The most common zeolite is clinoptilolite $(Na,K)_6Al_6Si_{30}O_{72} \cdot 20H_2O$, which belongs to the group of Heulandites (HEU) and has high porosity and absorption capacity [1–3]. Its framework of tetrahedral SiO_4 and AlO_4 units is formed by the intersection of three sets of channels with apertures of 0.31 × 0.76 nm, 0.36 × 0.46 nm, and 0.26 × 0.46 nm [4]. Using a top-down approach and mills, nanozeolites with particle sizes ranging from 50 to 200 nm [5–8] with improved catalytic activity [9, 10] and sorption properties [11, 12] can be obtained. The mechanochemistry of natural zeolites is poorly studied [13–15], however, it is a very promising area of research [16, 17]. To improve the physicochemical properties of clinoptilolite, its surface is modified with surfactants and polymers such as hexadecyltrimethylammonium chloride and n-cetylpyridinium bromide [8], chitosan [18–20], alginate [21], polyacrylamide [22], polydopamine [23], polypropylene [24], polyacrylonitrile [25], polypyrrole [26], polydimethylsiloxane [27], polyvinylpyrrolidone [28], poly-[5-(p-nitrophenylazo)-8-methacryloxyquinoline] [29], poly(ε-caprolactone), poly(ethylene glycol), poly(ε-caprolactone) [30], poly(ethylene glycol) and poly(vinylpyrrolidone) [31], nanohydroxyapatite, and chitosan and gelatin [32]. Modified polymer-zeolite materials are used for adsorption of heavy metal ions [18,21,22,24,26,29], aromatic hydrocarbons [7,25], methyl tert-butyl ether [2], dyes [18], and as catalytic [9] and photocatalytic [10] materials, as well as composite materials for bone tissue engineering [30, 32]. Zeolite-containing sorbents are characterized by their availability, environmental friendliness, low cost of purchase, and the possibility of recycling, which allows them to be considered for the removal of petroleum compounds [11, 33, 34]. For this, mineral substances are poured onto an (land-based) oil spill, spread onto the surface mechanically, and then collected together with the absorbed substance and transferred for recycling [35]. However, the process of surface modification of clinoptilolite with organic surfactants may not improve its sorption properties [36]. The important factor here is the diffusion of organic liquid into the mesopores. Modification of natural zeolites clinoptilolites by readily available inexpensive polymers solves the problem of increasing the hydrophobicity of the mineral matrix surface, which can contribute to the increase in oil capacity of materials.

The use of mechanical activation of solid substances leads to the formation of nanostructured porous materials. It also leads to the formation of defects in crystal lattices, which affects the number of active centers and adsorption. Modification of clinoptilolite with synthetic polymers, on the one hand, and application of mechanochemical activation, on the other hand, open prospects for obtaining efficient hybrid organomineral sorbents [37, 38]. Obtaining chitosan/zeolite sorbents by two-hour mechanochemical synthesis [39] requires significant energy consumption. Methods of 'soft' mechanical activation using short processing times are of interest. Previously, the authors have used polyvinyl alcohol [38] as well as polyacrylamide [40] as modifying polymers. The mechanochemical air-dry modification of clinoptilolite in the mild impact-abrasion regime with polyvinyl alcohol and polyacrylamide increased [38] and decreased [40] oil capacity, respectively. The use of polyethylene glycols as zeolite modifiers is known [41, 42]. This environmentally safe, biodegradable synthetic polymer has surface-active and sorption properties [43], is able to bind with porous materials by hydrogen bonds [41], so it is of interest to apply it to create oil sorbents.

We found that mechanical activation for 7 minutes increases the oil capacity of clinoptilolite-stilbite rock on solid and water surfaces by 10 and 16 %, respectively. An increase of oil capacity on solid and water surfaces for clinoptilolite rock is achieved by 7 and 10 %, respectively, after mechanical activation for 3 minutes [11]. The aim of the present work was to mechanochemically prepare polymer-zeolite sorbents based on clinoptilolite rocks and high molecular weight polyethylene glycol and evaluate the role of the organic modifier in changing their physical and sorption properties.

2. Experimental

2.1. Materials

The natural zeolites used in this work are clinoptilolite and clinoptilolite-stilbite rocks of Shivyrtuy and Kholinsky deposits, respectively (Transbaikal Territory, Russia). Their phase and chemical composition were studied earlier [11]. Polyethylene glycol (PEG-4000, NORPEG^{TM}, TU 2483-008-71150986-2006, Russia) was chosen as a polymer modifier. The kinematic viscosity of this polymer at 99 °C is 130 mm^2·s^{-1}, density at 20 °C is 1.2 g·cm^{-3}, melting range is 58 – 62 °C, water content does not exceed 1 wt%.

IR spectrum of PEG-4000, ν, cm^{-1}: 3460 (O–H); 2880 (C–H); 1470 and 1340 (C–H); 1280 and 1110 (C–O–C); 963 and 842 (C–O–C) [44].

Crude oil (technical, Cherkasy Chemicals Plant) for oil refineries (GOST 9965-76) was used in the study. Oil characteristics, presented as mean ± standard deviation, are as follows: density determined by the pycnometric method is 0.8411 ± 0.0011 g·cm^{-3}, the kinematic viscosity determined by a viscometer VPZh-2 is 8.35 ± 0.07 mm^2·sec^{-1}.

2.2. Modification of natural zeolites

The technological scheme for producing organomineral sorbents [38, 40] and the effects observed during mechanical activation of clinoptilolite zeolites with polymers are shown in Fig. 1.

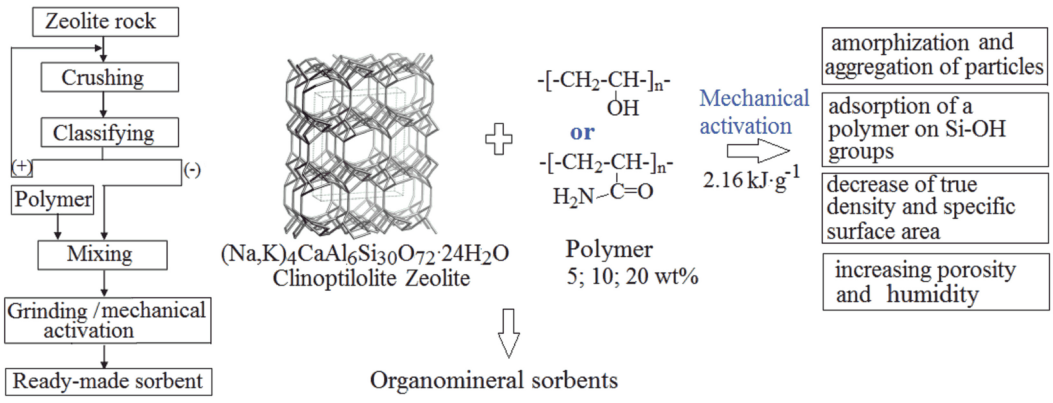

FIG. 1. Technological scheme for producing organomineral sorbents and the effects observed during mechanical activation of mixtures of clinoptilolite zeolites with polymers

Organomineral sorbents were obtained in a vibrating mill Retsch MM 400 (grinding principle is impact and attrition, max. speed 30 Hz; up to 8 mm feed size and 5 μm final fineness; power 0.9 kW; energy intensity 13 W·g^{-1}) by mechanoactivation of air-dry mixture of zeolite rocks: clinoptilolite-stilbite (I) and clinoptilolite (II) with additions of 10 wt % (I10, II10) and 20 wt % (I20, II20) of PEG-4000 for 166 s (superscript $'$) and 388 s (superscript $''$), which corresponds to doses of mechanical energy [11] equal to 2.16 and 5.04 kJ·g^{-1}.

2.3. Methods of characterization

IR spectra were obtained using a SHIMADZU FTIR-8400S FTIR spectrometer in the region from 4000 to 400 cm^{-1} in potassium bromide tablets. The ratio of intensities (I_2/I_1) of absorption bands (a.b.) at 1045 – 1070 and 3430 – 3450 cm^{-1} was calculated by measuring the length of each band to the zero line.

The true density (ρ_{tr}, g·cm^{-3}) was determined by the pycnometric method (working fluid – kerosine KO-25 $d_{20}{}^{\circ}\mathrm{C} = 0.795$ g·cm^{-3}), and the bulk density (ρ_b, g·cm^{-3}) and hygroscopic humidity content (W, %) were determined by the gravimetric method.

The porosity of the zeolite and organo-zeolite powder (P, %) was calculated using the following equation:

$$P = \left(\frac{\rho_{tr} - \rho_b}{\rho_{tr}} \right) \cdot 100\ \%. \tag{1}$$

The oil capacity of the sorbent on the solid surface was calculated as in [11, 38, 40], taking into account the blank sample after placing the powder in a tea bag, immersion in crude oil (GOST 9965-76), and incubation in it for 15 minutes.

Correlation coefficients (r_{xy}) between oil capacity and porosity, oil capacity and ratio of absorption band intensities, oil capacity and polymer content were calculated using MS Excel.

The characteristics of the PEG-modified clinoptilolite-stilbite and clinoptilolite rocks were compared to those of the rocks mechanically activated under the same conditions, but without polymer, as well as with samples modified with other polymers under the same conditions.

3. Results and discussion

It was found previously that the supplied dose of mechanical energy affects the structure and oil-sorption properties of clinoptilolite rocks [11]. Thus, the samples exhibit maximum oil capacity after their mechanical treatment for 3 and 7 minutes for clinoptilolite and clinoptilolite-stilbite rocks, respectively (Fig. 2).

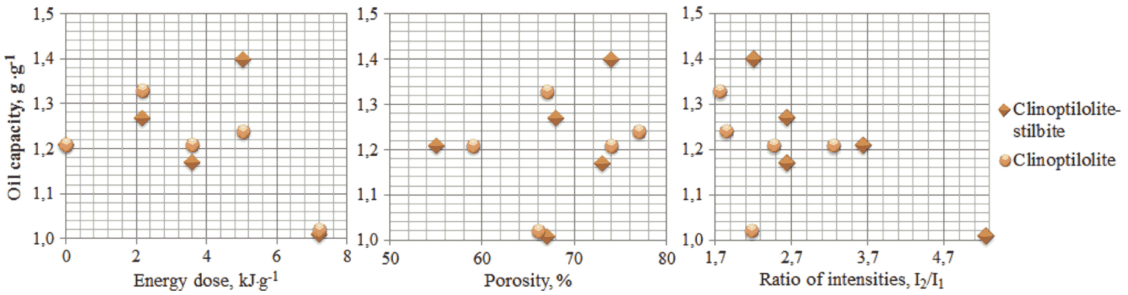

FIG. 2. Dependence of sorption of crude light oil by clinoptilolite zeolites on the dose of mechanical energy, porosity and ratio of intensities of absorption bands at 1045 – 1070 and 3430 – 3450 cm^{-1} (based on materials [11])

These samples have oil capacity values equal to 1.40 and 1.33 g/g and porosity, calculated using formula (1), equal to 74 and 67 %, respectively. In addition, the ratio of the intensities of the absorption bands caused by the stretching vibrations of siloxane bonds and silanol groups is on average $I_2/I_1 \sim 2$. However, the highest correlation coefficients were obtained only for the dependence of oil capacity on the ratio of the intensities of the absorption bands ($r_{xy} = -0.8766$) and porosity ($r_{xy} = -0.6565$) for clinoptilolite-stilbite and clinoptilolite rocks, respectively.

Figures 3 and 4 show IR spectra of samples of zeolite and polymer-zeolite sorbents resulting from the mechanochemical method with energy doses of 2.16 and 5.04 kJ·g^{-1}, respectively.

The samples of mechanically activated clinoptilolite-stilbite (samples I′, I″) and clinoptilolite rocks (samples II′, II″) are characterized by typical absorption bands in the infrared region of the spectrum [11]. The absorption bands with the highest intensities with maxima in the region from 1045 to 1069 cm^{-1} belong to the valence vibrations of Si–O–Si groups, and the absorption bands in the frequency region from 3599 to 3622 cm^{-1} belong to the valence vibrations of OH-groups of intra-complex water [11, 45].

The presence of polyethylene glycol in the modified organomineral samples is confirmed by the presence of absorption bands with maxima at 2882, 1451 (1462), 1343 (1346), 833 (845, 849) cm^{-1}, which are due to valence and scissor vibrations of CH_2 groups, vibrations of C–O–C groups, respectively [44]. The low-frequency shift and disappearance of the absorption bands of hydroxyl groups with maxima in the region of 3580 – 3630 cm^{-1} in the IR spectra of samples I10′ and I20′ (Fig. 3), I10″ and I20″ (Fig. 4), respectively, indicate the interaction between silanol groups of clinoptilolite and hydroxyl groups of polyethylene glycol.

Shifts of absorption bands of valence vibrations of hydroxyl groups are observed both in the long-wave region (samples II10′, II20″) and in the short-wave region (samples I10′, II20′, II10″) and indicate the rearrangement of the hydrogen

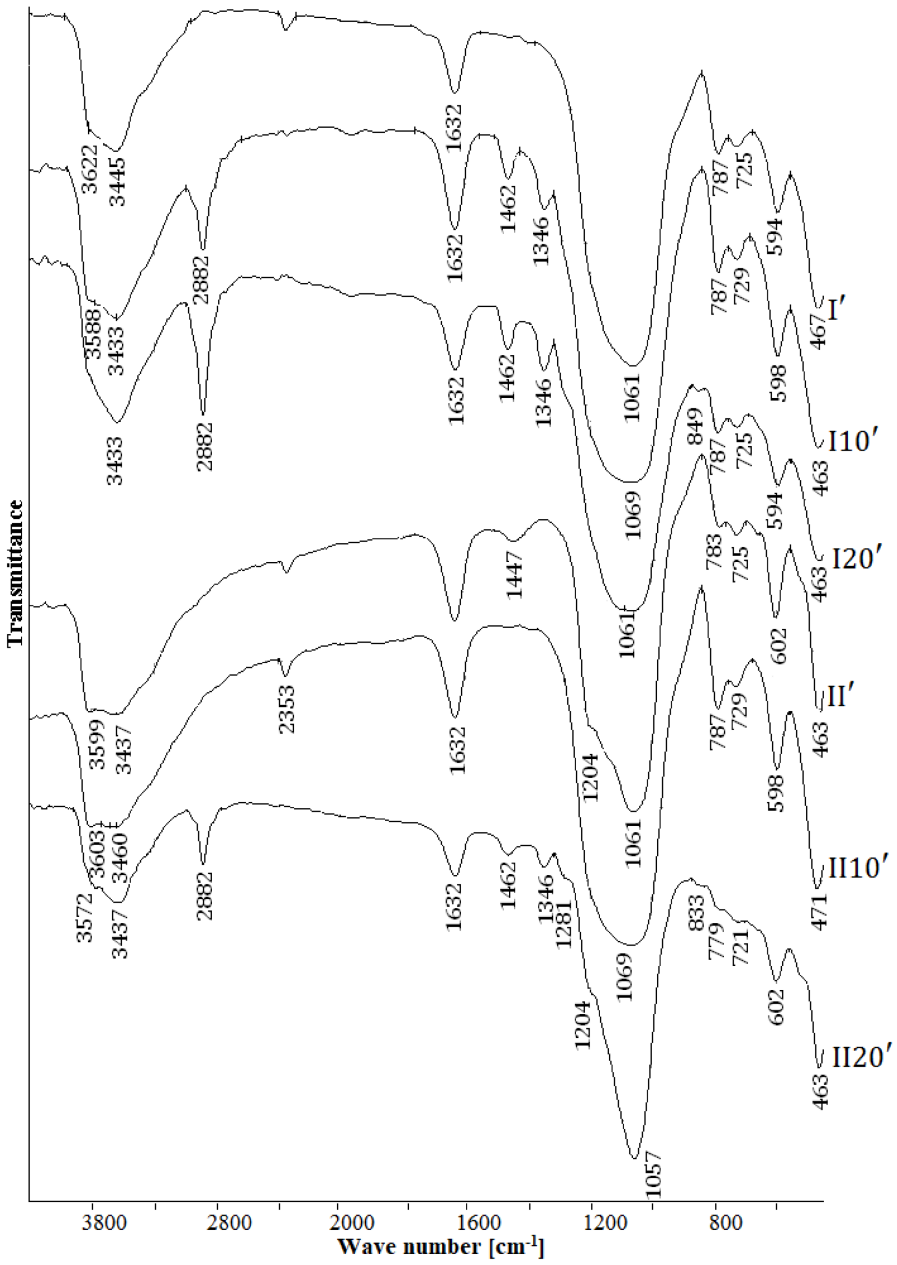

FIG. 3. IR spectra of the samples of the zeolite rocks mechanically activated with and without PEG as a modifier: I – clinoptilolite–stilbite rock, II – clinoptilolite rock; the subscripts 10 and 20 specify the weight percent of PEG in the samples; superscript ′ indicates the dose of induced mechanical energy 2.16 kJ·g^{-1}

bonding system due to modification of the mineral framework by polyethylene glycol. There are shifts of absorption bands corresponding to valence vibrations of siloxane bonds in the region of high frequencies (samples I10′, II10′), as well as in the region of low frequencies (sample II20′). A narrowing and an increase in the intensities of the absorption bands belonging to the valence vibrations of siloxane bonds and, at the same time, a decrease in the intensity of the absorption band corresponding to the valence vibrations of hydroxyl groups were observed (samples II20′, II10″). This pattern was also observed in the IR spectra of clinoptilolite rocks modified with 20 wt % of polyvinyl alcohol [38] with improved oil capacity.

The application of a higher dose of mechanical energy ($D = 5.04$ kJ·g^{-1}) is reflected in the IR spectrum of clinoptilolite-stilbite sorbent by a low-frequency shift of the absorption band maximum due to the valence vibrations of OH-groups at 3622 (sample I′, Fig. 3) to 19 cm^{-1} (sample I″, Fig. 4). In addition, there are high-frequency shifts of absorption bands due to valence vibrations of Si–O–Si, deformation vibrations of SiO_4, vibrations of twin rings between

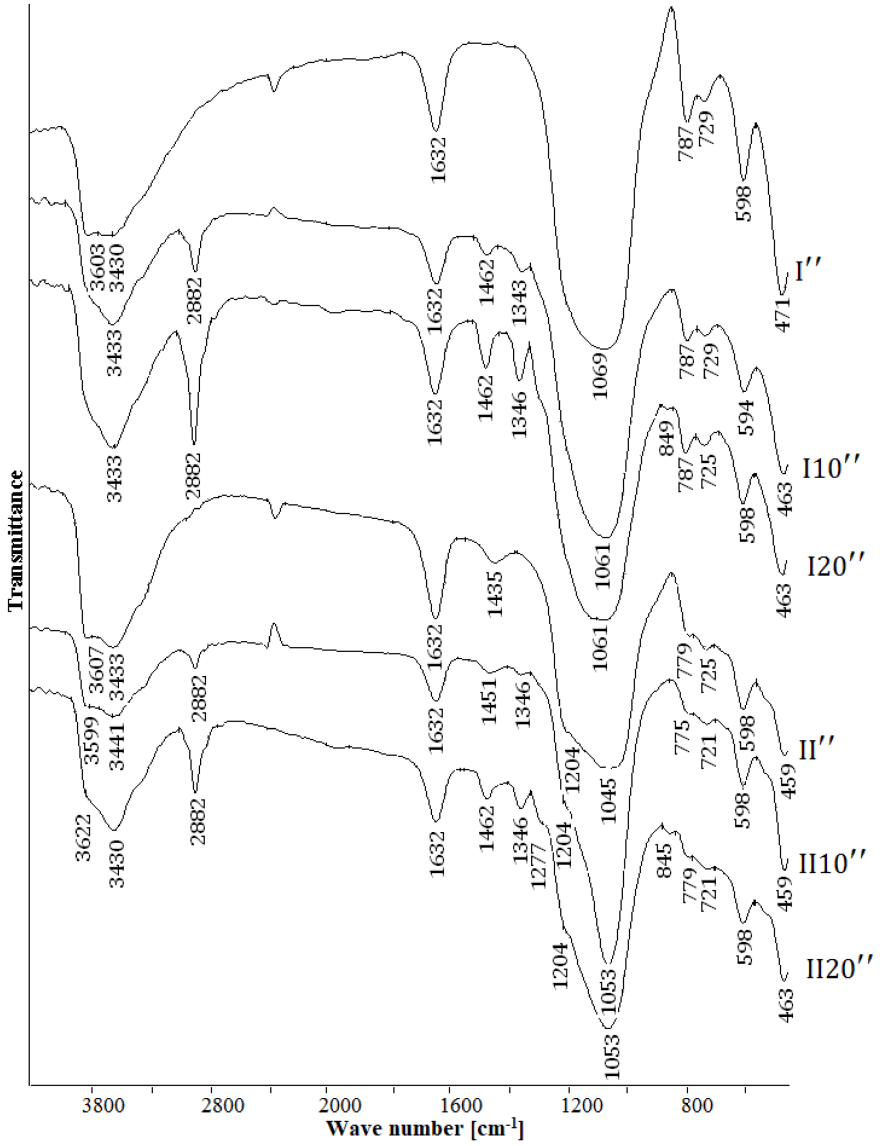

FIG. 4. IR spectra of the samples of the zeolite rocks mechanically activated with and without PEG as a modifier: I – clinoptilolite–stilbite rock, II – clinoptilolite rock; the subscripts 10 and 20 specify the weight percent of PEG in the samples; superscript ″ indicates the dose of induced mechanical energy 5.04 kJ·g^{-1}

(Si, Al)–O–Si tetrahedra, and deformation vibrations of Si–O–Si with maxima at 1061 and 725, 594, 467 cm^{-1}, respectively (sample I′, Fig. 3) by 8 and 4, 4, 4, 4 cm^{-1} (sample I″, Fig. 4). Structural changes in clinoptilolite rock under the action of the same dose of mechanical energy are manifested by a high-frequency shift of the absorption band with maximum at 3599 cm^{-1} (sample II′, Fig. 3) by 8 cm^{-1} (sample II″, Fig. 4) and low-frequency shifts of absorption bands with maxima at 1061 and 783, 602, 463 cm^{-1} (sample II′, Fig. 3) by 16 and 4, 4, 4, 4 cm^{-1}, respectively (sample II″, Fig. 4).

In the IR spectra of the modified organomineral samples, the increase in the dose of the applied mechanical energy is reflected by the following changes:

— disappearance of the absorption band of valence vibrations of free OH-groups, low-frequency shifts at 3, 8 and 4 cm^{-1} of the absorption bands of CH_2, Si–O–Si and (Si, Al)–O–Si groups, respectively (sample I10″, Fig. 4);
— high-frequency shift by 4 cm^{-1} of the absorption band belonging to vibrations of the twin rings between (Si, Al)–O–Si tetrahedra (sample I20″, Fig. 4);
— low-frequency shifts at 4 and 19 cm^{-1} of the absorption bands of valence vibrations of free and OH-groups bound to water molecules, low-frequency shifts at 16, 12, 4 and 12 cm^{-1} of the absorption bands of valence vibrations of Si–O–Si, Si–O groups, deformation vibrations of SiO_4 and Si–O–Si groups, respectively (sample II10″, Fig. 4);

— high-frequency shift by 50 cm^{-1} of the absorption band of valence vibrations of free OH-groups; low-frequency shift by 7 cm^{-1} of the absorption band of valence vibrations of OH-groups bound to water molecules, low-frequency shift by 4 cm^{-1} of the absorption band of valence vibrations of C–O–C; valence vibrations of Si–O–Si, vibrations of twin rings between (Si, Al)–O–Si tetrahedra, and a high-frequency shift of the absorption band of deformation vibrations of C–O–C bonds (sample II20″, Fig. 4).

The least structural changes affected sample I20″; therefore, no change in its physical and sorption properties should be expected. The most significant changes with increasing dose of mechanical energy are observed in the IR spectrum of sample II10″ and therefore it may show improved sorption properties.

Hygroscopic humidity, bulk and true densities, porosity, oil sorption capacity of the investigated zeolite and polymer-zeolite samples are given in Table 1.

The increase in moisture content of the samples with the increase in the content of polymer in the compositions of the samples is explained by the high content of hydroxyl groups. Maximum values of moisture content $\sim$ 3.5 wt % are observed in modified samples I20′ and II20′ (Table 1). The bulk density of polymer-zeolite sorbents is non-monotonically dependent on the PEG content. It increases by 2 to 4 % (samples I10″, I10′, II10′, II20′) and 17 % (sample II10″), and decreases by 3 % (sample II20″) and 9 to 12 % (samples I20″, I20′) compared to the values of the same characteristic of mechanically activated zeolites (samples I′, I″, II′, II″).

The bulk density of clinoptilolite-stilbite (sample I′) and clinoptilolite rocks (sample II′) decreases with increasing dosage of applied mechanical energy by 4 % (sample I″) and 6 % (sample II″). The true density of mechanically activated zeolite samples I″ and II″ increases by 7 and 3 % with increasing the mechanical energy dose by 2.88 $kJ \cdot g^{-1}$, which is explained by obtaining more compact pelletised particles and is in agreement with the data of [11]. The true density of PEG-zeolite sorbents decreases by 8 % (sample II20″), 14 % (samples I20′, II20′), 21 % (sample I20″) with the addition of 20 wt % polymer modifier, also observed in case of modification with polyvinyl alcohol [38], as well as polyacrylamide [40]. The oil capacity of PEG/clinoptilolite-stilbite sorbents with the addition of 20 wt % polyethylene glycol increases by 14 and 6 % in samples resulting from the application of energy doses of 2.16 and 5.04 $kJ \cdot g^{-1}$, respectively. The oil capacity of PEG/clinoptilolite sorbents also increases by 10 % with application of energy dose 2.16 $kJ \cdot g^{-1}$ and does not increase with application of energy dose 5.04 $kJ \cdot g^{-1}$ (Table 1). The maximum value of oil capacity resulting from the modification of clinoptilolite rock with polyethylene glycol is 1.4 $g \cdot g^{-1}$.

TABLE 1. Physical and sorption properties of zeolite and PEG/zeolite samples

Samples	Content, wt%		Time, t, s	Energy dose, D, $kJ \cdot g^{-1}$	Humidity, W, %	Density, ρ, $g \cdot cm^{-3}$		Oil capacity, SC, $g \cdot g^{-1}$
	Zeolite	PEG				Bulk	True	
Clinoptilolite – stilbite rock								
I	100	0	0	0	5.5	0.950	2.090	1.23
I′	100	0	166	2.16	2.6	0.635	2.258	1.12
I10′	90	10	166	2.16	2.6	0.651	2.141	1.19
I20′	80	20	166	2.16	3.5	0.558	1.932	1.28
I″	100	0	388	5.04	1.1	0.613	2.418	1.20
I10″	90	0	388	5.04	2.3	0.624	2.391	1.23
I20″	80	20	388	5.04	2.4	0.557	1.903	1.27
Clinoptilolite rock								
II	100	0	0	0	6.4	0.869	2.136	1.23
II′	100	0	166	2.16	1.3	0.518	2.218	1.27
II10′	90	10	166	2.16	2.7	0.538	2.309	1.37
II20′	80	20	166	2.16	3.5	0.534	1.898	1.40
II″	100	0	388	5.04	2.0	0.489	2.275	1.38
II10″	90	0	388	5.04	3.0	0.571	2.142	1.40
II20″	80	20	388	5.04	3.3	0.474	2.095	1.38

It was previously studied [11, 38] that the absorption bands corresponding to the valence vibrations of the siloxane bond are the most sensitive to mechanical effects. To evaluate the influence of the modifier (PEG) on the structural changes in the organomineral sorbent, the ratio of the intensities of the two most intense and susceptible to changes absorption bands due to the valence vibrations of siloxane and hydroxyl groups was calculated from the IR spectra. In addition, the porosity was calculated using formula (1). This is significant because of the existing relationship 'solid structure – sorption properties'. The final results of the calculations are summarized in Table 2.

Due to mechanical activation with an energy dose of 2.16 kJ·g^{-1}, the porosity of zeolite sorbents increases by ∼31 % for clinoptilolite-stilbite and clinoptilolite rocks (samples I′ and I; II′ and II). After applying a mechanical energy dose of 5.04 kJ·g^{-1}, this textural parameter increases by 36 and 34 % for the above rocks (samples I″ and I; II″ and II). A slight decrease (from 1 to 5 % compared to control samples) in the porosity of sorbents after their joint mechanical activation with polyethylene glycol is associated with partial blocking of pores by the polymer. The Si–OH bands of organomineral samples appear red- and blue-shifted to the same bands of mechanoactivated clinoptilolite zeolites (Table 2). The same characteristics calculated for PVA/zeolite [38] and PAA/zeolite [40] sorbents are included in the same table for comparative analysis. For modifiers containing functional groups in the compound repeating link, polyvinyl alcohol and polyacrylamide, with increasing polymer content, an increase in the relative intensity of the absorption band, as well as an increase in the porosity are observed. The maximum values of these parameters ($I_2/I_1 = 5.5$, $P = 78$ %) are observed in a sample of clinoptilolitic rock modified with 20 wt % PVA by mechanochemical method (Table 2), and the maximum value of oil capacity equal to 1.55 g·g^{-1} was registered in it [38]. The inverse regularity takes place for clinoptilolite-stilbite rock at its modification with polyethylene glycol. In this case, equal values of the ratio of the intensities of absorption bands and porosity (samples I20′; I20″, Table 2), as well as oil capacities (samples I20′; I20″, Table 1) were observed. This agrees with the conclusions described above based on the analysis of IR spectra of these samples.

TABLE 2. Relative intensity of a single absorption band in the IR spectra of polymer-modified zeolite samples and the porosity of the powder

Samples	Content, wt%		Time, t, s	Energy dose, D, kJ·g^{-1}	Ratio of intensities I_2/I_1	Shift a.b. $\Delta\nu_{\text{Si-OH}}$, cm^{-1}	Porosity, P, %
	Zeolite	Polymer					
The modifier is polyethylene glycol							
I′ / I″	Cl, St	—	166 / 388	2.16 / 5.04	2.15 / 2.73	0 / 0	72 / *75*
I10′ / I10″	Cl, St	10	166 / 388	2.16 / 5.04	2.11 / 2.40	−34 / —	70 / *75*
I20′ / I20″	Cl, St	20	166 / 388	2.16 / 5.04	1.73 / 1.73	— / —	71 / 71
II′ / II″	Cl	—	166 / 388	2.16 / 5.04	2.65 / 1.36	0 / 0	*77* / *79*
II10′ / II10″	Cl	10	166 / 388	2.16 / 5.04	2.74 / *3.79*	+4 / *−8*	*77* / *73*
II20′ / II20″	Cl	20	166 / 388	2.16 / 5.04	*3.18* / 1.86	*−27* / *+15*	*72* / *77*
The modifier is polyvinyl alcohol [38] / polyacrylamide [40]							
I′	Cl, St	—	180	2.16	2.50 / 2.60	0 / 0	68
I10′	Cl, St	10	180	2.16	*3.33* / 2.78	−3 / −13	*72* / 66
I20′	Cl, St	20	180	2.16	*3.33* / *3.57*	−3 / *−7*	*78* / 69
II′	Cl	—	180	2.16	*1.78* / *1.72*	0 / 0	67
II10′	Cl	10	180	2.16	*3.67* / 3.18	*+5* / −2	*73* / 69
II20′	Cl	20	180	2.16	*5.50* / 2.40	*+9* / −6	*78* / 71

Note. Cl – Clinoptilolite; St – Stilbite; I_2/I_1 – ratio of intensities of absorption bands with maxima at ∼ 1050 and ∼ 3620 cm^{-1}, corresponding to valence vibrations of Si–O–Si and OH-groups;

' — ' – there is no absorption band.

Modification of clinoptilolite-stilbite and clinoptilolite rocks by polyacrylamide and polyethylene glycol resulted in changes of porosity of samples by values from 2 to 5 %, and only addition of polyvinyl alcohol contributed to an increase of porosity by 9 % (I20) and 11 % (II20). It was calculated that the same high values of porosity ∼ 77 – 79 % are observed in samples of clinoptilolite rock mechanoactivated and modified with polyethylene glycol – II′; II10′, II20″, II″.

The relatively highest value of oil capacity ~ 1.4 g·g^{-1} is registered. The revealed regularities agree with the opinion [36] that the sorption capacity towards oil is determined by the diffusion of organic liquid through mesopores.

Porosity, in turn, is conveniently regulated by the mechanochemical method. It should be noted that the increase in porosity is accompanied by an increase in the ratio of intensities of absorption bands in the case of modification of clinoptilolite-stilbite and clinoptilolite rocks with polyvinyl alcohol and polyacrylamide (Table 2), and clinoptilolite rock with polyethylene glycol. However, such enhancement alone is not sufficient if, together with it, there is not a sufficient increase in the porosity of the organomineral sample. Consequently, in order for oil capacity to be approximately 1.4 g·g^{-1} at modification of clinoptilolitic rocks with water-soluble polymers (polyvinyl alcohol, polyacrylamide, polyethylene glycol), it is necessary that the ratio of absorption bands of Si–O–Si and OH-groups in the IR-spectrum was not less than 3.2 and, at the same time, the porosity was not less than 72 %.

In order to find out the influence of such factors as polymer content, structural changes, and porosity, the correlation analysis was carried out. The correlation coefficients were calculated and summarized in Table 3.

Analysis of the data in Table 3 showed that there is very strong dependence of oil capacity of mineral samples modified with polyvinyl alcohol on all three parameters ($r_{xy} > 0.91$), namely, polymer content, structural changes (ratio of intensities of absorption bands I_2/I_1) and porosity.

TABLE 3. Correlation coefficients between oil capacity and polymer content, ratio of absorption band intensities, porosity of sorbent powders resulting from the mechanochemical method

Polymers	Energy dose, D, kJ·g^{-1}	Clinoptilolite-stilbite rock			Clinoptilolite rock		
		r_{xy}, where y is a oil capacity and x is ...					
		weight of polymer	I_2/I_1	Porosity (P)	weight of polymer	I_2/I_1	Porosity (P)
PVA	2.16	0.9959	0.9078	0.9880	0.9954	0.9957	0.9991
PAA	2.16	0.0368	0.3757	0.9789	0.0908	−0.8392	0.0908
PEG	2.16	0.9974	−0.9341	−0.4364	0.9549	0.9605	−0.6717
PEG	5.04	−0.9803	−0.9938	−0.9632	0	0.9808	−0.9449

When using polyacrylamide as a modifier, a very strong dependence of oil capacity on porosity is observed for clinoptilolite-stilbite rock, and a fairly strong inversely proportional dependence on structural changes (the ratio of absorption band intensities) for clinoptilolite rock. At modification with polyethylene glycol and the mechanical energy dose of 2.16 kJ·g^{-1} for clinoptilolite-stilbite rock, there is a very strong direct dependence of oil capacity on the content of polyethylene glycol and its inverse dependence on structural changes and porosity. In this case, for clinoptilolite rock, there is a very strong direct dependence of oil capacity on the content of polyethylene glycol and on structural changes. In case of use of this modifier, an increase in mechanical energy dose from 2.16 to 5.04 kJ·g^{-1}, as a rule, contributes to approximation of correlation coefficients to the value -1 or $+1$. The exception is clinoptilolitic rock, the oil capacity of which does not depend on polymer content at all and is approximately 1.4 g·g^{-1}.

4. Conclusion

Organomineral sorbents based on clinoptilolite-stilbite and clinoptilolite rocks and safe synthetic polymer PEG-4000 were obtained by the method of 'soft' mechanoactivation in impact-attrition mode in an air atmosphere with processing times of 166 and 388 s, which corresponds to mechanical energy doses of 2.16 and 5.04 kJ·g^{-1}. The content of polyethylene glycol was 10 and 20 wt %.

It was found that mechanoactivation ($D = 2.16$ and 5.04 kJ·g^{-1}) of the powder leads to changes in bulk and true densities, hygroscopic moisture content of zeolite and PEG-zeolite sorbents. Infrared spectroscopy revealed that a more effective transformation of the structure, in the form of a decrease in the intensity and shift of the absorption band of free OH-groups and an increase in the intensity and shift of the absorption band of Si–O–Si groups, leads to a sorbent with improved sorption properties. Modification of clinoptilolitic rocks with polyethylene glycol leads to a decrease in bulk and true densities, an increase in hygroscopic humidity, and, as a rule, an increase in oil capacity. The oil capacity of clinoptilolite rock modified with 20 wt % PEG is ~ 1.4 g·g^{-1}, which is 8 – 15 % higher than that of analogues based on clinoptilolite-stilbite rock.

Comparative analysis of the data of mechanochemical modification of clinoptilolitic rocks with polyvinyl alcohol, polyacrylamide, and polyethylene glycol showed that organomineral samples having oil capacity not less than 1.4 g·g^{-1} exhibit, in infrared spectra, a ratio of intensity of absorption bands caused by vibrations of siloxane and hydroxyl groups not less than 3.2, and a porosity not less than 72 %. Calculation of correlation coefficients confirmed that the determining factors affecting the oil capacity of organomineral sorbents are the content of polyvinyl alcohol, structural changes, and

porosity. However, the oil capacity of clinoptilolite-stilbite rocks modified with polyacrylamide is strongly dependent only on the porosity. In this case, the required value of porosity for oil capacity increase is not achieved under mild mechanical action.

References

[1] Kakhki M.R., Zirjanizadeh S., Mohammadpoor M. A review of clinoptilolite, its photocatalytic, chemical activity, structure and properties: in time of artificial intelligence. *J. Mater. Sci.*, 2023, **58**, P. 10555–10575.

[2] Shojaeifar N., Mirzayi B., Saboor F.H. Highly efficient removal of MTBE using natural nanoporous adsorbents. *Int. J. Environ. Sci. Technol.*, 2024, **21**, P. 6553–6566.

[3] Grifasi N., Ziantoni B., Fino D., Piumetti M. Fundamental properties and sustainable applications of the natural zeolite clinoptilolite. *Environ. Sci. Pollut. Res.*, 2024, PMID: 38780851.

[4] Alsawalha M. Overview of current and future perspectives of Saudi Arabian natural clinoptilolite zeolite: a case review. *Hindawi. J. of Chemistry*, 2019, **3153471**, 16 p.

[5] Charkhi A., Kazemian H., Kazemeini M. Optimized experimental design for natural clinoptilolite zeolite ball milling to produce nano powders. *Powder Technology*, 2010, **203** (2), P. 389–396.

[6] Kuznetsov P.S., Dementiev K.I., Palankoev T.A., Kalmykova D.S., Malyavin V.V., Sagaradze A., Maksimov A.L. Synthesis of highly active nanozeolites using methods of mechanical milling, recrystallization, and dealumination (a review). *Pet. Chem.*, 2021, **61**, P. 649–662.

[7] Mukhtar N.Z.F., Borhan M.Z., Rusop M., Abdullah S. Nanozeolite produced by wet milling at different milling time. In: Gaol F., Webb J. (eds) *Recent trends in nanotechnology and materials science. Engineering Materials*. Springer, Cham. 2014.

[8] Seifi L., Torabian A., Kazemian H., Nabi R., Azimi A.A., Farhadi F., Nazmara Sh. Kinetic study of BTEX removal using granulated surfactant-modified natural zeolites nanoparticles. *Water Air Soil Pollut.*, 2011, **219**, P. 443–457.

[9] Amirsoleimani M., Khalilzadeh M.A., Zareyee D. Nano-sized clinoptilolite as a green catalyst for the rapid and chemoselective N-formylation of amines. *Reac Kinet Mech Cat.*, 2020, **131**, P. 859–873.

[10] Sydorchuk V., Vasylechko V.O., Khyzhun O., Gryshchouk G.V, Khalameida S., Vasylechko L. Effect of high-energy milling on the structure, some physicochemical and photocatalytic properties of clinoptilolite. *Applied Catalysis A-general*, 2021, **610**, 117930.

[11] Dabizha O.N., Derbeneva T.V., Khamova T.V., Shilova O.A. Controlling the sorption activity of clinoptilolites with mechanical activation. *Inorg. mater.*, 2021, **57** (4), P. 399–408.

[12] Jha V.K., Hayashi S. Modification on natural clinoptilolite zeolite for its NH_4^+ retention capacity. *J. Hazard Mater.*, 2009, **169** (1–3), P. 29–35.

[13] Buzimov A.Y., Kulkov S.N., Gömze L.A., Géber R., Kocserha I. Effect of mechanical treatment on the structure and properties of natural zeolite. *Inorg. Mater. Appl. Res.*, 2018, **9**, P. 910–915.

[14] Bohács K., Faitli J., Bokányi L., Mucsi G. Control of natural zeolite properties by mechanical activation in stirred media mill. *Archives of Metallurgy and Materials*, 2017, **62** (2), P. 1399–1406.

[15] Natsagdorj N., Lkhagvasuren N., Munkhjargal B., Temuujin J. Influence of co-milling oxide physical properties on the structural changes of natural clinoptilolite zeolites. *Mong. J. Chem.*, 2023, **24** (50), P. 27–32.

[16] Majano G., Borchardt L., Mitchell S., Valtchev V., Pérez-Ramírez J. Rediscovering zeolite mechanochemistry – A pathway beyond current synthesis and modification boundaries. *Microporous Mesoporous Mater.*, 2014, **194**, P. 106–114.

[17] Rainer D.N., Morris R.E. New avenues for mechanochemistry in zeolite science. *Dalton Trans.*, 2021, **50** (26), P. 8995–9009.

[18] Mohammed A.N. Adsorption efficiency of chitosan/clinoptilolite (CS/CZ) composite for effective removal of Cd^{+2} and Cr^{+6} ions from wastewater effluents of dairy cattle farms. *Environ. Monit. Assess*, 2024, **196**, 611.

[19] Miao J.L., Ren J.Q., Li H.J., Wu D.G., Wu Y.C. Mesoporous crosslinked chitosan-activated clinoptilolite biocomposite for the removal of anionic and cationic dyes. *Colloids Surf B Biointerfaces*, 2022, **216**, 112579.

[20] Li Z.C., Su M.Y., Yuan X.Y., Lv H.Q., Feng R., Wu L.J., Gao X.P., An Y.X., Li Z.W., Li M.Y., Zhao G.M., Wang X.P. Green fabrication of modified lignin/zeolite/chitosan-based composite membranes for preservation of perishable foods. *Food Chem.* 2024, **460** (3), 140713.

[21] Yıldız Yiğit M., Baran E.S., Moral Ç.K. A polymer – zeolite composite for mixed metal removal from aqueous solution. *Water Sci. Technol.*, 2021, **83** (5), P. 1152–1166.

[22] Baybaş D., Ulusoy U. Polyacrylamide-clinoptilolite/Y-zeolite composites: characterization and adsorptive features for terbium. *J. Hazard Mater.*, 2011, **187** (1–3), P. 241–249.

[23] Yu Y., Shapter J.G., Popelka-Filcoff R., Bennett J.W., Ellis A.V. Copper removal using bio-inspired polydopamine coated natural zeolites. *J. Hazard Mater.*, 2014, **273**, P. 174–182.

[24] Motsa M.M., Mamba B.B., Thwala J.M., Msagati T.A. Preparation, characterization, and application of polypropylene-clinoptilolite composites for the selective adsorption of lead from aqueous media. *J. Colloid Interface Sci.*, 2011, **359** (1), P. 210–219.

[25] Mollahosseini A., Rastegari M., Panahi-Dehghan M. Electrospun polyacrylonitrile/clinoptilolite coating for SPME of PAHs from water samples. *J. Chromatogr. Sci.*, 2022, **60** (4), P. 401–407.

[26] Olad A., Ahmadi Sh., Rashidzadeh A. Removal of Nickel (II) from aqueous solutions with polypyrrole modified clinoptilolite: kinetic and isotherm studies. *Desalination and water Treatment.*, 2013, **51** (37–39), P. 7172–7180.

[27] Yazdanbakhsh F., Alizadehgiashi M., Sawada J.A., Kuznicki S.M. A clinoptilolite-PDMS mixed-matrix membrane for high temperature water softening. *Water Sci. Technol.*, 2016, **73** (6), P. 1409–1417.

[28] Assar E., Meysami A., Zare M. Morphology analysis and characterization of clinoptilolite/polyvinylpyrrolidone-zeolite composite nanofibers. *J. of Mater. Eng. and Perform.*, 2020, **29**, P. 4233–4240.

[29] Savchenko I., Yanovska E., Sternik D., Kychkyruk O. Sorption properties of porous aluminosilicate minerals of Ukraine, in situ modified by poly[5-(*p*-nitrophenylazo)-8-methacryloxyquinoline] of toxic metal ions. *Appl. Nanosci.*, 2023, **13**, P. 7555–7567.

[30] Pazarçeviren E., Erdemli Ö., Keskin D., Tezcaner A. Clinoptilolite/PCL-PEG-PCL composite scaffolds for bone tissue engineering applications. *J. Biomater. Appl.*, 2017, **31** (8), P. 1148–1168.

[31] Jia B., Bing L., Xu B., Sun J., Bai S. Fabrication of functionalized UiO-66 anchored on disorderly layered clinoptilolite via surfactant-assisted induction for selective adsorption of CO_2 and CH_4. *Langmuir*, 2022, **38** (48), P. 14644–14655.

[32] Sadeghinia A., Soltani S., Aghazadeh M., Khalilifard J., Davaran S. Design and fabrication of clinoptilolite-nanohydroxyapatite/chitosan-gelatin composite scaffold and evaluation of its effects on bone tissue engineering. *J. Biomed. Mater. Res. A*, 2020, **108** (2), P. 221–233.

[33] Demirkiran A.R., Fullen M.A., Williams C.D. Comparative analysis of the physicochemical and oil adsorption characteristics of clinoptilolites from Turkey and the USA. *Oxidation Communications*, 2016, **39** (1–2), P. 787–807.

[34] Kalbuadi D.N., Goenadi D.H., Santi L.P., Nurtjahja, L.R. The potential use of natural clinoptilolite zeolite for crude oil spill removal from sea water. *J. of Minerals and Materials Characterization and Engineering*, 2019, **7**, P. 446–453.
[35] Bandura L., Woszuk A., Kolodynska D., Franus W. Application of Mineral Sorbents for Removal of Petroleum Substances: A Review. *Minerals*, 2017, **7**, P. 1–25.
[36] Muir B., Bajda T. Organically modified zeolites in petroleum compounds spill cleanup – Production, efficiency, utilization. *Fuel Processing Technology*, 2016, **149**, P. 153–162.
[37] Bugatti V., Bernardo P., Clarizia G., Viscusi G., Vertuccio L., Gorrasi G. Ball milling to produce composites based of natural clinoptilolite as a carrier of salicylate in bio-based PA11. *Polymers (Basel)*, 2019, **11** (4), 634.
[38] Dabizha O.N., Khamova T.V., Shilova O.A. Mechanochemical modification of zeolite rocks with polyvinyl alcohol for increasing their oil sorptium capacity. *Inorg. mater.*, 2022. **58** (12), P. 1335–1347.
[39] Method of production of organomineral sorbents (versions), Patent. 2184607 Russia: MPK B 01 J 20/26, 20/12, 20/32, C 02 F 1/56, Shapkin N.P., N 2000121520/04, Issue N , p. 8.
[40] Dabizha O.N., Khamova T.V., Shilova O.A. Mechanochemical modification of zeolite rocks with polyacrylamide for the production of oil sorbents. *Inorg. mater.*, 2023, **59** (10), P. 1127–1139.
[41] Fang Q., Liu X., Wang Na, Ma Chi, Yang F. The effect of zeolite particle modified by PEG on rubber composite properties. *Sci. Eng. Compos. Mater.*, 2015, **22** (6), P. 607–612.
[42] Toommee S., Pratumpong P. PEG-template for surface modification of zeolite: A convenient material to the design of polypropylene based composite for packaging films. *Results in Phisycs*, 2018, **9**, P. 71–77.
[43] Choopani L., Salehi M.M., Mashhadimoslem H., Khosrowshahi M.S., Rezakazemi M., AlHammadi A.A., Elkamel A., Maleki A. Removal of organic contamination from wastewater using granular activated carbon modified – Polyethylene glycol: Characterization, kinetics and isotherm study. *PLoS ONE*, 2024, **19** (7), e0304684.
[44] Gao N., Du J., Yang W., Sun B., Li J., Xia T., Li Y., Yang Ch., Liu X. Bio-based sunflower carbon/polyethylene glycol shape-stabilized phase change materials for thermal energy storage. *RSC Adv.*, 2024, **14**, 24141.
[45] Detrekoy E.J., Jacobs P.A., Kallo D., Uytterhoeven J.B. The nature of catalytic activity of hydroxyl groups in clinoptilolite. *J. of Catalysis*, 1973, **32**, P. 442–452.

Submitted 20 January 2025; revised 2 July 2025; accepted 21 August 2025

Information about the authors:

Olga N. Dabizha – Transbaikal State University, Aleksandro-Zavodskaya, 30, Chita, 672039, Russia; Branch of the Petersburg Nuclear Physics Institute named by B.P. Konstantinov of National Research Centre “Kurchatov Institute” – Institute of Silicate Chemistry, Makarova emb., 2, St. Petersburg, 199034, Russia; ORCID 0000-0002-8633-8082; dabiga75@mail.ru

NANOSYSTEMS:
PHYSICS, CHEMISTRY, MATHEMATICS

Kruchinin N.Yu. *Nanosystems: Phys. Chem. Math.*, 2025, **16** (5), 650–659.
http://nanojournal.ifmo.ru
DOI 10.17586/2220-8054-2025-16-5-650-659

Original article

Controlled release of homogeneous polypeptides from carbon nanotubes with varying PH: molecular dynamics simulation

Nikita Yu. Kruchinin[1,a]

[1]Orenburg State University, Center of Laser and Informational Biophysics, Orenburg, Russia

[a]kruchinin_56@mail.ru

Corresponding author: N. Yu. Kruchinin, kruchinin_56@mail.ru

PACS PACS 36.20.-r, 02.70.Ns, 61.46.+w

ABSTRACT Using molecular dynamics simulation at different pH levels, changes in the conformations of homogeneous polypeptides located singly or in pairs inside a carbon nanotube were studied. The radial distributions of the density of polypeptide atoms, the distribution of macrochain atoms along the nanotube axis, and the dependences of various components of the potential energy of the nanosystem were calculated. At the isoelectric point, the polypeptides were located in the central part of the carbon nanotube, spreading out along its walls. As the pH level deviated from the isoelectric point, the polypeptide located singly inside the carbon nanotube first unfolded and stretched along its axis, and when almost all links of the macromolecule acquired an electric charge, it exited the nanotube. Polypeptides located in pairs inside the carbon nanotube repelled each other with a change in the pH value and shifted to opposite ends of the nanotube, being released from it.

KEYWORDS molecular dynamics, carbon nanotube, polypeptide, pH, conformation, controlled release.

ACKNOWLEDGEMENTS The study was carried out with the financial support of the Ministry of Science and Higher Education of the Russian Federation within the framework of a grant for conducting large scientific projects in priority areas of scientific and technological development 075-15-2024-550.

FOR CITATION Kruchinin N.Yu. Controlled release of homogeneous polypeptides from carbon nanotubes with varying PH: molecular dynamics simulation. *Nanosystems: Phys. Chem. Math.*, 2025, **16** (5), 650–659.

1. Introduction

Currently, hybrid nanosystems consisting of carbon nanotubes with polymer macromolecules are widely used in the creation of various electrochemical and optical biosensors [1–7], as well as nanocarriers for drug delivery [8–10]. Flexible and uncharged peptide and lipid molecules are adsorbed on the outer surface of the carbon nanotube and form a polymer shell [11,12]. Highly charged and rigid macromolecules of polyelectrolytes, such as DNA [13] or synthetic polymers [14], wrap around the carbon nanotube. A similar nature of conformational changes in polypeptides was observed in molecular dynamics simulation on the surface of metal nanoparticles of various shapes (spherical, cylindrical and spheroidal) [15–18].

A different picture will be observed when polymer molecules are located inside a single-walled carbon nanotube. A number of studies have investigated the encapsulation of peptides inside a carbon nanotube, the transport of peptides under the influence of an external electric field inside a carbon nanotube and the pulling of short peptides through it, as well as the release of protein and peptide molecules encapsulated in a carbon nanotube under the influence of an external electric field [19–28]. In papers [20, 21], it was shown that a peptide molecule is encapsulated inside a carbon nanotube and oscillates near the center of the nanotube, where the Van der Waals interaction energy between the peptide and the carbon nanotube is minimal. It was shown that carbon nanotubes are capable of capturing peptide and protein molecules, with shorter nanotubes capable of encapsulating a peptide with a lower potential well depth [20, 21].

When the pH level changes, the conformations of peptides change significantly [29–31]. This is due to the fact that the more the value of the hydrogen index differs from the value of the isoelectric point of the peptide, the greater the charge acquired by the macromolecule, which becomes polyelectrolyte. In this case, the rigidity of the macrochain increases increasingly due to the repulsion of the polypeptide links from each other. Therefore, if the polypeptide is inside a carbon nanotube, then when the hydrogen index of the environment changes, its conformational structure should also change. And this can lead to the release (decapsulation) of the macromolecule located inside the carbon nanotube. Small medicinal or photoactive molecules can be associated with the polypeptide located inside the carbon nanotube. When the pH of the medium changes and, accordingly, the conformational structure of the polypeptide undergoes a significant restructuring, small molecules can be decapsulated from the nanotube separately or together with the macrochain. This effect can be used to create a nanocontainer with a controlled release of drugs or photoactive label molecules when the pH of the medium changes.

Of great interest is also the restructuring of the conformations of several polypeptide molecules located inside the carbon nanotube when the pH level changes. If the molecules of homogeneous polypeptides have the same composition of amino acid residues, then when the pH value deviates from the isoelectric point, they are charged with the same charge sign. This leads to the repulsion of like-charged polypeptides from each other and to a significant change in their configuration inside the carbon nanotube, which can lead to the expulsion of macromolecules from the carbon nanotube.

Thus, the aim of this work is to study changes in the conformational structure of macromolecules of homogeneous polypeptides located inside a single-layer carbon nanotube, singly and in pairs, when changing pH.

2. Molecular dynamics simulation

Full-atom molecular dynamics (MD) simulations were performed using the NAMD 2.14 software package [32] for a molecular system in which one or two identical polypeptide molecules were located inside a carbon nanotube. A single-walled carbon nanotube with a length of 30 nm, a diameter of about 6 nm, and a chirality of n = 45 and m = 45 was considered. The atoms of the nanotube remained fixed during the simulation.

The choice of a carbon nanotube of such a diameter was due to the need to place a polypeptide macromolecule in a coil conformation in the starting configuration, which had a sufficiently large size, inside it. In works [20–22], the processes of encapsulation of shorter peptides in a carbon nanotube of different diameters (from 2.2 to 3.8 nm) were considered, and with equal chirality indices n=m. Therefore, in this work, a carbon nanotube with the same chirality indices was also considered. In general, for nanotubes of the same diameter, but with different chirality indices, the results should not change significantly, since the main contribution to the encapsulation of peptides and their adsorption inside a carbon nanotube is made by the Van der Waals interaction of the peptide with the walls of the nanotube. Since the number of atoms for nanotubes of similar diameter, but with different chirality will be almost the same, then in general the interaction of the peptide with the walls of the carbon nanotube will be the same, and therefore the decapsulation of the macrochain will occur under the same conditions.

The pH level was changed indirectly, as was done in [29]. MD simulation was performed for polypeptides consisting of 100 amino acid residues of glutamic acid at different pH values. In the range of pH≈6–8, corresponding to a neutral medium, all amino acid residues of glutamic acid Glu have a negative charge of $-1e$ according to the titration curve. When the increasing of the acidity of the medium and the decreasing of the pH value begins, the proportion of amino acid residues in the polypeptide changes. It leads to changing their charge and becoming neutral Glu^0 [29]. Upon reaching the isoelectric point pI=3.22, all amino acid residues of glutamic acid in the macrochain become uncharged Glu^0.

In this work, a series of polypeptides from glutamic acid units with different proportions of neutral and negatively charged amino acid residues were considered, which corresponded to the state of the polyglutamate macrochain at pH values in the range from the isoelectric point pI=3.22 to a neutral environment pH≈6–8:

1) Glu_{100} polypeptide (total charge of the macrochain $-100e$) which corresponds to the values of pH≈6–8 according to the titration curve;

2) polypeptide $(Glu_{10}Glu^0Glu_9)_5$ (total charge $-95e$) which corresponds to the value of pH≈5.8;

3) polypeptide $(Glu_5Glu^0Glu_4)_{10}$ (total charge $-90e$), pH≈5.5;

4) polypeptide $(Glu_2Glu^0Glu_2)_{20}$ (total charge $-80e$), pH≈5;

5) polypeptide $(GluGlu^0Glu)_{33}Glu$ (total charge $-67e$), pH≈4.6;

6) polypeptide $(GluGlu^0)_{50}$ (total charge $-50e$), pH≈4.3;

7) polypeptide $(Glu^0GluGlu^0)_{33}Glu^0$ (total charge $-33e$), pH≈4;

8) polypeptide $(Glu^0_2GluGlu^0_2)_{20}$ (total charge $-20e$), pH≈3.8;

9) polypeptide $(Glu^0_5GluGlu^0_4)_{10}$ (total charge $-10e$), pH≈3.6;

10) polypeptide $(Glu^0_{10}GluGlu^0_9)_5$ (total charge $-5e$), pH≈3.4;

11) polypeptide Glu^0_{100} (uncharged macromolecule) at the isoelectric point pI=3.22.

For charged amino acid residues of glutamic acid, the CHARMM36 force field was used [33, 34], and to describe amino acid residues of glutamic acid in the neutral form, the interaction potentials developed in [35] and expanding the CHARMM36 force field were used. The parameters for the carbon atoms of the nanotube were set to the same as for the CA type atoms of the CHARMM36 force field, which are used to describe benzene molecules [36]. The van der Waals potential was cut off at a distance of 1.2 nm using a smoothing function between 1.0 and 1.2 nm. Electrostatic interactions were calculated directly at a distance of 1.2 nm, for larger distances the particle-mesh Ewald (PME) method [37] with a grid step of 0.11 nm was used. The entire molecular system was placed in a parallelepiped with edge dimensions of 54×18×18 nm, filled with TIP3P water molecules [38]. In total, more than 560 thousand water molecules were placed in the simulation area. Water molecules were also located inside the carbon nanotube. The interaction of water molecules with the polypeptide was also described using the CHARMM36 force field, including electrostatic interactions between partial charges of water molecules and the polypeptide, as well as Van der Waals interactions between atoms of water molecules and the polypeptide via the Lennard-Jones potential. The MD simulation was performed at a constant temperature of 300 K (NVT, Berendsen thermostat). The length of the time trajectory reached 30 ns, the simulation step was 1 fs.

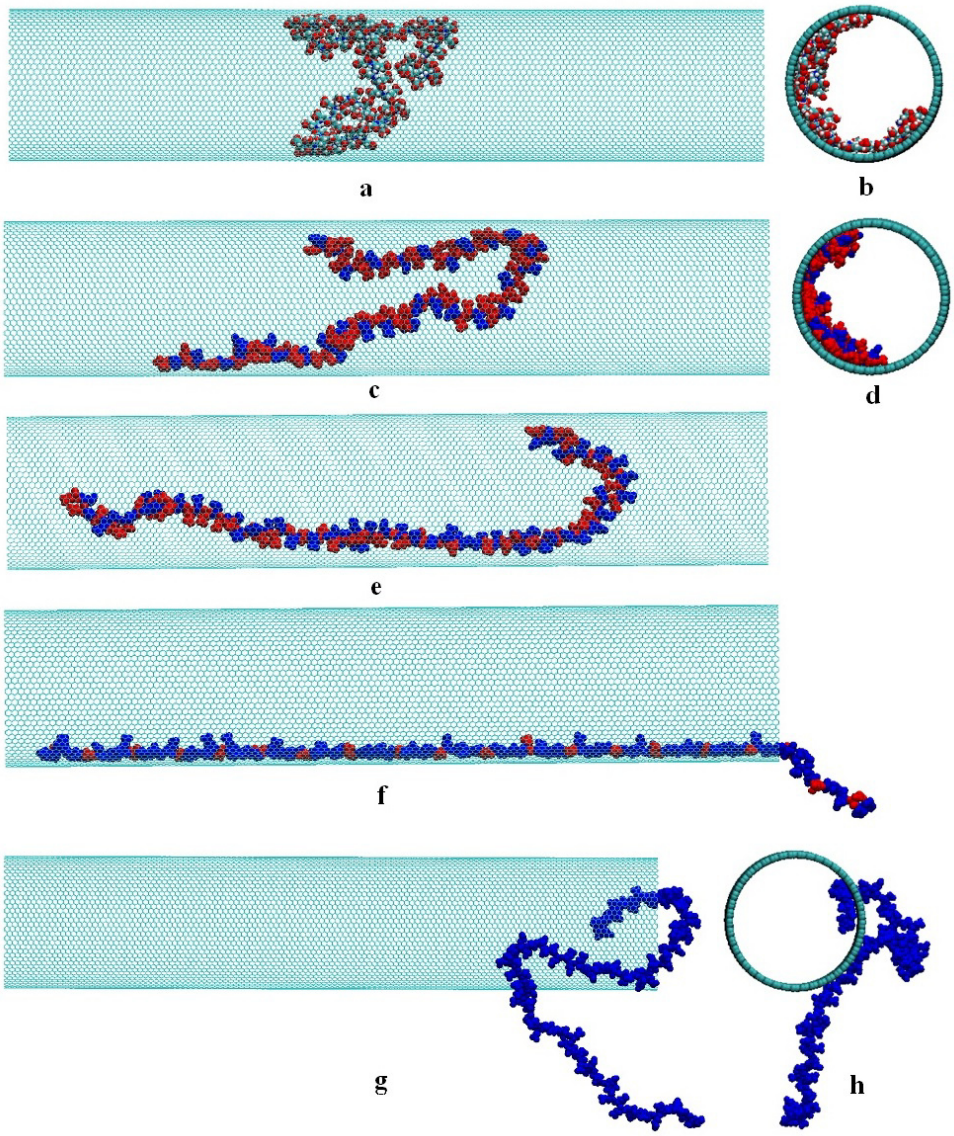

FIG. 1. A single polypeptide of 100 glutamic acid units inside a carbon nanotube after modeling at the isoelectric point pI=3.22 (a, b, each atom is shown in its own color), pH≈4 (c and d), pH≈4.3 (e), pH≈5 (f), pH≈6–8 (g and h). Water molecules are not shown for clarity; in figures c–h, uncharged amino acid residues Glu^0 are shown in red, and negatively charged Glu are shown in blue (a, c, e, f, g – side view, b, d and h – end view)

First, we considered the case when one or two macromolecules of the Glu^0_{100} polypeptide were located inside the carbon nanotube at a pH value equal to the isoelectric point pI=3.22, i.e. when the polypeptides were generally neutral. At the initial moment, the polypeptides were in the form of nonequilibrium coils inside the carbon nanotube. As a result of the modeling, adsorption of both a single macrochain (Fig. 1) and a system of two identical polypeptides (Fig. 5) on the inner surface of the carbon nanotube was observed. The obtained equilibrium structures of the polypeptides at the isoelectric point were subsequently used as starting ones at pH values in the range from 3.22 to 6–8. Three different starting conformations were considered for both a single polypeptide and a complex of two identical polypeptides inside the carbon nanotube.

Based on the results of modeling in the case of adsorption of a macrochain on the inner wall of a carbon nanotube, radial distributions of the density of polypeptide atoms, as well as the distribution of macrochain atoms along the nanotube axis were calculated for all the conformations obtained. The dependences of various components of the potential energy of the nanosystem (total, Van der Waals, electrostatic, as well as torsion angles of the polypeptide) were also calculated when changing the conformational structure of the polypeptide inside the carbon nanotube.

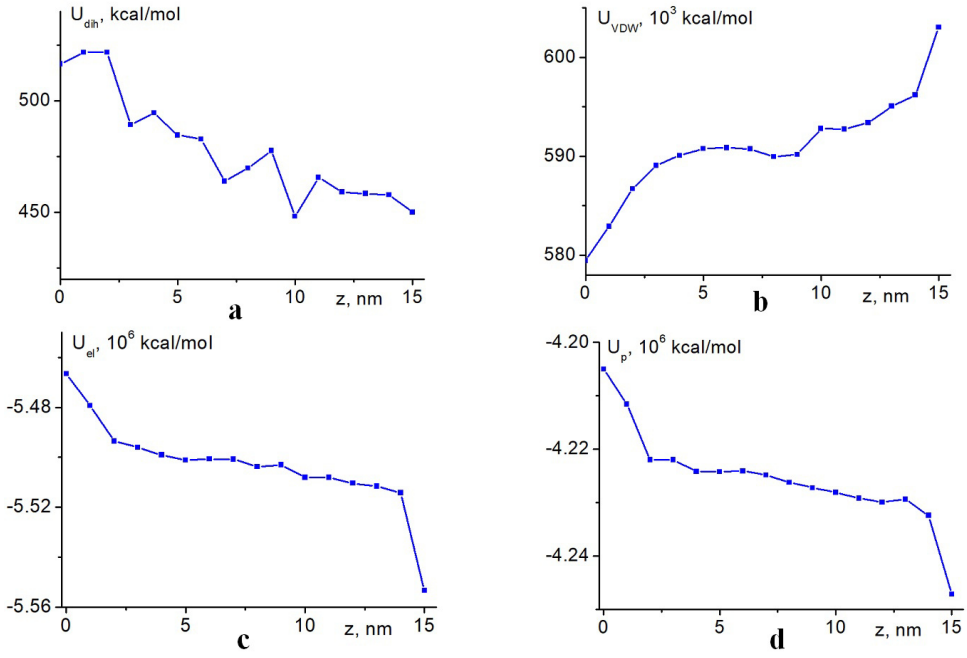

FIG. 2. Dependences of the potential energy of torsion (dihedral) angles (a), van der Waals (b), electrostatic (c) and total potential energy (d) of a single polypeptide inside a carbon nanotube as the center of mass of the macrochain moves away from the center of the nanotube along the axis at pH≈6–8

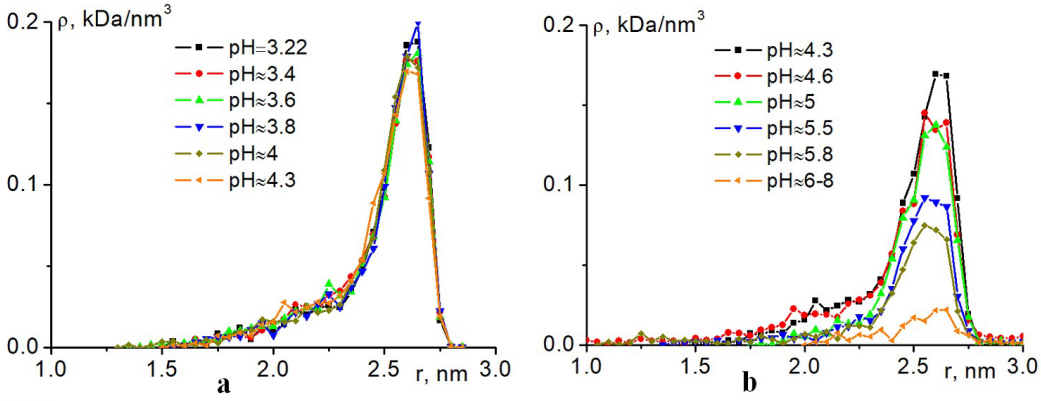

FIG. 3. Radial dependences of the average density of atoms of a single polyglutamate macrochain inside a carbon nanotube at the end of the simulation for different values of pH: a) from 3.22 to 4.3, b) from 4.3 to 6–8

3. Results

3.1. Conformational changes of a single polypeptide macrochain inside a carbon nanotube with pH changes

Figures 1a,b show a single macromolecule of a polypeptide consisting of 100 glutamic acid units after molecular dynamics simulation inside a carbon nanotube at the isoelectric point pI=3.22. In this case, the Glu^{0}_{100} macromolecule has a zero electric charge overall and is adsorbed on the inner surface of the nanotube. This is in good agreement with the results obtained in [20–23], where it was shown that the peptide is encapsulated inside a carbon nanotube and this arrangement of the peptide is the most energetically favorable.

As the pH value increased and the isoelectric point deviated, more and more polyglutamate units acquired a negative charge. Therefore, due to the increasingly strong repulsion of the links from each other and, accordingly, the increase in rigidity and persistent length of the macrochain, the polypeptide unfolded more and more (Figs. 1c,d). The macromolecule, initially adsorbed quite compactly on the inner surface of the nanotube (Fig. 1a), began to partially stretch along the nanotube starting from the pH value of pH≈4.3 (Fig. 1e), that is, when half of the polypeptide links became negatively charged. Starting with the values of the hydrogen index pH≈5, partial decapsulation of the polypeptide from

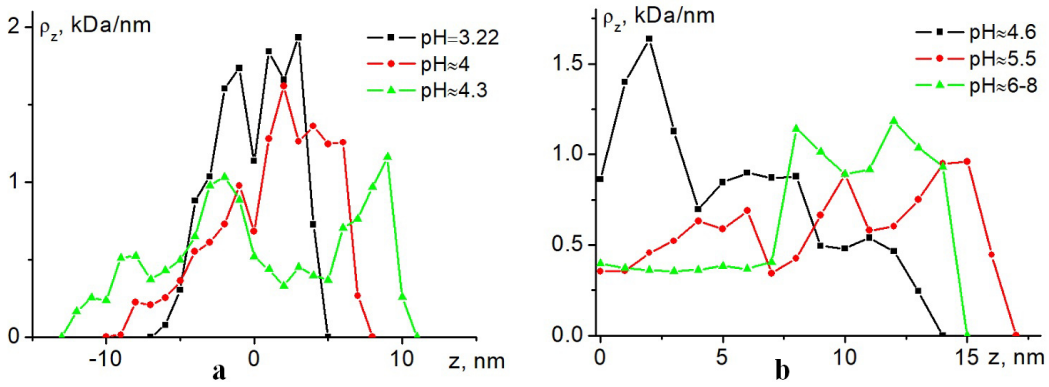

FIG. 4. Distributions of the average linear density of atoms of a single polypeptide from glutamic acid units at the end of the simulation at different values of pH from 3.22 to 4.3 along the axis of the carbon nanotube. b) Distribution of absolute values of the average linear density of atoms of a single polyglutamate with increasing distance from the center (z=0) of the nanotube along the axis of the nanotube at values of pH from 4.6 to 6–8

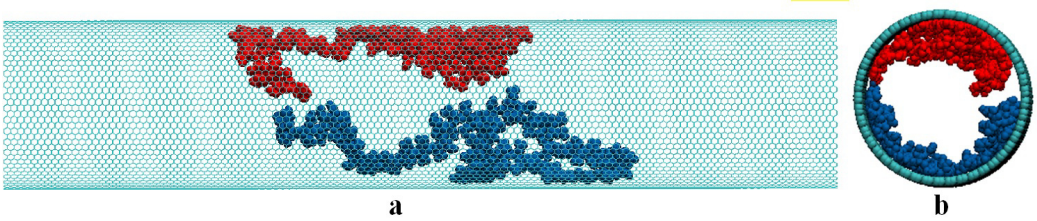

FIG. 5. Two polyglutamate macromolecules after modeling inside a carbon nanotube after MD simulation at pI=3.22 (a – side view, b – end view, the one shown in red and the second one in blue)

the carbon nanotube to the outside began to occur (Fig. 1f). In the case of an increase in the hydrogen index to pH≈5.8-8, when all or almost all links of the polypeptide became negatively charged, decapsulation of the polypeptide from the nanotube occurred (Figs. 1g,h). In this case, the polypeptide was concentrated near one of the ends of the carbon nanotube.

Figure 2 shows the dependences of the potential energy of torsion (dihedral) angles, as well as van der Waals, electrostatic and total potential energy of a single polypeptide of 100 glutamic acid units inside a carbon nanotube as the center of mass of the macrochain moves away from the center of the nanotube (z=0) at pH≈6-8. The position of the center of mass of the polypeptide at a distance of 15 nm from the center of the nanotube corresponds to the displacement of the macromolecule to the edge of the nanotube (Fig. 1g,h). It can be seen that the potential energy of the torsion angles gradually decreases as the polyelectrolyte unfolds and exits the nanotube (Fig. 2a). In this case, the potential energy of van der Waals interactions during decapsulation of the polypeptide gradually increased (Fig. 2b), which is in good agreement with the dependence of the energy of van der Waals interactions of the peptide with the carbon nanotube presented in [20, 21]. However, in this case, a more significant decrease in the electrostatic energy of the nanosystem occurred (Fig. 2c), which made the greatest contribution to the change in the total potential energy of the nanosystem, which also decreased when the charged polypeptide was shifted to the edge of the carbon nanotube (Fig. 2d). Thus, for the charged macrochain, the conformation in which the polypeptide was located on the outside at the edge of the carbon nanotube turned out to be energetically favorable.

Figure 3 shows a comparison of the radial dependences of the average atomic density of a single polypeptide made of glutamic acid units inside a carbon nanotube at the end of the simulation at different pH values from 3.22 to 4.3 (Fig. 3a) and from 4.3 to 6–8 (Fig. 3b). It is evident that in the range of pH values from 3.22 to 4.3 (Fig. 3a), that is, from the case of a neutral macromolecule to a half-charged one, the density of polypeptide atoms inside the carbon nanotube changed insignificantly, since most of the polypeptide units were adsorbed on its inner surface. In this case, a characteristic maximum of the macrochain atom density is observed near the surface of the nanotube [18], and the radial distribution curve of the average atomic density of the polypeptide drops to zero at approximately half the radius of the carbon nanotube. With an increase in the pH value from 4.3 to 6–8 (Fig. 3b), a significant decrease in the density of polyglutamate atoms inside the carbon nanotube is observed. This is due to the gradual release of the polypeptide from the carbon nanotube as the pH increases (Fig. 1g,h).

Figure 4a shows the distributions of the average linear density of atoms of a single polyglutamate macromolecule along the carbon nanotube axis at the end of the simulation at different values of pH in the range from 3.22 to 4.3. It is evident that at the isoelectric point pI=3.22 the macrochain was concentrated in the center of the carbon nanotube (Fig. 4a,

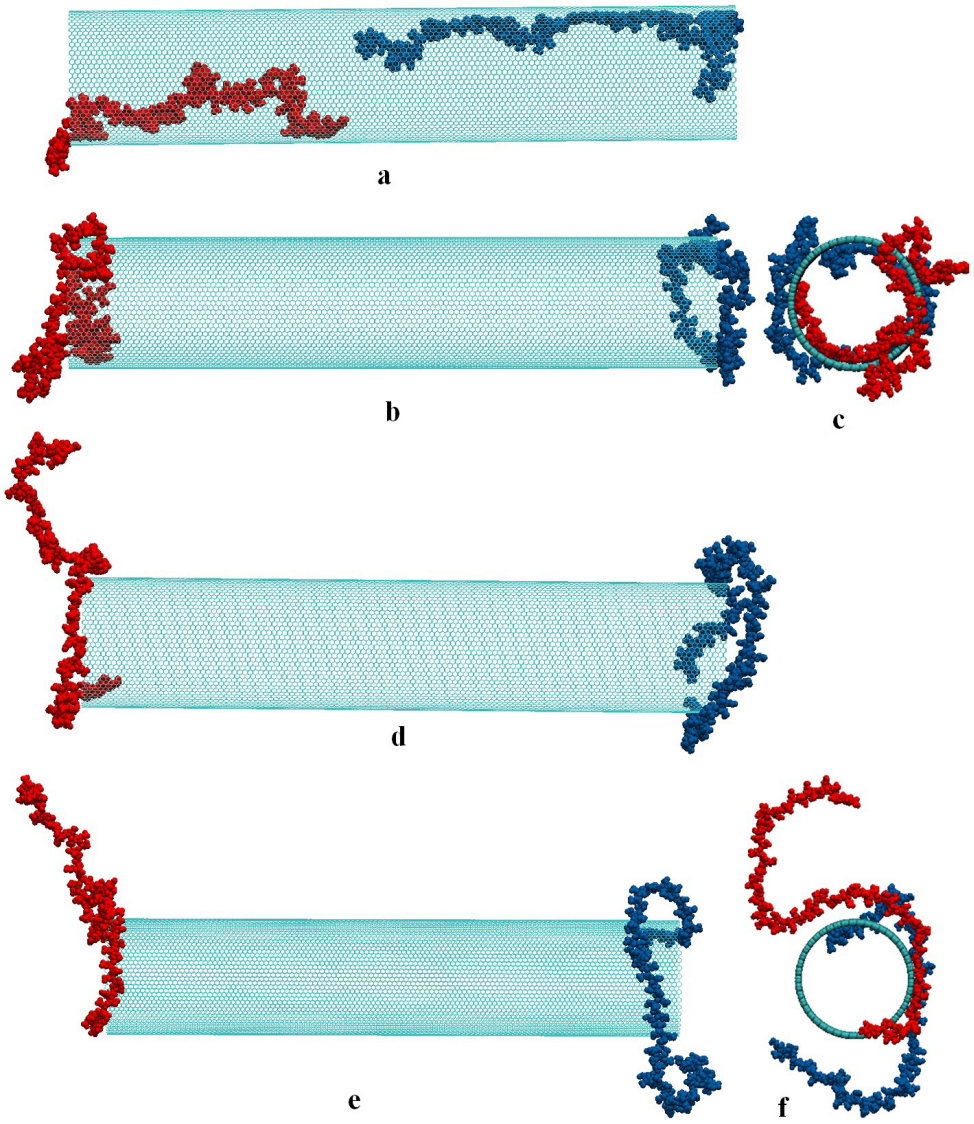

FIG. 6. Two macromolecules of glutamic acid units after modeling inside a carbon nanotube at different pH values: pH≈4 (a), pH≈4.3 (b and c), pH≈5 (d), and pH≈6–8 (e and f). The first polypeptide is shown in red, and the second one in blue (a, b, d, e – side view, c, f – end view)

zero along the z axis). As the hydrogen index increases, the distribution profile of the average density of polypeptide atoms along the nanotube axis broadens due to the increase in the rigidity of the macrochain and its stretching along the nanotube axis.

In Fig. 4b, the distributions of absolute values of the average linear density of atoms of a single polyglutamate are shown with increasing distance from the center (z=0) along the nanotube axis at pH from 4.6 to 6–8. It is evident that even at pH≈4.6 the macrochain is concentrated mainly in the center of the nanotube, and at pH≈5.5 most of the polypeptide links are already shifted to the end of the nanotube, which is associated with the partial exit of the polypeptide to the outside. At pH≈6–8 the fully charged macrochain is mostly decapsulated and is located at the end of the carbon nanotube, partially wrapping around it from the outside (Figs. 1g,h).

3.2. Conformational changes of two identical homogeneous polypeptides inside a carbon nanotube with pH changes

A different picture was observed when two identical macromolecules of homogeneous polypeptides were located inside the carbon nanotube. At the initial moment of time at the isoelectric point pI=3.22 they were adsorbed on the inner surface of the carbon nanotube (Fig. 5).

As the pH value increased, the polypeptides gradually became negatively charged, which increased their rigidity and their unfolding inside the carbon nanotube. At the same time, the charged links of the both polypeptides began to repel

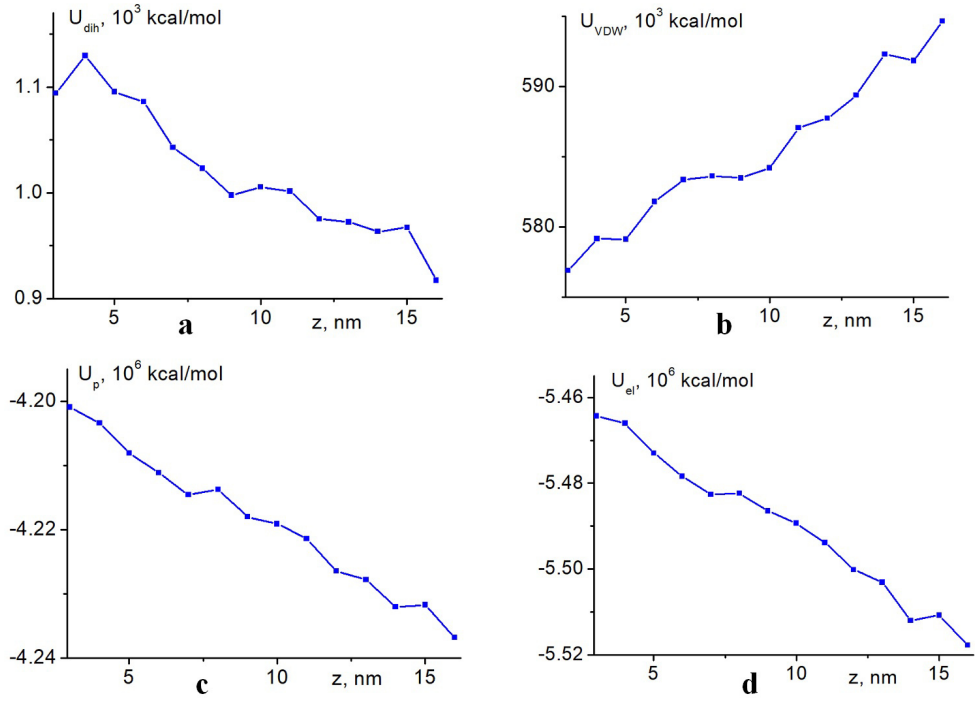

FIG. 7. Dependences of the potential energy of torsion (dihedral) angles (a), van der Waals (b), electrostatic (c) and total potential energy (d) of two polypeptides from glutamic acid units as a function of the average deviation of the centers of mass of the polypeptides from the center of the carbon nanotube along the axis at pH≈6–8

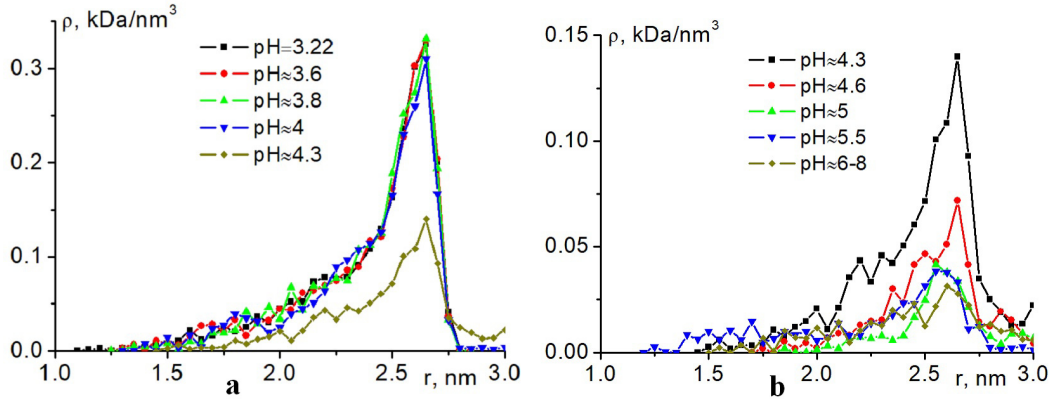

FIG. 8. Total radial dependences of the average density of atoms of two polyglutamate macromolecules inside a carbon nanotube at different values of pH: a) from 3.22 to 4.3, b) from 4.3 to 6–8

each other more and more strongly, which led to the macromolecules shifting outward to the two opposite ends of the nanotube (Fig. 6).

Figure 6a shows that even with a small charge of the macrochain and a small deviation from the isoelectric point (pH≈4), the polyglutamate molecules begin to shift away from each other. And when half of all the polypeptide links became negatively charged (pH≈4.3), both charged macromolecules shifted to opposite ends of the carbon nanotube (Figs. 6b,c). A further increase in the pH did not lead to desorption of the polypeptides, but an increasing unfolding of the macrochains was observed due to an increase in their rigidity with the ends of the polypeptides being thrown out into the surrounding space. At the same time, the macrochain remained at the ends of the carbon nanotube, partially wrapping around them (Figs. 6d-f).

Figure 7 shows the dependences of the potential energy of two polyglutamate molecules inside a carbon nanotube on the average deviation of the centers of mass of the polypeptides from the center of the nanotube along the axis at a hydrogen index of pH≈6–8. The z axis shows the average absolute value of the distance of the centers of mass of the polypeptides from the center of the nanotube: at z=15 nm, the polypeptides are at the opposite edges of the nanotube (Fig. 6e,f). It is evident that the potential energy of the torsion angles, as in the case of a single macrochain, gradually

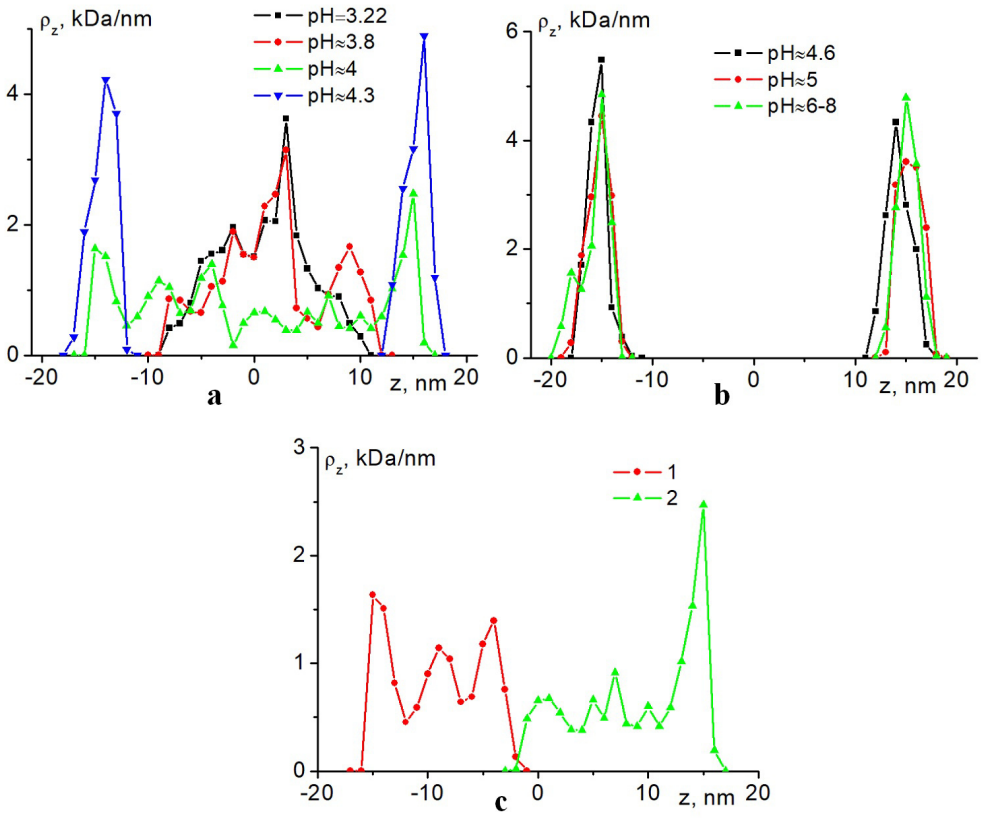

FIG. 9. Total distributions of the average linear density of atoms of two polyglutamate macromolecules along the axis of a carbon nanotube at different values of pH: a) from 3.22 to 4.3, b) from 4.6 to 6–8. c) Distributions of the linear density of atoms of two polyglutamate macromolecules separately (1 and 2) at pH≈4

decreased as the polypeptides unfolded and decapsulated from the nanotube (Fig. 7a). At the same time, the potential energy of van der Waals interactions increased (Fig. 7b). The electrostatic energy of the nanosystem decreased much more strongly when the polypeptides were shifted to the edges of the nanotube (Fig. 7c), as in the case of a single polypeptide molecule inside a carbon nanotube. Therefore, the total potential energy of the nanosystem consisting of two charged polypeptides inside a carbon nanotube also decreased upon their decapsulation (Fig. 7d). Thus, as in the case of a single polyelectrolyte, the most energetically favorable conformations were those in which the charged polypeptides were located outside at the ends of the carbon nanotube.

Figure 8 shows the total radial dependences of the average atomic density of two polypeptides from glutamic acid units inside a carbon nanotube at different pH values. It is evident that while both macromolecules are inside the carbon nanotube, i.e. at pH values from 3.22 to 4, the curves of the total radial distributions of their atomic density are very close to each other (Fig. 8a). The radial distribution peaks for the atomic density of the macrochains decreased as the polypeptides moved outward from the nanotube. (Fig. 8b). At the same time, the radial distributions of the average density of each of the polypeptides separately at all pH values were similar to each other.

Figure 9 shows the distributions of the average linear density of atoms of two polyglutamate macromolecules at different pH values along the carbon nanotube axis. At pH$<$4, the atoms of both macrochains are concentrated in the central part of the nanotube (Fig. 9a). At pH≈4, the profile of the total linear distribution of the density of polypeptide atoms spreads out along the entire length of the carbon nanotube (Fig. 9a), while the profiles of the linear density of atoms for individual polypeptides (Fig. 9c) hardly intersect. The case of the location of polypeptides at different ends of the carbon nanotube (pH≈4.3) corresponds to separate profiles of the linear distributions of the density of atoms with peaks at the ends of the nanotube: about -15 nm and $+15$ nm along the z axis (Figs. 9a,b).

4. Conclusion

When the pH value deviated from the isoelectric point, the single polypeptide macrochain adsorbed inside the carbon nanotube unfolded more and more and stretched along the nanotube. When all or almost all the polypeptide links became charged, the polypeptide was decapsulated from the carbon nanotube. Thus, by changing the charge of the links and, thereby, the rigidity of the macrochain, it is possible to control the release of the polypeptide molecule encapsulated [20, 21] inside the carbon nanotube. When two identical homogeneous polypeptides were located on the inner surface of the

carbon nanotube, then in case when the pH level deviated from the isoelectric point, they shifted outward to two opposite ends of the nanotube. In this situation, the release of charged macromolecules from the carbon nanotube began to occur when half of the amino acid residues of the polypeptide acquired an electric charge, that is, with a significantly smaller deviation of the pH value from the isoelectric point compared to a single polypeptide. Obviously, further increase in the number of polypeptides inside the carbon nanotube leads to even stronger repulsion of macromolecules from each other when the pH level deviates from the isoelectric point. This can cause not only the exit of polypeptides from the central part of the carbon nanotube to its ends, but also the desorption of macromolecules.

It should be noted that the ends of the carbon nanotube can be oxidized by carboxyl or hydroxyl groups, the presence of which can worsen both the capillary absorption of the polypeptide and complicate the release of the polypeptide from the carbon nanotube. The role of foreign ions was also not taken into account in this study.

If the encapsulated polypeptide contains small medicinal or photoactive molecules in the structure of its macrochain at the isoelectric point, then upon decapsulation of the polypeptide from the carbon nanotube, they can be released from the carbon nanotube or will be concentrated together with the macromolecule near its ends.

Thus, a nanosystem with one or more polypeptides inside a carbon nanotube can be used as a nanocontainer sensitive to changes in the pH of the medium. Encapsulation [20, 21] of polypeptides in a nanotube will be carried out at the isoelectric point, and decapsulation of macrochains will occur at a pH value significantly different from the isoelectric point characteristic of a certain composition of amino acid residues of the polypeptide. Instead of a homogeneous polypeptide, any polypeptide with amino acid residues of different types can be used. Since polypeptides with different sets of links have their own isoelectric point value, then by changing the combination of amino acid residues in the polypeptide, it is possible to select a pH value corresponding to an acidic, alkaline or neutral medium, at which the substances contained therein will be released from the carbon nanotube.

In addition, such a nanosystem can be used as a sensor element sensitive to changes in the hydrogen index of the medium. For example, in a luminescent-optical meter of the concentration of molecular (including singlet) oxygen, the operation of which is sensitive to changes in the conformational structure of a macromolecular chain in a nanopore or nanotube, with photoactive molecules (dyes) contained in the structure of the macromolecule [39]. The non-uniform distribution of photoactive centers associated with the macrochain inside a carbon nanotube has a significant effect on the kinetics of two-stage photoreactions involving electronically excited dye molecules and oxygen, and the shape of the pulse signal of delayed fluorescence depends on this [39]. Therefore, a significant change in the conformational structure of polypeptides together with dye molecules inside a carbon nanotube or nanopore will lead to a change in the shape of the time dependence of the intensity of delayed fluorescence, which will make it possible to create a molecular oxygen sensor sensitive to changes in the pH of the environment.

References

[1] Balasubramanian K., Burghard M. Biosensors based on carbon nanotubes. *Anal Bioanal Chem*, 2006, **385**, P. 452–468.

[2] Qi H., Mäder E., Liu J. Unique water sensors based on carbon nanotube–cellulose composites. *Sensors and Actuators B: Chemical*, 2013, **185**, P. 225–230.

[3] Tilmaciu C-M., Morris M.C. Carbon nanotube biosensors. *Front. Chem.*, 2015, **3**, P. 59.

[4] Ferrier D.C., Honeychurch K.C. Carbon nanotube (CNT)-based biosensors. *Biosensors*, 2021, **11**, P. 486.

[5] Ranjbari S., Bolourinezhad M., Kesharwani P., Rezayi M, Sahebkar A. Applications of carbon nanotube biosensors: Sensing the future. *Journal of Drug Delivery Science and Technology*, 2024, **97**, P. 105747.

[6] Dewey H.M., Lamb A., Budhathoki-Uprety J. Recent advances on applications of single-walled carbon nanotubes as cutting-edge optical nanosensors for biosensing technologies. *Nanoscale*, 2024, **16**, P. 16344–16375.

[7] Gazzato L., Frasconi M. Carbon nanotubes and their composites for flexible electrochemical biosensors. *Analysis & Sensing*, 2025, **5**, P. e202400038.

[8] Bianco A., Kostarelos K., Prato M. Applications of carbon nanotubes in drug delivery. *Current Opinion in Chemical Biology*, 2005, **9**(6), P. 674–679.

[9] Meng X., Zhang Z., Li L. Micro/nano needles for advanced drug delivery. Progress in Natural Science: Materials International, 2020, **30**(5), P. 589–596.

[10] Alshawwa S.Z., Kassem A.A., Farid R.M., Mostafa S.K., Labib G.S. Nanocarrier drug delivery systems: characterization, limitations, future perspectives and implementation of artificial intelligence. *Pharmaceutics*, 2022, **14**, P. 883.

[11] Roxbury D., Zhang S., Mittal J., DeGrado W.F., Jagota A. Structural stability and binding strength of a designed peptide-carbon nanotube hybrid. *J. Phys. Chem. C*, 2013, **117**, P. 26255–26261.

[12] Wang H., Michielssens S., Moors S.L.C., Ceulemans A. Molecular dynamics study of dipalmitoylphosphatidylcholine lipid layer self-assembly onto a single-walled carbon nanotube. *Nano Res.*, 2009, **2**, P. 945–954.

[13] Roxbury D., Manohar S., Jagota A. Molecular simulation of DNA β-sheet and β-barrel structures on graphite and carbon nanotubes. *J. Phys. Chem. C*, 2010, **114**, P. 13267–13276.

[14] Li L., Cao Q., Liu H., Qiao X., Gu Z., Yu Y., Zuo C. Understanding interactions between poly(styrene-cosodium styrene sulfonate) and single-walled carbon nanotubes. *J Polym Sci.*, 2021, **59**, P. 182–190.

[15] Kruchinin N.Yu., Kucherenko M.G. Molecular dynamics simulation of the conformational structure of uniform polypeptides on the surface of a polarized metal prolate nanospheroid with varying pH. *Russian Journal of Physical Chemistry A*, 2022, **96**(3), P. 624–632.

[16] Kruchinin N.Yu. Molecular dynamics simulation of the rearrangement of polyampholyte conformations on the surface of a charged oblate metal nanospheroid in a microwave electric field. *Nanosystems: Physics, Chemistry, Mathematics*, 2023, **14**(6), P. 719–728.

[17] Kruchinin N.Yu., Kucherenko M.G. Conformational structure of a complex of two oppositely charged polyelectrolytes on the surface of a charged spherical metal nanoparticle. *High Energy Chemistry*, 2024, **58**(6), P. 615–623.

[18] Kruchinin N.Yu., Kucherenko M.G. Conformational changes of two oppositely charged polyelectrolytes, including those combined into a single block copolymer, on the surface of a charged or transversely polarized cylindrical metal nanowire. *Journal of Polymer Research*, 2025, **32**(3), P. 79.
[19] Salimi A., Compton R.G., Hallaj R. Glucose biosensor prepared by glucose oxidase encapsulated sol-gel and carbon-nanotube-modified basal plane pyrolytic graphite electrode. *Anal Biochem*, 2004, **333**(1), P. 49–56.
[20] Chen Q., Wang Q., Liu Y.-C., Wu T., Kang Y., Moore J.D. Gubbins K. E. Energetics investigation on encapsulation of protein/peptide drugs in carbon nanotubes. *The Journal of Chemical Physics*, 2009, **131**(1), P. 015101.
[21] Kang Y., Wang Q., Liu Y.-C., Wu T., Chen Q., Guan W.-J. Dynamic mechanism of collagen-like peptide encapsulated into carbon nanotubes. *The Journal of Physical Chemistry B*, 2008, **112**(15), P. 4801–4807.
[22] Kang Y., Liu Y.-C., Wang Q., Shen J.-W., Wu T., Guan, W.-J. On the spontaneous encapsulation of proteins in carbon nanotubes. Biomaterials, 2009, **30**(14), P. 2807–2815.
[23] Zhang Z., Kang Y., Liang L., Liu Y., Wu T., Wang Q. Peptide encapsulation regulated by the geometry of carbon nanotubes. Biomaterials, 2014, **35**(5), P. 1771–1778.
[24] Yang N., Chen X., Ren T., Zhang P., Yang D. Carbon nanotube based biosensors. Sensors and Actuators B: Chemical, 2015, **207**(A), P. 90–715.
[25] Chavan K.S., Barton S.C. Confinement and Diffusion of Small Molecules in a Molecular-Scale Tunnel. *Journal of The Electrochemical Society*, **167**, P. 023505.
[26] Li W., Cheng S., Wang B., Mao Z., Zhang J., Zhang Y., Liu Q.H. The transport of a charged peptide through carbon nanotubes under an external electric field: a molecular dynamics simulation. RSC Adv., 2021, **11**, P. 23589–23596.
[27] Chen Q., Liang L., Zhang Z., Wang Q. Release of an encapsulated peptide from carbon nanotubes driven by electric fields: a molecular dynamics study. ACS Omega, 2021, **6**(41), P. 27485–27490.
[28] Andrade L.R.M., Andrade L.N., Bahú J.O., Concha V.O.C., Machado A.T., Pires D.S., Santos R., Cardoso T.F.M., Cardoso J.C., Albuquerque-Junior R.L.C., Severino P., Souto E.B. Biomedical applications of carbon nanotubes: A systematic review of data and clinical trials. *Journal of Drug Delivery Science and Technology*, 2024, **99**, P. 105932.
[29] Batys P., Morga M., Bonarek P., Sammalkorpi M. pH-Induced Changes in Polypeptide Conformation: Force-Field Comparison with Experimental Validation. *J. Phys. Chem. B*, 2020, **124**(14), P. 2961–2972.
[30] Resende L.F.T., Basilio F.C., Filho P.A., Therézio E.M., Silva R.A., Oliveira O.N., Marletta A., Campana P.T. Revisiting the conformational transition model for the pH dependence of BSA structure using photoluminescence, circular dichroism, and ellipsometric Raman spectroscopy. *International Journal of Biological Macromolecules*, 2024, **259**(1), P. 129142.
[31] Stepanenko D., Wang Y., Simmerling C. Assessing pH-Dependent Conformational Changes in the Fusion Peptide Proximal Region of the SARS-CoV-2 Spike Glycoprotein. *Viruses*, 2024, **16**, P. 1066.
[32] Phillips J.C., Braun R., Wang W., Gumbart J., Tajkhorshid E., Villa E., Chipot C., Skeel R.D., Kalé L., Schulten K. Scalable molecular dynamics with NAMD. *J Comput Chem.*, 2005, **26**, P. 1781–1802.
[33] MacKerell Jr. A.D., Bashford D., Bellott M., Dunbrack Jr. R.L., Evanseck J.D., Field M.J., Fischer S., Gao J., Guo H., Ha S., Joseph-McCarthy D., Kuchnir L., Kuczera K., Lau F.T.K., Mattos C., Michnick S., Ngo T., Nguyen D.T., Prodhom B., Reiher W.E., Roux B., Schlenkrich M., Smith J.C., Stote R., Straub J., Watanabe M., Wiórkiewicz-Kuczera J., Yin D., Karplus M. All-atom empirical potential for molecular modeling and dynamics studies of proteins. *J. Phys. Chem. B.*, 1998, **102**(18), P. 3586–3616.
[34] Huang J., Rauscher S., Nawrocki G., Ran T., Feig M., de Groot B.L., Grubmüller H., MacKerell Jr. A.D. CHARMM36m: an improved force field for folded and intrinsically dis-ordered proteins. Nature Methods, 2016, **14**, P. 71–73.
[35] Radak B.K., Chipot C., Suh D., Jo S., Jiang W., Phillips J.C., Schulten K., Roux B. Constant-pH Molecular Dynamics Simulations for Large Biomolecular Systems. *J. Chem. Theory Comput.*, 2017, **13**(12), P. 5933–5944.
[36] Zhu F, Schulten K. Water and Proton Conduction through Carbon Nanotubes as Models for Biological Channels. *Biophysical Journal*, 2003, **85**(1), P. 236–244.
[37] Darden T., York D., Pedersen L. Particle mesh Ewald: An N·log(N) method for Ewald sums in large systems. *J. Chem. Phys.*, 1993, **98**, P. 10089–10092.
[38] Jorgensen W.L., Chandrasekhar J., Madura J.D., Impey R.W., Klein M.L. Comparison of simple potential functions for simulating liquid water. *J. Chem. Phys.*, 1983, **79**, P. 926–935.
[39] Kucherenko M.G., Rusinov A.P., Chmereva T.M., Ignat'ev A.A., Kislov D.A., Kruchinin N.Yu. Kinetics of photoreactions in a regular porous nanostructure with cylindrical cells filled with activator-containing macromolecules. *Optics and Spectroscopy*, 2009, **107**(3), P. 480–485.

Submitted 20 March 2025; revised 17 September 2025; accepted 06 October 2025

Information about the authors:

Nikita Yu. Kruchinin – Orenburg State University, Center of Laser and Informational Biophysics, Orenburg, Russia; ORCID 0000-0002-7960-3482; kruchinin_56@mail.ru

Conflict of interest: the authors declare no conflict of interest.

NANOSYSTEMS:
PHYSICS, CHEMISTRY, MATHEMATICS

Original article

Subramanyam D., et al. *Nanosystems: Phys. Chem. Math.*, 2025, **16** (5), 660–668.
http://nanojournal.ifmo.ru
DOI 10.17586/2220-8054-2025-16-5-660-668

Effect of rotational speed on structural, morphological, and optical properties of sol-gel spin coated Sb doped SnO_2 thin films

Darla Subramanyam[1,2,a], Borra Rajesh Kumar[3,b], Kuntalo Chandrasekhara Reddy[1,4,c]

[1]Research and Development Centre, Bharathiar University, Coimbatore, 641046, Tamil Nadu, India
[2]Department of Physics, STSN Govt Degree College, Kadiri, 515591, Andhra Pradesh, India
[3]Department of Physics, School of Science, GITAM (Deemed to be University), Visakhapatnam, 530 045, Andhra Pradesh, India
[4]Department of Physics, Govt. Degree College, Uravakonda, 515812, Anantapur, Andhra Pradesh, India

[a]subramanyamdarla@gmail.com, [b]rajindphy@gmail.com, [c]chandrasekharreddyssbn@gmail.com

Corresponding author: B. Rajesh Kumar, rajindphy@gmail.com

PACS 68.55.Ln, 61.05.cp, 68.37.Hk, 68.37.Ps, 78.66.Bz, 73.61.-r

ABSTRACT Antimony doped SnO_2 (ATO) films were prepared on glass substrates by spin coating method at rotational speeds from 2000 to 3500 rpm. The impact of rotational speed on physical properties of Sb-doped SnO_2 films were reported. XRD profiles of Sb-doped SnO_2 films exhibits tetragonal rutile phase structure. The surface morphology shows homogeneous growth of the films with spherical structure, and an agglomeration of grains was observed at higher rotational speeds. Sb-doped SnO_2 films prepared at 3500 rpm show an optimum transmittance of 82 % at visible region. The optical bandgap energy of Sb-doped SnO_2 films were increased from 3.23 to 3.46 eV due to Burstein–Moss (B-M) effect. The electrical resistivity of Sb-doped SnO_2 films were increased from $2.80 \cdot 10^{-4}$ to $3.86 \cdot 10^{-4}$ Ω·cm with an increase of rotational speed from 2000 to 3500 rpm.

KEYWORDS Sb-doped SnO_2 films, X-ray diffraction, surface morphology, optical properties, electrical properties

ACKNOWLEDGEMENTS The facilities (FESEM, AFM, and XPS) available at CeNSE, IISc, Bengaluru were utilized to perform this research work. The author also thanks to DST-FIST Program, Govt. of India for providing spectroscopic ellipsometer to GITAM.

FOR CITATION Subramanyam D., Rajesh Kumar B., Chandrasekhara Reddy K. Effect of rotational speed on structural, morphological, and optical properties of sol-gel spin coated Sb doped SnO_2 thin films. *Nanosystems: Phys. Chem. Math.*, 2025, **16** (5), 660–668.

1. Introduction

Tin oxide (SnO_2) is related to semiconductor of n-type with ∼3.6 eV band gap, high electrical conductivity, and optical transparency [1,2]. The potential applications of SnO_2 include transparent electrodes, gas sensors, photodetectors, solar cells, etc., [3–6]. The physical properties of SnO_2 was influenced by crystallinity, defects which include oxygen vacancies, surface faults, and interstitials. The properties of SnO_2 can be varied with different conditions of synthesis methods, controlling the crystallite size, preferred crystalline growth, dopants, surface morphology, shape, and size distribution. The selection of the proper dopant in the host lattice will modify the parent system microstructure, affecting the structural, optical, and electrical properties [7–10]. Various dopants such as Cu [11], Mg [12], Sb [13] have been used to tune the properties of SnO_2. Among these dopants, n-type doping of Sb^{3+} leads to enhancement in the conductivity, preferably substitutional cations in the Sn^{4+} site, which releases electrons leads to an increase of electron density in the conduction band (CB) [14]. Sb^{3+} state can occupy interstitial sites of SnO_2 lattice because Sb^{3+} (0.74 Å) had a larger ionic radius compared to Sn^{4+} (0.69 Å) causing a larger number of dislocations [15].

Among the several preparation methods RF/DC magnetron sputtering [16], spray pyrolysis [17,18], sol-gel [19], and SILAR [20] for doped SnO_2. The versatile sol-gel spin coating method offers many notable benefits, such as depositing at lower temperatures, precise stoichiometry control, cost-effectiveness, deposit across the wide areas, and uniform film growth. The present work aims to study the rotational speed effect on comprehensive analysis of microstructural, morphological, optical and electrical properties of Sb-doped SnO_2 films.

2. Experimental details

Sb-doped SnO_2 (ATO) films was synthesized using the chemicals $SnCl_2{\cdot}2H_2O$, $SbCl_3$, and 2-methoxy ethanol as a precursor, dopant, and solvent. First, 0.2 M of $SnCl_2{\cdot}2H_2O$ and 0.05 M of $SbCl_3$ were mixed in 50 ml distilled water individually, and then solutions were mixed at 350 rpm for two hours at 80 °C. The precursor solution with a volume and molar ratio of [Sb]/[Sn] is 5:95 and 5 %, respectively. The monoethanolamine is used as a stabilizer and added at 5 ml/minute drop rate until a clear homogeneous solution with a pH of 9.2 is resulted. The final solution was aged for 48 hours to form a sol-gel.The final gel solutions was spin coated by using a spin coater (spinNXG-P1A, Apex Instruments Co. Pvt. Ltd, India) on glass substrates of size 2.5×2.5 cm^2 with varying rotational speeds from 2000 to 3500 rpm. The spin-coated samples was subsequently annealed under air atmosphere at 250 °C for 10 min. Film thickness uniformity was evaluated by spectroscopic ellipsometry (J.A. Woollam, SE-Alpha, wavelength: 380 – 900 nm, 70° incidence; B-spline model, spot ∼0.5 mm). A 9-point radial map (center, 4 mid-radius, 4 near edge) showed values ranging from 140 ± 1.8 to 235 ± 2.1 nm. X-ray diffraction patterns of ATO films were recorded using Cu Kα radiation ($\lambda = 1.5406$ Å) at 2θ = 10 – 80° with a step size of 0.02° and a scan speed of 2 °/min. The surface morphology of ATO films were examined by SEM (Ultra 55, Karl Ziess) and topographic images by AFM (Model-Bruker Dimension Icon). XPS (Axis Ultra-165) is employed for elemental analysis of ATO films. The wavelength range from 200 to 2500 nm was used to measure the optical transmittance using double beam UV-VIS-NIR spectrometer (Model-Hitachi U-2900). The electrical properties of the ATO films were examined by four probe method with Keithley 2450 source meter.

3. Results and discussion

3.1. Film thickness variation with rotational speed

It is noticed that the film thickness decreased from 235 to 140 nm with the rise in rotational speed from 2000 to 3500 rpm as shown in Fig. 1. The centrifugal force on the solution increases with rotational speed increases and casts away the surplus solution to form a uniform film. The thickness of the films is inversely proportional to the rotational speed. Generally, the solutions with low viscosity will make more liquid to radial outflow and driven out from the substrate due to centrifugal force leading to thinner film.

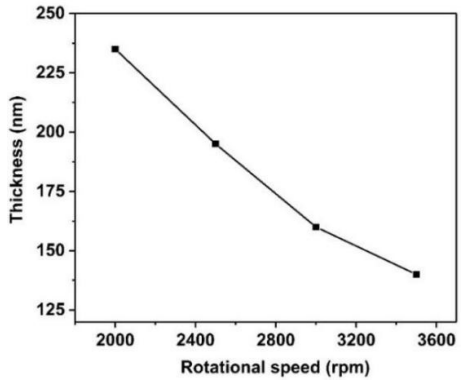

FIG. 1. Plot of film thickness with rotational speed

3.2. Structural properties

The XRD patterns of ATO films prepared at 2000, 2500, 3000, and 3500 rpm is illustrated in Fig. 2. All the peaks were matched to tetragonal cassiterite structure of SnO_2 according to the reported data in the JCPDS file no. 41-1445. No additional peaks was noticed in the spectra. The dominant spectra peaks correspond to planes (1 1 0) and (1 0 1) of Sb-doped SnO_2. It is observed from Fig. 2 that the intensities of diffraction peaks decrease with the rise in the rotational speed because the peak intensity is proportional to the film thickness [21]. Using the Debye–Scherrer relation [22], crystallite size reduced from 34 to 25 nm with the rise in spinning speed from 2000 to 3500 rpm. The decrease in crystallite size with increasing rotational speed can be attributed to the lattice stress arising from the ionic radius difference between Sn^{4+} (0.69 Å) and Sb^{3+} (0.74 Å) [23]. Sb^{3+} had a greater ionic radius when compared to Sn^{4+} it can be able to occupy at interstitial sites of the SnO_2 lattice which results in more dislocations. Sn^{4+} to Sb^{3+} replacement at lattice sites has the potential to enlarge the lattice due to the greater ionic radius. The lattice constants (a and c) and unit cell volume increase linearly with rotational speed in Sb-doped SnO_2 due to substitution of Sn^{4+} by larger Sb^{3+} ions. Similar results were observed in the previous literature ATO thin films [24, 25].

The dislocation density $\delta = [1/D^2]$, internal stress $\sigma = E \cdot \langle\varepsilon\rangle$ (SnO_2 – Young's Modulus, $E \sim 200$ GPa), and energy density strain $E_d = [0.5 \cdot E\langle\varepsilon\rangle^2]$ of ATO films were estimated [26] and reported in Table 1. The dislocation density of ATO thin films increased from $0.86 \cdot 10^{15}$ to $1.60 \cdot 10^{15}$ nm^{-2} with the rise of rotational speed from 2000 to

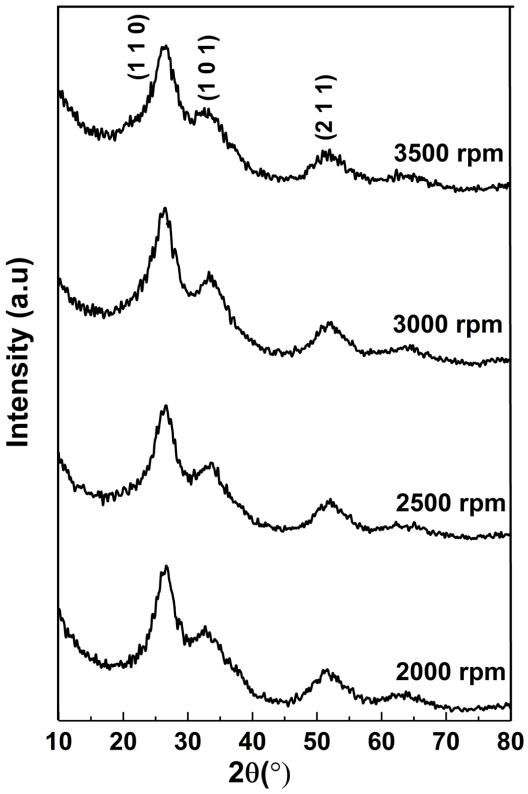

FIG. 2. XRD patterns of ATO films

3500 rpm due to grain boundary enhancement and reduced crystallite size. Other researchers also observe a similar trend in the coloration of ATO films [27, 28].

TABLE 1. Microstructural parameters of ATO films

Microstructural parameters	**2000 rpm**	**2500 rpm**	**3000 rpm**	**3500 rpm**
FWHM, β (°)	2.39	2.61	2.83	3.26
d-value (nm)	0.3356	0.3375	0.3413	0.342
Lattice constant, a (nm)	0.4746	0.4773	0.4826	0.4837
Lattice constant, c (nm)	0.3216	0.3232	0.3226	0.3281
Volume, $V = a^2c$ $(\mathring{A})^3$	72.46	73.65	75.14	76.77
Crystallite size, D (nm)	34	31	28	25
Microstrain, ε (line^{-2}m^{-4})	1.014	1.108	1.202	1.385
Dislocation density, $\delta \cdot 10^{15}$ (nm^{-2})	0.86	1.04	1.28	1.60
Stress, σ (GPa)	2.03	2.21	2.4	2.77
Strain energy density, $E_d \cdot 10^6$ (J·m^{-3})	10.29	12.28	14.45	19.19

Cassiterite SnO_2 had a tetragonal rutile structure belongs to $P4_2/mnm$ (136) space groupand D_{4h}^{14} symmetry. The atomic positions u, c/a, apical and equatorial (d_1 and d_2) distances of Sn–O in the unit cell of ATO films were calculated from the following equations

$$d_1 = \sqrt{2}\, ua, \tag{1}$$

$$d_2 = \sqrt{2\left(\frac{1}{2} - u\right)^2 \cdot a^2 + \left(\frac{c}{2}\right)^2}, \tag{2}$$

where u represents the O^{2-} ions position at $\pm(0.5 + u,\ 0.5 - u,\ 0.5)$ and $\pm(u,\ u,\ 0)$ [29, 30]. If $c/a = 2u$, the Sn^{4+} cation had bond with O^{2-} anion in tetragonal configuration [31]. The basal angle (θ) was determined from the relation

$\cos\theta = \left[a^2(1-4u+8u^2)-1\right] / \left[c^2+4a^2(0.5-u)^2+4a^2u^2\right]$ [32]. The variation in the d_1, d_2 values indicates more distorted octahedron symmetry, and the basal angle (θ) decreases with Sb^{3+}/Sn^{4+} ions substitution. The obtained values of d_1, d_2, and θ for Sb-doped SnO_2 films at various rotational speeds were reported in Table 2.

TABLE 2. Apical and equatorial (d_1 and d_2) distances, internal parameter (u), and basal angle (θ) for ATO films

Rotational speed (rpm)	**Interna parameter,** u	**Apical distance,** d_1 **(Å)**	**Equatorial distance,** d_2**(Å)**	**Basal angle** (θ)
2000	0.3389	2.274	1.938	24.09
2500	0.3386	2.285	1.950	23.96
3000	0.3342	2.281	1.970	23.79
3500	0.3392	2.320	1.975	23.63

3.3. Compositional analysis

XPS was used to analyse the presence of chemical elements in the ATO films. The XPS full survey spectrum in the range of electron binding energies from 0 to 1350 eV for ATO film prepared at the rotational speed of 3000 rpm is illustrated in Fig. 3(a) The peaks corresponding to Sn (4d), C (1s), Sn (3d), O (1s), Sn (3p), Sn (3s), and Sb (3d) exhibit in the XPS spectrum. The C element might be from hydrocarbons during the synthesis process. The two peaks observed at 487.1 and 495.5 eV binding energies were related to Sn $3d_{5/2}$ and Sn $3d_{3/2}$ orbitals as illustrated in Fig. 3(b). The distance between two peaks is ∼8.4 eV, which is assigned to the Sn lattice ion in SnO_2, similar to the previous reports [33,34]. The XPS peaks at 531.4 and 542.1 eV is assigned to the trivalent states Sb $3d_{5/2}$ and Sb $3d_{3/2}$ as illustrated in Fig. 3(c) [35–37]. The XPS spectrum of O 1s is shown in Fig. 3(d). The XPS peak at 531 eV towards higher binding energy side of O 1s spectra is assigned to adsorbed oxygen species [38, 39].

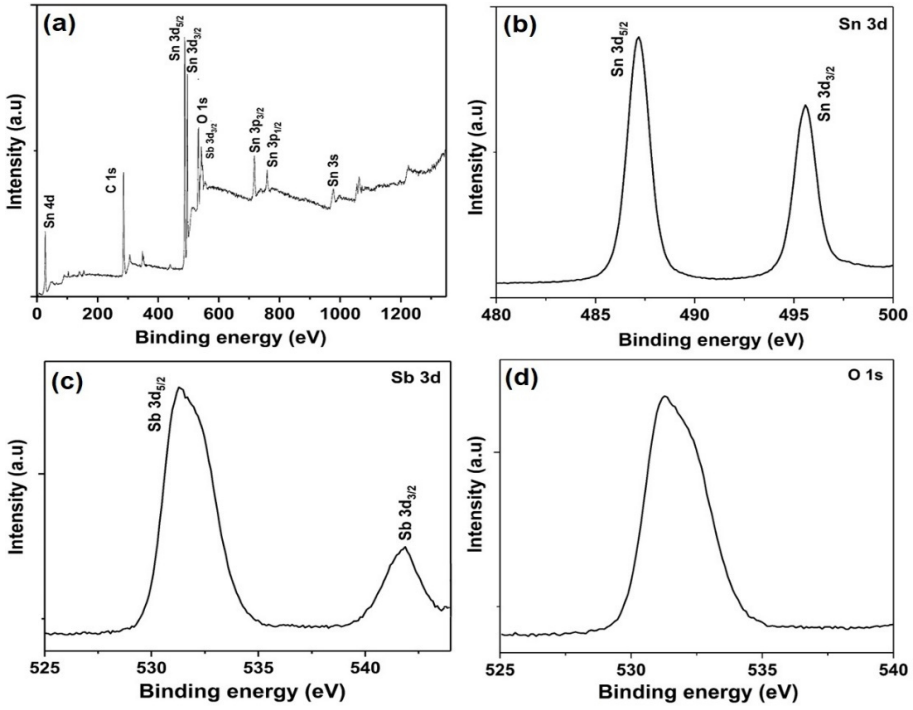

FIG. 3. XPS:(a) wide spectra, (b) Sn 3d, (c) Sb 3d , (d) O1s spectra of ATO film

3.4. Surface morphological studies

SEM images of ATO films prepared by varying rotational speeds from 2000 to 3500 is shown in Fig. 4. The surface morphology shows a dense homogeneous surface with small grains of aggregated form. The film morphology at 3000 and 3500 rpm shows an even surface of small spherical grains. The SEM images reveals that these grains are packed closely, and smaller particles consists of large surface free energy which tends to agglomerate to form enlarged grains.

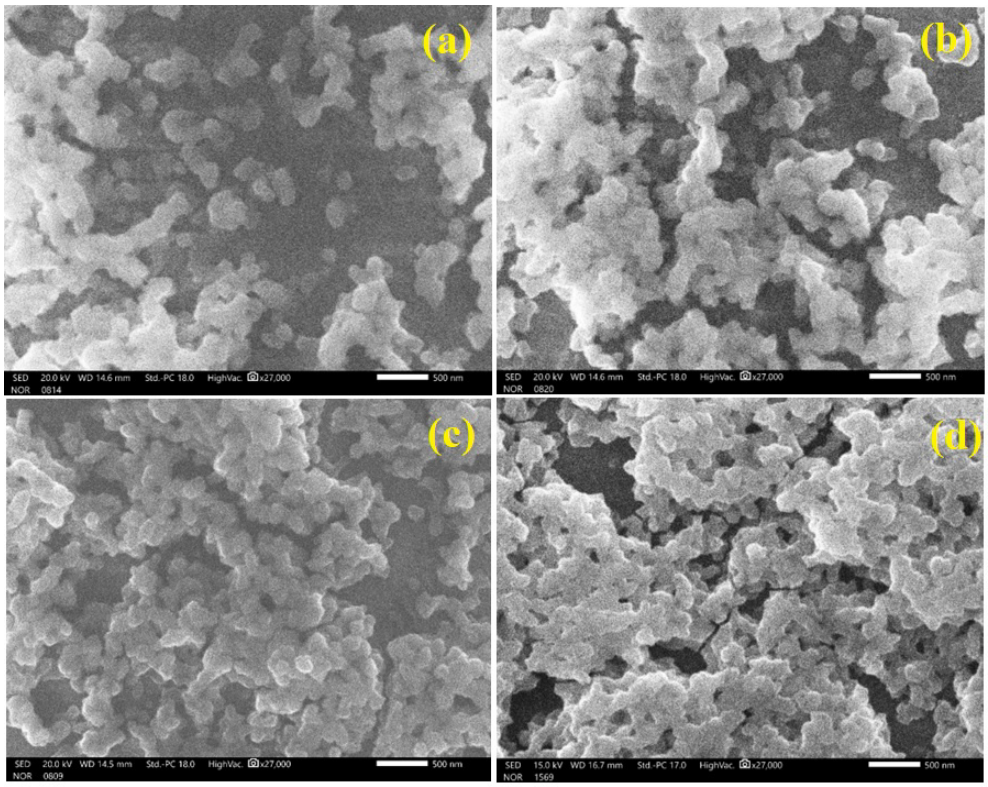

FIG. 4. SEM images of ATO films prepared at (a) 2000, (b) 2500, (c) 3000, and (d) 3500 rpm

AFM micrographs (5×5 μm^2) displaying the surface topography of ATO films were shown in Fig. 5. The thin film samples exhibit without crack surfaces and agglomerated grains. At the higher rotational speeds many valleys and hills appeared indicating well-segregated grains. The surface roughness parameters such as R_a, R_q, R_{ku}, and R_{sk} were listed in Table 3. However, the surface skewness of ATO films is positive which indicates the presence of numerous bumps. The films prepared at higher rotational speeds had rough surfaces lacking grain growth. The surface roughness varied with increasing rotational speed due to grain size reduction, and strain arising during the grain growth. The reduced grain size degrades the crystallinity of films which confirmed with XRD analysis.

TABLE 3. AFM roughness parameters of ATO films

Rotational speed (rpm)	**RMS roughness, R_q (nm)**	**Average roughness, R_a(nm)**	**Kurtosis, R_{ku}**	**Skewness, R_{sk}**
2000	14	11	0.63	2.33
2500	12	9	0.34	3.54
3000	11	8	0.49	2.98
3500	10	7	1.22	2.41

3.5. Optical properties

The optical transmittance spectra of ATO films prepared at different rotational speeds is shown in Fig. 6(a). The optical transmittance increases with increased rotational speed due to reduced film thickness from 235 to 140 nm. A smaller number of photons are being absorbed due to the decrease in thickness of the films, enhancing the film transparency. The increase in optical transmittance is due to the reduction in light scattering. The bandgap energy (E_g) of ATO films is determined from the Tauc's relation [40]:

$$(\alpha h\nu)^2 = A(h\nu - E_g)^{1/2}, \tag{3}$$

where α is the absorption coefficient, $h\nu$ is the photon energy and constant A depends on the transition nature. The linear portion of Tauc's plot $(\alpha h\nu)^2$ against $h\nu$ shown in Fig. 6(b) exhibits bandgap of ATO films. It was noticed that E_g increased from 3.23 to 3.46 eV with the rise in spinning speed because of Burstein–Moss (B-M) hypothesis. The optical absorption shifts towards the higher energy which is proportional to free-electron density. The fact that the light

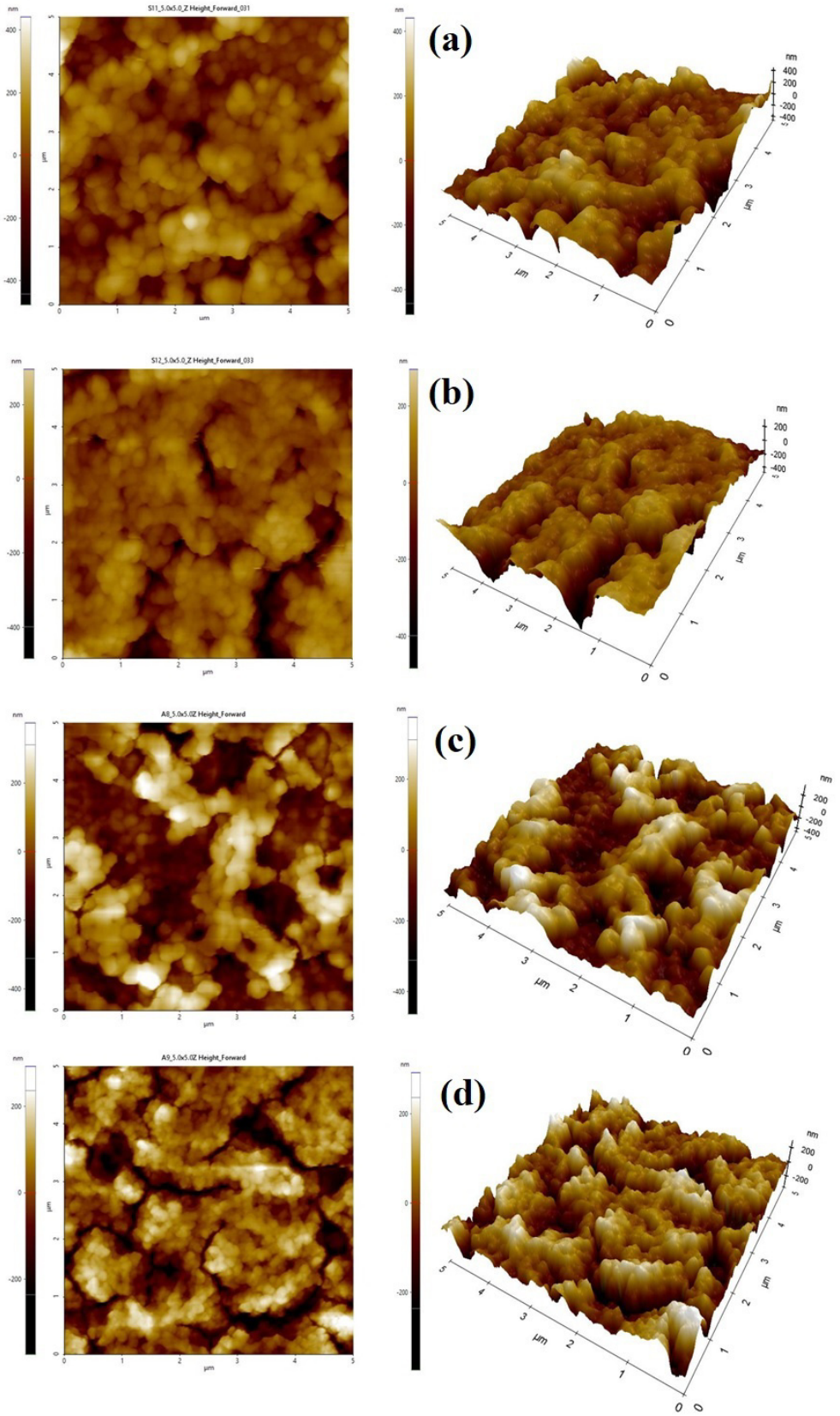

FIG. 5. AFM (2D and 3D) images of ATO films prepared at (a) 2000, (b) 2500, (c) 3000, and (d) 3500 rpm

absorption shifting towards the lower wavelengths with increasing rotational speed makes the films advantageous for its optical applications in the UV region. Similar behavior is reported by Abhijit A. Yadav et al. [41] for antimony-doped SnO_2 thin films. The optical band gap variation can be explained by B-M effect as a function of carrier concentration is given as [42]:

$$\Delta E_g^{BM} = \frac{h^2}{8m_e^*}\left(\frac{3}{\pi}\right)^{2/3} n^{2/3}, \tag{4}$$

where h, m_e^*, and n represents the Planck constant, effective electron mass, and carrier concentration. The carrier concentration of ATO films were decreased from $4.44 \cdot 10^{20}$ to $3.64 \cdot 10^{20}$ cm^{-3}. The decrease in carrier concentration is due to enhanced grain boundary density and comparable with AFM results [43].

The edge potentials of the conduction and valence band (E_{CB} and E_{VB}) of ATO thin films is determined from the relations [44]

$$E_{VB} = \chi - E_e + 0.5E_g, \tag{5}$$

$$E_{CB} = E_{VB} - E_g, \tag{6}$$

where χ (for SnO_2 ~6.24 eV) represents electronegativity. E_e (~4.5 eV) is the free electrons energy. The E_{VB} values for ATO films prepared at 2000, 2500, 3000, and 3500 rpm are obtained as 3.355, 3.39, 3.44, and 3.47 eV, whereas the E_{CB} values are 0.125, 0.09, 0.04, and 0.01, respectively.

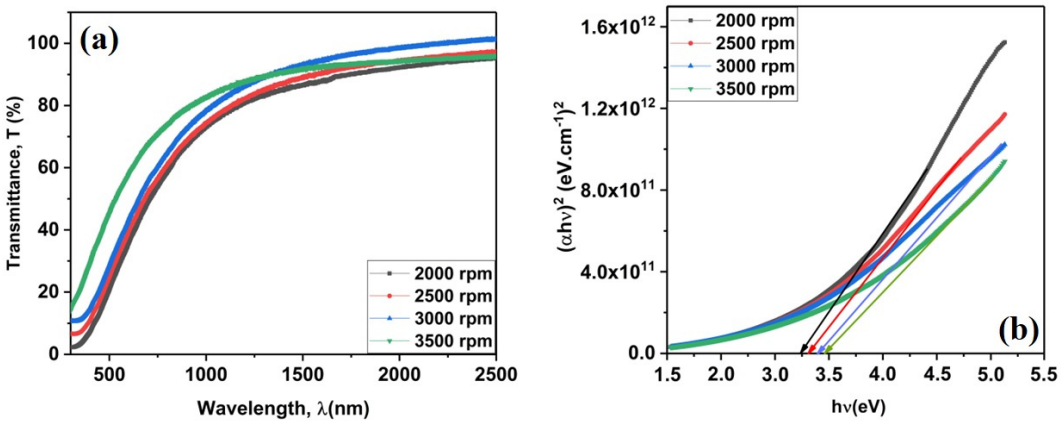

FIG. 6. (a) Optical transmittance spectra and (b) Tauc's plot of ATO films

3.6. Electrical properties

The rotational speed effect on carrier concentration (n), electrical resistivity (ρ) and mobility (μ) of ATO films is summarized in Fig. 7. The electrical resistivity of ATO films was increased from $2.80 \cdot 10^{-4}$ to $3.86 \cdot 10^{-4}$ Ω·cm with an increase of rotational speed from 2000 to 3500 rpm due to reduced carrier concentration. The increase in the electrical resistivity values with an increase of rotational speed or decrease in film thickness was previously reported by Shihui Yu et al. [45]. The mobility of ATO films decreased from 50.3 to 44.5 cm^{2}V^{-1}s^{-1} with an increase in rotational speed due to the domination by the surface scattering-limited mechanism.

4. Conclusions

Sb-doped SnO_2 thin films were successfully synthesized using the sol-gel spin coating method at different rotational speed ranges from 2000 to 3500 rpm. XRD patterns of ATO films exhibits tetragonal rutile phase with a preferred orientation along (1 0 1). The crystallite size decreased from 34 to 25 nm with an increase of rotational speed. The surface morphology of ATO films exhibits dense grains in agglomeration form. The optical transmittance of ATO films increases with an increase of rotational speed due to the decrease in the film thickness. The enhancement in the optical band gap energy from 3.23 to 3.46 eV with the rotational speed is due to the reduction in the density of defect states. The electrical resistivity of the ATO films increases from $2.80 \cdot 10^{-4}$ to $3.86 \cdot 10^{-4}$ Ω·cm with increasing rotational speed would degrade the carrier mobility of the films. The decrease in mobility of ATO films with rotational speed may be due to grain size reduction and enhancement in the grain boundary scattering. The ATO films prepared at higher rotational speed can make them suitable to be used as a transparent electrodes for the optoelectronic devices.

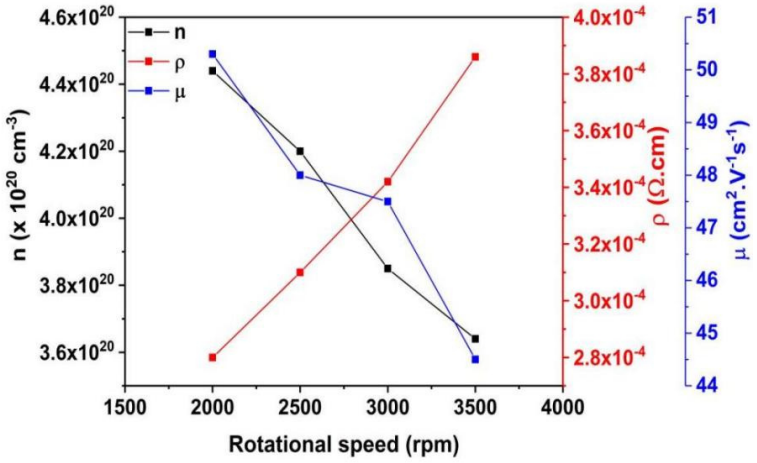

FIG. 7. Dependence of carrier concentration (n), electrical resistivity (ρ), and mobility (μ) of ATO films

References

[1] Manjeet Kumar, Akshay Kumar, Abhyankar A.C. Influence of Texture Coefficient on Surface Morphology and Sensing Properties of W-Doped Nanocrystalline Tin Oxide Thin Films. *ACS Applied Materials & Interfaces*, 2015, **7** (6), P. 3571–3580.

[2] Towseef Ahmad, Mohd Zubair Ansari. Temperature-dependent structural and optical properties of Sb-doped SnO_2 nanoparticles and their electrochemical analysis for supercapacitor application. *New J. of Chemistry*, 2024, **48**, P. 8495–8509.

[3] Asiyeh Kalateh, Ali Jalali, Mohammad Javad Kamali Ashtiani, Mohammad Mohammadimasoudi, Hajieh Bastami, Majid Mohseni. Resistive switching transparent SnO_2 thin film sensitive to light and humidity. *Scientific Reports*, 2020, **13**, P. 20036/1–11.

[4] Rosmalini Ab Kadir, Zhenyu Li, Abu Z. Sadek, Rozina Abdul Rani, Ahmad Sabirin Zoolfakar, Matthew R. Field, Jian Zhen Ou, Adam F. Chrimes, Kourosh Kalantar-zadeh. Electrospun Granular Hollow SnO_2 Nanofibers Hydrogen Gas Sensors Operating at Low Temperatures. *The J. of Physical Chemistry C*, 2014, **118** (6), P. 3129–3139.

[5] Xueying Kou, Chong Wang, Mengdi Ding, Changhao Feng, Xin Li, Jian Ma, Hong Zhang, Yanfeng Sun, Geyu Lu. Synthesis of Co-doped SnO_2 nanofibers and their enhanced gas-sensing properties. *Sensors and Actuators B: Chemical*, 2016, **236**, P. 425–432.

[6] Snaith H.J., Ducati C. SnO_2-Based Dye-Sensitized Hybrid Solar Cells Exhibiting Near Unity Absorbed Photon- to- Electron Conversion Efficiency. *Nano Letters*, 2010, **10** (4), P. 1259–1265.

[7] Terrier C., Chatelon J.P., Berjoan R., Roger J.A. Sb-doped SnO_2 transparent conducting oxide from the sol-gel dip-coating technique. *Thin Solid Films*, 1995, **263** (1), P. 37–41.

[8] Siya Haung, Hui Wu, Ming Zhou, Chunsong Zhao, Zongfu Yu, Zhichao Ruan, Wei Pan. A flexible and transparent ceramic nanobelt network for soft electronics. *NPG Asia Materials*, 2014, **6** (2), e86.

[9] Lorenzi R., Brovelli S., Meinardi F., Lauria A., Chiodini N., Paleari A. Role of sol-gel networking and fluorine doping in the silica Urbach energy. *J. of Non-Crystalline Solids*, 2012, **357** (8–9), P. 1838–1841.

[10] Arik Kar, Simanta Kundu, Amitava Patra. Surface Defect-Related Luminescence Properties of SnO_2 Nanorods and Nanoparticles. *The J. of Physical Chemistry C*, 2010, **115** (1), P. 118–124.

[11] Pawan Chetri, Priyanka Basyach, Amarjyothi Choudhury. Exploring the structural and Magnetic properties of TiO_2/SnO_2 core/shell nanocomposite: An experimental and density functional study. *J. of Solid State Chemistry*, 2014, **220**, P. 124–131.

[12] Mazumder N., Bharati A., Saha S., Sen D., Chattopadhyay K.K. Effect of Mg doping on the electrical properties of SnO_2 nanoparticles. *Current Applied Physics*, 2012, **12** (3), P. 975–982.

[13] Qi Wei, Peng Song, Zhuoqi Li, Zhongxi Yang, Qi Wang. Hierarchical peony-like Sb-doped SnO_2 nanostructures: Synthesis, characterization and HCHO sensing properties. *Materials Letters*, 2017, **191**, P. 173–177.

[14] Towseef Ahmad, Mohd Zubair Ansari. Structural and optical characteristics of Sb doped SnO_2 nanoparticles and their boosted photocatalytic activity under visible light irradiation. *Ceramics Int.*, 2023, **49** (22), P. 35740–35756.

[15] Martinez-Gazoni R.F., Allen M.W., Reeves R.J. Conductivity and transparency limits of Sb-doped SnO_2 grown by molecular beam epitaxy. *Physical Review B*, 2018, **98** (15), 155308.

[16] Bo Xu, Xiao-Guang Ren, Guang-Rui Gu, Lei-Lei Lan, Bao-Jia Wu. Structural and optical properties of Zn-doped SnO_2 films prepared by DC and RF magnetron co-sputtering. *Superlattices and Microstructures*, 2016, **89**, P. 34–42.

[17] Indira Gandhi T., Ramesh Babu R., Ramamurthi K. Structural, morphological, electrical and optical studies of Cr doped SnO_2 thin films deposited by the spray pyrolysis technique. *Materials Science in Semiconductor Processing*, 2013, **16** (2), P. 472–479.

[18] Ibrahim N.B., Abdi M.H., Abdullah M.H., Baqiah H. Structural and optical characterization of undoped and chromium doped tin oxide prepared by sol-gel method. *Applied Surface Science*, 2013, **271**, P. 260–264.

[19] Mejda Ajili, Michel Castagné, Najoua, Kamoun Turki. Spray solution flow rate effect on growth, optoelectronic characteristics and photoluminescence of SnO_2:F thin films for photovoltaic applications. *Optik*, 2015, **126** (7–8), P. 708–714.

[20] Irmak Karaduman Er., Memet Ali Yıldırım, Hasan Örkçü H., Aytunç Ateş, Selim Acar. Structural morphological and gas sensing properties of $Zn_{1-x}Sn_xO$ thin films by SILAR method. *Applied Physics A*, 2021, **127** (4), P. 230/1–14.

[21] Karthik T.V.K., Hernandez A.G., de la Olvera M.L., Maldonado A., Gómez Pozos H. Effect of Au and Ag contacts on the CO sensitivity of SnO_2 thick films. *J. of Materials Science: Materials in Electronics*, 2020, **31**, P. 7481–7489.

[22] Ali Yıldırıma M., Sümeyra Tuna Yıldırımb, Emine Fedakar Sakara, Aytunç Atesc. Synthesis, characterization and dielectric properties of SnO_2 thin films. *Spectrochimica Acta Part A: Molecular and Biomolecular Spectroscopy*, 2014, **133**, P. 60–65.

[23] Shimin Liu, Jindong Liu, Bin Wen, Weiwei Jiang, Chaoqian Liu, Wanyu Ding, Hualin Wang, Nan Wang, Zhihua Zhang, Weiping Chai. Structural, morphological, electrical and optical properties of SnO_2 nanoparticles: influence of Sb doping. *J. of Materials Science: Materials in Electronics*, 2016, **27**, P. 6932–6938.
[24] Ahmad A. Ahmad, Migdadi A.B., Qais M. Al-Bataineh. Structural, optical, and electrical properties of strontium – doped tin oxide films for high photoconductivity. *Thin Solid Films*, 2024, **796**, 140312.
[25] Sibel Gürakar, Tülay Serin. High quality optoelectronic properties of Sb-doped SnO_2 by spray pyrolysis with less solution. *Materials Research Express*, 2019, **6** (8), 086423.
[26] Subramanyam D., Rajesh Kumar B., Chandrasekhar Reddy K. Micro-Structural, Surface Morphological, and Optical Properties of Sol–Gel Spin Coated Sb-Doped SnO_2 Thin Films. *Physics of the Solid State*, 2025, **67**, P. 17–26.
[27] Elangovan E., Shivashankar S.A., Ramamurthi K. Studies on Structural and electrical properties of sprayed SnO_2: Sb films. *J. of Crystal Growth*, 2005, **276**, P. 215–221.
[28] Masahiko Kojima, Hisao Kato, Mitsuru Gatto. Blackening of tin oxide thin films heavily doped with antimony. *Philosophical Magazine Part B*, 1993, **68**, P. 215–222.
[29] Hamad B.A. First-principle calculations of structural and electronic properties of rutile-phase dioxides (MO_2), M = Ti, V, Ru, Ir and Sn. *The European Physical J. B*, 2009, **70**, P. 163–169.
[30] Aashish Kumar, Naveen Kumar, Mansi Chitkara, Gulshan Dhillon. Physicochemical investigations of structurally enriched Sm^{3+} substituted SnO_2 nanocrystals. *J. of Materials Science: Materials in Electronics*, 2022, **33**, P. 5283–5296.
[31] Soumen Das, Jayaraman V. SnO_2: A comprehensive review on structures and gas sensors. *Progress in Materials Science*, 2014, **66**, P. 112–255.
[32] Aragon F.H., Coaquira J.A.H., Villegas-Lelovsky L., da Silva S.W., Cesar D.F., Nagamine L.C.C.M., Cohen R., Menendez-Proupin E., Morais P.C. Evolution of the doping regimes in the Al-doped SnO_2 nanoparticles prepared by a polymer precursor method. *J. of Physics: Condensed Matter*, 2015, **27** (9), 095301.
[33] Liwei Wang, Jintao Li, Yinghui Wang, Kefu Yu, Xingying Tang, Yuanyuan Zhang, Shaopeng Wang, Chaoshuai Wei. Construction of 1D SnO_2-coated ZnO nanowire heterojunction for their improved n-butylamine sensing performances. *Scientific Reports*, 2016, **6** (1), 35079.
[34] Meihua Li, Chao Mou, Yunfan Zhang, Xiao Li, Huichao Zhu, Guangfen Wei. Zn-doped SnO_2 nanoparticles for ethanol vapor sensor: a combined experimental and first principles study. *J. of Materials Science: Materials in Electronics*, 2023, **34** (12), 1059.
[35] Yang Q., Tang K., Wang C., Qian Y., Yu W., Zhou G., Li F. Antimony sulfide tetragonal prismatic tubular crystals. *J. of Materials Chemistry*, 2011, **11** (2), P. 257–259.
[36] Kang Xiao, Qi-Zhi Xu, Kai-Hang Ye, Zhao-Qing Liu, Lu-Miao Fu, Nan Li, Yi-Bo Chen, Yu-Zi Su. Facile Hydrothermal Synthesis of Sb_2S_3 Nanorods and their magnetic and Electrochemical properties. *ECS Solid State Letters*, 2013, **2** (6), P. 51–54.
[37] Yanfen Niu, Libing Duan, Xiaoru Zhao, Cong Han, Jiale Guo, Wangchang Geng. Effect of Sb doping on structural and photoelectric properties of SnO_2 thin films. *J. of Materials Science: Materials in Electronics*, 2020, **31** (48), 3289.
[38] Wu J.M. A room temperature ethanol sensor made from p-type Sb-doped SnO_2 nanowires. *Nanotechnology*, 2010, **21** (23), 235501.
[39] Babar A.R., Shinde S.S., Moholkar A.V., Bhosale C.H., Kim J H., Rajpure K.Y. Structural and optoelectronic properties of antimony incorporated tin oxide thin films. *J. of Alloys and compounds*, 2010, **505** (2), P. 416–422.
[40] Ali Yıldırım M., Aytunç Ates. Influence of films thickness and structure on the photo-response of ZnO films. *Optics Communications*, 2010, **283** (7), P. 1370–1377.
[41] Abhijit A. Yadav. Influence of film thickness on structural, optical, and electrical properties of spray deposited antimony doped SnO_2 thin films. *Thin Solid Films*, 2015, **591**, P. 18–24.
[42] Mariem Chaari, Adel Matoussi. Effect of Sn_2O_3 doping on structural, optical and dielectric properties of ZnO ceramics. *Materials Science and Engineering B*, 2013, **178**, P. 1130–1139.
[43] Junji Sawahata, Tasuku Kawasaki. Structural and electrical properties of Sb-doped SnO_2 thin films prepared by metal organic decomposition. *Thin Solid Films*, 2019, **685**, P. 210–215.
[44] Wang J., Lu C., Liu X., Wang Y., Zhu Z., Meng D. Synthesis of tin oxide (SnO & SnO_2) micro/nanostructures with novel distribution characteristic and superior photocatalytic performance. *Materials & Design*, 2017, **115**, P. 103–111.
[45] Shihui Yu, Linghong Ding, Chuang Xue, Li Chen Li, Zhang W.F. Transparent conducting Sb-doped SnO_2 thin films grown by pulsed laser deposition. *J. of Non-Crystalline Solids*, 2012, **358** (23), P. 3137–3140.

Submitted 10 April 2025; revised 5 September 2025; accepted 6 October 2025

Information about the authors:

Darla Subramanyam – Research and Development Centre, Bharathiar University, Coimbatore, 641046, Tamil Nadu, India; Department of Physics, STSN Govt Degree College, Kadiri, 515591, Andhra Pradesh, India; ORCID 0009-0004-5805-6266; subramanyamdarla@gmail.com

Borra Rajesh Kumar – Department of Physics, School of Science, GITAM (Deemed to be University), Visakhapatnam, 530 045, Andhra Pradesh, India; ORCID 0000-0002-3015-6001; rajindphy@gmail.com;

Kuntalo Chandrasekhara Reddy – Research and Development Centre, Bharathiar University, Coimbatore, 641046, Tamil Nadu, India; Department of Physics, Govt. Degree College, Uravakonda, 515812, Anantapur, Andhra Pradesh, India; ORCID 0000-0002-2445-8054; chandrasekharreddyssbn@gmail.com;

Conflict of interest: the authors declare no conflict of interest.

NANOSYSTEMS:
PHYSICS, CHEMISTRY, MATHEMATICS

Kavitha M., et al. *Nanosystems: Phys. Chem. Math.*, 2025, **16** (5), 669–680.
http://nanojournal.ifmo.ru
DOI 10.17586/2220-8054-2025-16-5-669-680

Original article

Incorporating manganese selenide with polymerized reduced carbon sheets: an efficient and stable electro-catalyst for methanol oxidation

Kavitha Murugan[1,a], Kalaiarasi Senthurpandi[2,b], Vedhi Chinnapaiyan[1], Muthuchudarkodi Rajaram[1]

[1]PG and Research Department of Chemistry, V.O. Chidambaram College, Thoothukudi-628008, Tamilnadu. Affiliated to Manonmaniam Sundaranar University, Abishekapatti, Tirunelveli-627012, Tamilnadu, India

[2]PG and Research Department of Chemistry, A.P.C Mahalaxmi College for Women, Thoothukudi-628002, Tamilnadu, India

[a]kavithakrithiv35@gmail.com , [b]kalaiarasi@apcmcollege.ac.in

Corresponding author: Kavitha Murugan, kavithakrithiv35@gmail.com

ABSTRACT Reduced graphene oxide/Manganese selenide @Poly-N-methyl pyrrole (RGO/MnSe@P-NMPy) polymer nanocomposite are synthesized via chemical oxidative in-situ polymerization process. The RGO/MnSe@P-NMPy polymer nanocomposite was examined using FTIR spectroscopy, UV-Visible, XRD, TEM and electrochemical investigations in addition to FESEM with EDAX. The methanol oxidation reaction in basic environments was validated using the cyclic voltammetry method. The RGO/MnSe@P-NMPy polymer nanocomposite electro-catalyst shows excellent electrocatalytic activity, lower oxidation potential (0.1 V), improved current density (96 mA/cm^2), and excellent stability towards methanol oxidation reaction (MOR) in basic medium. It was observed RGO/MnSe@P-NMPy nanohybrid electrocatalyst, the ECSA value is 183.7 m^2/g. This result clearly depicts that RGO/MnSe@P-NMPy polymer nanocomposite electro-catalyst has more active sites for MOR reaction. Chronoamperometry was utilized to show that, in comparison to the other nanocomposite, the existence of RMP polymer nanocomposite enhanced stability (1000's) and produced higher current densities (27.71 mA/cm^2) for methanol oxidation. According to the results, the P-NMPy introduction in RGO/MnSe structure can enhance the performance of methanol oxidation and increase the resistance to CO in comparison with mono metallic catalyst. This study makes the case for the potential development of high-performance, inexpensive catalysts for energy storage, conversion and useful uses.

KEYWORDS RGO, MnSe, Poly-N-methyl pyrrole (P-NMPy), RGO/MnSe@P-NMPy (RMP), current density, methanol oxidation reaction (MOR)

ACKNOWLEDGEMENTS The authors are extremely grateful to Department of Science and Technology (FAST TRACK and FIST) New Delhi, INDIA for using CHI Electrochemical workstation at V.O. Chidambaram College, Tuticorin-8 and Jasco UV-VISIBLE Spectrophotometer. We are thankful to The Secretary of A.P.C Mahalaxmi College for women, Thoothukudi.

FOR CITATION Kavitha M., Kalaiarasi S., Vedhi C., Muthuchudarkodi R.R. Incorporating manganese selenide with polymerized reduced carbon sheets: an efficient and stable electro-catalyst for methanol oxidation. *Nanosystems: Phys. Chem. Math.*, 2025, **16** (5), 669–680.

1. Introduction

Graphene oxide layers undergo reduction to eliminate oxygen functional components, which increases the material's electrical conductivity, this results in RGO. For the effective reduction of GO, reducing agents such sodium borohydride, hydroquinone, hydrogen sulphide, and hydrazine hydrate have been utilised extensively [1]. There has been a lot of interest in the optical, electrical power and transport properties of transition metal dichalcogenides and chalcogenides [2]. One of the carbon-based materials that have been extensively studied is oxide of reduced graphene (RGO), due to its exceptionally large surface area, chemical stability, and excellent electrical conductivity. Transition-metal chalcogenides MXn (where X is one of S, Se, or Te and M is a transition metal) generated a lot of fascination owing to their unique optical, magnetic, and electrical characteristics [3–5]. For modifying the characteristics and improving the performance of nanocrystals (NCs) in a wide range of applications, such as solar cells [6], electro-catalysts, spintronic devices, and biological labelling, it has always been thought that control over the NCs' size and shape is essential. Therefore, research into the production and manipulation of $MnSe_2$ at the nanoscale has garnered a great deal of interest [7, 8]. One crucial component of the first row of transition metals is manganese. Manganese compounds are valuable electrode materials due to their inexpensive cost, high operating voltage, good natural abundance, and environmental friendliness. Recent years have seen research on manganese selenide for magneto optical devices, super capacitive behavior, battery applications

and thermoelectric properties [9]. The electrochemical performance should therefore be enhanced by attaching MnSe on RGO.

There are two main approaches to enhance catalysts: either by making electro-catalysts more intrinsically active or by enhancing the amount of active sites on the electrode surface [10]. The catalytic activity of MOR may be substantially enhanced by the combined action of Ni and WC species. Incorporating hetero atoms is an effective method for enhancing the intrinsic activity of catalysts [11]. The microstructure engineering of the electrical and crystal structures can be changed by doping foreign materials into the bulk catalysts [12]. The adsorption and desorption capabilities of the reaction intermediates would change as a result of the dislocations in the initial lattice and the local electron redistribution caused by the heteroatoms' distinct atomic radii, thus altering the catalytic performance [11, 13]. One process that has been extensively studied for creating hydrogen from alcohols (methanol) is methanol electro-oxidation into hydrogen and carbon dioxide.

Numerous compounds based on carbon have been found that enhance the cost-effectiveness and catalytic activity of methanol oxidation [14]. Generally speaking, the anode catalyst has strong stability, high toxin tolerance, and high electro-catalytic activity, all of which greatly contribute to the high MOR efficiency. Recent research has categorized exceptional electro-catalysts as nanoparticles possessing a high specific surface area, excellent electrical conductivity, and remarkable durability even under severe electrochemical conditions [15–17]. In addition the enhanced polarization of the MnSe interface, RGO/MnSe interface and P-NMPy/MnSe interface can possibly be the source of the EA enhancement seen in our work. As far as we are aware, no prior research on the RGO/MnSe@P-NMPypolymer nanocomposite has been published. In this work, a straightforward chemical oxidative polymerization technique has been used to successfully manufacture the triple-component nanocatalyst, RGO/MnSe@P-NMPy. When all three components are incorporated together, new electrode materials with dramatically better electrochemical features are produced. Furthermore, increasing the active surface area and electrical conductivity of catalysts is required to enhance their performance. When compared to P-NMPy/MnSe, RGO/MnSe and MnSe electro-catalysts, the RGO/MnSe@P-NMPy nanohybrids significantly outperform them in alkaline media for the methanol oxidation reaction (MOR), exhibiting greater reactivity and stability.

2. Experimental section

2.1. Materials and nethods

2.1.1. Synthesis of MnSe nanoparticles. In a beaker, ethylene glycol, hydrazine hydrate, and double-distilled water were combined in a 3:1:7 ratios. Using a magnetic stirrer, the mixture was stirred for thirty minutes. One gram of $MnCO_3$ salt was added, and the mixture was agitated for a further thirty minutes to aid in dissolving. The mixture was then refluxed for three hours at 90 °C after 0.5 g of Na_2SeO_3 powder was added. The mixture was vacuum-filtered and then rinsed with ethanol and double-distilled water when a black precipitate formed. The resultant dark residue was then vacuum-dried for 20 minutes and heated in a hot air oven at 60 °C for six hours.

2.1.2. Synthesis of P-NMPy decorated MnSe binary nanocomposite. For this process, synthetic MnSe was employed. 0.1 g of MnSe was dispersed 30 ml of water with sonicated at 30 mins. 2.48 g of (0.1 M) $FeCl_3$ was dissolved in 30 ml of (0.1 M)HCl with magnetic stirring for one hour. Then (0.1 M) of N-Methyl Pyrrole was dissolved in 30 ml of HCl(0.1 M) and stirred under an ice bath for one hour. Following an hour, the solutions of $FeCl_3$ and MnSe were combined with the monomer solution under an ice bath. The mixture was continuously stirred for 6 hours. After 6 hours, the reaction mixture was left undisturbed for an additional 12 hours, during which a black-colored residue formed. The black residue was filtered, and distilled water was used to wash the residue to remove any impurities. To further purify the final product, it was treated with an appropriate amount of ethanol and then dried in a vacuum oven at 60 °C.

2.1.3. Synthesis of RGO decorated MnSe nanocomposite. 0.02 g of synthesized RGO was ultrasonicated at 30 min. At room temperature, ethylene glycol, hydrazine hydrate, and double-distilled water were combined in a 3:1:7 ratio while being stirred magnetically. Followed by addition of 0.83 g of $MnCO_3$ salt and 1.12 g of Na_2SeO_3 were dissolved in 70 ml deionised water under vigorous magnetic stirring for 30 min to facilitate the dissolution. Dirty color solutions appeared immediately and get well dispersed status, and then the mixture was transferred into the round bottom flask. The RGO solution was added to the above mixture, and then kept under 90 °C mantle at 3 h. Following filtration, the precipitate was rinsed with an appropriate volume of ethanol to further purify it. Subsequently, the purified precipitate was dried in a vacuum oven at 60 °C.

2.1.4. Synthesis of RGO/MnSe@P-NMPy ternary polymer nanocomposite. The synthesized RGO/MnSe was used for this reaction.0.1 g of RGO/MnSe was dissolved 30 ml of water with sonicated at 30 mins. 2.48 g (0.1 M) of $FeCl_3$ was dissolved in 30 ml of (0.1 M) HCl with magnetic stirring for one hour. Then (0.1 M) N-Methyl Pyrrole was dissolved in 30 ml of HCl (0.1 M). This mixture was stirred under ice bath for one hour. After one hour the $FeCl_3$ solution and monomer solution was combined with the RGO/MnSe solution. The combined solution was continuously stirred under an ice bath for 6 hours. After completing the reaction, the resulting mixture was permitted to entirely polymerize for 12 hours, and the residue was vacuum-filtered out. Double-distilled water and ethanol were used to wash the precipitate.

After washing, the precipitate was air dried for 20 minutes. Finally, the precipitate was heated in a hot air oven at 60 °C for 6 hours to complete the drying and purification process.

2.2. Characterization

Computer controlled Thermo Scientific Instrument with iD Transmission (Model P4600) was used to record the FTIR spectra, which was then followed by the KBr pellet method. Photoluminescence (PL) Spectra of the samples were recorded on a spectrofluorometer (JASCO, FP8300). The computer controlled XRD system JEOL IDX 8030 was used to record the X-ray diffraction of samples. EDAX and FESEM measurements were carried by JEOL JSM-6700F field emission scanning electron microscope. The atomic force microscopy was completed with Nanosurf easy2scan B02218 profilemeter; a sharp cantilever tip interacts with the sample surface sensing the local forces with the molecules and tip. TEM (High Resolution with EDX). FEI-TECHANAI T20. The electrochemical behaviors of nanocomposite have been investigated through CH-Instrument INC., TX, USA.

3. Results and discussion

3.1. Spectroscopic studies

Using UV-visible spectroscopy, the development of the RGO/MnSe@P-NMPy nanocomposite has been investigated. The absorbance was measured between 200 to 800 nm. The π-π* transition may be connected to the peak in the MnSe at 285 nm shown in Fig. 1(a). As can be seen, the UV-Vis absorption spectra of P-NMPy using MnSe nanocomposite material. The figure unequivocally demonstrates that the three prominent peaks in both absorption spectra located at 293, 361 and 566 nm are caused by the π-π* and n-π* transitions. Compared to pure MnSe, there is a larger wavelength shift at 293 nm when MnSe nanoparticles are introduced to P-NMPy chains. The transitions involving the highest occupied molecular orbital (HOMO) and the lowest unoccupied molecular orbital (LUMO) in conducting polymers are generally denoted as π* and π, respectively [18]. The absorption peaks at 361 and 566 nm correspond to the polaron-π* transitions observed in P-NMPy and MnSe/P-NMPy structures, respectively [19]. The production of RGO/MnSe hybrid nanomaterial is depicted in figure. It is noted that absorbance bands, characteristic of RGO and MnSe surface plasmon resonance band, occur at 302 nm, suggesting the formation of MnSe nanoparticle of the RGO [20, 21]. Due to the oxidised condition of P-NMPy, two tiny absorption peak in the 470 – 598 nm regions are responsible to the bipolaron transition [22]. P-NMPy was identified to lead to a red shift in the absorption band, which indicated a reduction in the electronic transition's band gap.

The FT-IR spectra of MnSe, P-NMPy/MnSe, RGO/MnSe and RMP nanocomposite, which were acquired from the materials, are displayed in Fig. 1(b). FTIR spectroscopy was employed to analyze the functional groups found in the generated samples across the spectral range from 4000 to 500 cm^{-1}. The vibrations of Mn–Se have been attributed to the high frequency modes at 604 and 529 cm^{-1} [23]. When the concentration of the inorganic filler (MnSe) rose, the band found that the band at 2924 and 2362 cm^{-1} for MnSe were significant. Owing to the water molecules adhered to the materials layer, the large absorption at 3422 cm^{-1} is attributed to the O–H stretching vibration mode. The P-NMPy/MnSe spectrum was illustrating the absorption frequencies, which support the creation of P-NMPy as a result of the identified distinctive peaks. The broad peak in the P-NMPy spectra at 3421 cm^{-1} is caused by the N–H stretching vibration. The band at 1638 cm^{-1} was found to be C=C and C–C stretching of the P-NMPy rings. For C–N and C–C, band at 1448 cm^{-1} was attributed to P-NMPy ring stretching vibration, while the peak at 1384 cm^{-1} was assigned to plane distortion. The peak 1050 cm^{-1} was associated with the distorted vibrations of C–H and C–N [24]. Two vibration peaks at 1161 and 880 cm^{-1} were identified as the stretching peaks of P-NMPy, and the polymerization of pyrrole was suggested by the =C–H out of plane vibration [23, 25]. The existence of the band at 772 cm^{-1} indicated the presence of polymerized pyrrole [23]. Because of the significant interaction between P-NMPy and MnSe, the P-NMPyat 1161 and 1050 cm^{-1} shift to lower wave numbers. Lower wave numbers are shifted by the P-NMPy at 1161 and 1050 cm^{-1} due to the substantial interaction between P-NMPy and MnSe. These findings provide strong validation for the fabricated MnSe/P-NMPy nanocomposite materials.

The RGO/MnSe was observed at 3422 cm^{-1} indicates O–H bonding. C=C stretching vibration of RGO can be seen at 1628 cm^{-1}. The C–O stretching vibrations of carboxyl and alkoxy groups are denoted by the peaks located at 1448 and 863 cm^{-1}, respectively [26]. The FTIR spectrum shows peaks for RGO, MnSe, and P-NMPy, indicating that these components have successfully integrated into the structure of the nanocomposite. This accomplishment in synthesis shows that the ternary (RGO/MnSe@P-NMPy) polymer nanocomposite and binary (RGO/MnSe) nanocomposite have been effectively fabricated, with each component providing its unique spectrum characteristics. Consequently, the peaks observed in the FTIR spectrum serve as strong evidence of the successful synthesis and integration of RGO, MnSe, and P-NMPy into the polymer nanocomposite, confirming the desired composition and structure of the material.

The XRD pattern displayed in Fig. 1(c) depicts the crystal structures of the material. The prominent peak in the XRD image of pure MnSe is displayed in the figure, which corresponds to the (111), (210), (200), (220), (023), (321), (400), and (420) reflection peak, at 2θ = 19.01°, 23.58°, 29.77°, 31.39°, 41.46°, 43.68°, 45.44° and 51.74°. Crystallographic planes depicts an RS type MnSe crystal structure (JCPDS-270311) [27]. The MnSe crystalline size was calculated to be

19 nm. The P-NMPy/MnSe polymer nanocomposite has five peaks, which are defined by the planes (111), (200), (310), (311), and (321) at 2θ = 23.66°, 29.73°, 43.73°, 45.42° and 51.89°. The average size of the P-NMPy/MnSe crystallite is 16 nm. The RGO/MnSe nanocomposite was estimated to be 23.85°, 30.08°, 31.69°, 41.67°, 43.88°, 45.65°, 52.03° and 55.88° are attributed to (111), (200), (211), (220), (221), (321), (310) and (311) illustrates the crystaline seen in the figure. The RGO/MnSe nanohybrid was determined to be 12 nm. In the equivalent lattice plane of (111), (210), (200), (222), (320), (321), and (331), the RGO/MnSe@P-NMPy polymer nanocomposite displays peaks at 2θ=20.19°, 23.46°, 29.73°, 41.36°, 43.63°, 45.28°, and 51.71°. In the RGO/MnSe@P-NMPy nanohybrid material, the inclusion of RGO improved the MnSe crystal structure and decreased the peaks of selenium impurities. The RMP nanocomposite was discovered to have an average crystalline size of 10 nm. The active peak indicates the excellent crystalline clarity of MnSe. The connection between RGO, MnSe and P-NMPy polymer matrix is further confirmed by the variation in diffraction intensity.

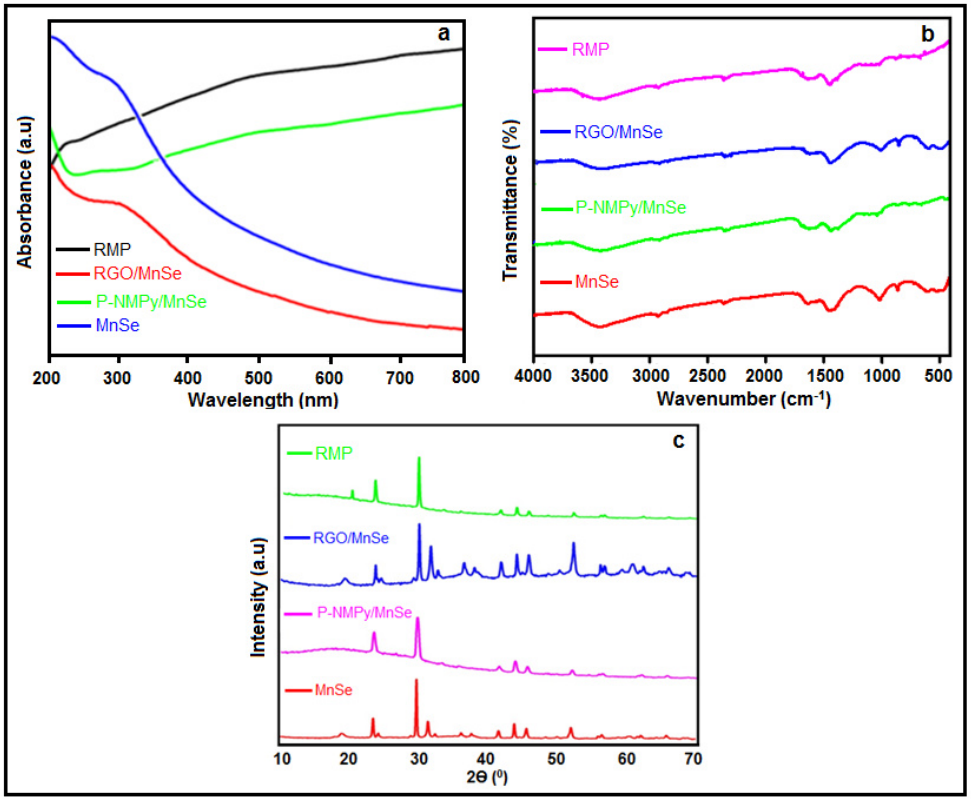

FIG. 1. a) UV-Visible spectra; b) FT-IR spectra and c) XRD patterns of MnSe, P-NMPy/MnSe, RGO/MnSe and RGO/MnSe@P-NMPy polymer nanocomposite

3.2. Morphological study

FESEM depicts of MnSe, RGO/MnSe, P-NMPy/MnSe and RMP polymer nanohybride are displayed in Fig. 2. The result shows pure MnSe has a structure resembling a crystal. The P-NMPy/MnSe polymer nanocomposite showed sphere-like structure. It suggests that MnSe nanoparticles are evenly distributed across the P-NMPy's crumpled surface. The infected RGO in the RGO/MnSe nanomaterial was found to prevent the MnSe nanoparticles from clumping together as demonstrated in the figure. The RGO/MnSe nanocomposite exhibits a multilayer structure including a small quantity of micro nanoplates. P-NMPy was dispersed unifor mly across the RGO and MnSe nanocomposite. The RMP polymer nanocomposite revealed excellent dispersion as well as random distribution of NPs in the host polymer matrix indicating the formation of closely-packed uniform network structure. These nanoparticles were successfully mixed and dispersed unifor mly. The elemental mapping of selected area in RMP polymer nanocomposite was done by FESEM equipped with energy dispersive X-ray spectroscopy (EDX) mapping to verify the distribution of the elements (C, O, N, Mn and Se) and the obtained results (Fig. 3(a)) reveal good distribution of elements throughout the material. The synthesized RGO/MnSe@P-NMPy polymer nanocomposite is found to have a maximum atomic percentage of C and a minimum value of Se, Mn, O, and N, which confirmed the formation of the RGO/MnSe@P-NMPy polymer nanocomposite. Table 1 displays the atomic composition of the RGO/MnSe@P-NMPy polymer nanocomposite.

The microstructure of RMP nanohybrid was studied by TEM shows in Fig. 4 (a and b). Polymer was indicated by the black spot of the RGO layer. The nanoplates shape and uniformity remain disturbed by the incorporation of P-NMPy

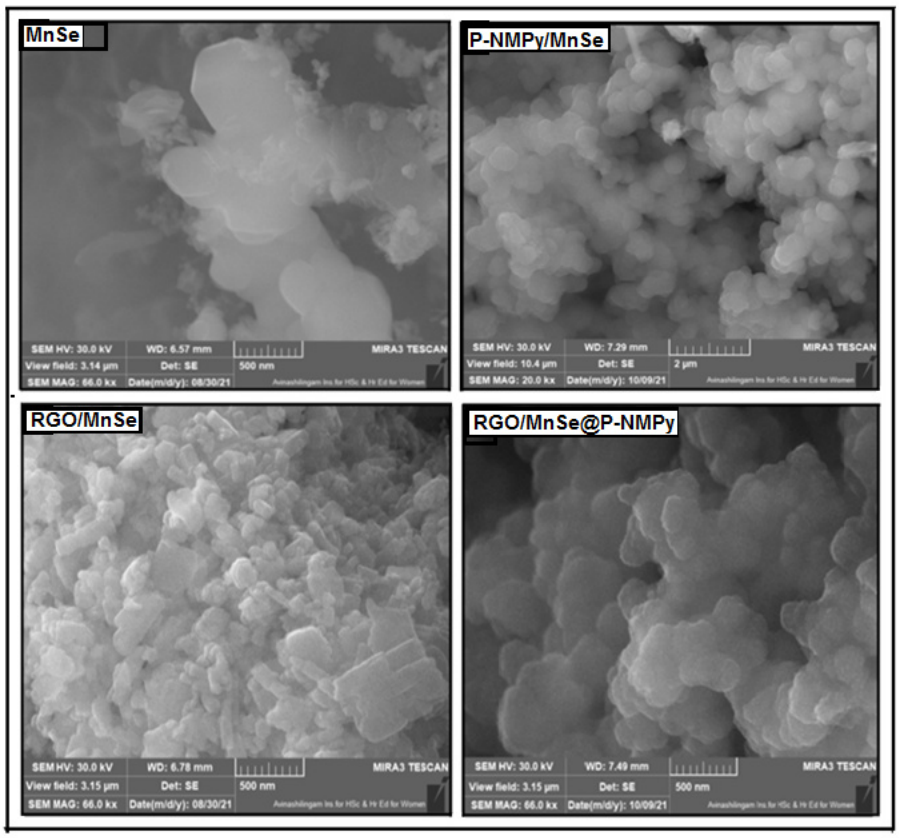

FIG. 2. FESEM images of MnSe, P-NMPy/MnSe, RGO/MnSe and RGO/MnSe@P-NMPy polymer nanocomposite

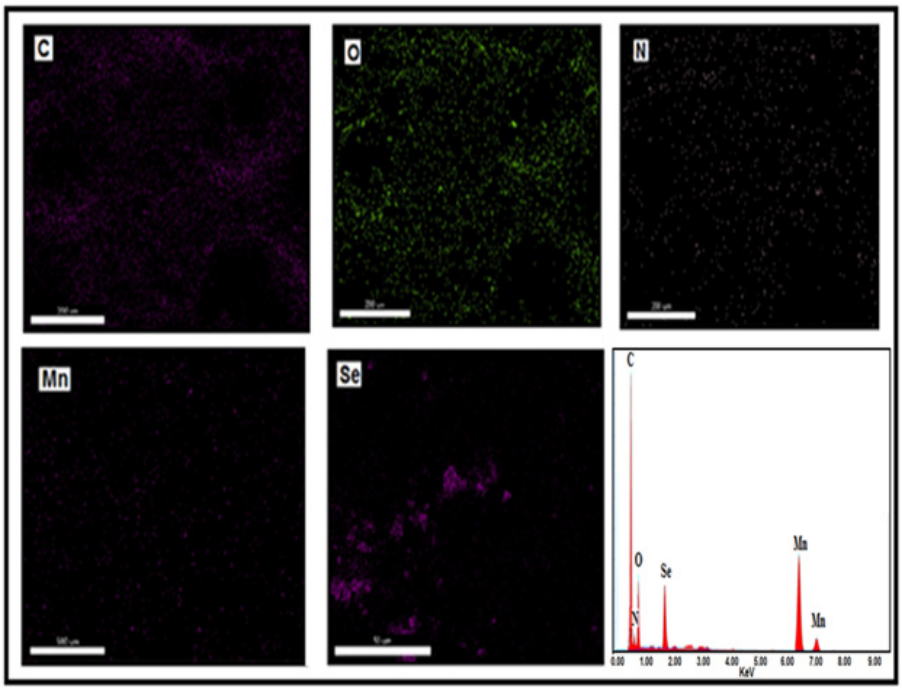

FIG. 3. Elemental mappings C, O, N, Mn and Se of RGO/MnSe@P-NMPy polymer nanocomposite

TABLE 1. Atomic composition of RGO/MnSe@P-NMPy polymer nanocomposite

Sample	Element	Atomic %
RGO/MnSe@Poly-N-methyl pyrrole nanocomposite	C	69.12
	O	21.33
	N	2.16
	Mn	3.93
	Se	3.46

in the RGO/MnSe matrix and its uneven spherical form. The TEM images clearly show that these nanoplates (Fig. 2) got well-dispersed over the thin graphene sheet, as was mentioned in the FESEM section. These findings are consistent with the elemental mapping investigations that were subjected to EDX analyses. (Fig. 3). Since P-NMPy was integrated into the RGO/MnSe matrix; the SAED pattern illustrates the transition from single-crystalline to polycrystalline nature.

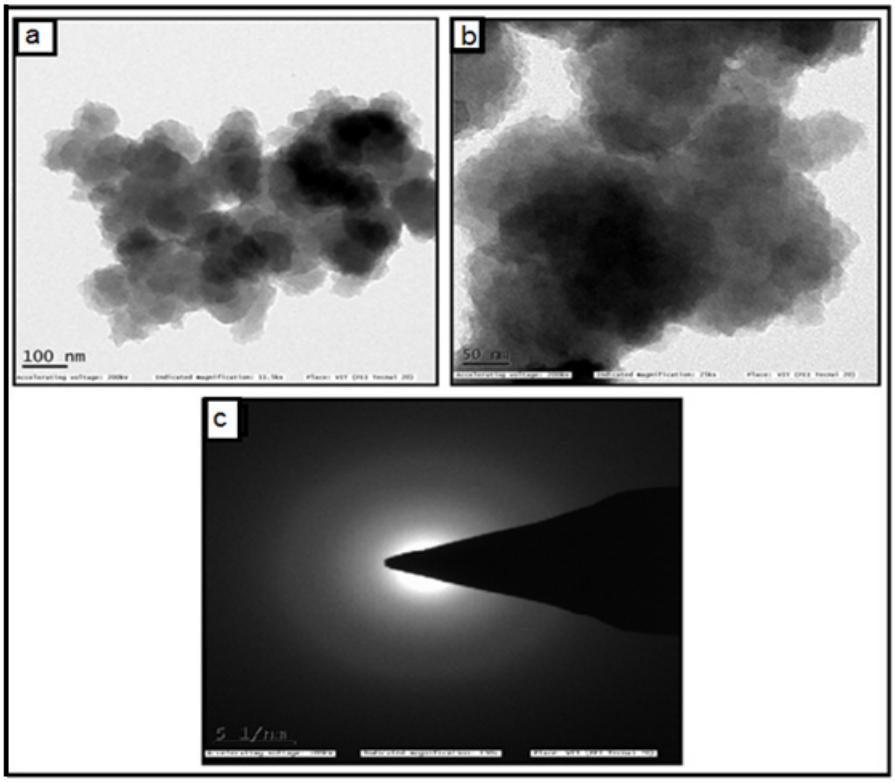

FIG. 4. TEM images of (a&b) RGO/MnSe@P-NMPy polymer nanocomposite and c) SAED pattern

3.3. Electrochemical measurements

3.3.1. Cyclic voltammetry activity of the modified polymer nanocomposite electrode. Cyclic voltammograms were used to examine the electrochemical behavior of MnSe, P-NMPy/MnSe, RGO/MnSe and RMP polymer nanocomposite. Platinum wire electrodes serve as a counter electrode, and the reference electrode is made of Ag/AgCl electrodes. The glassy carbon electrode (GCE) served as the working electrode for this experiment, it possesses an area of cross section is 0.0314 cm^2. Peak separation increases as scan rate increases, indicating the quasi-reversibility of the process of electron transfer. The peaks are acquired during different scan speeds of 30, 50, 100, 150 and 200 mVs^{-1}. As illustrated in Fig. 5, modified electrodes were created in 0.5 M KOH. The potential range displayed by the MnSe nanoparticle is -1.2 to 1.2 V. The chemical nature of the peaks on the cyclic voltammograms measured in KOH solutions, often exhibit oxidation and reduction peaks. The potential range of 0.54 to 0.80 V, 0.08 to -0.18 and 0.63 to -0.91 V shows three reduction peaks, whereas the conspicuous peak of the oxidation peak is found at 0.85 to 1.10 V. The rate at which the electron transfer occurs between the working electrode and the solution redox species. This suggests that the electro chemical process is highly reversible. For the P-NMPy/MnSe polymer nanocomposites, an appropriate range of -1.0 to 1.2 V was observed.

The figure shows one anodic peak at −0.80 to 1.05 V and one cathodic peak with a potential range of 1.11 to 0.38 V. It revealed that in cathodic scan modes, RGO/MnSe nanocomposite display two separate peaks, while in anodic scan modes, there is only one peak. The range from −0.8 to 1.0 V represents the potential window. The range of the anodic peak potential is 0.68 to 0.93 V. There are two cathodic peak potential ranges: 0.0092 to −0.33 V and −0.41 to 0.65 V. The potential range of RMP polymer nanocomposite was found between −1.0 and 1.2 V. One oxidation peak can be observed in the anodic scan between 1.101 and 0.413 V and in the anodic scan between −0.82 and −1.0 V potential range.

Electrochemically active surface area (ECSA) of catalysts must be calculated in order to compare their electrocatalytic performance. By measuring the charge collected oxidation area, the ECSA for various catalysts was computed using the cyclic voltammograms (Fig. 5). Using the double layer capacitance (DLC) electrochemical measurement method is one frequently used method to determine the surface area. Therefore, a differential capacitance measurement (DCM) with a limited potential range and variable scan rates is being used. If this test is done in a range where there is no Faradic response, the resulting differential capacitance equals the double layer capacitance (CDL) [28]. The electrochemical active surface area (ECSA) can be computed using this capacitance by using the formula

$$\mathrm{ECSA} = \mathrm{C_{dL}}/\mathrm{C_S}. \tag{1}$$

The ECSA cannot be calculated without the specific capacitance (CS). The ECSA values for MnSe, P-NMPy/MnSe, RGO/MnSe and RGO/MnSe@P-NMPy polymer nanocomposite were calculated as follows: 69.9, 84.5, 129.2 and 183.7 m^2/g, respectively. The value is the optimal flat surface capacitance of the catalyst. Electro-catalysts of methanol require multiactive centers to catalyze both oxygen reduction reaction (ORR) and oxygen evolution reaction(OER). This result clearly indicates that RGO/MnSe@P-NMPy polymer nanocomposite has more active sites than other electrocatalysts [26, 29]. The RMP polymer nanocomposite has a substantially higher ECSA value than the other MnSe, P-NMPy/MnSe and RGO/MnSe values, indicating a higher number of active sites.

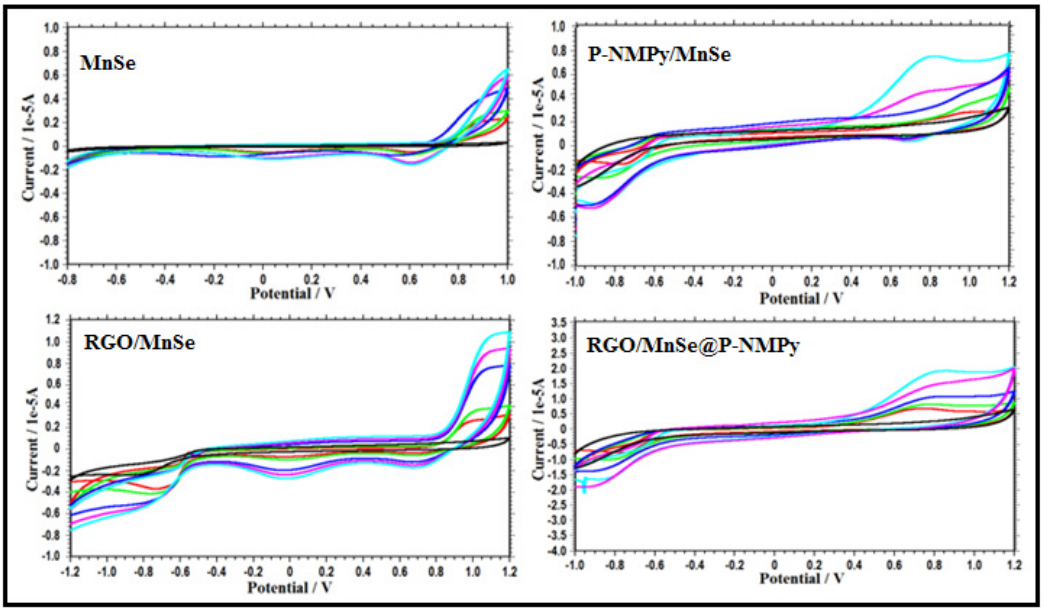

FIG. 5. Cyclic voltammetric behavior of MnSe, P-NMPy/MnSe, RGO/MnSe and RGO/MnSe@P-NMPy polymer nanocomposite in 0.5 M KOH at different scan rate (30, 50, 100, 150 and 200 mVs^{-1})

3.3.2. Electrochemical impedance measurements. Fig. 6 illustrates the charge transfer resistance of the as-prepared electrodes in a 0.5 M KOH solution using electrochemical impedance spectroscopy (EIS) curves. Similar semi-circular arcs were seen in the high frequency area of all EIS graphs, and the radius of these arcs indicates the electrode resistance's reaction to charge transfer. The electrochemical series resistance (ESR) of the symmetric cells is represented by the x-axis intercept of the half circle seen in the high-frequency region. The charge transfer resistance (R_{ct}) at the electrode and electrolyte interface was identified as the cause of the arc seen in the high-medium frequency region. When compared to MnSe, P-NMPy/MnSe and RGO/MnSe, the resistance (R_s) values of the RMP nanohybrid electrodes were lower, suggesting greater conductivity and better charge transfer. Because the impedance arc width of the RMP polymer nanocomposite was significantly smaller than that of the other materials, the EIS diagram showed the lowest electrical transfer resistance. The outcomes demonstrated that RGO/MnSe@P-NMPy polymer nanocomposite was advantageous to MOR.

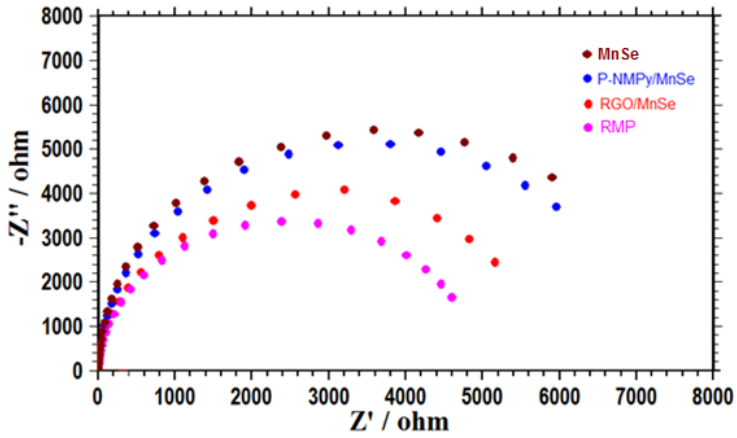

FIG. 6. EIS spectra of RGO, P-NMPy/MnSe, RGO/MnSe and RGO/MnSe@P-NMPy polymer nanocomposite

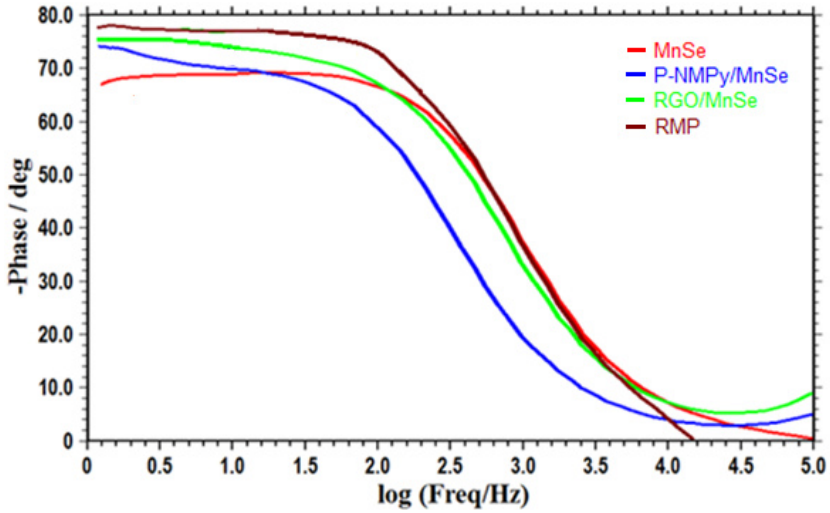

FIG. 7. Bode plot of phase angle/ degree versues log(freq/Hz) of MnSe, P-NMPy/MnSe, RGO/MnSe and RGO/MnSe@P-NMPy polymer nanocomposite

3.3.3. Pseudo capacitive behavior. The Bode plot illustrates the Bode phase change with applied frequency. The phase angle θ can range from 90° for a perfect capacitor ($n = 1$), but it can be 0° for a perfect resistor ($n = 0$) [30]. The Bode plot (-phase angle (degree) vs. $\log f$ (Hz) is shown in Fig. 7. The value of n is obtained by plotting the frequency against the $|Z|$ plot. The phase angle of 78° in the instance of RGO/MnSe@P-NMPy suggests that the material is pseudo capacitive. These findings imply that the behaviour of the RGO/MnSe@P-NMPy nanocomposite-coated electrode shifts from that of a pure resistor at high frequencies to that of pseudo capacitors at low frequencies. Bode phase angle of MnSe, P-NMPy/MnSe, RGO/MnSe and RGO/MnS@PMPyis found to be 67°, 73°, 76° and 78° respectively. It implies to a pseudo capacitor's characteristics. Bode phase angle values of MnSe, P-NMPy/MnSe, RGO/MnSe and RGO/MnSe@P-NMPy nanocomposite are presented in Table 2.

TABLE 2. Bode phase angle for MnSe, P-NMPy/MnSe, RGO/MnSe and RGO/MnSe@P-NMPy polymer nanocomposite

Sl. No	Samples	Bode phase angle°
1.	MnSe nanoparticles	67
2.	P-NMPy/MnSe polymer nanocomposite	73
3.	RGO/MnSe polymer nanocomposite	76
4.	RGO/MnSe@P-NMPy polymer nanocomposite	78

3.4. Electrochemical application

3.4.1. Methanol oxidation pathway. As equations (2) and (3) make evident, an essential component of the reaction process in the oxidation of methanol is the supporting electrolyte. The complete oxidation of methanol in both acid and base media is a 6 electron oxidation that releases CO_2, as indicated by equations (2) for methanol oxidation in acidic medium and (3) for basic medium:

$$CH_3OH + H_2O \rightarrow CO_2 + 6H^+ + 6e^-, \tag{2}$$

$$CH_3OH + 6OH^- \rightarrow CO_2 + 5H_2O + 6e^-. \tag{3}$$

The aforementioned equations clearly show that the pH of the supporting electrolyte is critical during methanol oxidation given the roles that protons and hydroxide ions play in the overall reaction. In each step, several intermediate organic molecules are transported along with six electrons. Throughout this process, CO is the main poisoning species, whereas formate and CO_2 (as carbonate) are the main dissolved products of the reaction. Studies in the literature indicate that because cations in solution have been demonstrated to affect reactions, Mn-based catalyst is appropriate for MOR reactions in alkaline media.

3.4.2. Oxidation of methanol using at various pH medium. As illustrated in Fig. 8, the CV was carried out using RMP polymer nanocomposite coated GCE in 1.0 M CH_3OH, scanning at 100 mVs^{-1} in the potential range of -1.0 to 1.2 V. The anodic current densities of RMP polymer nanocomposite varied significantly with different pH values; 63 mA/cm^2 at pH 1.0, 65 mA/cm^2 at pH 4.0, 58 mA/cm^2 at pH 7.0, 96 mA/cm^2 at pH 9.0 and 61 mA/cm^2 at pH 13.0. These results showed that the RMP polymer nanocomposite (pH 9.0) demonstrates the best conceivable methanol electro-oxidation efficiency in an alkaline medium [30]. The outcome of MnSe nanoparticles, RGO and P-NMPy is responsible for the higher electrochemical performance of ternary compound. Notably, Fig. 8 shows that pH 9.0 exhibits the highest current density and anodic oxidation potential, confirming its superior catalytic activity for methanol oxidation reactions (MOR) [32].

The electro-catalyst of RGO/MnSe@P-NMPy polymer nanocomposite has higher oxidation peaks at 0.9 V (pH 9) [33]. At this potential, it was proposed that methanol oxidation appears as a moderate increase in current density. These results clearly show that Mn/Se participates directly in this electro-catalytic methanol oxidation process. In the region around $\sim$0.9 V, at which only Mn species exist at the electrode surface, a new anodic peak was usually observed with a larger peak current (96 mA/cm^2 at pH 9.0) than that of alkali electrolyte (25 mA/cm^2) [34,35]. The height of this peak increases linearly with the methanol concentration in the solution, showing that it is related to a process involving methanol, in good agreement [36].

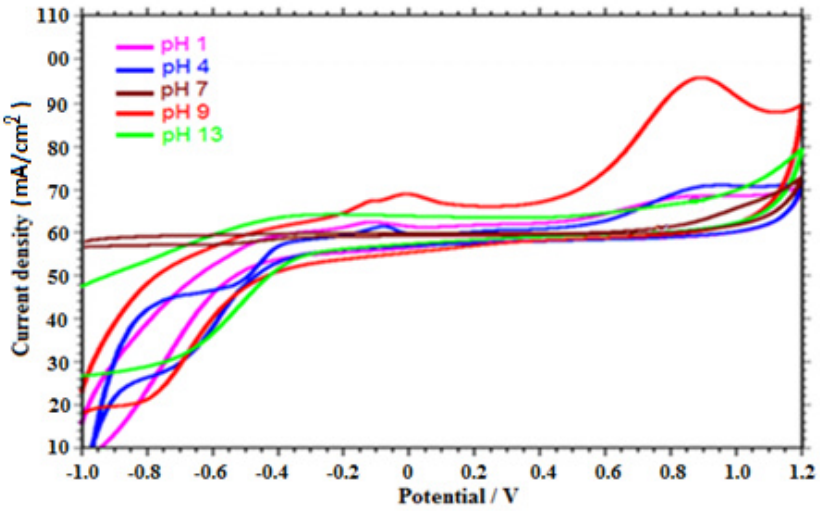

FIG. 8. Cyclic voltammogram of methanol using RGO/MnSe@P-NMPy polymer nanocomposite of pH 1.0, pH 4.0, pH7.0, pH 9.0 and pH 13.0

3.4.3. Chronoamperometry studies. Chronoamperometric measurements are a valuable technique for assessing catalyst stability. Modified anodes were subjected to extended tests at lower voltages against an Ag/AgCl electrode in 1.0 M CH_3OH and 0.5 M KOH. Fig. 9 displays chronoamperometry results for each catalyst used in methanol oxidation reactions. These curves illustrate how the initial adsorption of poisoning intermediates causes a rapid decline in current density, which then stabilizes over time. Notably, due to its higher ECSA (electrochemical surface area) and reduced CO poisoning effects, RGO/MnSe@P-NMPy nanohybrid exhibits a slower initial drop in current density and ultimately achieves a higher final current density compared to other materials [37, 38]. The findings indicate that RGO/MnSe@P-NMPy

polymer nanocomposite demonstrates superior stability and catalytic efficiency for methanol oxidation, as evidenced by the highest sustained current density observed in Fig. 9 [39]. The comparison of current density values from the figures reveals distinct performances: MnSe (13.00 – 0.38 mA/cm^2), P-NMPy/MnSe (15.27 – 0.58 mA/cm^2), RGO/MnSe (18.39 – 0.72 mA/cm^2), and RGO/MnSe@P-NMPy (27.71 – 0.97 mA/cm^2). This analysis underscores the synergistic impact of RGO/MnSe@P-NMPy polymer nanocomposite, which demonstrates remarkable catalytic activity as our proposed catalyst. The synergistic effect observed in the hybridization of multiple species enhances catalytic performance by leveraging complementary strengths and compensating for the limitations of individual active sites. This approach is pivotal in advancing catalyst design for efficient electrochemical processes.

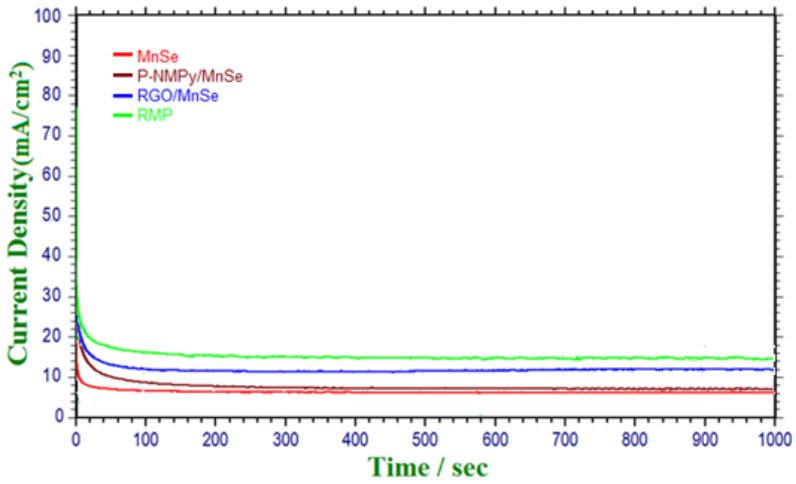

FIG. 9. Chronoamperometric curves of MnSe, P-NMPy/MnSe, RGO/MnSe and RGO/MnSe@P-NMPy polymer nanocomposite

4. Conclusion

MnSe nanoparticles supported on P-NMPy and RGO surfaces were synthesized using a novel and straightforward method. These were successfully utilized to modify RMP polymer nanocomposites, creating active electrodes for methanol oxidation reactions (MOR). One significant characteristic of the polymer nanocomposite is its ability to adopt a spherical shape, which likely contributes to enhanced MOR electrocatalytic activity. This approach suggests potential for multifunctional electrode applications in electrocatalysis. Characterization analyses confirm that MnSe nanoparticles are evenly dispersed within the RGO/P-NMPy matrix. The electrocatalytic performance of these catalysts in the oxidation of methanol (CH_3OH) in basic media was extensively studied. The RGO/MnSe@P-NMPy polymer nanocomposite exhibited a notable current density of 96 mA/cm^2 when exposed to methanol. The synergistic interaction among MnSe nanoparticles, P-NMPy and RGO (RMP) polymer nanocomposite significantly enhances their electrochemical and electrocatalytic capabilities. The RMP polymer nanocomposite electro-catalyst demonstrated an ECSA value of 183.7 m^2/g, indicating a high density of active sites crucial for MOR. During chronoamperometric measurements over extended periods (1000's), the RMP polymer nanocomposite modified electrode showed a higher initial current density (27.71 mA/cm^2) and a slower decline, ultimately achieving a stable state. This stability and high current density during electrochemical MOR highlight the superior performance of the RGO/MnSe@P-NMPy catalyst. These attributes underscore the potential of this catalyst for industrial-scale electrolysis, validated by its high electrocatalytic activity and robust electrochemical stability in methanol oxidation applications.

References

[1] Compton O.C., Jain B., Dikin D.A., Abouimrane A., Amine K., Nguyen S.T. Chemically active reduced graphene oxide with tunable C/O ratios. *ACS Nano*, 2011, **5** (6), P. 4380–4391.

[2] Ennaoui A., Fiechter S., Jaegermann W., Tributsch H. Photo electrochemistry of highly quantum efficient single-crystalline n-FeS_2 (pyrite). *J. Electrochem. Soc.*, 1986, **133**, P. 97–106.

[3] Kwon S.G., Hyeon T. Collodial Chemical Synthesis and Formation Kinetics of Uniformly Sized Nanocrystals of metals, Oxides and Chalcogenides. *Acc. Chem. Res.*, 2008, **41**, P. 1696–1709.

[4] Johari P., Shenoy V.B. Tuning the electronic properties of semiconducting transition metal dichalcogenides by applying mechanical strains. *ACS Nano*, 2012, **6**, P. 5449–5456.

[5] Wang D.S., Zheng W., Hao C.H., Peng Q., Li Y.D. A Synthetic Method for Transition-Metal Chalcogenide Nanoccrystals. *Chem. Eur. J.*, 2009, **15**, P. 1870–1875.

[6] Santra P.K., Kamat P.V. Mn-Doped Quantum Dot Sensitized Solar Cells:A Strategy to Boost efficiency over 5 %. *J. Am. Chem. Soc.*, 2012, **134**, P. 2508–2511.

[7] Wang L., Chen L., Luo T., Bao K., Qian Y. A facile method to the cube-like $MnSe_2$ micro crystallines via a hydrothermal process. *Solid State Commun.*, 2006, **138**, P. 72–75.
[8] Sobhani A., Salavati-Niasari M. Morphological control of $MnSe_2$/Se nanocomposites by amount of hydrazine through a hydrothermal process. *Mater. Res. Bull.*, 2013, **48**, P. 3204–3210.
[9] Zheng L., Li J., Zhou B., Liu H., Bu Z., Chen B., Ang R., Li W. Thermoelectric properties of p-type MnSe. *J. Alloy Comp.*, 2019, **789**, P. 953–959.
[10] She Z.W., Kibsgaard J., Dickens C.F., Chorkendoree I., Norskov J.K., Jaramillo T.F. Combine in theory and experiment in electrocatalysis: Insight into materials design. *Science*, 2017, **355**.
[11] Wang J., Liao T.L., Wei Z., Sun J., Guo J., Sun Z. Heteroatom-doping of non-noble metal-based catalysts for electrocatalytiic for hydrogen evolution: an electronic structure tuning strategy. *Small Methods*, 2021, **5**.
[12] Suh J., Tan T.L., Zhao W., Park J., Lin D.Y., Park T.E., Kim J., Jin C., Saigal N., Ghosh S., Wong Z., Chen Y., Wang F., Walukiewicz W., Eda G., Wu J. Reconfiguring crystal and electronic structures of MoS_2 by substitutional doping. *Nat. Commun.*, 2018, **9**, P. 199.
[13] Santhosh S., Teller H., Schechter A., Kalarikkal N. Effect of Mndoped NI–Co mixed oxide catalysts on urea oxidation. *Chem. Catchem.*, 2022, **14**.
[14] Li W., Liang C., Qiu J., Zhou W., Han H., Wei Z. Carbon nanotubes as support for cathode catalyst of a direct methanol fuel cell. *Carbon*, 2002, **40**, P. 787–790.
[15] Zhang L., Zhang D., Ren Z. Mesoporous $NiCo_2O_4$ micro/nanospheres with Hierarchicals structures for Supercapacitors and Methanol Electro-oxidation. *Chem. Electro Chem.*, 2017, **4**, P. 441–449.
[16] Wu J.B., Li Z.G., Huang X.H., Lin Y.J. Porous Co_3O_4/NiO core/shell nanowire array with enhanced catalytic activity for methanol electro-oxidation. *Power Sources*, 2013, **224**, P. 1–5.
[17] Li Z., Li M., Han M., Zeng J., Li Y., Guo Y., Liao S.J. Preparation And Characterization Of Carbon-Supported PTOs electrocatalysts via polyol reduction method for methanol oxidation reaction. *Power Sources*, 2014, **268**, P. 824–830.
[18] Zhang W., Pan Z., Yang F.K., Zhao B. A facile in situ approach to polypyrrole functionalization through bioinspired catechol. *Adv. Funct. Mater*, 2015, **25**, P. 1588–1597.
[19] Abaci U., Guney H.Y., Kadiroglu U. Morphological and electrochemical properties of PPy, PAni bilayer films and enhanced stability of their electrochromic devices (PPy/Pani-PEDOT, Pani/PPy-PEDOT). *Electrochim. Acta*, 2013, **96**, P. 214–224.
[20] Vellaichamy B., Periakaruppan P. Silver nanoparticle-embedded RGO-nano sponge for superior catalytic activity towards 4-nitrophenol reduction. *RSC Advances*, 2016, **6**, P. 88837–88845.
[21] Wu X., Zhou J., Xing W., Wang G., Cui H., Zhuo S. High-rate capacitive performance of graphene aerogel with a super high C/O molar ratio. *J. of Materials Chemistry*, 2012, **22**, P. 23186–23193.
[22] Vellaichamy B., Prakash P., Thomas J. Synthesis of AuNPs@RGO nanosheets for sustainable catalysis toward nitrophenols reduction. *Ultrasonics Sonochemistry*, 2018, **48**, P. 362–369.
[23] Onari S., Arai T. Infra-red lattice vibrations and dielectric dispersion in antiferro magnetic semiconductor $MnSe_2$. *J. Phys. Soc. Jpn.*, 1979, **46**, P. 184–188.
[24] Gemeiner P., Kulocek J., Mikula M., Hatala M., Sovre L., Hlavata L., Micusl M., Omastova M. Polypyrrole coated multi-walled carbon nanotubes for the simple preparation of counter electrodes in dye-sensitized solar cells. *Synth. Met.*, 2015, **210**, P. 323–331.
[25] Xu C., Sun J., Gao L. Synthesis of novel hierarchical graphene/polypyrrole nanosheet composites and their superior electrochemical performance. *J. of Materials Chemistry*, 2011, **21**, P. 11253–11258.
[26] Zhu C., Guo S., Fang Y., Dong S. Reducing sugar: New functional molecules for the green synthesis of graphene nanosheets. *ACS NAno*, 2010, **4**, P. 2429–2437.
[27] Murrary R.M., Forbes B.C., Heyding R.D. The Copper-Selenium System at Temperatures to 850 K and Pressures To 50 Kbar. *J. of Chemistry*, 1975, **53**, P. 4059–4061.
[28] Meher S.K., Rao G.R., Jia Y. Coatings in glewalled carbon nanotube with SnO_2 and its electrochemical properties. *Power Technol.*, 2012, **224**, P. 306–310.
[29] Bing Zhang, Shaofeng Lin, Jingjing Zhang, Xiaopeng Li, Xiaodong. Sun Facile Synthesis of Sandwich-Like rGO/CuS/Polypyrrole Nano architectures for Ecient. *Electromagnetic Absorption Materials*, 2020, **13**, 446.
[30] Bajpai A.K., Bhatt R.K., Kaatare R. Atomic force microscopy enabled roughness analysis of nanostructured poly (diaminonaphthalene)dopedpoly(vinyl alcohol) conducting polymer thin flims. *Micron*, 2016, **96**, P. 12–17.
[31] Fajin J.L., Cordeiro M.N.D. Insights into the mechanism of methanol steam reforming for hydrogen production over Ni-Cu-Based Catalysts'. *American Chemical Society of Catalyst*, 2021, **12**, P. 512–526.
[32] Chang R., Zheng L., Wang C., Yang D., Zhang G., Sun S. Synthesis of hierarchic al platinium-palladium-copper nanodendrites for efficient methanol oxidation. *Appl. Catal. B: Environ.*, 2017, **211**, P. 205–211.
[33] Kavitha M., Muthuchudarkodi R.R., Shakina J. NiSe integrated with Polymerized Reduced Carbon Sheet: As an effective electro-catalyst formethanol oxidation. *Int. J. Hydrogen Energy*, 2024, **51**, P. 1050–1059.
[34] Asgari M., Maragheh M.G., Davarkhah R., Lohrasbi E. Methanol Electrooxidation on the Nickel Oxide Nanoparticles/Multi-Walled Carbon Nanotubes Modified Glassy Carbon Electrode Prepared Using Pulsed Electrodeposition. *J. Electochem. Soc.*, 2011, **158**, K225–K229.
[35] Seghiour A., Chevalet J., Barhoum A., Lantelme F. Electrochemical oxidation of nickel in alkaline solutions: a voltammetric study and modelling. *J. Electroanal. Chem.*, 1998, **442**, P. 113–123.
[36] Pieta I.S., Rathi A., Pieta P., Nowakowski R., Hołdynski M., Pisarek M., Kaminska A., Gawande M.B., Zboril R. Electrocatalytic methanol oxidation over Cu,Ni and bimetallic Cu–Ni nanoparticles supported on graphitic carbon nitride. *Applied Catalysis B: Environmental*, 2019, **244**, P. 272–283.
[37] Gracita M., Tomboc, Hern Kim. Utilization of the superiorproperties of highly mesoporous PVP modified $NiCo_2O_4$ with accessible 3D nanostructure and flower-like morphology towards electrochemical methanol oxidation reaction. *J. of Energy Chemistry*, 2018, **29**, P. 136–146.
[38] Daryoush Afzali, Fariba Fathirad, Zahra Afzali, Mehdi Esmaeili Bidhendi. Design of PdxIr/g-C_3N_4 modified FTO to facilitate electricity generation and hydrogen evolution in alkaline media. *Int. J. of Hydrogen Energy*, 2020, **45**, P. 22965–22972.
[39] Meenakshi Choudhary, Samarjeet Siwal, Debkumar Nandi, Kaushik Mallick. Catalytic performance of thein situ synthesized palladium– polymer nanocomposite. *New J. Chem.*, 2016, **40**, P. 2296–2303.

Submitted 12 April 2025; revised 7 July 2025; accepted 8 August 2025

Information about the authors:

Kavitha Murugan – PG and Research Department of Chemistry, V.O. Chidambaram College, Thoothukudi-628008, Tamilnadu. Affiliated to Manonmaniam Sundaranar University, Abishekapatti, Tirunelveli-627012, Tamilnadu, India; ORCID 0009-0000-7962-8666; kavithakrithiv35@gmail.com

Kalaiarasi Senthurpandi – PG and Research Department of Chemistry, A.P.C Mahalaxmi College for Women, Thoothukudi-628002, Tamilnadu, Affiliated to Manonmaniam Sundaranar University, Abishekapatti, Tirunelveli-627012, Tamilnadu, India; ORCID 0000-0001-6855-8375; kalaiarasi@apcmcollege.ac.in

Vedhi Chinnapaiyan – PG and Research Department of Chemistry, V.O. Chidambaram College, Thoothukudi-628008, Tamilnadu. Affiliated to Manonmaniam Sundaranar University, Abishekapatti, Tirunelveli-627012, Tamilnadu, India; ORCID 0000-0002-3446-0641; cvedhi23@gmail.com

Muthuchudarkodi Rajaram – PG and Research Department of Chemistry, V.O. Chidambaram College, Thoothukudi628008, Tamilnadu. Affiliated to Manonmaniam Sundaranar University, Abishekapatti, Tirunelveli-627012, Tamilnadu, India; ORCID 0000-0002-2769-8045; muthu.rajaram@gmail.com

Conflict of interest: The authors declare that they have no known competing financial interests or personal relationships that could have appeared to influence the work reported in this paper.

NANOSYSTEMS:
PHYSICS, CHEMISTRY, MATHEMATICS

Shah K.A., et al. *Nanosystems: Phys. Chem. Math.*, 2025, **16** (5), 681–692.
http://nanojournal.ifmo.ru
DOI 10.17586/2220-8054-2025-16-5-681-692

Original article

Modified ZnSe nanoparticles for removal of heavy metal iron (Fe) from aqueous solution

Khurshed A. Shah[1], Humaira S. Wani[2], S. M. A. Andrabi[2], Quinton L. Williams[3]

[1]PG Department of Physics, Sri Pratap College, Cluster University Srinagar, J&K-190001, India
[2]Department of Applied Sciences, Institute of Technology, Zakura Campus, University of Kashmir, Srinagar, J&K-190006, India
[3]Department of Physics and Astronomy, Howard University, NW, Washington, DC 20059, USA

Corresponding author: Khurshed A. Shah, drkhursheda@gmail.com

ABSTRACT Iron is a heavy metal found in water due to natural geological sources, household trash, industrial waste, and numerous by-products. An excessive amount of iron in drinking water can lead to significant health issues in humans. In the current study, metallic Zn–Se NPs modified with Ag and urea were synthesised via the sol-gel method and characterised by XRD, FESEM, EDX and FTIR. The synthesised ZnSe:Ag:Urea nanoparticles were used for the adsorptive removal of iron, a heavy metal, from water. Herein, we have utilised adsorption technology to extract iron ions from water, considering the toxicity of iron at high concentrations. Experimental batch adsorption studies were conducted on an aqueous solution containing Fe (III) ions under various conditions, including temperature, contact time, adsorbent dosage, and initial metal ion concentration. Results showed that iron adsorption was favourable, with a maximum removal percentage of 89.5 % under optimal room temperature conditions, optimal adsorbent dosage, and initial metal ion concentration. of 0.1 g/L and 100 mL, respectively. The iron absorption also reached an equilibrium state within 80 minutes of contact time by using ZnSe:Ag:Urea as the adsorbent.

KEYWORDS ZnSe nanoparticles, iron, heavy metal, absorption

ACKNOWLEDGEMENTS This work was supported by the JKST&IC-funded project (Grant No. JKST&IC/SRE/1172-74), CSIR-HRDG funded project (scheme no. 1510/23/EMR-II) and SERB (Grant No. CRG2022/006428-G)).

FOR CITATION Shah K.A., Wani H.S., Andrabi S.M.A., Williams Q.L. Modified ZnSe nanoparticles for removal of heavy metal iron (Fe) from aqueous solution. *Nanosystems: Phys. Chem. Math.*, 2025, **16** (5), 681–692.

1. Introduction

Clean water is one of the essential requirements for the existence of life on Earth. However, in recent years, the contamination of water has become a significant problem all around the globe. This is mainly because of industrialisation and huge population growth spurred by expanding urbanisation, leading to an increase in contamination of water at an alarming rate [1,2]. Heavy metals, the major water pollutant, pose the most significant damage to human health and the environment as they are highly poisonous, even at low concentrations. This non-biodegradable material accumulates through the food chain and destroys aquatic life while posing significant risks to human health [3]. There is a substantial increase in water pollution due to heavy metals because of the continuous increase in urban and rural industrial and agricultural activities such as the preservation of wood and dyes, electroplating, steel production, industrial smelting, sewage irrigation, textiles, fertilisers, battery manufacturing, construction, pharmaceutical, metallurgical industries, etc. [4]. Heavy metals like Hg, Cr, As, Zn, Ni, and Cd are highly hazardous to human beings, and exposure to even small amounts of these heavy metals cause severe damage to human health [5]. These metals naturally infiltrate water bodies as rainwater seeps through rocks, resulting in the dissolution of trace amounts of metals into the water. This water subsequently flows into larger water bodies, which are utilized by individuals for various purposes. Iron is one of the metals that is naturally present in water. It is the fourth most abundant element on the planet, and it holds the second position in terms of abundance within the earth's crust [6]. It is present in significant amounts within rocks and soil systems globally. This mineral nutrient is essential, contributing to the regulation of energy metabolism. Moreover, it serves as a crucial component in hemoglobin, myoglobin, and various enzymes. Insufficient iron levels in the body can lead to iron deficiency, anemia, fatigue, and a heightened vulnerability to various infections [7]. Water bodies obtain iron from either natural geological sources or through the disposal of household waste and industrial discharges [8]. The primary sources of iron in surface water include pollution originating from the iron and steel industries, as well as mining activities and the corrosion of metals [9]. In addition to surface water, iron is found in groundwater as well. The primary cause of iron's presence in groundwater

is the leaching process from iron-rich rocks and minerals [10]. The levels of iron found in both surface and groundwater range from 3 to 4 mg/L up to 15 mg/L [11]. The concentration of iron in the groundwater of West Bengal, India, ranges from 2 to 10 mg/L [12]. In the Ganga river, near the Fazalpur industrial area located in the Moradabad district of Uttar Pradesh, India, iron concentrations have been recorded as high as 6 mg/L [13]. Furthermore, the groundwater in Assam, an eastern state of India, exhibits significant contamination with high levels of iron [14–16]. It is important to note that the permissible limit for iron in drinking water is set at 0.3 mg/L [17, 18]. While initial concentrations exceeding this limit may not pose immediate health risks, prolonged consumption of water with elevated iron levels can lead to a condition known as iron overload [19]. Excessive consumption of iron can result in the disruption of hematopoiesis by harming both the progenitor cells and the supportive microenvironment necessary for this process. If iron overload is not addressed, it may progress to hemochromatosis, which can cause damage to various organs in the body [20–25]. The initial manifestations consist of weight reduction, joint discomfort, and exhaustion. Additionally, ocular conditions like retinitis, conjunctivitis, and choroiditis, along with cancer and cardiovascular diseases, represent some of the prevalent health challenges associated with elevated levels of iron in the water [26]. In addition to the aforementioned health-related concerns, various other issues associated with elevated iron levels in water have been documented. At higher concentrations, this metal contributes to an unpleasant odor, a metallic flavor, and a reddish hue in the water [27]. It also leads to the formation of stains and streaks on laundry and plumbing fixtures. The accumulation of softeners and pipelines caused by the precipitation of iron can result in unfavorable conditions within the water distribution systems [28]. Elevated levels of iron can serve as a substrate for specific bacterial species. The interior surfaces of pipes provide an optimal environment for these bacteria. Their populations can grow to such an extent that they begin to obstruct pipes, thereby diminishing the water flow rate within the pipeline. Once these bacterial colonies become established, their removal from the pipeline poses significant challenges. Additionally, pipelines constructed from iron frequently encounter issues such as punctures and leaks, as noted in references [28, 29]. The decomposition of these bacteria results in the generation of foul odors and undesirable tastes in the water supply [28].This calls for the effective treatment of water in order to remove the elevated levels of iron and produce safe and clean water. A number of methods have been reported in the past for such purpose.

In the present study, ZnSe nanoparticles doped with Ag and functionalized with urea (denoted ZnSe:Ag:Urea) were synthesized via the sol-gel method and comprehensively characterized by X-ray diffraction (XRD), field emission scanning electron microscopy (FESEM), energy-dispersive X-ray spectroscopy (EDX), and Fourier transform infrared spectroscopy (FTIR). Set experiments were conducted to investigate the adsorptive removal of Fe(III) under varying conditions of temperature, contact time, adsorbent dosage, and initial ion concentration. The synthesized ZnSe:Ag:Urea nanoparticles demonstrated a maximum iron removal efficiency of 89.5 % at optimal conditions – an adsorbent dosage of 0.1 g/L, solution volume of 100 mL, room temperature, and equilibrium achieved within 80 minutes.

This work aims to (i) validate the synthesis and modification strategy for ZnSe:Ag:Urea nanoparticles; (ii) Assess their potential as an efficient and regenerable nano-adsorbent for water treatment applications.

2. Experimental details

2.1. Materials

Zinc acetate dihydrate ($Zn(CH_3CO_2)_2{\cdot}2H_2O$), selenium powder, Silver nitrate ($AgNO_3$), urea (NH_2CONH_2), hydrazine hydrate (N_2H_6), ethylene glycol ($OHCH_2CH_2OH$) and methanol were used in this study. All chemicals, purchased from Merck, India, were used as received and without further purification and were of analytical reagent grade (> 95 % purity).

2.2. Methodology

Urea and silver modified ZnSe nanoparticles were synthesised by a chemical route called the sol-gel method. In a typical reaction, 0.5 M zinc acetate solution was prepared by dissolving 1.317 g of zinc acetate dehydrate salt in 12 mL of methanol, whereas that of selenium(1 M) was prepared by dissolving 0.631 g of selenium in 8 mL of methanol. The two solutions were sonicated for 30 minutes in an ultrasonic bath, transferred to a 200 mL beaker, and again sonicated for 30 minutes. Next, the prepared solution was refluxed at 80 °C on a hot plate magnetic stirrer for 3 hours. After the first 10 minutes,10 ml hydrazine hydrate, a reducing agent, and 15 ml ethylene glycol, a stabilising agent, were added dropwise to the solution. Then, the solution was doped with 50 % silver nitrate and 50 % urea. After about 40 minutes, the reaction was completed (i.e., the solution was converted into gel) and stirring was stopped. The gel that formed was kept at a temperature of 80 °C to allow the volatile impurities to escape, and a dark-grey coloured xerogel was formed, which was then washed with deionised water 3-4 times using a centrifuge at a speed of 6000 rpm. Finally, the resultant product was dried in an oven at 70 °C for 24 hours and yielded a dry mass which was crushed in a mortar and pestle to reduce particle sizes to the nanoscale. Fig. 1. illustrates the detailed Experimental procedure for synthesising the Urea:Ag:ZnSe nanoparticles.

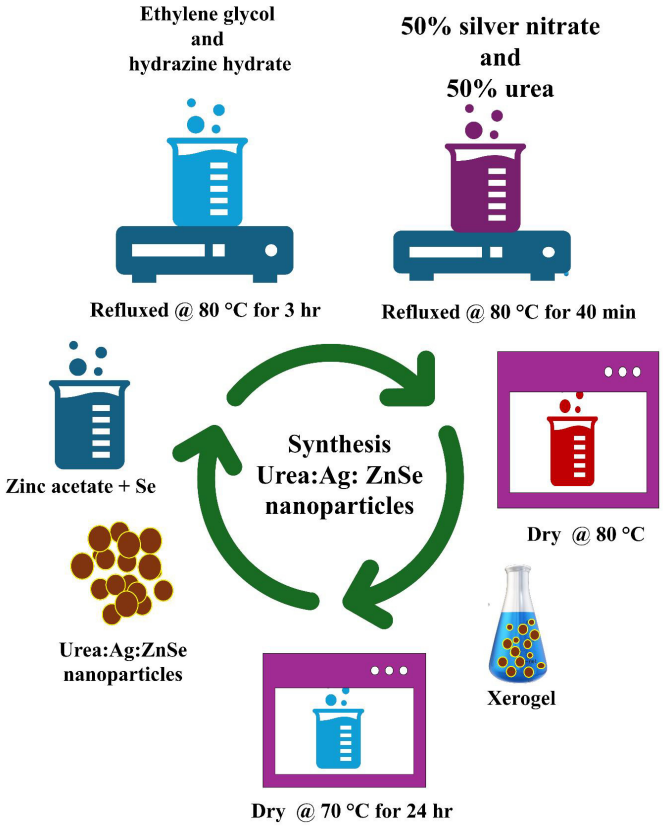

FIG. 1. Experimental procedure for the synthesis of the Urea:Ag:ZnSe nanoparticles

3. Results and discussion

3.1. Characterization of Urea:Ag:ZnSe nanoparticles

The synthesised ZnSe nanoparticles were characterised using X-ray diffraction (XRD), Field Emission Scanning Electron Microscopy (FE-SEM), Fourier Transform Infrared Spectroscopy (FTIR), Energy Dispersive X-Ray (EDX), Particle Analyzer and Zeta Potential studies. The crystal structure of the sample ZnSe NPs was investigated by XRD using Smart Lab 3kW X-ray Diffractometer from Rigaku operating at a voltage 40 kV and filament current 30 mA with CuKβ radiation($\lambda = 1.392$ Å) and scanning rate of 5.0985 deg/min and scan range set from 20° to 80°.The FE-SEM (Gemini SEM 500 from Carl Zeiss) and ultra dry Compact EDS Detector (Thermo Scientific™) are used for high-resolution imaging and elemental analysis. Energy Dispersive X-Ray Spectra (EDS) was used to identify samples' elemental composition and purity by atom percentage of metal, and FE-SEM examination confirmed the surface shape of ZnSe NPs.The phase composition and molecular structure analysis were done using FTIR (Shimadzu). A lithium tantalate detector, a Perkin Elmer Spectrum 2 (USA), was used to obtain Fourier-Transform Infrared Spectra in the 400 – 4000 cm^{-1} range. With a resolution of 4 cm^{-1}, a single scan produced the spectra to identify and characterise functional groups.

3.1.1. XRD analysis. Powder X-ray diffraction (XRD) investigations were conducted on Ag and urea-doped ZnSe NPs. CuKβ radiation of wavelength 1.392 Å and scanning rate of 5.0985 deg/min).The XRD profile (Fig. 2) reveals the presence of zinc selenide (ZnSe), silver selenide (Ag_2Se), Urea (NH_2CONH_2) and selenium (Se) in the as-prepared nanoparticles. The peak at 2θ = 27.2° (111), 45.22° (220), 53.58° (311), 67.31° (400) and 72.68° (203) corresponds to ZnSe [30–37]. The peak at 2θ=33.4°(112), 34.68°(121), 39.94°(103) and 40.268°(122) correspond to Ag_2Se [38, 39]. Two peaks of NH_2CONH_2 (urea) have been obtained at 2θ=22.76° and 36.92° due to diffraction from (110) and (210) planes, respectively [40, 41]. A single diffraction peak for by-product Se has also been obtained. Also the peak corresponding to Ag obtained at 2θ = 37° (111), 46° (200), 64° (220), and 78° (311) [42]. The average crystallite size has been estimated using Scherrer's formula: $G = (0.9\lambda)/(\beta \cos\theta)$, where λ is the wavelength of CuKα radiation ($\lambda = 1.541$ Å), β is the full width at half maximum (FWHW) of the intensity of the corresponding peak and θ is half the angle between the incident and the scattered X-ray beams. The average particle size of ZnSe:Ag:Urea NPs was calculated to be 19.911 nm.

3.1.2. Morphological studies by FE-SEM. The surface morphology of urea and silver-modified zinc selenide nanoparticles was studied using an FE-SEM.The FE-SEM images (Fig. 3(a,b,c,d)) show that the synthetic Urea:Ag:Zn:Se nanoparticles are almost spherical and round-shaped with porous surfaces. Surface modification by silver and urea of ZnSe NPs

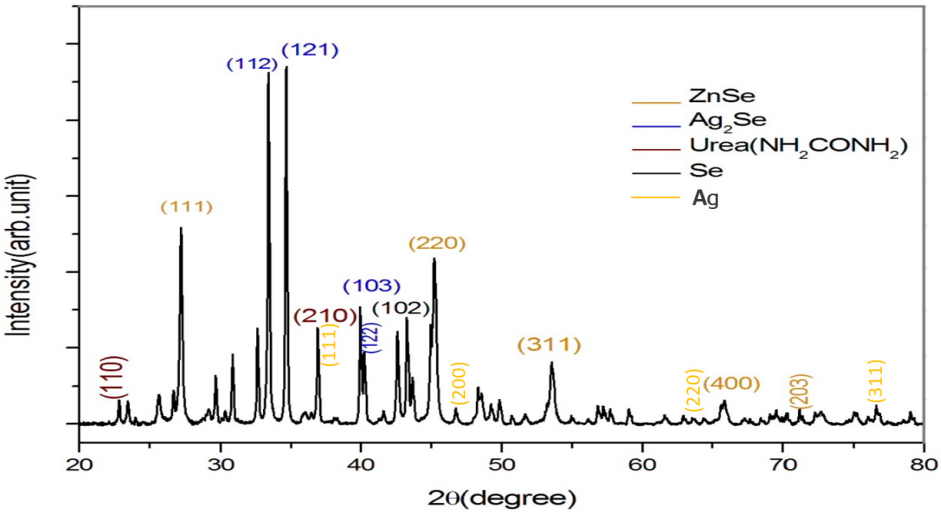

FIG. 2. XRD spectra of Urea and Ag doped ZnSe nanoparticles

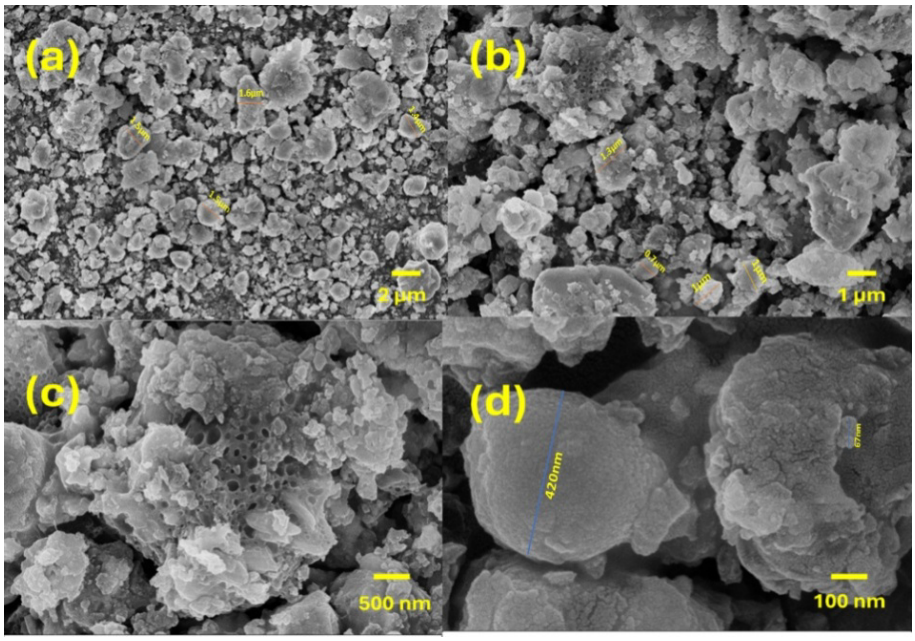

FIG. 3. FESEM images (a,b,c and d) of urea: Ag:Zn:Se nanoparticles for various magnifications

forms the porous structure. The material, as synthesised, consisted of highly facetted nanoparticles that were connected and clustered together.

3.1.3. Elemental composition analysis by EDX. The elemental composition of synthesised Urea:Ag:Zn:Se NPs was determined by Energy Dispersive X-Ray (EDX) spectroscopy. In the EDX spectra displayed in Fig. 4(a), 11 peaks could be seen for the parent material of urea:Ag:Zn:Se nanoparticles: three peaks for elemental zinc, three for selenium, two for silver and three for elements carbon, oxygen and nitrogen present in urea. Other small peaks in the spectrum indicate the presence of minor levels of Au, which are attributed to the coating procedure that the samples were subjected to preceding the EDX examination analysis confirms the presence of Zn (9.6 %), Se(19.7 %), Ag(16.2 %), urea (29.3 % C, 15.2 % N, 10.2 % O) as shown in Fig. 3(b).

3.1.4. Analysis of FTIR spectra. A view of the pure urea FTIR spectrum is presented in Fig. 5(a). The C=O stretching frequency is visible at 1677 cm^{-1}. Stretching and deformation frequencies for N–H are observed at 3455 and 1625 cm^{-1}, respectively. The C–N stretching frequency is visible at 1453 cm^{-1} [43]. The FTIR spectra of pure ZnSe nanoparticles are depicted in Fig. 4(b). ZnSe vibrations are characterised by distinctive peaks at 480, 552, 612, 664, and 960 cm^{-1}. The trace amount of H_2O in the solution explains the peak at 3204 cm^{-1}, which was attributed to O–H stretching. Additionally,

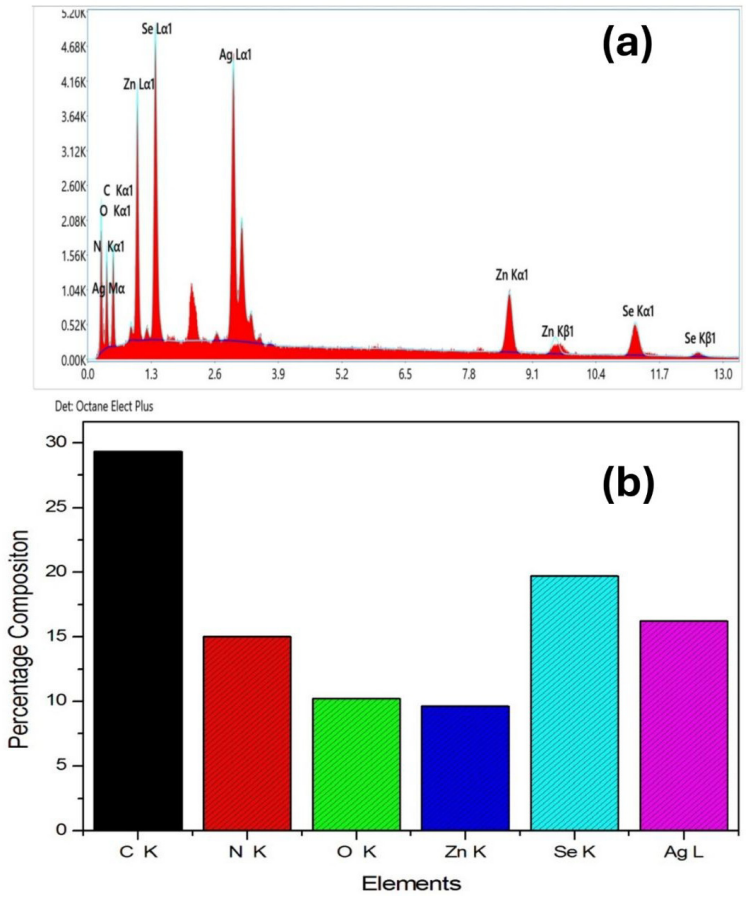

FIG. 4. (a) EDX spectrum;(b) The percentage elemental composition of urea: Ag:Zn:Se nanoparticles

the characteristic ZnSe absorption peak is represented by the peak at 960 cm^{-1}, while the Se–O stretching bond causes the peak at 1134 cm^{-1}. The peak at 3199 cm^{-1} corresponds to the N–H stretching vibration band, indicating N_2H_4's interaction with the zinc ion [44].

On the other hand, the FTIR spectra of ZnSe nanoparticles modified with silver and urea, as displayed in Fig. 5(c), show deviated and different numbers of peaks from those of pure ZnSe and pure urea, which suggests that new bonds are formed. ZnSe vibrations characterised by distinctive peaks 480, 550, 610 and 664 cm^{-1} are shifted to 546, 620, 721 and 815 cm^{-1}. The characteristic ZnSe absorption peak at 960 cm^{-1} is shifted to 1051 cm^{-1} while the peak at 1134 cm^{-1}, caused by the Se–O stretching bond, is shifted to 1150 cm^{-1}. This suggests an Ag–Se bond formation, which is also supported by XRD studies as Ag_2Se peaks are observed in XRD spectra. The kind and nature of the metal appear to impact how urea coordinates with metal ions. While Zn(II) coordinates to the oxygen of urea, Ag(II) preferentially coordinates to the nitrogen. If a nitrogen-to-metal connection exists in urea-metal complexes, the complex's vibrational spectrum differs greatly from that of the free urea molecule. The C=O (C=O)) would be adjusted to a higher frequency at roughly 1700 cm^{-1}, and the N–H stretching frequencies would be shifted to lower values [45–48].

Here, in the FTIR spectra of synthesised Urea:Ag:Zn:Se NPs as shown in Fig. 4(c), the C=O stretching frequency 1677 cm^{-1} of pure urea is shifted to 1701 cm^{-1}. The C–N stretching frequency has shifted from 1453 to 1480 cm^{-1}. However, the nitrogen-hydrogen bond stretching vibration peaks provide the best infrared signal for nitrogen. Two of these are seen in Fig. 4(c) at 3257 and 3142 cm^{-1}, indicating the shift of the N–H stretching frequency to 3455 cm^{-1} from that of pure urea. Also, hydrogen bonding is the reason for these peaks' reduced amplitudes but broader bases. It should be noted that the N–H stretching peaks are smaller and narrower than the O–H stretching peaks, which are broad and strong, although the O–H stretching peaks of functional groups such as alcohols and carboxylic acids also fall within this range (3500 to 3100 cm^{-1}). Note that the O–H stretching peaks of functional groups like alcohols and carboxylic acids also fall in this range (3500 to 3100 cm^{-1}), but these peaks are broad and strong compared to N–H stretching peaks, which are narrower and smaller. The N–H deformation frequency is visible at 1630 cm^{-1}. This suggests urea has coordinated to the metal (Ag) through nitrogen. Further, the peaks at around 2887 and 2826 cm^{-1} can be attributed to C–H stretching of urea. Thus, the FTIR study leads to the conclusion that Ag bridges the bond formation between ZnSe NPs and urea's Ag forms the bond with Se of ZnSe NPs, and nitrogen of NH_2 group of urea leads to the deviation of FTIR spectra of synthesised nanomaterial from that of pure urea and pure ZnSe NPs, respectively.

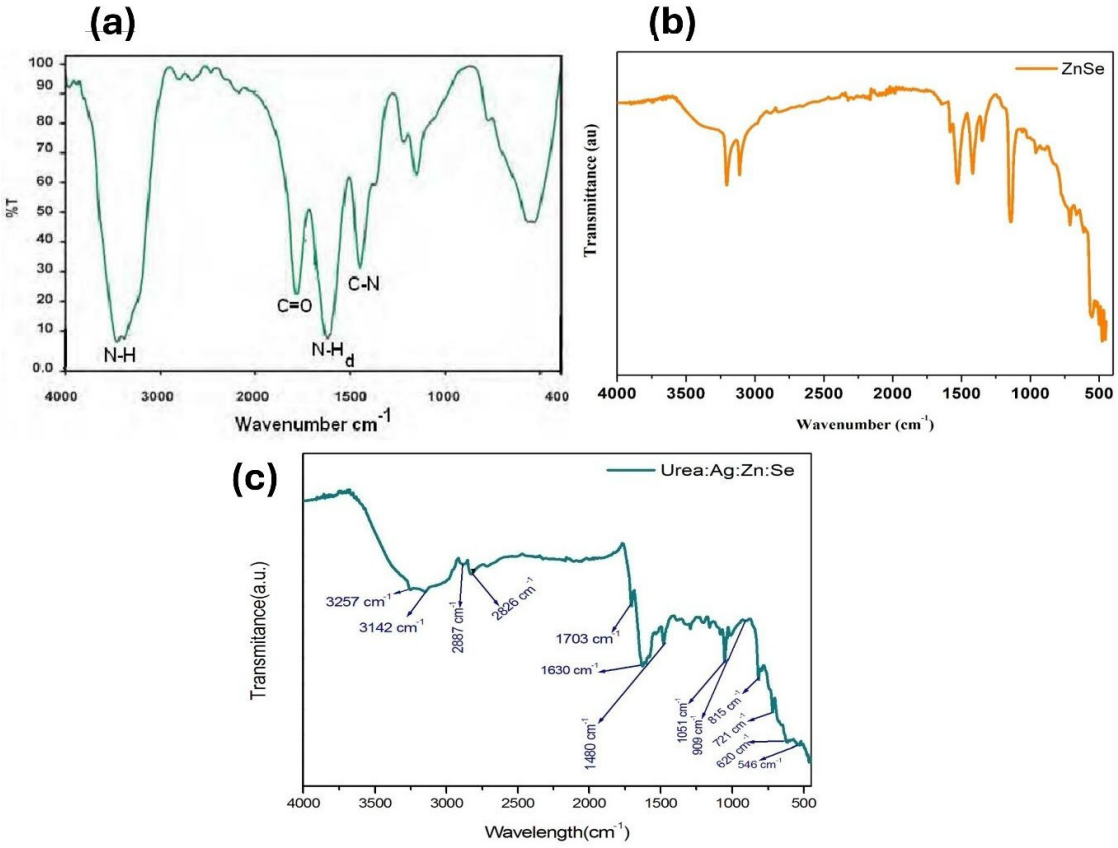

FIG. 5. FTIR spectra of (a) pure urea, (b) pure ZnSe NPs and synthesised Urea:Ag:Zn:Se NPs

4. Adsorption experiments

Batch adsorption experiments were conducted to determine how different parameters (initial conc of metal ion, amount of adsorbent, contact time and temperature) affected the removal rate of Fe and adsorption capacity of Ag and Urea modified ZnSe nanomaterial. Fe removal experiments were performed using 100 mL Erlenmeyer flasks containing 50 mL metal solution of desired concentration and specific amounts of adsorbent. An electric orbital shaker was used to shake the Erlenmeyer flasks at 200 rpm continuously. After the elapsed time, each flask's solution was filtered using Whatman filter paper, and the concentration of iron ions was determined using AAS(atomic absorption spectrophotometer). The ideal contact time was calculated at room temperature with 0.1 g/L of adsorbent and 100 mg/L of Fe. The 0.01 – 0.4 g/L and 5 – 250 mg/L, respectively, were used to study the effects of adsorbent dose and initial Fe concentration. At 25, 50, and 80 °C, the impact of solution temperature (25, 50, and 80 °C) on the effectiveness of Fe removal was examined. The amount of Fe adsorbed onto the adsorbent at each contact time (q_e) was calculated using the eq. (1):

$$q_e = (C_0 - C_e) \cdot \frac{V}{m}, \tag{1}$$

where C_0 and C_e are initial and equilibrium concentration of Fe (mg/L), respectively. V is the volume of the aqueous phase (L) and m is the mass of adsorbent (ZnSe:Ag:Urea). The removal percentage of Fe was calculated using the following eq. (2):

$$\text{Removal efficiency } (\%) \ = \frac{C_0 - C_i}{C_0} \cdot 100\ \%. \tag{2}$$

4.1. Effect of contact time

Figure 6 shows the effect of time on the Fe adsorption with an adsorbent dosage of 0.1 g and an initial Fe concentration = 100 mg/L/L. The removal rate increased significantly within the first 70 minutes, then increased marginally, reaching its steady state within 80 minutes. The availability of many empty active sites on the adsorbent surface may cause a substantial increase in adsorption efficiency. However, extending the duration of contact reduces the availability of iron ions to the adsorbent surface's active sites, decreasing the removal efficacy [49]. In other words, the reason for the constant value throughout the equilibrium phase is that heavy metal ions entirely occupy the vacant space. As time passes, no more adsorbent sites are available for the heavy metal ions to bind to [50]. Thus, the 90-minute contact period has been chosen as the ideal contact time for subsequent study.

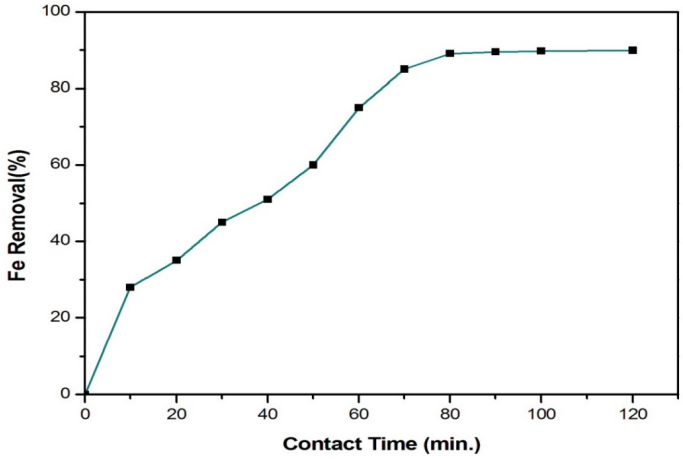

FIG. 6. Effect of contact time on the percentage removal of iron ions (adsorbentdosage, 0.1 g; initial Fe conc. = 100 mg/L; 200 rpm agitation speed; room temperature)

4.2. Effect of initial metal (Fe) concentration

It was observed initially as the metal ion (Fe) concentration. Increases from 0 – 100 mg/L, the percentage of Fe removal increased from 46 to 89.6 %, which can be attributed to the higher number of available vacant sites on the adsorbent and the rise in the concentration gradient between the Fe ions in the solution and the Fe ions on the surface of the adsorbent [51]. Then, by further increasing the initial Fe ion concentration from 100 – 250 mg/L, the Fe removal percentage decreased from 89.6 to 73.46 %. This is because with the progress of the adsorption process, the available vacant sites of the adsorbent reduce [52] and the concentration. The gradient of metal ions also decreases, leading to a decrease in iron removal percentage, eventually leading to equilibrium. Table 1 shows the impact of different Fe concentrations (5, 10, 50, 100, 150, and 250 mg/L) on the percentage removal of iron, the same is plotted in Fig. 7.

TABLE 1. Adsorption data for Fe removal

Initial Fe conc. (mg/L) C_0	**Eq. Fe conc. (mg/L)** C_e	**Fe Removal (%)** $[(C_0 - C_e)/C_0] \cdot 100$	**Eq. Adsorption Capacity (mg/g)** $q_e = [(C_0 - C_e) \cdot V]/m$
5	2.7	46 %	1150
10	4.59	45.9 %	2705
50	13.9	72.2 %	18050
100	10.4	89.6 %	44800
150	24.6	83.6 %	62700
250	66.35	73.46 %	91825

4.3. Effect of adsorbent dosage

The experiment employed several adsorbent concentrations (0.01, 0.05, 0.1, 0.2, 0.3, and 0.4 g), with an initial concentration of 100 mg/L of Fe metal and a 90-minute contact duration.

As shown in Fig. 8, it is clear that initially,as the adsorbent dosage increases from 0.01 to 0.2 g, the removal percentage of Fe was enhanced from 42.34 to 85.76 % for 100 mg/L of Fe. This is because the availability of active sites on adsorbent increases, and hence there is a rise in the adsorption of Fe ions. Further, as the adsorbent dosage increases from 0.01 to 0.1 g, the rate of increase in percent removal is higher than when the adsorbent dosage is increased from 0.1 to 0.2 g. This indicates that with the adsorption, saturation of adsorption sites takes place, and hence with further increase in the adsorbent dosage from 0.2 to 0.4, the percentage of Fe removal remains almost constant. This may also result from aggregation by large adsorbates, reducing the adsorbent's active surface area [49].

4.4. Effect of temperature

The removal of iron ions by the adsorbent was observed to increase from 89.5 % at 25 °C to 93.2 % at 50 °C, and with further increase in temperature at 80 °C, the percentage of Fe removal was found to be 93.4 %, and equilibrium is almost established, as shown in Fig. 9. Higher diffusion rates and improved ion mobility at high temperatures may have

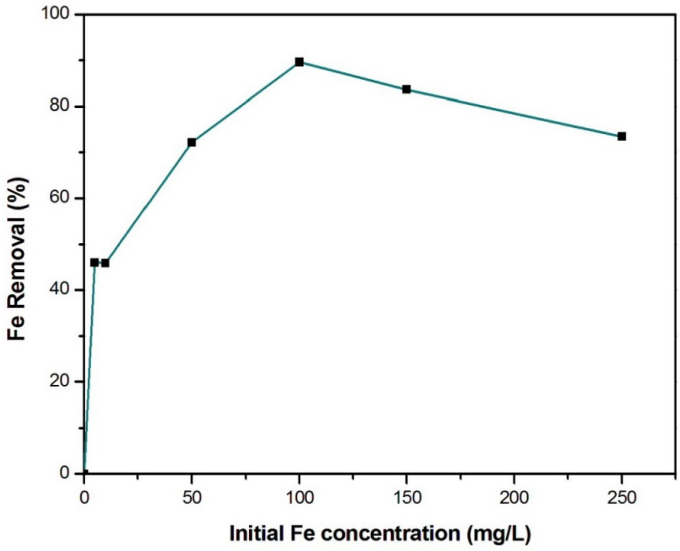

FIG. 7. Effect of initial metal ion (Fe) conc. on percentage removal of iron ions (adsorbent dosage, 0.1 g; contact time = 90 min.; 200 rpm agitation speed; room temperature)

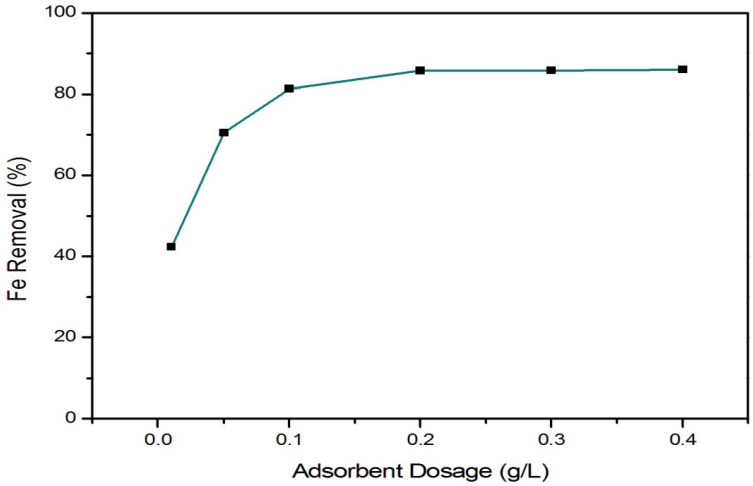

FIG. 8. Effect of adsorbent dose on percentage removal efficiency of iron (initial Fe conc. 100 mg/L; contact time = 90 min.; 200 rpm agitation speed; room temp.)

contributed to an increase in the percentage removal of iron ions [53]. Furthermore, the adsorbate's kinetic energy and surface activity increase with temperature [54].

4.5. Adsorption isotherms

The removal of Fe ions by ZnSe:Ag:Urea nanoparticles at various initial Fe concentrations was examined using two fundamental adsorption isotherm models (Langmuir and Freundlich). The following are the equations for the Langmuir (3) and Freundlich (4) models [55]:

$$\frac{1}{q_e} = \frac{1}{q_0} + \frac{1}{q_0 K_L} \cdot \frac{1}{C_e}, \tag{3}$$

$$\ln q_e = \ln K_f + \frac{1}{n} \ln C_e, \tag{4}$$

where q_e is the equilibrium adsorption capacity (mg·g^{-1}), q_m is the monolayer adsorption capacity (mg·g^{-1}), K_L is the Langmuir constant (L·mg^{-1}), K_F is the Freundlich constant (L·g^{-1}), n is the Freundlich exponent and C_e is the concentration at equilibrium (mg·L^{-1}). The adsorption isotherm provides information on the dependency of adsorption on the initial metal ion concentration and characterises the equilibrium of the adsorption material at the adsorbent surface. The Langmuir isotherm describes the monolayer adsorption onto a surface with homogenous adsorption sites, while the Freundlich model applies to multilayer adsorption on a heterogeneous surface (Fig. 11).

The Langmuir isotherm model (Fig. 10) has a higher correlation coefficient ($R^2 = 0.976$) than the Freundlich isotherm model ($R^2 = 0.958$). This result implies that the experimental data accords fairly well with the Langmuir

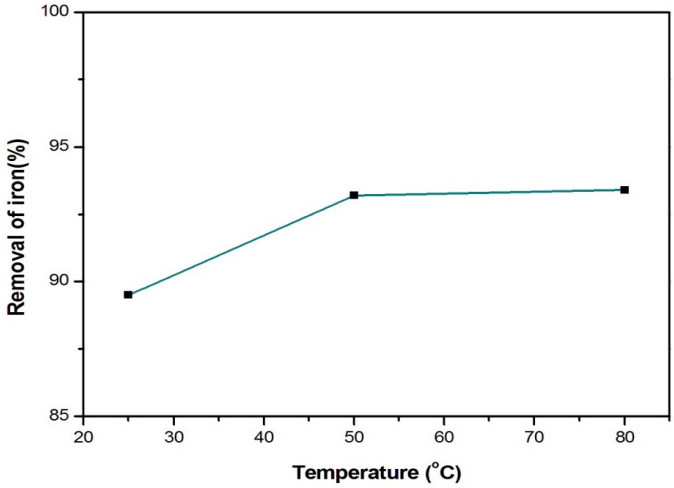

FIG. 9. Effect of temperature on percentage removal of iron (initial Fe conc.= 100 mg/L; contact time = 90 min.; 200 rpm agitation speed; adsorbent dosage = 0.2 g)

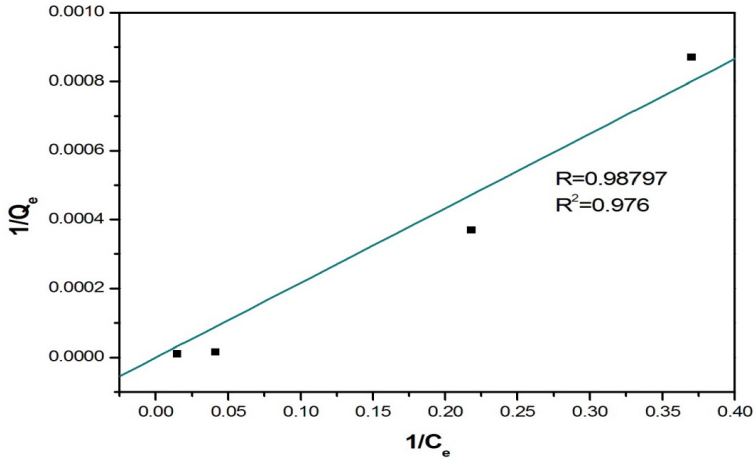

FIG. 10. Langmiur plot for adsorption of Fe on ZnSe:Ag:Urea

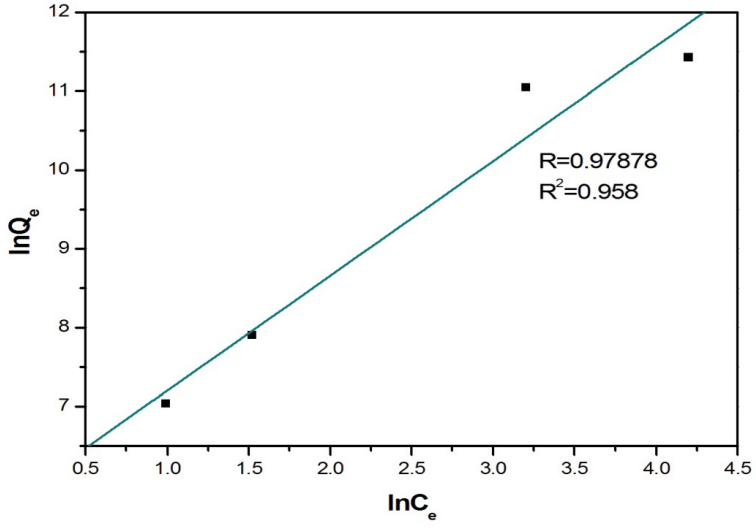

FIG. 11. Freundlich plot for adsorption of Fe on ZnSe:Ag:Urea

isotherm model. This indicates that the removal of Fe ions by ZnSe:Ag:Urea nanoparticles takes place through monolayer adsorption, with Fe ions homogeneously distributed on the adsorption sites on the adsorbent material surface.

5. Conclusions

The present study reports the successful synthesis of nanostructured, urea and silver modified zinc selenide by a simple sol-gel method using hydrazine hydrate as a reducing agent and ethylene glycol as a stabilising agent, which prevents the agglomeration of synthesised nanoparticles. An investigation was conducted on their effectiveness as adsorbents to remove heavy metal iron ions from aqueous solutions. The physicochemical characterisation involved XRD, FE-SEM, EDX and FTIR spectroscopy. SEM images show spherical-like structures, which are more convenient for bactericidal and catalytic activation, evidencing the presence of N,C, O, Ag, Se and Zn. The XRD analysis gives the possible different phases and the diameter of the nanomaterial. The diameter of ZnSe:Ag:Urea was determined to be 19.911 nm. FTIR spectra confirm the new bond formation. Results from adsorption studies reveal that the equilibrium of the adsorption process was reached within a contact time of 80 minutes under room temperature. The increase in temperature increases the Fe removal percentage. Furthermore, with an increase in adsorbent dosage, the percentage removal of Fe first increases and eventually reaches an equilibrium state; however, with an increase in the initial iron concentration, the Fe removal percentage first increases and then decreases slightly until it reaches equilibrium. The maximum rate of Fe removal was found to be 89.5 % under the optimal room temperature conditions, with an adsorbent dosage of 0.1 g and an initial Fe concentration of 100 mg/L.

References

[1] Tabassum H., Ahmad I.Z. Applications of metallic nanomaterials for the treatment of water. *Letters in Applied Microbiology. The Society for Applied Microbiology*, 2021, **75**, P. 731–743.

[2] Shaikh R.B., Saifullah B., Rehman F.U. Greener Method for the Removal of Toxic Metal Ions from the Wastewater by Application of Agricultural Waste as an Adsorbent. *Water*, 2018, **10** (10).

[3] Kolluru S.S., Agarwal S., Sireesha S., Sreedhar I., Kale S.R. Heavy metal removal from wastewater using nanomaterials-process and engineering aspects. *Process Safety and Environmental Protection*, 2021, **150**, P. 323–355.

[4] Beena V., Rayar S.L., Ajitha S., Ahmad A., Albaqami M.D., Alsabar F.A.A., Sillanpää M. Synthesis and Characterization of Sr-Doped ZnSe Nanoparticles for Catalytic and Biological Activities. *Water*, 2021, **13**, 2189.

[5] Baby R., Hussein M.Z., Abdullah A.H., Zainal Z. Nanomaterials for the Treatment of Heavy Metal Contaminated Water. *Polymers*, 2022, **14**, 583.

[6] Silver J. *Chemistry of Iron*, first ed., Springer Science + Business Media, Dordrecht, 1993.

[7] Green R., Charlton R., Seftel H., Bothwell T., Mayet F., Adams B., Finch C., Layrisse M. Body iron excretion in man: a collaborative study. *Am. J. Med.*, 1968, **45**, P. 336–353.

[8] Khatri N., Tyagi S. Influences of natural and anthropogenic factors on surface and groundwater quality in rural and urban areas. *Front. Life Sci.*, 2015, **8**, P. 23–39.

[9] Jusoh A.B., Cheng W.H., Low W.M., Nora'aini A., Noor M.J.M. Study on the removal of iron and manganese in groundwater by granular activated carbon. *Desalination*, 2005, **182**, P. 347–353.

[10] Tekerlekopoulou A.G., Pavlou S., Vayenas D.V. Removal of ammonium, iron and manganese from potable water in biofiltration units: a review. *J. Chem. Technol. Biotechnol.*, 2013, **88**, P. 751–773.

[11] Ellis D., Bouchard C., Lantagne G. Removal of iron and manganese from groundwater by oxidation and microfiltration. *Desalination*, 2000, **130**, P. 255–264.

[12] Sengupta A., Gupta A., Deb A.K. Arsenic crisis in Indian subcontinent: a local solution to a global problem. *Water*, 2001, **21**, P. 34–36.

[13] Kumar V., Bharti P.K., Talwar M., Tyagi A.K., Kumar P. Studies on high iron content in water resources of Moradabad district (UP), India. *Water Sci.*, 2017, **31** (1), P. 44–51.

[14] Mahanta D.B., Das N.N., Dutta R.K. A chemical and bacteriological study of drinking water in tea gardens of central Assam. *Indian J. Environ. Prot.*, 2004, **24**, P. 654–660.

[15] Sharma R., Shah S., Mahanta C. Hydrogeochemical study of groundwater fluoride contamination: a case study from Guwahati city India. *Asian J. Water Environ. Pollut.*, 2005, **2**, P. 47–54.

[16] Houben G.J. Iron oxides in wells. Part 1. Genesis, mineralogy and geochemistry. *Appl. Geochem.*, 2003, **18**, P. 927–939.

[17] World Health Organization. Iron in drinking water. In: *Guidelines for drinking-water quality*, 2nd ed. Vol. 2. Health criteria and other supporting information. World Health Organization, Geneva, 1996.

[18] Khatri N., Tyagi S., Rawtani D. Assessment of drinking water quality and its health effects in rural areas of Harij Taluka, Patan district of Northern Gujarat. *Environ. Claims J.*, 2016, **28** (3), P. 223–246.

[19] Zheng Q., Zhao Y., Guo J., Zhao S., Song L., Fei C., Zhang Z., Li X., Chang C. Iron overload promotes erythroid apoptosis through regulating HIF-1a/ROS signalling pathway in patients with myelodysplastic syndrome. *Leuk. Res.*, 2017, **58**, P. 55–62.

[20] Hartmann J., Braulke F., Sinzig U., Wulf G., Maas J.H., Konietschke F., Haase D. Iron overload impairs proliferation of erythroid progenitors cells (BFU-E) from patients with myelodysplastic syndromes. *Leuk. Res.*, 2013, **37**, P. 327–332.

[21] Chai X., Li D., Cao X., Zhang Y., Mu J., Lu W., Xiao X., Li C., Meng J., Chen J., Li Q., Wang J., Meng A., Zhao M. ROS-mediated iron overload injures the hematopoiesis of bone marrow by damaging hematopoietic stem/progenitor cells in mice. *Sci. Rep.*, 2015, **5**, 10181.

[22] Jang Y.Y., Sharkis S.J. A low level of reactive oxygen species selects for primitive hematopoietic stem cells that may reside in the low-oxygenic niche. *Blood*, 2007, **110**, P. 3056–3063.

[23] Shao L., Li H., Pazhanisamy S.K., Meng A., Wang Y., Zhou D. Reactive oxygen species and hematopoietic stem cell senescence. *Int. J. Hematol.*, 2011, **94**, P. 24–32.

[24] Frippiat C., Dewelle J., Remacle J., Toussaint O. Signal transduction in H_2O_2-induced senescence-like phenotype in human diploid fibroblasts. *Free Radic. Biol. Med.*, 2002, **33**, P. 1334–1346.

[25] Prus E., Fibach E. Effect of iron chelators on labile iron and oxidative status of thalassaemic erythroid cells. *Acta Haematol.*, 2010, **123**, P. 14–20.

[26] Alimohammadi V., Sedighi M., Jabbari E. Experimental study on efficient removal of total iron from wastewater using magnetic-modified multi-walled carbon nanotubes. *Ecol. Eng.*, 2017, **102**, P. 90–97.
[27] Das B., Hazarika P., Saikia G., Kalita H., Goswami D.C., Das H.B., Dube S.N., Dutta R.K. Removal of iron by groundwater by ash: a systematic study of a traditional method. *J. Hazard. Mater.*, 2007, **141**, P. 834–841.
[28] Michalakos G.D., Nieva J.M., Vayenas D.V., Lyberatos G. Removal of iron from potable water using a Trickling filter. *Wat. Res.*, 1997, **31** (5), P. 991–996.
[29] Shalini chaturvedi. Removal of iron for safe drinking water. *Desalination*, 2012, URL: https://www.academia.edu/125112372/Removal_of_iron_for_safe_drinking_water.
[30] Helal E.H.D., Dessouki H.A., Nassar M.Y., Ahmed I.S. Preparation and spectral analysis of nanosized ZnSe particles. *J. Basic Environ. Sci.*, 2018, **5**, P. 20–24.
[31] Dehghani S., et al. Zinc selenide nanoparticles: Green synthesis and biomedical applications. *Nanomed. J.*, 2022, **9**, P. 15–23.
[32] Yang Y., Wu Z., Yang R., Li Y., Liu X., Zhang L., Yu B. Insights into the mechanism of enhanced photocatalytic dye degradation and antibacterial activity over ternary ZnO/ZnSe/$MoSe_2$ photocatalysts under visible light irradiation. *Appl. Surf. Sci.*, 2021, **539**, 148220.
[33] Beena V., Ajitha S., Rayar S.L., Parvathiraja C., Kannan K., Palani G. Enhanced Photocatalytic and Antibacterial Activities of ZnSe Nanoparticles. *J. Inorg. Organomet. Polym. Mater.*, 2021, **4**, P. 1–12.
[34] Archana J., Mani S., M N., Ponnusamy S., Muthamizhchelvan C., Hayakawa Y. Chemical synthesis and functional properties of hexamethylenetetramine capped ZnSe nanorods. *Mater Lett.*, 2014, **125**, P. 32–35.
[35] Yang J., Wang G., Liu H., Park J., Gou X., Cheng X. Solvothermal synthesis and characterization of ZnSe nanoplates. *J Cryst Growth.*, 2008, **310**, P. 3645–3648.
[36] Lei Z., Wei X., Bi S., He R. Reverse micelle synthesis and characterization of ZnSe nanoparticles. *Mater. Lett.*, **2008**, **62**, P. 3694–3696.
[37] Hao H., Yao X., Wang M. Preparation and optical characteristics of ZnSe nanocrystals doped glass by sol-gel in situ crystallization method. *Opt Mater.*, 2007, **29**, P. 573–577.
[38] Panneerselvam A., Malik A., O'Brien P., Nguyen C.Q. The CVD of silver selenide films from dichalcogenophosphinato and imidodichalcogenodiphosphinatosilver(I) single-source precursors. *J. of Materials Chemistry*, 2009, **19** (3).
[39] Sharma P. Synthesis and characterization of Ag-chalcogenide nanoparticles for possible applications in photovoltaics. *Materials Science – Poland*, 2018, **36** (3), P. 375–380.
[40] Thendral M., et al. Nucleation and spectroscopic studies of manganese doped new nlo organic crystal. *Int. J. of Current Research in Life Sciences*, 2018, **7** (5), P. 2121–2125.
[41] Madhurambal G., Mariappan M. Growth and characterization of urea-thiourea non-linear optical organic mixed crystal. *Indian J. of Pure & Applied Physics*, 2010, **48**, P. 264–270.
[42] Shameli K., et al. Green biosynthesis of silver nanoparticles using Curcuma longa tuber powder. *Int. J. of Nanomedicine*, 2012, P. 5603–5610.
[43] Manivannan M., et al. Investigation of inhibitive action of urea-Zn2+ system in the corrosion control of carbon steel in sea water. *Int. J. of Engineering Science and Technology*, 2011, **3** (11), P. 8048–8060.
[44] Ahamed A.J., et al. Synthesis and Characterization of ZnSe Nanoparticles by Co-precipitation Method. *J. of Nanoscience and Technology*, 2016, **2**, P. 148–150.
[45] Penland R.B., Mizushima S., Curran C., Quagliano J.V. Infrared Absorption Spectra of Inorganic Coördination Complexes. X. Studies of Some Metal-Urea Complexes. *J. of the American Chemical Society*, 1957, **79** (7), P. 1575–1578.
[46] Jackovitz J.F., Walter J.L. Infrared absorption spectra of metal-amino acid complexes–V. The infrared spectra and normal vibrations of metal-leucine chelates. *Spectrochimica Acta*, 1966, **22** (8), P. 1393–1406.
[47] Megahed A.S., Ibrahim O.B., Adam A.M.A., AL-Majthoub M.M. The Chelating Behavior of Urea Complexed with the Metal Ions of Copper (II), Zinc (II), Silver (I), Cadmium (II) and Mercury (II) at Room Temperature. *Research J. of Pharmaceutical, Biological and Chemical Sciences*, 2014, **5** (2), P. 970–980.
[48] Nakamoto K. *Infrared and Raman spectra of inorganic and coordination compounds, part B: applications in coordination, organometallic, and bioinorganic chemistry*. John Wiley & Sons, 2009.
[49] Kakavandi B., Esrafili A., Mohseni-Bandpi A., Jafari A.J., Kalantary R.R. Magnetic Fe_3O_4@C nanoparticles as adsorbents for removal of amoxicillin from aqueous solution. *Water Sci. Technol.*, 2014, **69** (1), P. 147–155.
[50] Arbanah M., Najwa M.R.M., Halim K.H.K. Biosorption of Cr (III), Fe (II), Cu (II), Zn (II) ions from liquid laboratory chemical waste by Pleurotus ostreatus. *Int. J. Biotechnol. Wellness Ind.*, 2012, P. 152–162.
[51] Luo C., Tian Z., Yang B., Zhang L., Yan S. Manganese dioxide/iron oxide/acid oxidized multi-walled carbon nanotube magnetic nanocomposite for enhanced hexavalent chromium removal. *Chem. Eng. J.*, 2013, **234**, P. 256–265.
[52] Jung C., Heo J., Han J., Her N., Lee S.-J., Oh J., Ryu J., Yoon Y. Hexavalent chromium removal by various adsorbents: powdered activated carbon, chitosan, and single/multi-walled carbon nanotubes. *Sep. Purif. Technol.*, 2013, **106**, P. 63–71.
[53] Kaveeshwar A.R., Sanders M., Ponnusamy S.K., Depan D. et al. Chitosan as a biosorbent for adsorption of iron (II) from fracking wastewater. *Polym. Adv. Technol.*, 2018, **29**, P. 961–969.
[54] Jain C.K., Malik D.S., Yadav A.K. Applicability of plant based biosorbents in the removal of heavy metals: A review. *Environ. Process*, 2016, **3**, P. 495–523.
[55] Li J., Fan M.J., Li M., Liu X. Cr(VI) removal from groundwater using double surfactant-modified nanoscale zero-valent iron (nZVI): Effects of materials in different status. *Sci. Total Environ.*, 2020, **717**, 137112.

Submitted 23 May 2025; revised 4 September 2025; accepted 30 September 2025

Information about the authors:

Khurshed A. Shah – PG Department of Physics, Sri Pratap College, Cluster University Srinagar, J&K-190001, India; ORCID 0000-0002-2694-4515; drkhursheda@gmail.com

Humaira S. Wani – Department of Applied Sciences, Institute of Technology, Zakura Campus, University of Kashmir, Srinagar, J&K-190006, India; ORCID 0009-0003-1238-9412; wanihumaira1@gmail.com

S. M. A. Andrabi – Department of Applied Sciences, Institute of Technology, Zakura Campus, University of Kashmir, Srinagar, J&K-190006, India; ORCID 0009-0001-7331-1358; muzaffar2000@gmail.com

Quinton L. Williams – Department of Physics and Astronomy, Howard University, 2355 6th St., NW, Washington, DC 20059, USA; ORCID 0000-0002-9244-6661; quinton.williams@howard.edu

Data availability statement: The datasets generated or analysed during the current study are available from the corresponding author upon reasonable request.

Conflict of interest: The authors declare that they have no known competing financial interests or personal relationships that could have appeared to influence the work reported in this paper.

NANOSYSTEMS:
PHYSICS, CHEMISTRY, MATHEMATICS

Enyashin A.N. *Nanosystems:*
Phys. Chem. Math., 2025, **16** (5), 693–699.
http://nanojournal.ifmo.ru
DOI 10.17586/2220-8054-2025-16-5-693-699

Original article

GdI_3 fullerenes: a DFT study of structural and electronic properties

Andrey N. Enyashin

Institute of Solid State Chemistry UB RAS, Ekaterinburg, Russia

enyashin@ihim.uran.ru

PACS 61.48.-c, 73.90.+f

ABSTRACT The existence of zero-dimensional fullerene-like gadolinium(III) iodide is proposed. The models of tetrahedral, octahedral and icosahedral GdI_3 fullerenes with the size up to ∼1000 atoms are constructed. Their stability and electronic properties are investigated by means of a density functional theory method. Similarly to other known inorganic fullerenes and nanotubes, the strain energies of GdI_3 fullerenes decrease with the radii increase, exceeding always the strain energies of GdI_3 nanotubes of the same radii. At that octahedral and icosahedral morphologies are the most preferable. Irrespective size and morphology, all considered GdI_3 fullerenes are semiconductors with possibly ferromagnetic ordering at extremely low temperatures. The HOMO-LUMO gaps of GdI_3 fullerenes are narrower on 1.1 – 1.7 eV, when comparing to the band gap of the flat GdI_3 monolayer.

KEYWORDS gadolinium triiodide, fullerenes, DFT calculations

ACKNOWLEDGEMENTS This study was carried out within the framework of the state assignment for the Institute of Solid State Chemistry UB RAS (No. 124020600024-5).

FOR CITATION Enyashin A.N. GdI_3 fullerenes: a DFT study of structural and electronic properties. *Nanosystems: Phys. Chem. Math.*, 2025, **16** (5), 693–699.

1. Introduction

Trivalent gadolinium (Gd^{3+}) is an ion that possesses the maximum number of unpaired electrons of any stable ions due to the presence of 7 unpaired electrons in the inner $4f$-electronic shell. Exhibiting large magnetic moments and achievable low magnetic ordering temperatures, both solid and molecular compounds of Gd^{3+} are attractive as magnetic refrigerants [1, 2]. Yet, Gd^{3+} ions are more honored in biomedical applications as working element of various contrast agents. At temperatures above 20 °C they hold innate paramagnetic properties and a high sensitivity to external magnetic field, allowing enhanced magnetic resonance imaging (MRI) [3]. Besides, the attenuation of X-rays by gadolinium can be greater than that of iodine, which opens a perspective to design the more sensitive radiographic contrast agents and even the agents with dual MRI and radiographic modality [4]. Association of gadolinium and iodine in a single compound like GdI_3 might enhance X-rays' attenuation, which can be further utilized for sensitization of composite luminescent materials for a particle radiation detection [5].

Apart of the design of new gadolinium chelates [6] or endofullerenes ("gadofullerenes") [7], a significant effort was undertaken to improve the MRI contrast performance by means of gadolinium accumulation using inorganic compounds. Chimie douce encapsulation of $GdCl_3$ into ultra-short and narrow carbon nanotubes [8, 9] produced both exo- and endohedral composites of highly-defective nanotubes with superparamagnetic clusters of Gd^{3+} ions and Gd atoms ("gadonanotubes"), amplifying MRI in order of magnitude [10]. High-temperature imbibition of GdI_3 into multi-walled carbon nanotubes [11] or into inorganic WS_2 nanotubes [12] yielded their endohedral composites with one-dimensional nanoribbons or nanotubes of GdI_3, which remain paramagnetic and could be considered as potential MRI contrast agents protected by carbon or WS_2 wall. Fabrication of one-dimensional GdI_3 and concomitant gadolinium compounds has prompted theoretical research of capillarity of carbon and non-carbon nanotubes in relation to molten GdI_3, $GdBr_3$ and $GdCl_3$ using molecular dynamics simulations [13] as well as stability and electronic properties of individual GdI_3 nanotubes using quantum-chemical calculations [14]. Yet, an in-depth research of both the properties and the metabolism of such nanocomposites is still required.

Morphology of Gd^{3+}-ion containing nanoparticles, especially, GdI_3 as a dual contrast agent for MRI and X-ray imaging may be a tool for manipulation on its magnetic, magnetocaloric, optic and X-ray absorption properties. So far, only one-dimensional nanostructures of GdI_3 were reported [11, 12, 14], while corresponding zero-dimensional nanostructures like fullerenes or fullerene-like particles have been not even predicted. This can be found in drastic contrast to layered halides of d- and p-elements – $NiCl_2$ [15], $NiBr_2$ [16], $CdCl_2$ [17], CdI_2 [18], LaF_3 [19], which can be folded up into both nanotubes and fullerenes or fullerene-like nanoparticles [20, 21]. Here, we suggest the construction principles and explore theoretically the stability and electronic properties of GdI_3 fullerenes as an essential prerequisite to understanding the chemistry and physics of gadolinium compounds with zero-dimensional morphology.

2. Computational details

The spin-polarized calculations of all nanostructures were performed within the framework of the density-functional theory (DFT) as implemented in the SIESTA 4.0 software [22, 23]. The exchange-correlation potential was described within the Generalized Gradient Approximation with the Perdew–Burke–Ernzerhof parameterization. The core electrons were treated within the frozen core approximation, applying norm-conserving Troullier–Martins pseudopotentials. The valence electron configurations were chosen as $6s^2 5d^1 4f^7$ for Gd and $5s^2 5p^5$ for I with the wave-functions described using the double-ζ polarized basis set. The real-space grid used for the numeric integrations was set to correspond to the energy cutoff of 300 Ry. All calculations were performed using the full geometry optimization until the maximum residual force component of 0.05 eV/Å.

3. Results and discussion

3.1. Construction principles of GdI_3 fullerenes

In the thermodynamically stable polymorph of gadolinium triiodide, Gd^{3+} cations are arranged in the honeycomb networks in edge-sharing octahedral coordination by six I^- anions, which are each bonded to two Gd^{3+} cations. The resulting three-atom thick layers of composition GdI_3 are hexagonal and form via vdW interaction rhombohedral crystal with the BiI_3 structure type (space group R-3) [24]. The unstable polymorph of GdI_3 is stabilized at pressures 1 – 4 GPa as orthohombic crystal with the $PuBr_3$ structure type (space group Cmcm), where Gd^{3+} cations adopt a bicapped trigonal prismatic coordination by eight I^- anions [25]. Our preliminary geometry optimizations of both the bulk and the monolayer of GdI_3 have revealed preservation of their hexagonal symmetries and have validated the chosen calculation scheme. The equilibrium lattice parameters of the bulk GdI_3 were found as $a = 7.39$ Å and $c = 19.69$ Å in a fair agreement with experimental data $a = 7.54$ Å and $c = 20.83$ Å [24]. Single GdI_3 layer undergoes a slight in-plane contraction, resulting in the equilibrium lattice parameter $a = 7.35$ Å.

While the bending of a layer in one dimension, such as into a seamless nanotube, does not impose any constraint on the structure of the layer, but mechanical stress, the construction of the fully closed shell as a layer bent in two dimensions imposes a number of topological restrictions. Construction principles of both carbon and inorganic fullerenes rely on insertion of point defects into monolayer, which can provide a surface with positive curvature and serve as vertices of polyhedral fullerenes. The most famous example is the closure of graphene into a fullerene, which requires introduction of such defects as 12 pentagons into its honeycomb lattice [26]. A stable closure of layers of binary compounds with triangular lattices like hexagonal BN, metal dichalcogenides or dihalides requires introduction of 6 tetragons ("square-like defects") to preserve alternant heteronuclear bonding [21]. Then, the facets of fullerenes are represented as triangular or rhombi-like layers' patches, where the sewing of equilateral facets may release the fullerenes with perfect symmetric morphology of icosahedron for graphene or octahedron for inorganic layers.

While GdI_3 is a binary compound, cationic sublattice of its layer is honeycomb like graphene. Therefore, the first trial to build the atomistic models of GdI_3 fullerenes could rely on the known generations of carbon fullerenes. However, simple transfer of construction principles is not applicable here: symmetry of GdI_3 layer (point group D_3) is lower, than symmetry of graphene (point group D_6), imposing an additional constrain on sewing of anionic sublattice of GdI_3 facets at edges. The most obvious construction of the edge between two GdI_3 facets consists of the boundary of Gd^{3+} cations with trigonal prismatic coordination by I^- anions (Fig. 1). Such type of boundary violates neither the coordination numbers of ions nor the stoichiometry of compound. Prismatic coordination of cations is typical for layered compounds with a high degree of covalent bonding like chalcogenides and pnictogenides [27]. Yet, the layered oxides and nitrides with a more ionic bonding and, simultaneously, with prismatic coordination of cations are known, too [28]. The proposed prismatic coordination of Gd^{3+} cations is also reminiscent of the bicapped prismatic coordination in the high-pressure GdI_3 polymorph [25]. Moreover, the Gd–I phase diagram possesses gadolinium diiodide GdI_2 with the only prismatic coordination of Gd^{2+} cations [29].

These simple construction principles allowed design of three families of stoichiometric GdI_3 fullerenes with different right morphologies (Fig. 1). First family included icosahedral GdI_3 fullerenes with cationic sublattice equivalent to the lattice of carbon fullerenes from C_{60} family and consisting of $N = 60n^2$ units, where n is an integer. Second and third families were represented by octahedral and tetrahedral GdI_3 fullerenes consisting of $N = 24n^2$ and $N = 12n^2$ units, respectively. Cationic sublattices of the latter families are not related to the lattices of classic carbon fullerenes, since containing either 4 trigons or 6 tetragons as vertices. Though, irrespective the fullerene morphology the facets and the edges consist, respectively, of octahedral and prismatic GdI_6 coordination polyhedra.

The physical meaning of n is the half-quantity of Gd^{3+} cations forming a single edge. In the following, stability and electronic properties of GdI_3 nanoicosahedra with n = 1, 2, GdI_3 nanooctahedra and GdI_3 nanotetrahedra with n = 1 – 3 are discussed.

3.2. Thermodynamic stability of GdI_3 fullerenes

Fundamental criterion for thermodynamic stability of a hollow nanostructure (fullerene, nanotube, nanoroll etc.) is the energy of nanostructure relative to corresponding infinite planar layer, so-called strain energy. An early study

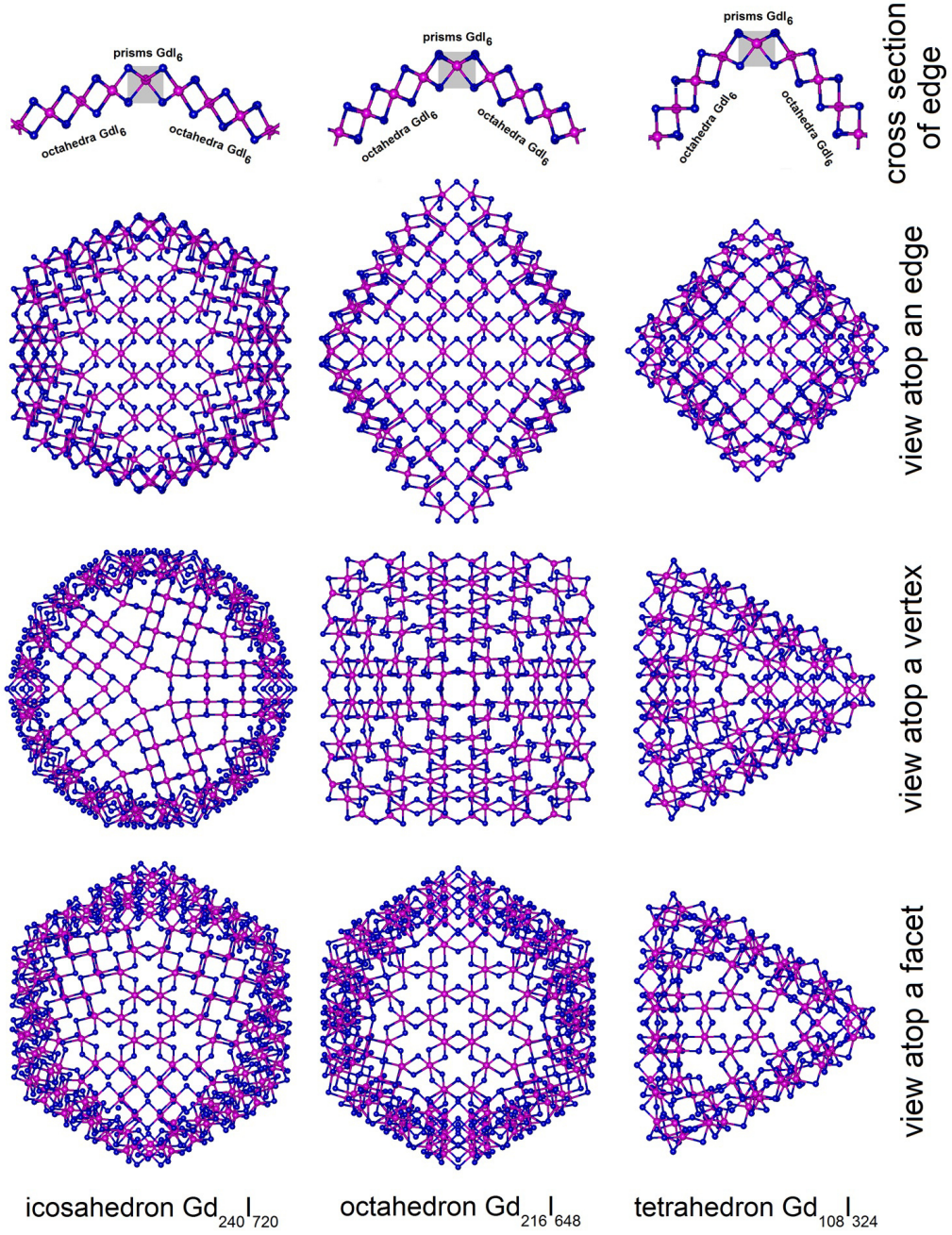

FIG. 1. The ball-and-stick models of GdI_3 fullerenes with optimized structure, revealing the construction principles of their vertices and edges. Gd and I atoms are painted in violet and blue, respectively. DFT calculations

of GdI_3 nanotubes as cylindrical seamless layers revealed their tolerable strain energies ΔE, when comparing to the commercially manufactured MoS_2 or WS_2 nanotubes [14]. Particularly, for nanotubes, the specific ΔE per GdI_3-unit ($\Delta E/N$) obeys classical $\sim 1/R^2$ rule from the elasticity theory for the bending of a layer into cylinder of radius R. The proportionality factor between $\Delta E/N$ and $1/R^2$ for GdI_3 nanotubes is equal to 12.57 (eV·Å^2)/unit, what is found in-between 0.5 (eV·Å^2)/unit for carbon nanotubes and 48.3 (eV·Å^2)/unit for MoS_2 nanotubes. Noteworthy, the strain energy of nanotubes is contributed mostly by elastic deformation of the layer consisting of GdI_6 octahedra. The strain energy of fullerenes should contain also the contribution from GdI_6 prisms as the less favorable coordination polyhedra for GdI_3.

The fully relaxed structures of some GdI_3 fullerenes are shown in the Fig. 1. Morphology and integrity of all these nanoparticles including the smallest representatives are preserved during geometry optimization. No major reconstruction or a crack occurs at vertices or at edges. Facets of all giant representatives become visibly flattened like their parent monolayer.

The specific strain energies $\Delta E/N$ for GdI_3 fullerenes are plotted in Fig. 2(a) against the mean radii $\langle R\rangle$ of their Gd-sublattices. Similarly to carbon fullerenes and nanotubes [30] or sulfide fullerenes and nanotubes [31,32], $\Delta E/N$ of a GdI_3 fullerene due to the fully closed morphology is one order of magnitude larger, than that for GdI_3 nanotube of the same radius. Like for cylindrical nanotubes, the functions $\Delta E/N$ for all types of fullerenes decrease with the size growth, yet, with the different slopes. An analytical expression for any of these functions can be derived using phenomenological model stipulating a fullerene as nanoparticle with perfect polyhedral morphology. The total energy of a fullerene E can be written as

$$E = N_r\varepsilon_r + N_i\varepsilon_i, \tag{1}$$

where: N_i is the number of Gd atoms forming the flat facets, N_r is the number of Gd atoms forming the edges, and their sum is equal to the total number of stoichiometric GdI_3 units $N = N_i + N_r$. The values ε_i and ε_r are the corresponding specific energies of atoms at facets and edges. N_i and N_r are defined by the number n in accordance to the family: for nanoicosahedra $N_i = 60n(n-1)$, $N_r = 60n$; for nanooctahedra $N_i = 24n(n-1)$, $N_r = 24n$; for nanotetrahedra $N_i = 12n(n-1)$, $N_r = 12n$. Then, specific energy E/N can be written as:

$$\frac{E}{N} = \frac{N_r}{N}\varepsilon_r + \frac{N_i}{N}\varepsilon_i = \frac{1}{n}\varepsilon_r + \frac{n-1}{n}\varepsilon_i, \tag{2}$$

or after transformations

$$\frac{E}{N} = \frac{\sqrt{12}}{\sqrt{N}}(\varepsilon_r - \varepsilon_i) \quad \text{for nanotetrahedra,} \tag{3}$$

$$\frac{E}{N} = \frac{\sqrt{24}}{\sqrt{N}}(\varepsilon_r - \varepsilon_i) \quad \text{for nanooctahedra,} \tag{4}$$

$$\frac{E}{N} = \frac{\sqrt{60}}{\sqrt{N}}(\varepsilon_r - \varepsilon_i) \quad \text{for nanoicosahedra.} \tag{5}$$

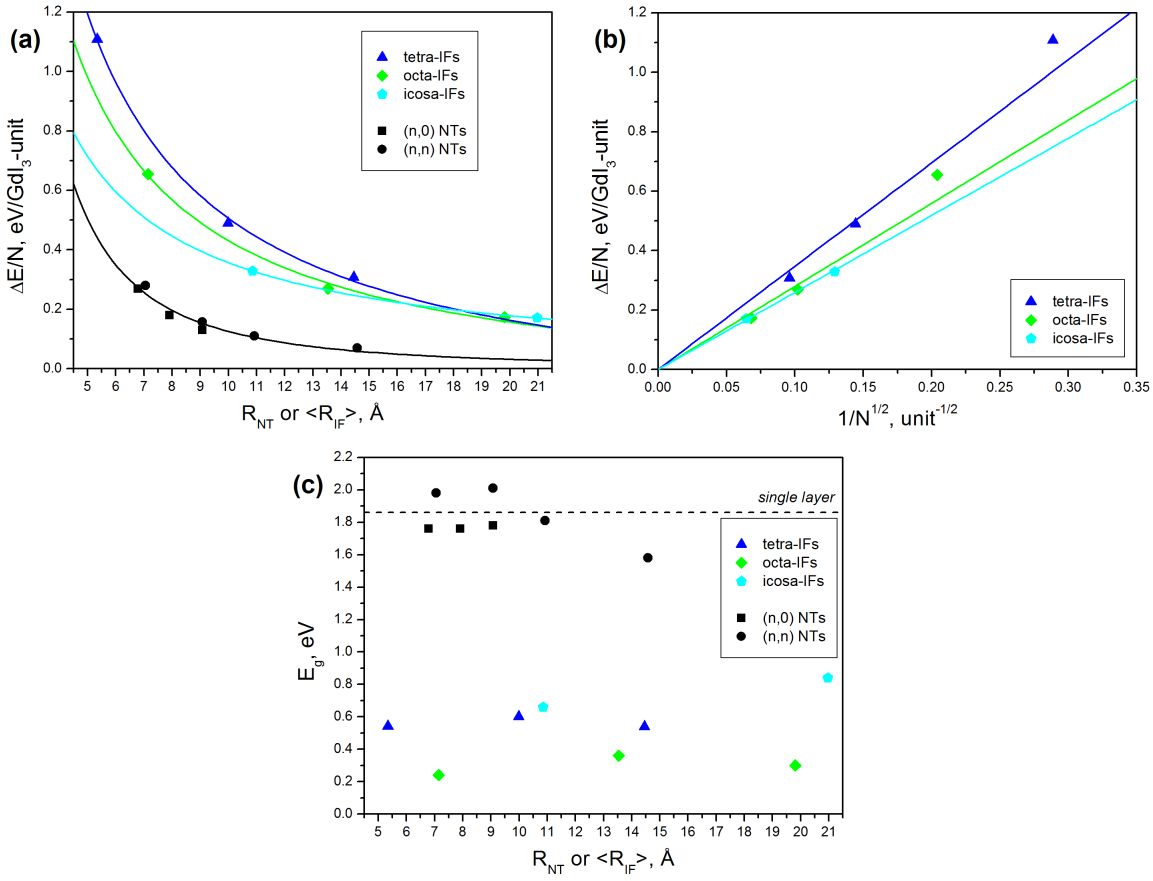

FIG. 2. Thermodynamic and electronic properties for GdI_3 fullerenes (IFs) of different morphology in comparison to those for parent monolayer and for GdI_3 nanotubes (NTs) of different chirality [14]: (a) specific strain energies $\Delta E/N$ for various nanostructures depending on the mean particles' radii R and their morphology; (b) specific strain energies $\Delta E/N$ for fullerenes depending on the number N of constituting units; (c) band gap values E_g. DFT calculations

The value $(\varepsilon_r - \varepsilon_i)$ is nothing more, than the specific strain energy contributed exclusively by an edge atom, i.e. excessive energy of GdI_6 prism relative to GdI_6 octahedron. Therefore, Eqs. (3–5) may be ascribed to homogeneous linear functions:

$$\frac{\Delta E}{N} = \frac{\sqrt{12}}{\sqrt{N}}\Delta\varepsilon_r \quad \text{for nanotetrahedra,} \tag{6}$$

$$\frac{\Delta E}{N} = \frac{\sqrt{24}}{\sqrt{N}}\Delta\varepsilon_r \quad \text{for nanooctahedra,} \tag{7}$$

$$\frac{\Delta E}{N} = \frac{\sqrt{60}}{\sqrt{N}}\Delta\varepsilon_r \quad \text{for nanoicosahedra.} \tag{8}$$

These strain energies for GdI_3 fullerenes show a somewhat different behavior, than that for carbon fullerenes. They appear to be proportional to $1/\sqrt{N}$, whereas for carbon fullerenes $\Delta E/N$ is proportional to $1/N$ [30]. It points to the dominant role of strain at edges in regulation of thermodynamic stability of a whole GdI_3 fullerene. The data on the total energies of GdI_3 fullerenes available from DFT calculations were fitted using Eqs. (6–8), estimating $\Delta\varepsilon_r = 1.00$ eV/unit$^{1/2}$, $\Delta\varepsilon_r = 0.57$ eV/unit$^{1/2}$ and $\Delta\varepsilon_r = 0.34$ eV/unit$^{1/2}$ for tetrahedral, octahedral and icosahedral morphology, respectively (Fig. 2 (b)). Such order of $\Delta\varepsilon_r$ correlates with the local curvature at edges within particular morphology: from the largest curvature within tetrahedron to the least one within icosahedron. Obviously, GdI_3 fullerenes would tend to form icosahedral and octahedral morphologies, if synthesized.

3.3. Electronic structure of GdI_3 fullerenes

The calculated densities of electronic states (DOS) for several fullerenes and monolayer of GdI_3 are visualized in Fig. 3. Irrespective of size and morphology, electronic structure of different GdI_3 fullerenes is qualitatively similar and mainly resembles that for monolayer or nanotubes of GdI_3 [14]. In accordance to the polar covalent character of the Gd–I bonding, the topmost valence band consists of mainly I5p-states with a small admixture of Gd6s- and Gd5d-states and settles at $-1... - 4$ eV below Fermi level. While this valence band is characterized by a minor spin polarization, the conduction band at $+1... + 2.5$ eV above Fermi level is spin-polarized and consists of Gd5d-states grouped in two subbands in accordance to the splitting of d-orbitals in octahedral crystal field. The bands' splitting becomes smoothed in the case of fullerenes, since their symmetries possess a greater variety of inequivalent atom types, than symmetries of monolayer or nanotubes do. Occupied and unoccupied Gd4f-states form two strongly localized narrow bands of different spin-polarization at energies around -7.5 eV and $+3.5$ eV, respectively.

Therefore, all studied GdI_3 fullerenes should be magnetic semiconductors like their parent monolayer. Monolayer possesses the fundamental band gap E_g of at least 1.8 eV with the gap edges formed by states of the same spin projection and with indirect $\Gamma - M$ transition. The calculated E_g is found underestimated, when comparing to the experimental value E_g of 5.1 eV [33]. Such a mismatch is typical for standard calculational DFT schemes [34] and does not preclude discussion of relative values. When comparing with monolayer and nanotubes, the values E_g for fullerenes can be found distinctly smaller as 0.2 –0.8 eV (Fig. 2(c)). This reduction of the band gap has two origins: first, the presence of prismatic coordination polyhedra with another crystal field for splitting of Gd5d-orbitals and, second, an enhanced overlap between Gd5d- and I5p-orbitals from atoms at internal surface of the mechanically stressed parts of fullerene – vertices and edges. Electronic levels of these orbitals tend to localize at the bottom of conduction band and at the top of valence band and, in some cases, they even separate as localized mid-gap states (Fig. 3).

A little is known about magnetic transition in the lattice of GdI_3. The chemically related bulk trichloride $GdCl_3$ orders ferromagnetically below 2.2 K, the bulk $GdBr_3$ becomes magnetic below 1.3 K with the not yet clearly defined type of ordering, while the bulk GdI_3 might be magnetic below 1 K [35]. DFT+U calculations claimed that, GdI_3 monolayer is antiferromagnetic as bipartite lattice, yet, neither the used U parameter nor independence of energy difference between magnetic orderings on U was verified [36].

The presented here DFT calculations vote for ferromagnetic lattice of GdI_3 monolayer with energy gain 5.7 meV/unit over its antiferromagnetic bipartite lattice. The model of octahedral fullerene $(GdI_3)_{96}$ offers an opportunity to study magnetic ordering of GdI_3 monolayer at zero-dimensionality. First, it contains only even cycles of Gd-sublattice, hence, it is magnetically unfrustrated and might appear as bipartite lattice. Second, two types of coordination polyhedra (prisms GdI_6 and octahedra GdI_6 forming the edges and the facets) are given in equimolar ratio, hence, suggesting a configuration with the antiferromagnetically ordered edges and facets. The results approve a preservation of ferromagnetic ordering within single GdI_3 layer even folded into fullerene with the energy gains 2.7 and 0.5 meV/unit over the first and the second configurations, respectively.

4. Summary

In summary, the models of GdI_3 fullerenes were constructed and fullerenes' stability and electronic structure were studied by means of quantum-chemical calculations. The results reveal a higher stability of GdI_3 fullerenes with octahedral and icosahedral shapes, than these with tetrahedral shape. The derived functional dependence of stability on the size

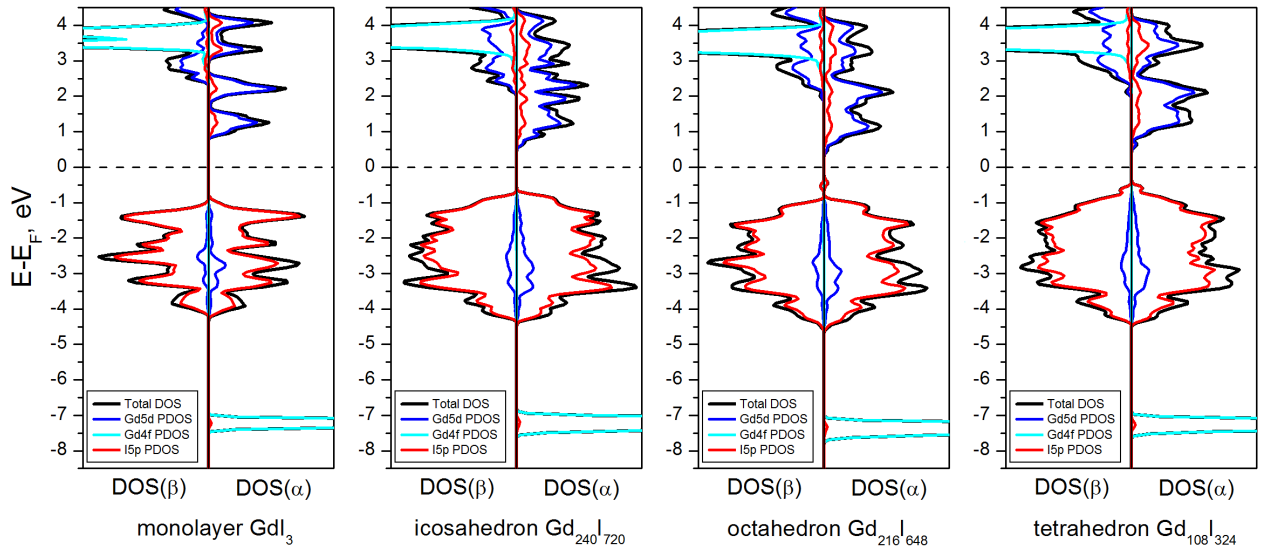

FIG. 3. Total and partial densities of spin-projected electronic states (DOS) for monolayer of GdI_3 and descendant fullerenes of different morphology. DFT calculations

confirms that, the strain at the fullerenes' edges contributes the most into the total strain energy of fullerenes. The electronic structure of all GdI_3 fullerenes considered here has a HOMO-LUMO gap of 0.2 – 0.8 eV, which is narrower than the band gap of GdI_3 monolayer due to an enhanced overlap between Gd5d- and I5p-orbitals at internal curved surface of the vertices and edges.

The present calculations do not hint on fabrication route to GdI_3 fullerenes. Though, by analogy to known fullerenes of layered dihalogenides [15–18], the physical methods employing high energetic processes like laser ablation from or electron-beam irradiation of the bulk material show a great promise.

References

[1] Luo X.-M., Hu Z.-B., Lin Q.-F., Cheng W., Cao J.-P., Cui C.-H., Mei H., Song Y., Xu Y. Exploring the Performance Improvement of Magnetocaloric Effect Based Gd-Exclusive Cluster Gd_{60}. *J. of the American Chemical Society*, 2018, **140**, P. 11219–11222.

[2] Xu Q., Liu B., Ye M., Zhuang G., Long L., Zheng L. Gd(OH)F_2: A Promising Cryogenic Magnetic Refrigerant. *J. of the American Chemical Society*, 2022, **144**, P. 13787–13793.

[3] Iyad N., Ahmad M.S., Alkhatib S.G., Hjouj M. Gadolinium contrast agents – challenges and opportunities of a multidisciplinary approach: Literature review. *European J. of Radiology Open*, 2023, **11**, 100503.

[4] Thomsen H.S., Almén T., Morcos S.K., members of the Contrast Media Safety Committee of ESUR. Gadolinium-containing contrast media for radiographic examinations: a position paper. *European Radiology*, 2002, **12**, P. 2600–2605.

[5] Saha S., Ntarisa A.V., Quang N.D., Kim H.J., Kothan S., Kaewkhao J. Synthesis and elemental analysis of gadolinium halides (GdX_3) in glass matrix for radiation detection applications. *Optical Materials*, 2022, **129**, 112490.

[6] Caravan P., Ellison J.J., McMurry T.J., Lauffer R.B. Gadolinium(III) Chelates as MRI Contrast Agents: Structure, Dynamics, and Applications. *Chemical Reviews*, 1999, **99**, P. 2293–2352.

[7] Ghiassi K.B., Olmstead M.M., Balch A.L. Gadolinium-containing endohedral fullerenes: structures and function as magnetic resonance imaging (MRI) agents. *Dalton Transactions*, 2014, **43**, P. 7346–7358.

[8] Sitharaman B., Kissell K.R., Hartman K.B., Tran L.A., Baikalov A., Rusakova I., Sun Y., Khant H.A., Ludtke S.J., Chiu W., Laus S., Tóth É., Helm L., Merbach A.E., Wilson L.J. Superparamagnetic gadonanotubes are high-performance MRI contrast agents. *Chemical Communications*, 2005, **2005**, P. 3915–3917.

[9] Sitharaman B., van der Zande M., Ananta J.S., Shi X., Veltien A., Walboomers X.F., Wilson L.J., Mikos A.G., Heerschap A., Jansen J.A. Magnetic resonance imaging studies on gadonanotube-reinforced biodegradable polymer nanocomposites. *J. of Biomedical Materials Research A*, 2010, **93**, P. 1454–1462.

[10] Hartman K.B., Laus S., Bolskar R.D., Muthupillai R., Helm L., Toth E., Merbach A.E., Wilson L.J. Gadonanotubes as Ultrasensitive pH-Smart Probes for Magnetic Resonance Imaging. *Nano Letters*, 2008, **8**, P. 415–419.

[11] Fidiani E., Costa P.M.F.J., Wolter A.U.B., Maier D., Buechner B., Hampel S. Magnetically Active and Coated Gadolinium-Filled Carbon Nanotubes. *The J. of Physical Chemistry C*, 2013, **117**, P. 16725–16733.

[12] Anumol E.A., Enyashin A.N., Batra N.M., Costa P.M.F.J., Deepak F.L. Structural and chemical analysis of gadolinium halides within WS_2 nanotubes. *Nanoscale*, 2016, **8**, 12170.

[13] Deepak F.L., Enyashin A.N. Capillary Imbibition of Gadolinium Halides into WS_2 Nanotubes: a Molecular Dynamics View. *Israel J. of Chemistry*, 2017, **57**, P. 501–508.

[14] Batra N., Anumol E.A., Smajic J., Enyashin A.N., Deepak F.L., Costa P.M.F.J. Morphological Phase Diagram of a Metal Halide Encapsulated in Carbon Nanotubes. *The J. of Physical Chemistry C*, 2018, **122**, P. 24967–24976.

[15] Hacohen Y.R., Popovitz-Biro R., Grunbaum E., Prior Y., Tenne R. Vapor–Liquid–Solid (VLS) Growth of $NiCl_2$ Nanotubes via Reactive Gas Laser Ablation. *Advanced Materials*, 2002, **14**, P. 1075–1078.

[16] Bar-Sadan M., Popovitz-Biro R., Prior Y., Tenne R. Closed-cage (fullerene-like) structures of $NiBr_2$. *Materials Research Bulletin*, 2006, **41**, P. 2137–2146.

[17] Tenne R., Popovitz-Biro R., Twersky A., Hacohen Y.R. Nanoparticles of $CdCl_2$ with closed cage structures. *Israel J. of Chemistry*, 2001, **41**, P. 7–14.
[18] Sallacan N., Popovitz-Biro R., Tenne R. Nanoparticles of CdI_2 with closed cage structures obtained via electron-beam irradiation. *Solid State Sciences*, 2003, **5**, P. 905–908.
[19] Wang X., Li Y. Fullerene-Like Rare-Earth Nanoparticles. *Angewandte Chemie International Edition*, 2003, **42**, P. 3497–3500.
[20] Bar-Sadan M., Kaplan-Ashiri I., Tenne R. Inorganic fullerenes and nanotubes: Wealth of materials and morphologies. *European Physical J. Special Topics*, 2007, **149**, P. 71–101.
[21] Enyashin A.N. Theoretical studies of inorganic fullerenes and fullerene-like nanoparticles. *Israel J. of Chemistry*, 2010, **50**, P. 468–483.
[22] Ordejón P., Artacho E., Soler J.M. Self-consistent order-N density-functional calculations for very large systems. *Physical Review B*, 1996, **53**, R10441.
[23] García A., Papior N., Akhtar A., Artacho E., Blum V., Bosoni E., Brandimarte P., Brandbyge M., Cerdá J.I., Corsetti F., Cuadrado R., Dikan V., Ferrer J., Gale J., García-Fernández P., García-Suárez V.M., García S., Huhs G., Illera S., Korytár R., Koval P., Lebedeva I., Lin L., López-Tarifa P., Mayo S.G., Mohr S., Ordejón P., Postnikov A., Pouillon Y., Pruneda M., Robles R., Sánchez-Portal D., Soler J.M., Ullah R., Yu V.W., Junquera J. SIESTA: Recent developments and applications. *The J. of Chemical Physics*, 2020, **152**, 204108.
[24] Asprey L.B., Keenan T.K., Kruse F.H. Preparation and Crystal Data for Lanthanide and Actinide Triiodides. *Inorganic Chemistry*, 1964, **3**, P. 1137–1141.
[25] Beck H.P., Gladrow E. Zur Hochdruckpolymorphie der Seltenerd-Trihalogenide. *Zeitschrift für Anorganische und Allgemeine Chemie*, 1979, **453**, P. 79–92.
[26] Hargittai I. In the shadow's shadow: Ivan V. Stankevich and C_{60}. *Structural Chemistry*, 2025, **36**, P. 1531–1533.
[27] Huisman R., de Jonge R., Haas C., Jellinek F. Trigonal-prismatic coordination in solid compounds of transition metals. *J. of Solid State Chemistry*, 1971, **3**, P. 56–66.
[28] Miura A., Tadanaga K., Magome E., Moriyoshi C., Kuroiwa Y., Takahiro T., Kumada N. Octahedral and trigonal-prismatic coordination preferences in Nb-, Mo-, Ta-, and W-based ABX_2 layered oxides, oxynitrides, and nitrides. *J. of Solid State Chemistry*, 2015, **229**, P. 272–277.
[29] Kasten A., Müller P.H., Schienle M. Magnetic ordering in GdI_2. *Solid State Communications*, 1984, **51**, P. 919–921.
[30] Seifert G., Vietze K., Schmidt R. Ionization energies of fullerenes – size and charge dependence. *J. of Physics B*, 1996, **29**, P. 5183–5192.
[31] Bar-Sadan M., Enyashin A.N., Gemming S., Popovitz-Biro R., Hong S.Y., Prior Y., Tenne R., Seifert G. Structure and Stability of Molybdenum Sulfide Fullerenes. *The J. of Physical Chemistry B*, 2006, **110**, P. 25399–25410.
[32] Enyashin A.N., Brontvein O., Seifert G., Tenne R. Structure and Stability of GaS Fullerenes and Nanotubes. *Israel J. of Chemistry*, 2017, **57**, P. 529–539.
[33] Birowosuto M.D., Dorenbos P. Novel γ- and X-ray scintillator research: on the emission wavelength, light yield and time response of Ce^{3+} doped halide scintillators. *Physica Status Solidi A*, 2009, **206**, P. 9–20.
[34] Li W., Walther C.F.J., Kuc A., Heine T. Density Functional Theory and Beyond for Band-Gap Screening: Performance for Transition-Metal Oxides and Dichalcogenides. *J. of Chemical Theory and Computation*, 2013, **9**, P. 2950–2958.
[35] Hovi V., Vuola R., Salmenperä L. The Specific Heats of $GdCl_3$, $GdBr_3$, and GdI_3 at Low Temperatures. *J. of Low Temperature Physics*, 1970, **2**, P. 383–387.
[36] You H., Zhang Y., Chen J., Ding N., An M., Miao L., Dong S. Peierls transition driven ferroelasticity in the two-dimensional d-f hybrid magnets. *Physical Review B*, 1970, **2**, P. 383–387.

Submitted 27 June 2025; accepted 18 August 2025

Information about the authors:

Andrey N. Enyashin – Institute of Solid State Chemistry UB RAS, Ekaterinburg, Russia; ORCID 0000-0001-6195-7971); enyashin@ihim.uran.ru

NANOSYSTEMS:
PHYSICS, CHEMISTRY, MATHEMATICS

Tolstoy V.P., et al. *Nanosystems: Phys. Chem. Math.*, 2025, **16** (5), 700–705.
http://nanojournal.ifmo.ru
DOI 10.17586/2220-8054-2025-16-5-700-705

Original article

Effect of labyrinth-like arrays formation of nickel nanorods on nickel surface as a result of galvanic substitution reaction in aqueous solutions of $CuCl_2$ and NaCl mixture

Valeri P. Tolstoy[a], Kirill D. Nikitin[b], Elisaveta V. Batischeva[c]

Institute of Chemistry, St. Petersburg State University, St. Petersburg, Russia

[a]v.tolstoy@spbu.ru, [b]st069423@student.spbu.ru, [c]batischevaelisaveta@gmail.com

Corresponding author: Valeri P. Tolstoy, v.tolstoy@spbu.ru

PACS 81.65.Cf

ABSTRACT The article describes the nickel surface treatment conditions in aqueous solutions of a mixture of $CuCl_2$ and NaCl salts. This investigation reveals the occurrence of selective etching on the nickel surface, facilitated by a galvanic replacement reaction (GRR). The etching process gives rise to the formation of arrays of labyrinths with walls of nickel nanorods with a diameter ranging from 10 to 50 nanometers and a length of up to 0.5 micrometers are formed, located primarily in the direction perpendicular to the surface. The experimental results obtained have enabled the formulation of hypotheses concerning the sequence of chemical reactions occurring on the surface and the role of the A. Turing diffusion-chemical model in the formation of the observed labyrinths. It has been demonstrated that the presence of such labyrinths on the surface of nickel leads to a decrease in the angles of its wetting with water.

KEYWORDS nickel, $CuCl_2$, galvanic replacement, nanorods, arrays

ACKNOWLEDGEMENTS This work was partly supported by the Russian Science Foundation (Grant No. 23-19-00566).

FOR CITATION Tolstoy V.P., Nikitin K.D., Batischeva E.V. Effect of labyrinth-like arrays formation of nickel nanorods on nickel surface as a result of galvanic substitution reaction in aqueous solutions of $CuCl_2$ and NaCl mixture. *Nanosystems: Phys. Chem. Math.*, 2025, **16** (5), 700–705.

1. Introduction

Galvanic replacement reactions of atoms on the surface of nickel are carried out by processing it in aqueous solutions of salts or complex compounds of more noble metals, and this makes it possible to obtain a fairly wide range of practically important nanoscale particles on its surface, including Au(0) [1], Pd(0) [2], Pt(0) [3–5], and a number of their alloys [6]. In such reactions, a salt or a complex compound of a more noble metal plays a role of an oxidiser of Ni(0) atoms on the surface. This process leads to the transition of nickel cations into solution and the formation of noble metal nanoparticles with different morphologies on the surface.

Among such reactions, the galvanic replacement reaction in $CuCl_2$ solutions is of particular importance. This reaction has been repeatedly used to create a layer of CuCl [7] nanoparticles on the nickel surface or to dissolve nickel particles in various composite ceramics [8]. A discussion of the features of this reaction on the nickel surface inevitably gives rise to consideration of the results that were previously obtained during the treatment of the surface and other metals with a solution of this salt. In particular, a mixture of $CuCl_2$ and NaCl solutions in [9] and [10] was used to dissolve Pd or Pd and Ag, respectively, on the surface of waste printed circuit boards.

In these articles, the selection of aqueous solutions of a mixture of $CuCl_2$ and NaCl salts was due to the fact that in these solutions, at the initial stage of the reaction, a galvanic replacement reaction occurs on the surface of the marked metals and Cu(0) nanocrystals are formed, which then react with an excess of $CuCl_2$ and form CuCl nanocrystals. In turn, the latter, dissolve in excess of NaCl to form a complex compound $CuCl_2^-$ in solution. In this case, the conditions of these reactions were primarily selected with the objective of resolving the issues associated with hydrometallurgy, i.e., the complete dissolution of crystals of these metals and their transfer to solutions resulting in the formation of corresponding salts.

The aim of this work was to research the features of selective etching of the nickel surface in aqueous solutions of $CuCl_2$, during which various types of ”patterns” were formed on it.

2. Experiment

GRRs were carried out on the surface of NP-2 nickel foil, which had been cut into plates with dimensions of approximately $15\times10\times0.05$ mm. The processing of such foil was carried out in aqueous solutions of $CuCl_2{\cdot}2H_2O$, NaCl and HCl, which were produced by JSC "Nevareactive" and their degree of purity corresponded to "analytical grade reagent". In order to prepare the reagent solutions, the salt samples were dissolved in deionised water with continuous stirring on a magnetic stirrer. The interval between the preparation of the solution and its subsequent application was at least a day.

To remove organic contaminants, the initial nickel foil samples were processed 2 times in isopropyl alcohol for 10 minutes in an ultrasonic bath with a generator power of 50 watts and an operating frequency of 35 kHz. Then they were etched in a 3 M aqueous HCl solution for 30 minutes at a temperature of 60 °C also in an ultrasonic bath and then washed 3 times with deionised water and dried in air.

In the course of the research, the characteristics of the GRR on the nickel surface in aqueous solutions of $CuCl_2$ and a mixture of $CuCl_2$ and NaCl were studied. The copper salt concentration was set at 0.2 increments in the range of 0.2 – 1.0 m, and the NaCl concentration was set at 0.5 increments in the range of 0.5 – 5 m. The duration of each treatment ranged from 5 minutes to 2 hours or more. To study the effect of the composition of the gaseous atmosphere on the processes on the surface of nickel, a number of experiments were conducted not only in the atmosphere of air, but also oxygen and argon. The solutions were pre-saturated with the appropriate gases by passing them through the solutions for 20 minutes. The surface treatment of the samples with all solutions was carried out at room temperature and atmospheric pressure.

In the course of the study, the orientation of crystals on the nickel surface was determined by means of an Oxford Instruments Electron Backscattered Diffraction (EBSD) system when the samples were observed under a Zeiss Merlin electron microscope. The composition of compounds on the nickel surface was determined by Electron Microprobe Analysis (EMPA) using an Oxford INCA-350 EDX spectrometer when the samples were observed under a Zeiss EVO40EP microscope. The wetting angles were measured using an Open Science goniometer equipped with a ToupCam digital camera. For this purpose, 1 μl of deionized water was applied to the sample surface from a distance of 2 mm using a Thermo Scientific Light microdoser. For each sample, the angles were measured at 3 to 4 points on its surface.

3. Results and discussion

At the first stage of the work, the effect of salt concentration in solutions of a mixture of $CaCl_2$ and NaCl on the formation of ordered structures on the nickel surface was studied. In order to achieve this, a series of samples were obtained through nickel processing for 1 hour. The study of the surface morphology of such samples by the SEM method showed that at concentrations of $CuCl_2$ in the range of 0.4 – 1.0 m and NaCl concentrations of 2.5 – 5.0 m, etching pits with walls arranged in the form of peculiar labyrinths can be observed on the surface. Moreover, the effect of the formation of such labyrinths is most pronounced after treatment in a solution of a mixture of salts with a concentration of $CuCl_2$ equal to 1.0 m and NaCl equal to 5.0 m. Subsequently, the effect of processing time on the formation of these structures was analysed for this mixture of salts. The analysis of the nickel surface by SEM of a series of such samples allowed us to identify the main stages of the process.

As demonstrated in the micrographs shown in Fig. 1, the GRR proceeds locally at the first stages, resulting in the formation of individual depressions with a diameter of several tens of nanometers on the surface (Fig. 1a). Over time, the size of these depressions increases and new ones are formed (Fig. 1b). These depressions gradually evolve into a discernible "pattern" on the surface. It is our contention that this "pattern" is primarily attributable to the dimensions of nickel polycrystals. The process of depression widening gives rise to the formation of a groove-like structure on the surface. Arrays of grooves form more pronounced patterns, visually resembling mazes (Fig. 1b). Then the grooves in these labyrinths deepen and widen (Fig. 1c,d). Further widening of the grooves leads to a decrease in the thickness of the walls between them. Consequently, as shown in Fig. 2 micrographs, several solid groove wall transforms into a set of individual nanorods with a diameter of approximately 10 – 50 nm and a length of up to 0.5 microns, oriented mainly along the normal to the surface. Nickel surface treatment in a similar solution for 3, 5, and 7 hours showed that a proportion of the nanorods dissolved and the pattern of the labyrinths became less pronounced (these micrographs are not shown in Figs. 1, 2).

As demonstrated by the experimental findings, the formation of such labyrinths is influenced by oxygen dissolved in a mixture of these salts. Fig. 3 shows a change in the morphology of the labyrinths with a change in the concentration of O_2 in solution. When O_2 is completely removed using Ar (Fig. 3a,d), the depth of resultant labyrinths exhibit a reduced depth when compared to those formed under the conditions of the reaction is carried out in an air atmosphere (Fig. 3b,e). When using a solution that is saturated with O_2, during the same treatment time, the walls of the labyrinths actually collapse and arrays of Ni nanorods oriented normally to it form on the nickel surface (Fig. 3b). From the results presented, we are able to conclude that the presence of O_2 accelerates the reaction of anisotropic nickel etching under the conditions of the GRR.

Examination of the Ni surface after treatment in a solution of a mixture of $CuCl_2$ ($C = 1$ m) and NaCl ($C = 5$ m) salts for two hours using the EBSD method showed that the vertices of the maze walls represent the faces of a Ni crystal with a crystallographic index $\{110\}$ (Fig. 3). Accordingly, anisotropic etching occurs mainly perpendicular to this and its

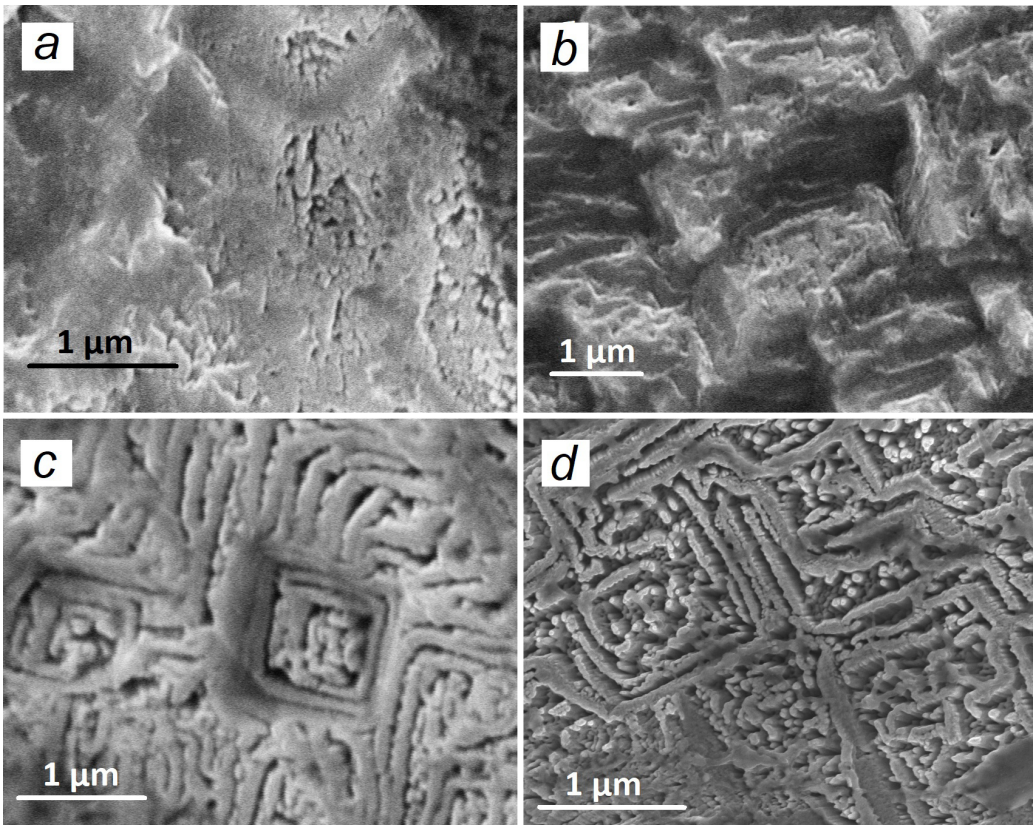

FIG. 1. SEM images of the nickel surface after treatment in a solution of a mixture of $CuCl_2$ ($C = 1$ m) and NaCl ($C = 5$ m) salts for (a) 5 minutes, (b) 15 minutes, (c) 30 minutes, (d) 2 hours. The images are obtained by observing from above

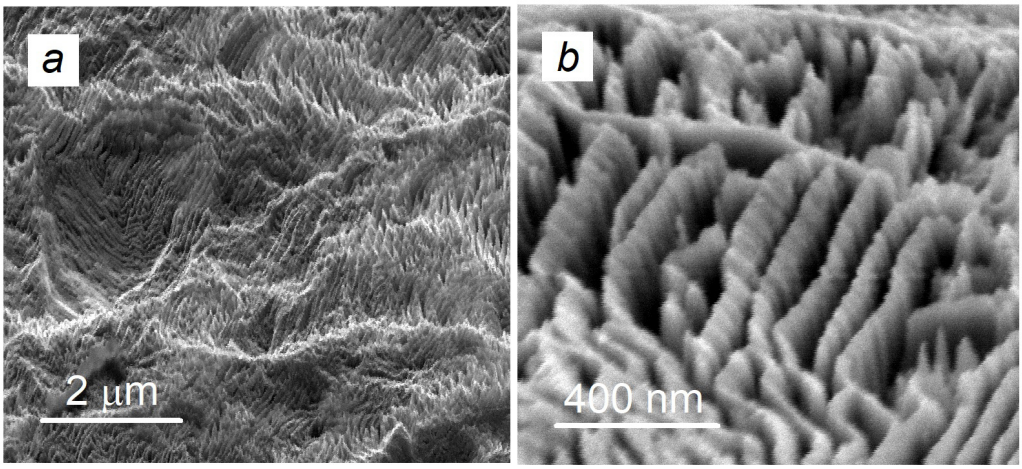

FIG. 2. SEM images of the nickel surface after treatment in a solution of a mixture of $CuCl_2$ ($C = 1$ m) and NaCl ($C = 5$ m) salts for 2 hours. The images were obtained when viewed at an angle of 45°

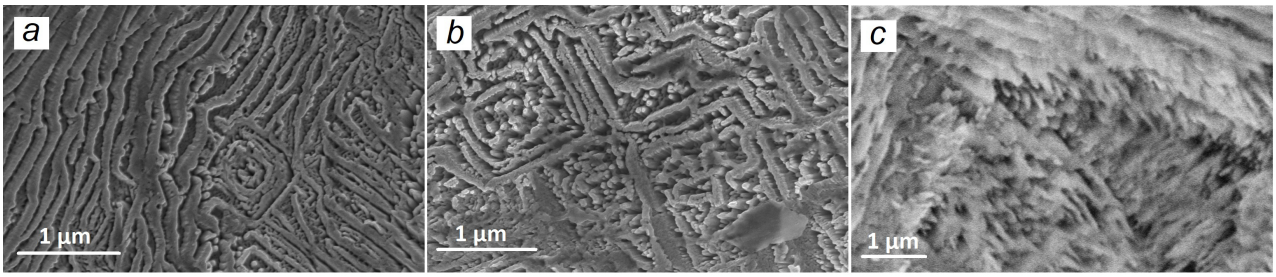

FIG. 3. SEM images of the nickel surface after treatment for 2 hours in a solution of a mixture of $CuCl_2$ ($C = 1$ m) and NaCl ($C = 5$ m) salts. (a) – treatment in an Ar atmosphere; (b) – treatment in an air atmosphere; (c) – treatment in an O_2 atmosphere

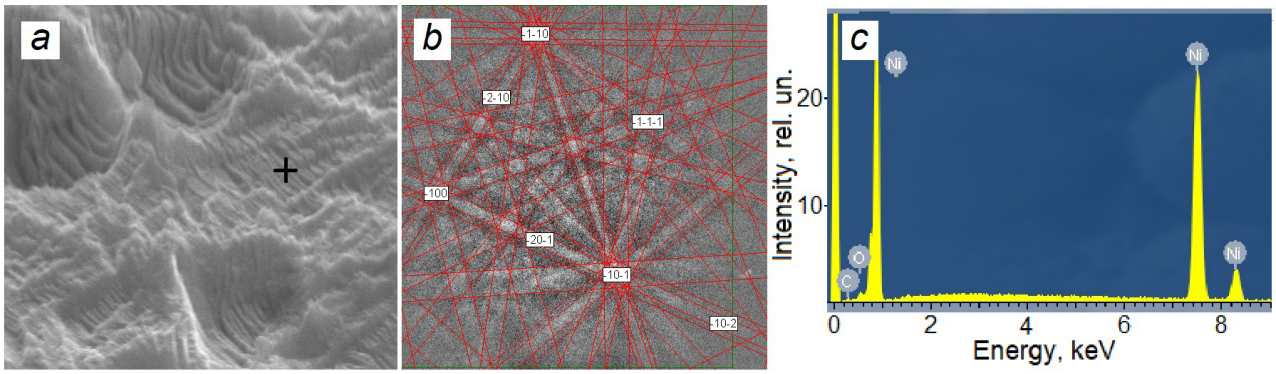

FIG. 4. SEM micrography (a) of the nickel surface after treatment for 2 hours in a solution of a mixture of $CuCl_2$ ($C = 1$ m) and NaCl ($C = 5$ m) salts and a diffraction pattern of backscattered electrons (b), which was obtained at the point indicated by the crosshair in Fig. 4a

equivalent faces. It is important that the results of the EMPA indicate the absence of copper, sodium and chlorine atoms on the surface, which could remain on the surface of the sample treatment field in a solution of a mixture of the marked salts taken in such a high concentration (Fig. 4d).

Based on the above facts, the following model of the processes occurring on the surface of Ni during its treatment in a solution of a mixture of $CuCl_2$ and NaCl salts can be proposed. Thus, at the first stage of the GRR Cu(0) nanoparticles are formed on the nickel surface (1). These nanoparticles subsequently react with Cu^{2+} ions from solution, resulting in the formation of a difficult-to-dissolve CuCl precipitate on the surface (2). It blocks the access of Cu^{2+} ions to Ni(0), which slows down the GRR and, consequently, the further formation of CuCl.

$$Ni(0) + CuCl_2 \rightarrow NiCl_2 + Cu(0), \quad (1)$$

$$Cu(0) + CuCl_2 \rightarrow 2CuCl. \quad (2)$$

Concurrently, the CuCl precipitate is dissolved in an excess of chloride ions by reaction (3) thereby releasing the Ni(0) surface is for further GRR, resulting in accelerated formation of new Cu(0) nanoparticles:

$$CuCl + Cl^- \rightarrow [CuCl_2]^-. \quad (3)$$

Along with the formation of $[CuCl_2]^-$, the formation of $[CuCl_3]^{2-}$ can also be observed in solution (Fig. 5a).

In addition, it was observed that with increasing treatment time in a solution of a mixture of salts, its pH increases from an initial value of 2.1 to 4.1 after the reaction has been carried out for 2 hours. This leads to the formation of a difficult-to-dissolve compound $CuCl_2 \cdot 3Cu(OH)_2$ by reaction (4), which exists in solutions with pH values in the range of 3 – 8 as illustrated in Fig. 5a. Furthermore, this compound is apparently deposited mainly on the nickel surface, as a local pH increase occurs there.

$$4CuCl_2 + 6OH^- \rightarrow CuCl_2 \cdot 3Cu(OH)_2 + 6Cl^-. \quad (4)$$

Thus, several successive and competing reactions occur in the system. Reaction (2) slows down reaction (1). Concurrently, reaction (3) accelerates reaction (1) by freeing the surface of Ni(0) from the presence of insoluble compounds. In turn, reaction (4) slows down reactions (1–3). The state of such a system is controlled by the ratio of the rates of chemical reactions and ion diffusion, which change dynamically. Such systems are referred to as reaction-diffusion or A. Turing systems in the literature, and are currently under active study, as they provide a unique approach to the self-assembly of nano- and micro-dimensional structures [12–14]. Such systems have been demonstrated to be responsible, for example,

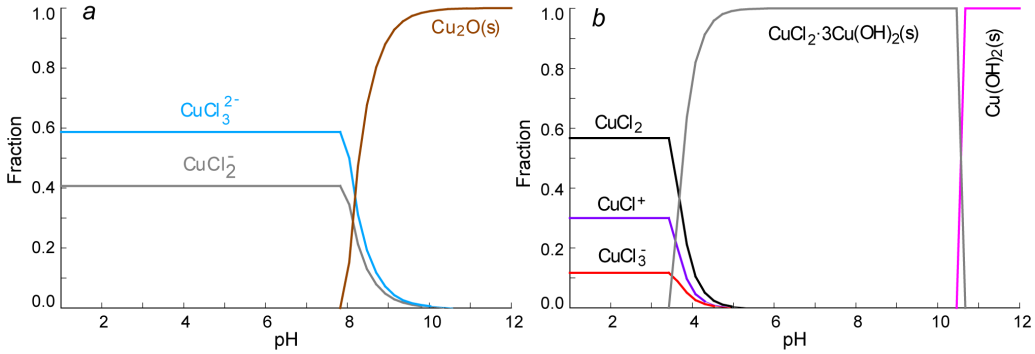

FIG. 5. The change in the calculated values of the mole fractions of various complex compounds in solutions of mixtures of CuCl and NaCl (a) and $CuCl_2$ and NaCl (b) salts, depending on the pH values. The calculations were performed using the Hydra-Medusa hydrochemical equilibrium modeling program [11]

for the formation of patterns on the skin of animals during their growth [15–19]. In addition, when interpreting these results, it should be borne in mind that GRR occurs inside the grooves at the stage of pattern formation, which means that self-organisation in the system is observed under conditions of spatial constraints, which, as is known [20], contribute to the morphology of reaction products.

As already noted, the transition of the complex compound $[CuCl_2]^-$ from the nickel surface to the solution is a relatively slow process. In our opinion, the process of oxidation of Cu(I) cations to the degree of Cu(II) can play a role in the dissolution process, which is realised, for example, by reaction (5). As demonstrated in Fig. 5b, at the equilibrium pH of the mixed salt solution, Cu(II) cations easily dissolve in the presence of excess chloride ions (reaction 6):

$$CuCl + O_2 + 2H_2O \rightarrow 4CuOHCl, \quad (5)$$

$$Cu(OH)Cl + 2Cl^- \rightarrow [CuCl_3]^- + OH^-. \quad (6)$$

As shown in Fig. 3, the presence of oxygen molecules in the solution accelerates the GRR reaction. This experimental result appears to provide confirmation of the considered model of the sequence of chemical reactions on the nickel surface under GRR conditions.

In a series of experiments, it was also found that when Ni is treated in a solution of a mixture of $CuCl_2$ and NaCl, its surface acquires a greater degree of hydrophilicity than that of the original nickel surface. Furthermore, it was determined that this degree increases with increasing treatment time in soluti from 1 to 2 hours. As illustrated in Fig. 6, the angle of wetting nickel with water was measured in a series of several samples. It was found that the maximum treatment time in a solution of a mixture of salts resulted in a 20° decrease in the edge angle of wetting the surface with water in comparison with the untreated surface of nickel. This effect is purportedly attributable to a distinctive "flow" of water into the grooves of the maze. These results, therefore, indicate the possibility of a controlled change in the wetting angles of the nickel surface in a relatively simple way by treating it in a solution of a mixture of salts.

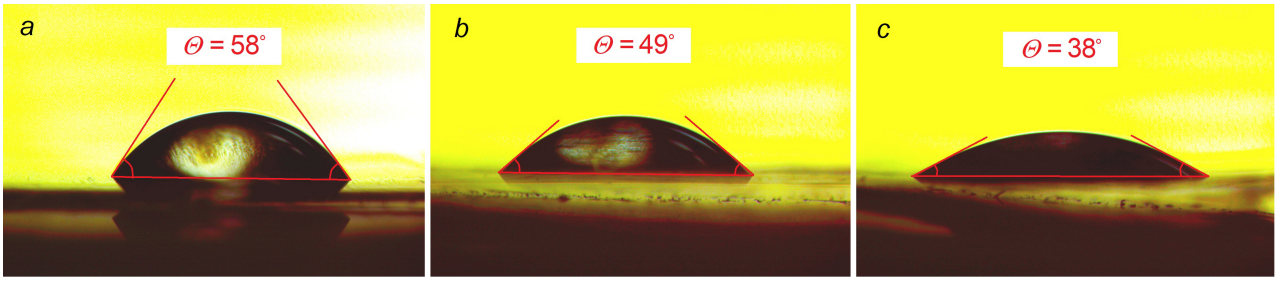

FIG. 6. The angles of wetting the nickel surface with water. (a) – before the measurement, the nickel is treated in HCl solution; (b) – treated in a solution of a mixture of $CuCl_2$ (1 m) and NaCl (5 m) for 1 hour; (c) – treated in a solution of a mixture of $CuCl_2$ (1 m) and NaCl (5 m) for 2 hours

4. Conclusion

A research of the features of nickel surface treatment in solutions of a mixture of $CuCl_2$ and NaCl salts showed that the effect of etching pits on its surface in the form of labyrinths with walls of nickel nanorods is most pronounced at a concentration of $CuCl_2$ equal to 1 m and NaCl concentration equal to 5 m with a treatment time of 2 hours. An increase in the reaction rate of GRR and the depth of the labyrinths was demonstrated with an increase in the concentration of oxygen dissolved in the mixture of the indicated salts. It is shown that the treatment of nickel in a solution of such salts leads to an increase in the degree of hydrophilicity of its surface.

References

[1] Reboul J., Li Z.-Y., Yuan J., Nakatsuka K., Saito M., Mori K., Yamashita H., Xia Y., Louis C. Synthesis of small Ni-core–Au-shell catalytic nanoparticles on TiO_2 by galvanic replacement reaction. *Nanoscale Advances*, 2021, **3** (3), P. 823–835.

[2] Lei H., Li X., Sun C., Zeng J., Singh S.S., Zhang Q. Galvanic Replacement–Mediated Synthesis of Ni-Supported Pd Nanoparticles with Strong Metal-Support Interaction for Methanol Electro-oxidation. *Small*, 2019, **15** (11), 1804722.

[3] Kaneva M.V., Borisov E.V., Tolstoy V.P. Pt(0) microscrolls obtained on nickel surface by galvanic replacement reaction in H_2PtCl_6 solution as the basis for creating new SERS substrates. *Nanosystems: Physics, Chemistry, Mathematics*, 2022, **13** (5), P. 509–513.

[4] Tolstoy V., Nikitin K., Kuzin A., Zhu F., Li X., Goltsman G., Gorin D., Huang G., Solovev A. and Mei Y. Rapid synthesis of Pt (0) motors-microscrolls on a nickel surface via H_2PtCl_6-induced galvanic replacement reaction. *Chemical Communications*, 2024, **60** (23), P. 3182–3185.

[5] Kaneva M.V., Tolstoy V.P. The "rolling up" effect of platinum layer obtained on nickel surface by interaction with solution of H_2PtCl_6 and its electrocatalytic properties in hydrogen evolution reaction during water electrolysis in alkaline medium. *Nanosystems: Physics, Chemistry, Mathematics*, 2021, **12** (5), P. 630–633.

[6] Shviro M., Polani S., Zitoun D. Hollow octahedral and cuboctahedral nanocrystals of ternary Pt–Ni–Au alloys. *Nanoscale*, 2015, **7** (32), P. 13521–13529.

[7] Batishcheva E.V., Tolstoy V.P. Formation of Arrays of 1D Copper (II) Oxide Nanocrystals on the Nickel Surface upon Its Galvanic Replacement in a $CuCl_2$ Solution and Their Electrocatalytic Properties in the Hydrogen Evolution Reaction during Water Splitting in an Alkaline Medium. *Russian J. of Inorganic Chemistry*, 2022, **67** (6), P. 898–903.

[8] Muscetta M., Andreozzi R., Clarizia L., Marotta R., Palmisano G., Policastro G., Race M., Yusuf A., Di Somma I., Recovery of nickel from spent multilayer ceramic capacitors: A novel and sustainable route based on sequential hydrometallurgical and photocatalytic stages. *Separation and Purification Technology*, 2023, **326**, 124780.

[9] Muscetta M., Minichino N., Marotta R., Andreozzi R., Di Somma I. Zero-valent palladium dissolution using NaCl/$CuCl_2$ solutions. *J. of Hazardous Materials*, 2021, **404**, 124184.

[10] Yazici E.Y., Deveci H.A.C.I. Cupric chloride leaching (HCl–$CuCl_2$–NaCl) of metals from waste printed circuit boards (WPCBs). *Int. J. of Mineral Processing*, 2015, **134**, P. 89–96.

[11] Gulina L.B., Gurenko V.E., Tolstoy V.P., Mikhailovski V.Y., Koroleva A.V. Interface-Assisted Synthesis of the $Mn_{3-x}Fe_xO_4$ Gradient Film with Multifunctional Properties. *Langmuir*, 2019, **35** (47), P. 14983–14989.

[12] Grzybowski B.A., Bishop K.J., Campbell C.J., Fialkowski M., Smoukov S.K. Micro- and nanotechnology via reaction–diffusion. *Soft Matter*, 2005, **1** (2), P. 114–128.

[13] Gu J., Li L., Xie Y., Chen B., Tian F., Wang Y., Zhong J., Shen J., Lu J. Turing structuring with multiple nanotwins to engineer efficient and stable catalysts for hydrogen evolution reaction. *Nature Communications*, 2023, **14** (1), 5389.

[14] Fromenteze T., Yurduseven O., Uche C, Arnaud E., Smith D.R., Decroze C. Morphogenetic metasurfaces: unlocking the potential of turing patterns. *Nature Communications*, 2023, **14** (1), 6249.

[15] Kondo S., Iwashita M., Yamaguchi M. How animals get their skin patterns: fish pigment pattern as a live Turing wave. *Proceeding of "Systems Biology"*, Springer, Tokyo, 2009, P. 37–46.

[16] Ishida T. Emergence of Diverse Epidermal Patterns via the Integration of the Turing Pattern Model with the Majority Voting Model. *Biophysica*, 2024, **4**, P. 283–297.

[17] Staddon M.F. How the zebra got its stripes: Curvature-dependent diffusion orients Turing patterns on three-dimensional surfaces. *Physical Review E*, 2024, **110**, 034402.

[18] Kondo S., Watanabe M., Miyazawa S. Studies of Turing pattern formation in zebrafish skin. *Phil. Trans. R. Soc. A*, 2021, **379**, 20200274.

[19] Hunter P. Of Turing and zebras. *EMBO reports*, 2023, **24**, e57405.

[20] Almjasheva O.V., Popkov V.I., Proskurina O.V., Gusarov V.V. Phase formation under conditions of self-organization of particle growth restrictions in the reaction system. *Nanosystems: Physics, Chemistry, Mathematics*, 2022, **13** (2), P. 164–180.

Submitted 19 June 2025; revised 24 August 2025; accepted 25 August 2025

Information about the authors:

Valeri P. Tolstoy – Institute of Chemistry, Saint Petersburg State University, University St. 26, Peterhof, Saint Petersburg, 198504, Russia; ORCID 0000-0003-3857-7238; v.tolstoy@spbu.ru

Kirill D. Nikitin – Institute of Chemistry, Saint Petersburg State University, University St. 26, Peterhof, Saint Petersburg, 198504, Russia; ORCID 0009-0007-1409-5214; st069423@student.spbu.ru

Elisaveta V. Batischeva – Institute of Chemistry, Saint Petersburg State University, University St. 26, Peterhof, Saint Petersburg, 198504, Russia; ORCID 0000-0001-8264-2135; batischevaelisaveta@gmail.com

Conflict of interest: the authors declare no conflict of interest.

NANOSYSTEMS:
PHYSICS, CHEMISTRY, MATHEMATICS

Kaneva M.V., et al. *Nanosystems: Phys. Chem. Math.*, 2025, **16** (5), 706–711.
http://nanojournal.ifmo.ru
DOI 10.17586/2220-8054-2025-16-5-706-711

Original article

Influence of precursors variation on the morphology and electrochemical performance of NiS_x thin films synthesized via the SILAR

Maria V. Kaneva[a], Alexandra A. Meleshko[b], Maxim I. Tenevich[c], Maria O. Enikeeva[d], Ilya A. Kodintsev[e], Artem A. Lobinsky[f]

Ioffe Institute, Hydrogen Energy Laboratory, St. Petersburg, Russia

[a]skt94@bk.ru, [b]alya_him@mail.ru, [c]mtenevich@gmail.com, [d]enikeeva123@mail.ioffe.ru, [e]i.a.kod@mail.ru, [f]lobinski.a@mail.ru

Corresponding author: Maria V. Kaneva, skt94@bk.ru

PACS 81.07.Bc

ABSTRACT In this work, nickel sulfide thin films were synthesized via the SILAR method using different nickel salts as precursors. The influence of the precursor salt on the morphology and electrochemical performance of the layers was systematically investigated. SEM analysis revealed that NiS_x films prepared from nickel chloride exhibited the most uniform and crack-free morphology. Electrochemical measurements demonstrated a strong correlation between film quality and capacitive behaviour. Notably, the NiS_x electrode synthesized using nickel chloride achieved a maximum specific capacitance of 1902 F/g at a current density of 1 A/g. These findings highlight the critical role of precursor selection in optimizing the structural and electrochemical properties of nickel sulfide electrodes for energy storage applications.

KEYWORDS nickel sulfide, precursors, thin films, SILAR, electrode, supercapacitor

ACKNOWLEDGEMENTS This work was supported by Russian Science Foundation (grant number 24-19-20060, https://rscf.ru/project/24-19-20060/) and St. Petersburg Science Foundation (agreement number 24-19-20060). The authors are very grateful to Dr. Dmitry Danilovich for their invaluable research assistance of FTIR spectroscopy. FTIR and SEM studies of the samples performed using devices of the Engineering Center of the St. Petersburg State Technological Institute (Technical University).

FOR CITATION Kaneva M.V., Meleshko A.A., Tenevich M.I., Enikeeva M.O., Kodintsev I.A., Lobinsky A.A. Influence of precursors variation on the morphology and electrochemical performance of NiS_x thin films synthesized via the SILAR. *Nanosystems: Phys. Chem. Math.*, 2025, **16** (5), 706–711.

1. Introduction

The development of high-performance supercapacitors is crucial for advancing modern energy storage technologies aimed at supporting sustainable energy systems. Supercapacitors are widely recognized for their remarkable power density, fast charge–discharge rates, and long cycle life, which enable them to bridge the gap between conventional dielectric capacitors and rechargeable batteries. These attributes make them ideal candidates for applications ranging from electric vehicles to renewable energy integration, where high power output and rapid energy delivery are essential [1].

Among various classes of electrode materials, transition metal sulfides have emerged as particularly promising for next-generation supercapacitors due to their excellent redox activity, high electrical conductivity, and large theoretical capacitance. Compared to their oxide counterparts, sulfides provide a greater number of accessible redox-active sites and lower electronegativity, which contribute to enhanced charge storage performance and improved structural flexibility. These features allow metal sulfides to achieve higher energy and power densities, along with excellent cycling stability [2, 3].

Nickel sulfide (NiS), in particular, has attracted significant attention due to its abundance, low cost, and outstanding electrochemical properties. Various crystalline forms of nickel sulfide, such as NiS, Ni_3S_2, and Ni_3S_4, exhibit high theoretical capacitances and reversible redox behavior, making them suitable candidates for use in hybrid and pseudocapacitor systems [4, 5].

To date, the synthesis of nickel sulfide nanostructures for supercapacitor applications has been primarily achieved through hydrothermal [6, 7] and solvothermal methods [8], often conducted at elevated temperatures (typically 160 – 180 °C) and in the presence of surfactants. Other methods such as electrodeposition [9], chemical bath deposition [10], and ultrasound-assisted soaking [11] have also been reported. While these techniques can yield high-performance materials, they often require complex conditions, long synthesis times, and additional reagents.

In this work, we report a facile and surfactant-free approach for the synthesis of nickel sulfide thin films directly on nickel foam substrates using the Successive Ionic Layer Adsorption and Reaction (SILAR) method at room temperature [12–14]. The SILAR technique offers a simple, low-cost, and easily controllable route for thin film fabrication, making it a viable alternative to traditional synthesis methods.

As is known, anions of precursor salts have a significant effect on the crystallization process, nucleation, determining the rate of crystal grown, morphology and structure of the crystals formed. Changes in the concentration and nature of anions can lead to significant changes in these parameters, as evidenced by earlier in detail studies [15, 16]. However, no systematic studies have been conducted on the effect nature of the anion on the morphology of the transition metal sulfides thin films obtained via SILAR synthesis. By varying the nickel salt precursor used during deposition we systematically investigated the influence of precursor chemistry on the resulting film morphology and electrochemical behavior. Among the synthesized samples, the electrode derived from nickel chloride demonstrated the most uniform crack-free surface morphology and exhibited the highest electrochemical performance, achieving a specific capacitance of 1902 F/g at a current density of 1 A/g in 1 M KOH electrolyte. Moreover, this sample displayed excellent rate capability and stable cycling performance over 1000 charge-discharge cycles.

2. Experimental

2.1. Synthesis of nickel sulfides on Ni foam

Aqueous solutions of nickel (II) chloride hexahydrate ($NiCl_2 \times 6H_2O$), nickel (II) sulfate heptahydrate ($NiSO_4 \times 7H_2O$), nickel (II) acetate tetrahydrate ($NiAc_2 \times 4H_2O$), nickel (II) nitrate hexahydrate ($Ni(NO_3)_2 \times 6H_2O$) were used for the synthesis of nickel sulfides by SILAR as the cationic precursors. Sodium sulfide nonahydrate ($Na_2S \times 9H_2O$) was used as the anion precursor. All solutions were prepared at a concentration of 0.05 M using distilled water. Nickel foam (NF) with a porosity of 110 PPI and dimensions of approximately 15×15 mm was used as the substrate. Prior to synthesis, the NF substrates were treated with ethanol in combination with ultrasound to remove organic contaminants. To eliminate the surface oxide layer, the substrates were subsequently immersed in 6 M hydrochloric acid (HCl) for 15 minutes, rinsed thoroughly with distilled water, and dried at 60 °C in air.

In the first step of SILAR, the pretreated substrates were fixed in clamps of the automated installation, immersed for 15 s into solution of nickel salt, and then washed with distilled water to remove excess reagent. In the second step, the substrates were immersed for 15 s in the Na_2S solution and again washed in distilled water. This sequence of treatments constituted a single SILAR cycle, which was repeated 10 times. After completion of layering cycles, the substrates were dried in an air atmosphere.

2.2. Materials characterizations and electrochemical measurements

The morphological characteristics of the synthesized nickel sulfide films were examined using a Tescan Vega 3 SBH scanning electron microscope (SEM). Elemental composition and surface distribution of elements were determined via energy-dispersive X-ray spectroscopy (EDX) using an Oxford Instruments INCA x-act system coupled to the SEM. FTIR transmittance spectra were recorded on Shimadzu IRTracer-100 FTIR spectrophotometer. Phase composition and crystallinity were assessed by powder X-ray diffraction (PXRD), carried out on a DRON-8H diffractometer (Russia, Bourevestnik, JSC) (Cu Kα radiation ($\lambda = 1.5406$ Å)). Diffraction patterns were recorded in Bragg–Brentano geometry in the ω-2θ scanning mode using PSD in the angle range $2\theta = 30 - 65^\circ$ in increments of 0.01°. Phase identification was performed by comparing the obtained patterns with standard reference data from the PDF-2 database.

The electrochemical properties of NiS/NF as cathode of supercapacitor was investigated in standard three-electrode cell measurements with 1 M KOH electrolyte using SmartStat PS-250 (SmartStat, Russia, Chernogolovka) at room temperature. The reference and counter electrodes were an Hg/HgO and a carbon rod, respectively. Cyclic voltammetry (CV) measurements were obtained in the potential windows from 0.0 to 0.6 V (vs. Hg/HgO) at scan rates of 10 mV/s. Galvanostatic charge discharge (GCD) measurements were obtained at current densities of 1 A/g. The specific capacitance (C, F/g) of the prepared electrode was calculated from the GCD measurements using eq. (1):

$$C = \frac{It}{mV}, \tag{1}$$

where I is the applied current (A), t is the discharge time (s), V is the potential window (V) and m is the mass of the electroactive material (g). The mass of the electroactive material was determined from the difference in mass between the initial substrate and the substrate with the NiS layer.

3. Results and discussion

In this study, we investigated the synthesis conditions of nickel sulfide (NiS) using the SILAR method, with a particular focus on the influence of different nickel salts as precursors. Specifically, nickel sulfate, nickel acetate, nickel chloride, and nickel nitrate were employed as sources of Ni^{2+} ions. The primary objective was to examine how the nature of the nickel salt affects the morphology of the resulting nickel sulfide layers.

The SEM images and EDX spectra are shown in Fig. 1.

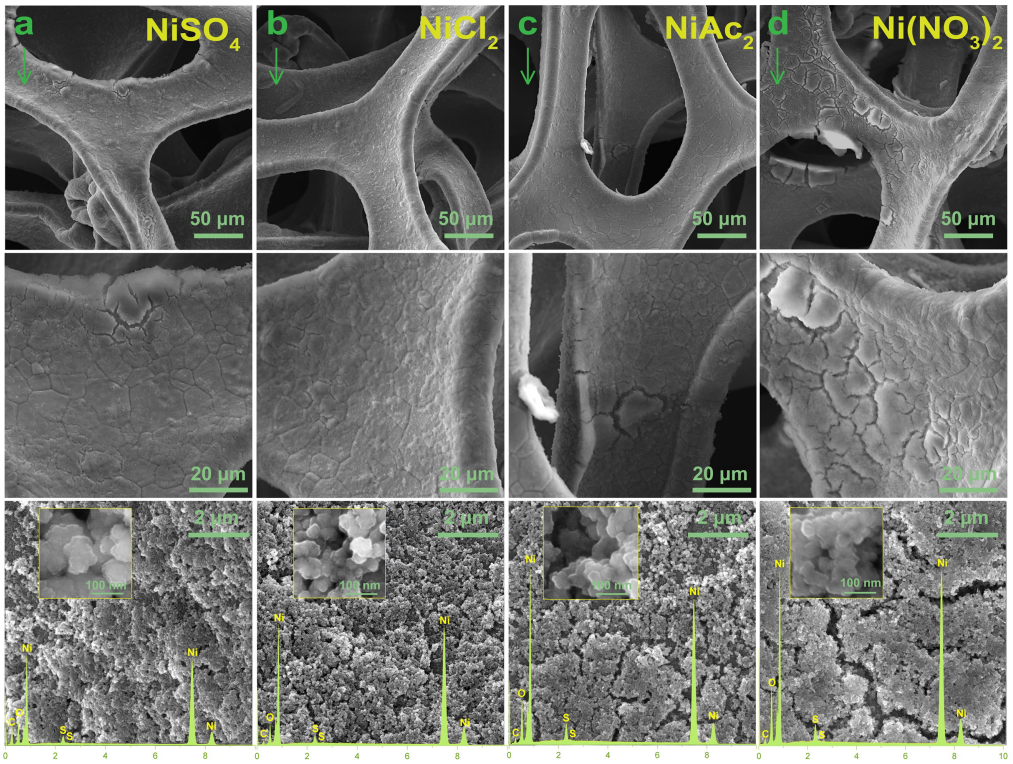

FIG. 1. SEM images and EDX spectra of nickel sulfides synthesized using $NiSO_4$, $NiCl_2$, $NiAc_2$ and $Ni(NO_3)_2$ on NF after 10 SILAR cycles at different magnifications

Our findings reveal that the choice of precursor salt plays a critical role in determining the quality and uniformity of the NiS film deposited on the substrate. Notably, the use of nickel chloride resulted in the formation of a more uniform and continuous NiS layer (Fig. 1b). In contrast, films synthesized using nickel sulfate, acetate, and nitrate exhibited noticeable cracking and inhomogeneities, suggesting that these salts lead to less favorable deposition characteristics under the given conditions (Fig. 1a,c,d). The observed cracking in NiS layers synthesized from nickel sulfate, acetate, and nitrate precursors can be attributed to several factors. These salts likely promote less controlled or uneven nucleation and growth of the NiS layer during the SILAR process, resulting in internal stresses within the film. Additionally, highly hydrated anions such as sulfate and nitrate may alter the deposition kinetics, leading to rapid precipitation and structural inhomogeneities. Upon drying or crystallization, these stresses can manifest as cracks due to shrinkage and poor mechanical integrity. In contrast, the use of nickel chloride as the precursor yields a more uniform and compact NiS thin film, likely due to its lower degree of ion hydration and more favorable deposition behavior.

EDX spectrum data demonstrate presence of Ni, S, O and C atoms in synthesized nanolayers.

Figure 2(a) illustrates the FTIR spectra of nickel sulfides synthesized using $NiSO_4$, $NiCl_2$, $NiAc_2$ and $Ni(NO_3)_2$. Absorption bands characteristic of nickel sulfide with minor differences in intensity are observed in all spectra. Weak bands observed at about 3670 and 1640 cm^{-1} are corresponding to valence and bending vibrations bonds of O–H bond in water molecules, respectively. Bands with peaks at 1080 and 2339 cm^{-1} are correlated to CO_2, which is thought to be adsorbed on the surface of samples from the atmosphere during sample preparation [17]. The peaks at 500, 555 and 670 cm^{-1} could be assigned to bending vibration mode in Ni–S [18].

Figure 2(b) show the XRD pattern thin film of nickel sulfide obtained from nickel chloride precursor. It should be noted that a similar diffraction pattern was observed for sulfides obtained from other precursors. A single intense peak is observed with value 33.7° corresponding to lattice parameter (002), respectively, in agreement with standard data card (JCPDS: 12-0041) of NiS_x. Peak with value 62.1° correspond to K_β of substrate.

The electrochemical performance of the NiS electrode was evaluated by cyclic voltammetry (CV) and galvanostatic charge discharge technology (GCD). Fig. 3(a) shows the CV curves of NiS electrodes synthesized using $NiSO_4$, $NiCl_2$, $NiAc_2$ and $Ni(NO_3)_2$ on Ni foam after 10 SILAR cycles. The peaks present are related to typical redox peaks of Ni^{2+} to Ni^{3+} [19]. Probable reaction mechanism of these redox peaks may be related to the following eq. (2):

$$NiS + OH^- \rightleftharpoons NiSOH + e^-. \quad (2)$$

However, it can be noted that the Ni^{2+} to Ni^{3+} transition potential is different for each electrode. Moreover, the lowest potential at which this process occurs corresponds to nickel sulfide synthesized from nickel chloride. It can be hypothesized that the anions (such as sulfate, chloride, nitrate, etc.) exert an influence on the electrochemical behavior

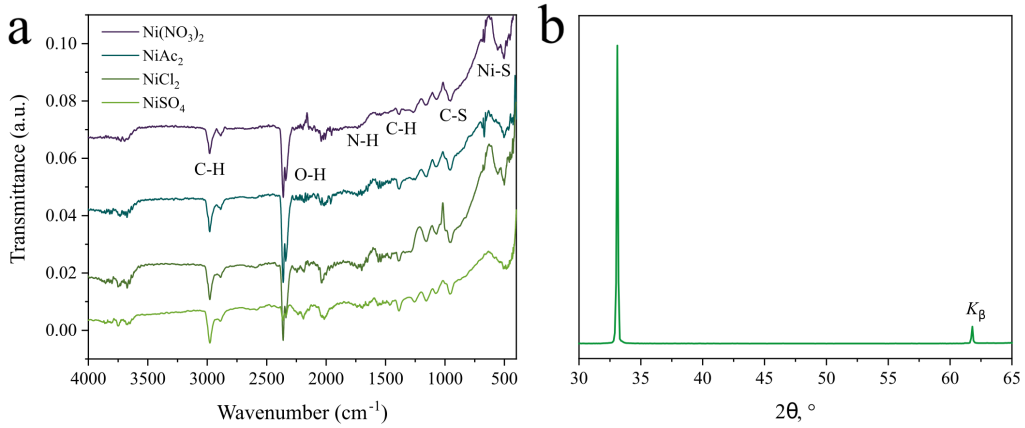

FIG. 2. (a) FTIR spectra of nickel sulfides synthesized using $NiSO_4$, $NiCl_2$, $NiAc_2$ and $Ni(NO_3)_2$ and (b) XRD pattern of nickel sulfides synthesized using $NiCl_2$

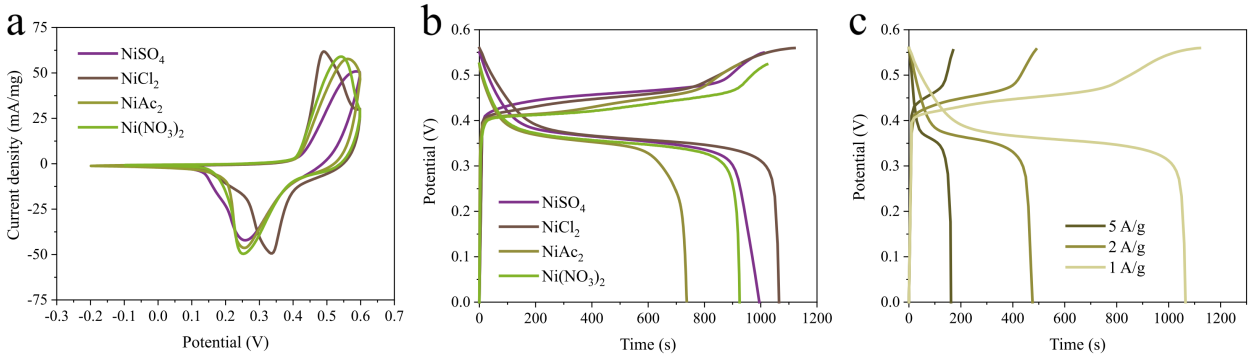

FIG. 3. (a) CV curves at scan rate of 10 mV/s and (b) GCD curves at current density of 1 A/g in 1 M KOH electrolyte of nickel sulfides synthesized using $NiSO_4$, $NiCl_2$, $NiAc_2$ and $Ni(NO_3)_2$ on NF after 10 SILAR cycles, (c) GCD curves at different current density of nickel sulfide synthesized using $NiCl_2$ after 10 SILAR cycles

of nickel, potentially through the formation of surface complexes or modifications in the material's structural properties. These effects could lead to a shift in the oxidation/reduction peak potential, depending on the chemical nature and reactivity of the anions.

The galvanostatic charge-discharge curves of electrodes are shown in Fig. 3(b). The nonlinear shape of the curves indicates the pseudocapacitive properties of the electrodes. The specific capacitance values calculated from the charge-discharge curves at a current density of 1 A/g (Fig. 3b) for electrodes synthesized using $NiSO_4$, $NiCl_2$, $NiAc_2$ and $Ni(NO_3)_2$ were 1809, 1902, 1401 and 1762 F/g, respectively. Thus, the sample synthesized from nickel chloride has the best capacitive characteristics. This enhanced electrochemical performance directly correlates with improved morphology electrode synthesized using $NiCl_2$, as the continuous and crack-free structure facilitates better electron and ion transport, reduces charge transfer resistance, and ensures more effective utilization of electroactive sites. Consequently, the NiS layer derived from nickel chloride exhibits superior electrochemical properties compared to the more fractured and structurally defective layers obtained used other salts.

A comparative analysis of the electrochemical performance of the synthesized nickel sulfide with nickel sulfide-based electrodes obtained by other synthetic techniques is presented in Table 1. The results provide compelling evidence for the efficacy of the SILAR method as an effective approach for the synthesis of nickel sulfide. Furthermore, a detailed investigation into the influence of various synthesis conditions such as the choice of nickel salts and deposition parameters on the electrochemical properties of the resulting material has been conducted. These findings contribute to a deeper understanding of how synthesis conditions can be optimized to enhance the performance of nickel sulfide electrodes, highlighting the potential of this method for future applications in energy storage and conversion technologies.

TABLE 1. Comparative characteristics of electrodes based on nickel sulfide obtained by different synthetic techniques

Electrode	Substrate	Method	Specific capacitance (F/g)	Electrolyte	Stability	Ref
NiS_x	Ni foam	SILAR	1902 at 1 A/g	1 M KOH	100 % after 1000 cycles	This article
Ni_3S_2 (h-NS20)/Co_3O_4	Ni foam	SILAR	1901 at 1 A/g	1 M KOH	91.8 % after 10000 cycles	[20]
NiS/NiSSe nanosheet	Ni foam	hydrothermal technique	1908 at 1 A/g	PVA/KOH gel electrolyte	>90 % after 28000 cycles	[21]
NiS/ACNTs	Ni foam	hydrothermal method and subsequent annealing treatment	1266 at 1 A/g	3 M KOH	83 % after 2000 cycles	[22]
NiS NPs	Ni foam	hydrothermal method	1073.8 at 1.2 A/g	2 M KOH	89 % after 1000 cycles	[23]

4. Conclusion

This study demonstrates the impact of nickel salt precursors on the morphology and electrochemical performance of nickel sulfide films synthesized via the SILAR method. Among the salts investigated, nickel chloride produced the most uniform and mechanically stable NiS_x layer, free of visible cracks and defects. This improved film quality was found to be directly responsible for the superior electrochemical performance, with the chloride-derived NiS_x electrode achieving a specific capacitance of 1902 F/g at 1 A/g. In contrast, layers formed from nickel sulfate, acetate, and nitrate exhibited significant cracking, which negatively affected charge transport and capacitance. The results underscore the importance of precursor selection in controlling the microstructure and optimizing the electrochemical properties of nickel sulfide-based electrodes, offering valuable insights for the development of advanced materials for supercapacitor and energy storage technologies.

References

[1] Lakshmi K.C.S., Vedhanarayanan B. High-performance supercapacitors: a comprehensive review on paradigm shift of conventional energy storage devices. *Batteries*, 2023, **9** (4), P. 202–247.

[2] Shariq M., Alhashmialameer D., Adawi H., Alrahili M.R., Almashnowi M.Y.A., Alzahrani A., Sharma M., Ali S.K., Slimani Y. Advancements in transition metal sulfide supercapacitors: a focused review on high-performance energy storage. *J. Ind. Eng. Chem.*, 2025, **144**, P. 269–291.

[3] Gao Y., Zhao L. Review on recent advances in nanostructured transition-metal-sulfide-based electrode materials for cathode materials of asymmetric supercapacitors. *CEJ*, 2022, **430** (2), 132745.

[4] Guan Y., Hu K., Su N., Zhang G., Han Y., An M. Review of NiS-based electrode nanomaterials for supercapacitors. *Nanomaterials*, 2023, **13** (6), P. 979–1014.

[5] Pothu R., Bolagam R., Wang Q.H., Ni W., Cai J.F., Peng X.X., Feng Y.Z., Ma J.M. Nickel sulfide-based energy storage materials for high-performance electrochemical capacitors. *Rare Met.*, 2021, **40**, P. 353–373.

[6] Yan H., Zhu K., Liu X., Wang Y., Wang Y., Zhang D., Lu Y., Peng T., Liu Y., Luo Y. Ultra-thin NiS nanosheets as advanced electrode for high energy density supercapacitors. *RSC Adv.*, 2020, **10**, P. 8760–8765.

[7] Gou J., Xie S., Yang Z., Liu Y., Chen Y., Liu Y., Liu C. A high-performance supercapacitor electrode material based on NiS/Ni_3S_4 composite. *Electrochim. Acta*, 2017, **229**, P. 299–305.

[8] Parveen N., Ansari S.A., Ansari S.G., Fouad H., El-Salam N.M.A., Cho M.H. Solid-state symmetrical supercapacitor based on hierarchical flower-like nickel sulfide with shape-controlled morphological evolution. *Electrochim. Acta*, 2018, **268**, P. 82–93.

[9] Chen X., Sun M., Jaber F., Nezhad E.Z., Hui K.S, Li Z., Bae S., Ding M. A flexible wearable self-supporting hybrid supercapacitor device based on hierarchical nickel cobalt sulfide@C electrode. *Sci Rep.*, 2023, **13**, 15555.

[10] Patil A.M., Lokhande V.C., Lokhande A.C., Chodankar N.R., Ji T., Kim J.H., Lokhande C.D. Ultrathin nickel sulfide nano-flames as an electrode for high performance supercapacitor; comparison of symmetric FSS-SCs and electrochemical SCs device. *RSC Adv.*, 2016, **6**, P. 68388–68401.

[11] Yu L., Yang B., Liu Q., Liu J., Wang X., Song D., Wang J., Jing X. Interconnected NiS nanosheets supported by nickel foam: soaking fabrication and supercapacitors application. *J. Electroanal. Chem.*, 2015, **739**, P. 156–163.

[12] Ratnayake S.P., Ren J., Colusso E., Guglielmi M., Martucci A., Gaspera E.D. SILAR deposition of metal oxide nanostructured films. *Small*, 2021, 2101666.

[13] Lobinsky A.A., Kodintsev I.A., Tenevich M.I., Popkov V.I. A novel oxidation–reduction route for the morphology-controlled synthesis of manganese oxide nanocoating as highly effective material for pseudocapacitors. *Coatings*, 2023, **13** (2), 361.

[14] Lobinsky A.A., Kaneva M.V., Tenevich M.I., Vadim Popkov V.I., Direct Synthesis of $Mn_3[Fe(CN)_6]_2 \cdot nH_2O$ Nanosheets as Novel 2D Analog of Prussian Blue and Material for High-Performance Metal-Ion Batteries. *Micromachines*, 2023, **14** (5), 1083.

[15] Zhang F., Ouyang R., Zhou T., Xiong C., Shi W., Su X., Zeng T., Chen Y., Dong G. The effect of different anions on the crystallization course of α-Al_2O_3 powder in hydrothermal method. *App. Cer. Tech.*, 2024, **21** (3), P. 1450–1460.

[16] Matussin S.N., Rahman A., Khan M.M. Role of Anions in the Synthesis and Crystal Growth of Selected Semiconductors. *Front. Chem.*, 2022, **10**, 881518.
[17] Khan N.A., Rashid N., Junaid M., Zafar M.N., Faheem M., Ahmad I. NiO/NiS Heterostructures: An Efficient and Stable Electrocatalyst for Oxygen Evolution Reaction. *ACS Applied Energy Materials*, 2019, **2** (5), P. 3587–3594.
[18] Nachimuthu S., Kannan K., Thangavel S., Gurushankar K. Electrochemical and magnetic properties of 3D porous NiS/CuS nanocomposites. *Applied Surface Science Advances*, 2022, **7**, 100209.
[19] Liu H., Liu X.-J., Dong F.-Y., Sun X.-Z. A direct-write method for preparing a bimetal sulfide/graphene composite as a free-standing electrode for high-performance microsupercapacitors. *RSC Advances*, 2020, **10**, 35490.
[20] Mishra D., Kim S.Y., Jin S.H. Hierarchically-Formed Nickel Sulfide Heterostructure via SILAR on Hydrothermally Grown Cobalt Oxide Scaffolds: Role of Number of Over-Coating and Evolution of Electrochemical Performance in Supercapacitor Electrodes. *Applied Surface Science*, 2021, **564** (4), 150436.
[21] Charis C., Batabyal S.K., Pramana S.S., Das B. Nickel sulfide-nickel sulfoselenide nanosheets as a potential electrode material for high performance supercapacitor with extended shelf life. *J. of Energy Storage*, 2023, **68**.
[22] Ouyang Y., Chen Y., Peng J., Yang J., Wu C., Chang B., Guo X., Chen., Luo Z., Wang X. Nickel sulfide/activated carbon nanotubes nanocomposites as advanced electrode of high-performance aqueous asymmetric supercapacitors. *J. of Alloys and Compounds*, 2021, **885**, 160979.
[23] Bandari N., Punnoose D., Rao S.S., Subramabnian A., Ramesh B.R., Kim H.-J. Hydrothermal synthesis and pseudocapacitive properties of morphology-tuned nickel sulfide (NiS) nanostructures. *New J. Chem.*, 2018, **42**, P. 2733–2742.

Submitted 21 August 2025; accepted 26 August 2025

Information about the authors:

Maria V. Kaneva – Ioffe Institute, Hydrogen Energy Laboratory, St Petersburg, 194021, Russia; ORCID 0000-0003-2816-7059; skt94@bk.ru

Alexandra A. Meleshko – Ioffe Institute, Hydrogen Energy Laboratory, St Petersburg, 194021, Russia; ORCID 0000-0002-7010-5209; alya_him@mail.ru

Maxim I. Tenevich – Ioffe Institute, Hydrogen Energy Laboratory, St Petersburg, 194021, Russia; ORCID 0000-0003-2003-0672; mtenevich@gmail.com

Maria O. Enikeeva – Ioffe Institute, Hydrogen Energy Laboratory, St Petersburg, 194021, Russia; ORCID 0000-0002-9633-4421; enikeeva123@mail.ioffe.ru

Ilya A. Kodintsev – Ioffe Institute, Hydrogen Energy Laboratory, St Petersburg, 194021, Russia; i.a.kod@mail.ru

Artem A. Lobinsky – Ioffe Institute, Hydrogen Energy Laboratory, St Petersburg, 194021, Russia; ORCID 0000-0001-5930-2087; lobinski.a@mail.ru

Conflict of interest: the authors declare no conflict of interest.

Paper abstracts in Russian / Аннотации статей

Нелинейное оптимальное управление в двухточечной краевой задаче для псевдопараболического уравнения с условиями типа Самарского-Ионкина

Юлдашев Т.К., Кадиркулов Б.Ж., Шермаматов Ж.Ж., Рамазанова А.Т.

В данной работе рассматривается задача оптимального управления подвижной точкой для псевдопараболического уравнения с нелинейной управляющей функцией при двухточечном нелинейном граничном условии. Уравнение исследуется при краевых условиях типа Самарского-Ионкина по пространственной переменной *x*. Изучена спектральная задача и найдены собственные значения, собственные функции и условия оптимальности. Получены нагруженные нелинейные функциональные уравнения относительно управляющей функции. Методом сжимающих отображений доказано существование и единственность управляющей функции. Определена функция состояния. Доказана сходимость ряда Фурье для функции состояния.

Ключевые слова: Нелинейное загруженное функциональное уравнение, псевдопараболическое уравнение, двухточечное краевое условие, условия типа Самарского-Ионкина, собственные числа, собственные функции, ряды Фурье, теоремы существования и единственности.

Спектральный анализ двухчастичных гамильтонианов с короткодействующими взаимодействиями

Ахмадова М.О., Азизова М.А.

Мы анализируем спектральные характеристики решеточных операторов Шрёдингера $H_{\gamma\lambda\mu}(K)$, $K\in(-\pi,\pi]^3$, которые представляют систему двух идентичных бозонов, расположенных на решетке $\mathbb{Z}^3$. Модель включает в себя взаимодействия на узлах решетки и взаимодействия ближайших соседей, параметризованные $\gamma,\lambda,\mu\in R$. Наше исследование оператора $H_{\gamma\lambda\mu}(0)$ выявляет инвариантное подпространство, на котором его ограниченная форма $H^{ea}_{\lambda\mu}(0)$ зависит исключительно от λ и μ. Чтобы прояснить механизмы рождения и уничтожения собственных значений для $H^{ea}_{\lambda\mu}(0)$, мы определяем критический оператор. Впоследствии на плоскости, натянутой на λ и μ, разрабатывается подробный критерий, который включает: (i) вывод гладких критических кривых, которые отмечают наступление критичности для оператора, и (ii) доказательство точных условий существования именно α собственных значений ниже и β собственных значений выше существенного спектра, где $\alpha,\beta\in\{0,1,2\}$ и $\alpha+\beta\leq 2$.

Ключевые слова: Двухчастичная система, решёточный оператор Шрёдингера, существенный спектр, связанные состояния, детерминант Фредгольма

Асимптотическое разложение определенного интеграла, ассоциированного с семейством моделей Фридрихса, возникающих в квантовой механике

Расулов Т.Х., Умиркулова Г.Х.

В данной работе рассматривается семейство моделей Фридрихса, возникающих в квантовой механике, соответствующих гамильтониану двухчастичной системы на одномерной решетке.

Проанализировано количество, расположение и условия существования собственных значений этого семейства. Получено асимптотическое разложение соответствующего определителя Фредгольма в окрестности начала координат.

Ключевые слова: модель Фридрихса, квантовая механика, решетка, двухчастичная система, определитель Фредгольма, собственное значение, разложение.

Включения метастабильной сверхпроводящей фазы галлия в $SmGa_2$

Шитов А.Е., Волков М.П.

Намагниченность M соединения $SmGa_2$ в широкой области температур имеет парамагнитный характер, а при понижении температуры ниже 30 K наблюдается существенный рост намагниченности, который указывает на образование магнито-упорядоченного состояния. При температурах ниже 5 K на зависимостях M(H) наблюдается резкая особенность, представляющая собой вклад от намагниченности сверхпроводящих суб-микронных включений галлия. Анализ зависимостей M(H), измеренных при разных температурах ниже 5 K, позволил предположить наличие двух сверхпроводящих фаз галлия. Критическая температура T_C = 5.9 K и критическое поле H_C (0) = 560 Oe соответствуют образованию метастабильной β-фазы галлия, а критическая температура T_C = 8.4 K и критическое поле H_C (0) = 1100 Oe могут быть связаны с образованием тонкого слоя аморфного галлия на поверхности включений β-фазы.

Ключевые слова: намагниченность, $SmGa_2$, сверхпроводимость, микрочастицы, метастабильная фаза, галлий.

Непредсказуемая и равномерная генерация случайных чисел на основе времени прибытия с использованием детекторов InGaAs

Дипика Аггарвал, Аниндита Банерджи, Анкуш Шарма, Ганеш Ядав

Квантовые генераторы случайных чисел становятся обязательными в требовательном технологическом мире высокопроизводительных алгоритмов обучения и правил безопасности. Наша реализация, основанная на принципах квантовой механики, позволяет нам достичь необходимой случайности. Мы сгенерировали высококачественные квантовые случайные числа из слабого когерентного источника на телекоммуникационной длине волны. Энтропия основана на времени прибытия квантовых состояний в пределах заданного интервала времени. Детектирование фотонов детекторами одиночных фотонов InGaAs и высокоточное измерение времени 5 пс позволяют нам генерировать 16 случайных битов за время прибытия, что является самым высоким показателем, зарегистрированным на сегодняшний день. Мы представили теоретический анализ и экспериментальную проверку методологии генерации случайных чисел. Метод устраняет необходимость в каком-либо экстракторе случайности, тем самым используя принципы квантовой физики для генерации случайных чисел. Средняя скорость передачи данных на выходе составляет 2,4 Мбит/с. Сгенерированные необработанные квантовые случайные числа сравниваются с предписанным NIST генератором псевдослучайных чисел Блюма-Блюма-Шуба и собственным аппаратным генератором случайных чисел от FPGA на платформе ENT и NIST.

Ключевые слова: генерация случайных чисел, InGaAs-детектор.

Физико-химические аспекты и биологическая активность конъюгатов нанодисперсного диоксида церия с сывороточным альбумином человека

Проскурнина Е.В., Костюк С.В., Созарукова М.М., Ершова Е.С., Вейко Н.Н., Попков М.А., Костюк Э.В., Мартынов А.В., Иванов В.К.

Нанодисперсный диоксид церия (CeO_2) обладает уникальной каталитической активностью в реакциях с участием активных форм кислорода (АФК), играющих роль медиаторов ключевых сигнальных путей. Альбумин является наиболее распространенным белком плазмы крови, взаимодействие с которым может влиять как на свойства наночастиц CeO_2, так и на саму биомолекулу. На модели эмбриональных фибробластов легкого человека (*in vitro*) исследовано, как конъюгация нанодисперсного CeO_2 с альбумином влияет на ряд биохимических параметров: жизнеспособность клеток, уровень внутриклеточных АФК, экспрессию NOX4, NRF2 и NF-κB, окислительное повреждение и репарацию ДНК, апоптоз, пролиферацию клеток и аутофагию. Результаты демонстрируют, что связывание диоксида церия с альбумином изменяет его физико-химические свойства, способствуя более эффективному поглощению наночастиц CeO_2 клетками. Конъюгация CeO_2 с белком ослабляет влияние наночастиц на внутриклеточный баланс АФК и митохондриальный мембранный потенциал. Примечательно, что конъюгаты CeO_2 с альбумином индуцируют более сильную активацию NOX4, что приводит к повышенному генотоксическому стрессу. Однако этот эффект компенсировался более эффективной активацией систем репарации ДНК по сравнению с немодифицированным диоксидом церия. Помимо этого, конъюгаты наночастиц CeO_2 с белком модулировали сигнальные пути, усиливая подавление провоспалительного каскада NF-κB и активируя процессы аутофагии. Таким образом, конъюгация наночастиц CeO_2 с альбумином не только снижает их цитотоксичность, но и усиливает противовоспалительный и регенеративный потенциалы диоксида церия.

Ключевые слова: наночастицы диоксида церия, сывороточный альбумин человека, цитотоксичность, генотоксичность, гены окислительного метаболизма, пролиферация, аутофагия, эмбриональные фибробласты легкого человека.

Совмещая точность и эффективность: оценка универсальных машиннообучаемых межатомных потенциалов для кластеров ниобий-кислород

Попов И.С., Валеева А.А., Еняшин А.Н.

Машиннообучаемые межатомные потенциалы (MLIP) обещают сочетание вычислительной точности теории функционала плотности (DFT) со скоростью типичной для методов молекулярной механики. Однако их надежность для сложных многокомпонентных систем требует тщательной валидации. В данной работе мы проводим оценку трех ведущих универсальных MLIP на примере кластеров оксида ниобия (Nb_nO_m, $n \leq 6$, $m \leq 6$), как сложнейшего теста. Система Nb-O хорошо подходит для этой задачи благодаря сложным межатомным взаимодействиям, проявление которых в макрокристаллической фазе приводит к стабилизации решётки с 25% упорядоченных вакансий, а на наноуровне – к широкому спектру нестехиометрических кластеров. В качестве референса используется набор данных о глобальных минимумах структур кластеров Nb-O, идентифицированных с помощью эволюционного поиска (USPEX) и DFT расчетов. Путем прямого сравнения структур, энергий и относительной стабильности, предсказываемых эволюционным поиском с использованием MLIP разного уровня, мы даём всестороннюю оценку точности и ограничений современных универсальных потенциалов для моделирования сложных наноразмерных оксидов.

Ключевые слова: DFT, машиннообучаемые потенциалы, MLIP, эволюционный алгоритм, оксид ниобия, NbO, наночастица, кластер, USPEX.

Формирование высокодисперсных композиций V – C – O – Ni и V – N – O – Ni в условиях низкотемпературной азотной плазмы

Авдеева Ю.А., Лужкова И.В., Мурзакаев А.М., Ермаков А.Н.

В условиях плазмохимического синтеза в низкотемпературной (4000-6000^{0}C) азотной плазме из механических смесей, содержащих в своем составе карбид или нитрид ванадия с металлическим никелем в соотношении 1:1, получены ультрадисперсные и нанокристаллические порошковые композиции VC – Ni и VN – Ni. Рентгенографические исследования показали, что полученные плазмохимические частицы содержат в своем составе оксикарбиды и оксинитриды ванадия, металлический никель, а также характеризуются присутствием оксидных фаз системы V – O. Электронно-микроскопические исследования нанокристаллических фракций порошковых композиций VC – Ni и VN – Ni в рамках просвечивающей электронной микроскопии высокого разрешения визуализировали строение полученных частиц. В условиях использования быстрого преобразования Фурье было показано, что тугоплавкие составляющие и металлический никель формируют индивидуальные частицы нанометрового диапазона, не контактирующие между собой. На основе проведенных исследований сформулирован химический механизм организации высокодисперсных механических смесей V – C – O – Ni и V – N – O – Ni в условиях закалочных процессов в турбулентном потоке газообразного азота, протекающих со скоростью $10^{5\,0}$C/c.

Ключевые слова: карбид ванадия, нитрид ванадия, никель, плазмохимический синтез, рентгенофазовый анализ, просвечивающая электронная микроскопия высокого разрешения.

Цеолит клиноптилолит, механохимически модифицированный полиэтиленгликолем для получения нефтесорбентов

Дабижа О.Н.

Исследовано влияние «мягкой» механохимической активации в воздушной атмосфере смеси клиноптилолит-цеолитовых пород с 10; 20 мас. % полиэтиленгликоля ПЭГ-4000 на структуру, физические и нефтеадсорбционные свойства. Дозы приложенной механической энергии составили 2,16 и 5,04 кДж/г. Показано, что клиноптилолитовая порода, модифицированная 10 мас. % полиэтиленгликоля при дозе механической энергии 5,04 кДж/г, и клиноптилолитовая порода, модифицированная 20 мас. % этого полимера при дозе энергии 2,16 кДж/г, имеют нефтеемкость на твердой поверхности 1,4 г/г. Установлено, что в ИК-спектрах этих образцов отношение интенсивностей полос поглощения, обусловленных валентными колебаниями силоксановых и гидроксильных групп, составляет не менее 3,2, а пористость слоя - не менее 72 %. Выявлена корреляция между нефтеемкостью и содержанием полимера, пористостью, структурными изменениями.

Ключевые слова: клиноптилолитовый цеолит, механохимическая активация, полимер, полиэтиленгликоль, маслоемкость.

Контролируемый выход однородных полипептидов из углеродной нанотрубки при изменении водородного показателя: молекулярно-динамическое моделирование

Кручинин Н.Ю.

С использованием молекулярно-динамического моделирования при различных уровнях pH исследованы изменения конформаций однородных полипептидов, которые располагались по одиночке или попарно внутри углеродной нанотрубки. Рассчитаны радиальные распределения плотности атомов полипептида, распределения атомов макроцепи вдоль оси

нанотрубки, а также зависимости различных компонентов потенциальной энергии наносистемы. В изоэлектрической точке полипептиды находились в центральной части углеродной нанотрубки, распластываясь по ее стенкам. По мере отклонения уровня pH от изоэлектрической точки одиночно расположенный внутри углеродной нанотрубки полипептид сначала разворачивался и вытягивался вдоль ее оси, а когда почти все звенья макромолекулы приобретали электрический заряд – происходил ее выход из нанотрубки. Попарно расположенные внутри углеродной нанотрубки полипептиды при изменении водородного показателя отталкивались друг от друга и смещались на противоположные концы нанотрубки, высвобождаясь из нее.

Ключевые слова: молекулярная динамика, углеродная нанотрубка, полипептид, водородный показатель, конформация, контролируемый выход.

Влияние скорости вращения на структурные, морфологические и оптические свойства тонких пленок легированной сурьмой окиси олова (SnO□), полученных методом золь-гель центрифугирования

Субраманьям Д., Раджеш Кумар Б., Чандрасекара Редди К.

Пленки диоксида олова, легированного сурьмой (ATO), были получены на стеклянных подложках методом центрифужного нанесения при скоростях вращения от 2000 до 3500 об/мин. Исследовано влияние скорости вращения на физические свойства пленок Sb-SnO_2. Рентгенограммы пленок Sb-SnO_2 демонстрируют тетрагональную структуру рутила. Морфология поверхности показывает однородный рост пленок со сферической структурой, а при более высоких скоростях вращения наблюдалась агломерация зерен. Пленки Sb-SnO_2, полученные при 3500 об/мин, показывают оптимальное пропускание 82% в видимой области. Энергия оптической запрещенной зоны пленок Sb-SnO_2 увеличилась с 3.23 до 3.46 эВ вследствие эффекта Бёрстайна-Мосса. Удельное электрическое сопротивление пленок Sb-SnO_2 увеличилось с 2.80×10^{-4} до 3.86×10^{-4} Ом·см при увеличении скорости вращения с 2000 до 3500 об/мин.

Ключевые слова: пленки Sb-SnO_2, рентгеноструктурный анализ, морфология поверхности, оптические свойства, электрические свойства.

Включение селенида марганца в полимеризованные листы восстановленного углерода: эффективный и стабильный электрокатализатор окисления метанола

Кавита Муруган, Калайараси Сентурпанди, Ведхи Чиннапайян, Мутучударкоди Раджа Рам

Полимерный нанокомпозит восстановленный оксид графена/селенид марганца @поли-N-метилпиррол (RGO/MnSe@P-NMPy) синтезирован методом химической окислительной полимеризации in situ. Исследование полимерного нанокомпозита RGO/MnSe@P-NMPy проводилось с помощью ИК-Фурье-спектроскопии, УФ-видимой спектроскопии, рентгеновской дифракции, просвечивающей электронной микроскопии (ПЭМ) и электрохимических исследований, а также методом FESEM с использованием EDAX. Реакция окисления метанола в основных средах была подтверждена методом циклической вольтамперометрии. Электрокатализатор RGO/MnSe@P-NMPy демонстрирует превосходную электрокаталитическую активность, более низкий окислительный потенциал (0,1 В), повышенную плотность тока (96 мА/см²) и превосходную стабильность в реакции окисления метанола (MOR) в основных средах. Для наногибридного электрокатализатора RGO/MnSe@P-NMPy значение ECSA составило 183,7 м²/г. Этот результат наглядно демонстрирует, что полимерный нанокомпозит RGO/MnSe@P-NMPy имеет больше

активных центров для реакции MOR. Хроноамперометрия использовалась для демонстрации того, что по сравнению с другими нанокомпозитами наличие полимерного нанокомпозита RMP повышает стабильность (в 1000 раз) и обеспечивает более высокую плотность тока (27,71 мА/см²) окисления метанола. Согласно полученным результатам, введение P-NMPy в структуру RGO/MnSe может улучшить эффективность окисления метанола и повысить устойчивость к CO по сравнению с монометаллическим катализатором. Данное исследование обосновывает потенциальную разработку высокоэффективных и недорогих катализаторов для хранения, преобразования энергии и других полезных применений.

Ключевые слова: RGO, MnSe, поли-N-метилпиррол (P-NMPy), RGO/MnSe@P-NMPy (RMP), плотность тока, реакция окисления метанола (MOR).

Модифицированные наночастицы селенида цинка для удаления тяжелого металла железа (Fe) из водных растворов

Хуршед А. Шах, Хумайра С. Ван, С.М.А. Андраби, Квинтон Л. Уильямс

Железо является тяжелым металлом, который присутствует в воде вследствие природных геологических источников, бытовых отходов, промышленных стоков и многочисленных побочных продуктов. Чрезмерное количество железа в питьевой воде может вызывать серьезные проблемы со здоровьем у людей. В настоящем исследовании металлические наночастицы Zn-Se, модифицированные серебром и мочевиной, были синтезированы золь-гель методом и охарактеризованы с помощью РФА, FESEM, EDX и ИК-Фурье спектроскопии. Синтезированные наночастицы ZnSe:Ag:Urea использовались для адсорбционного удаления железа – тяжелого металла – из воды. В данной работе для извлечения ионов железа из воды была применена адсорбционная технология, учитывая токсичность железа при высоких концентрациях. Проведены эксперименты по адсорбции в периодическом режиме на водном растворе, содержащем ионы Fe (III), в различных условиях: температуры, времени контакта, дозы сорбента и начальной концентрации ионов металла. Результаты показали, что адсорбция железа протекает эффективно с максимальной степенью удаления 89,5% в оптимальных условиях: комнатная температура, доза сорбента 0,1 г/л и объем раствора 100 мл. Равновесие адсорбции железа достигалось в течение 80 минут при использовании ZnSe:Ag:Urea в качестве сорбента.

Ключевые слова: наночастицы ZnSe, железо, тяжелый металл, адсорбция.

Фуллерены GdI_3: Изучение структурных и электронных свойств методом DFT

Еняшин А.Н.

В работе предложено существование нуль-мерной фуллереноподобной формы иодида гадолиния (III). Сконструированы модели фуллеренов GdI_3 тетраэдрической, октаэдрической и икосаэдрической морфологии с размерами до ~1000 атомов. Методом функционала электронной плотности исследованы их стабильность и электронные свойства. Аналогично другим известным неорганическим фуллеренам и нанотрубкам энергии свёртки фуллеренов GdI_3 уменьшаются с увеличением радиуса и всегда оказываются больше энергий свёртки нанотрубок GdI_3 тех же радиусов. Фуллерены с морфологией октаэдра или икосаэдра оказываются наиболее стабильными. Вне зависимости от размера и морфологии все рассмотренные фуллерены GdI_3 являются полупроводниками с вероятно ферромагнитным типом упорядочения при сверхнизких температурах. Щели ВЗМО-НСМО в электронной структуре фуллеренов GdI_3 оказываются на 1.1-1.7 эВ меньше, чем запрещённая щель для плоского монослоя GdI_3.

Ключевые слова: Трииодид гадолиния, фуллерены, расчёты DFT

Эффект формирования лабиринтообразных массивов никелевых наностержней на поверхности никеля в результате реакции гальванического замещения в водных растворах смеси $CuCl_2$ и NaCl

Толстой В.П., Никитин К.Д., Батищева Е.В.

В статье излагаются условия обработки поверхности никеля в водных растворах смеси солей $CuCl_2$ и NaCl. В результате исследования впервые установлено наличие селективного травления поверхности никеля, обусловленного реакцией гальванического замещения (ГРЗ). В процессе травления формируются массивы лабиринтов со стенками из никелевых наностержней диаметром от 10 до 50 нанометров и длиной до 0,5 мкм, расположенных преимущественно в направлении, перпендикулярном поверхности. Полученные экспериментальные результаты позволили сформулировать гипотезы о последовательности химических реакций, протекающих на поверхности, и роли диффузионно-химической модели А. Тьюринга в формировании наблюдаемых лабиринтов. Показано, что наличие таких лабиринтов на поверхности никеля приводит к уменьшению углов его смачивания водой.

Ключевые слова: никель, $CuCl_2$, гальваническое замещение, наностержни, массивы.

Влияние варьирования прекурсоров на морфологию и электрохимические характеристики тонких пленок NiS_x, синтезированных с помощью метода SILAR

Канева М.В., Мелешко А.А., Теневич М.И., Еникеева М.О., Кодинцев И.А., Лобинский А.А.

В данной работе тонкие пленки сульфида никеля были синтезированы методом SILAR с использованием различных солей никеля в качестве прекурсоров. Было систематически исследовано влияние соли-прекурсора на морфологию и электрохимические характеристики слоев. Анализ СЭМ показал, что пленки NiS_x, полученные из хлорида никеля, демонстрируют наиболее однородную и свободную от трещин морфологию. Электрохимические измерения показали корреляцию между морфологией пленок и емкостными характеристиками. В частности, электрод на основе NiS_x, синтезированный с использованием раствора соли хлорида никеля, показал максимальную удельную емкость, равную 1902 Ф/г при плотности тока 1 А/г. Полученные результаты подчеркивают решающую роль выбора прекурсора в оптимизации структурных и электрохимических свойств электродов на основе сульфида никеля для применения в устройствах хранения энергии.

Ключевые слова: сульфид никеля, прекурсоры, тонкие пленки, SILAR, электрод, суперконденсатор.

NANO ФХМ

NANOSYSTEMS:

PHYSICS, CHEMISTRY, MATHEMATICS

INFORMATION FOR AUTHORS

The journal publishes research articles and reviews, and also short scientific papers (letters) which are unpublished and have not been accepted for publication in other magazines. Articles should be submitted in English. All articles are reviewed, then if necessary come back to the author to completion.

The journal is indexed in Web of Science Core Collection (Emerging Sources Citation Index), Chemical Abstract Service of the American Chemical Society, Zentralblatt MATH and in Russian Scientific Citation Index.

Author should submit the following materials:

1. Article file in English, containing article title, the initials and the surname of the authors, Institute (University), postal address, the electronic address, the summary, keywords, MSC or PACS index, article text, the list of references.
2. Files with illustrations, files with tables.
3. The covering letter in English containing the article information (article name, MSC or PACS index, keywords, the summary, the literature) and about all authors (the surname, names, the full name of places of work, the mailing address with the postal code, contact phone number with a city code, the electronic address).
4. The expert judgement on possibility of publication of the article in open press (for authors from Russia).

Authors can submit a paper and the corresponding files to the following addresses: nanojournal.ifmo@gmail.com, popov1955@gmail.com.

Text requirements

Articles should be prepared with using of text editors MS Word or LaTex (preferable). It is necessary to submit source file (LaTex) and a pdf copy. In the name of files the English alphabet is used. The recommended size of short communications (letters) is 4-6 pages, research articles– 6-15 pages, reviews – 30 pages.

Recommendations for text in MS Word:

Formulas should be written using Math Type. Figures and tables with captions should be inserted in the text. Additionally, authors present separate files for all figures and Word files of tables.

Recommendations for text in LaTex:

Please, use standard Latex without macros and additional style files. The list of references should be included in the main LaTex file. Source LaTex file of the paper with the corresponding pdf file and files of figures should be submitted.

References in the article text are given in square brackets. The list of references should be prepared in accordance with the following samples:

[1] Surname N. *Book Title*. Nauka Publishing House, Saint Petersburg, 2000, 281 pp.
[2] Surname N., Surname N. Paper title. *Journal Name*, 2010, **1** (5), P. 17-23.
[3] Surname N., Surname N. Lecture title. In: Abstracts/Proceedings of the Conference, Place and Date, 2000, P. 17-23.
[4] Surname N., Surname N. Paper title, 2000, URL: http://books.ifmo.ru/ntv.
[5] Surname N., Surname N. Patent Name. Patent No. 11111, 2010, Bul. No. 33, 5 pp.
[6] Surname N., Surname N. Thesis Title. Thesis for full doctor degree in math. and physics, Saint Petersburg, 2000, 105 pp.

Requirements to illustrations

Illustrations should be submitted as separate black-and-white files. Formats of files – jpeg, eps, tiff.

НАНОСИСТЕМЫ:

ФИЗИКА, ХИМИЯ, МАТЕМАТИКА

Научный журнал
ISSN 2220-8054
DOI: 10.17586/2220-8054

2025. Том 16. № 5

Свидетельство о регистрации средства массовой информации ПИ № ФС 77–49048
выдано 22.03.2012 г. Федеральной службой по надзору в сфере
связи, информационных технологий и массовых коммуникаций (Роскомнадзор)

Учредитель и издатель:
федеральное государственное автономное образовательное учреждение высшего
образования «Национальный исследовательский университет ИТМО»
197101, Российская Федерация, Санкт-Петербург, Кронверкский пр., 49, литер А

Адрес редакции:
191002, Санкт-Петербург г., ул. Ломоносова, д. 9, литер А
телефон: (812) 607-02-54, e-mail: nanojournal@itmo.ru
http://nanojournal.ifmo.ru/

Главный редактор: д.ф.-м.н., проф. Попов Игорь Юрьевич, iypopov@itmo.ru

Подписано в печать 27.06.2025 Дата выхода в свет 01.07.2025

Тираж 100 экз. 1 завод – 16 экз. Заказ № 17. Подписная цена.

Отпечатано: в ООО «Университетские телекоммуникации» Типография на Биржевой
Адрес: 199034, Санкт-Петербург, В.О., Биржевая линия, д. 16
Телефон: +7(812) 915-14-54, e-mail: zakaz@TiBir.ru

Журнал распространяется по подписке.
Подписку можно оформить online по Объединенному каталогу «Пресса России»
(http://www.pressa-rf.ru), подписной индекс 57385